Università degli Studi di Napoli Federico II

Scuola Politecnica e delle Scienze di Base

Dipartimento di Ingegneria Industriale

Corso di Dottorato in

Ingegneria Industriale

Modelling and dynamic simulation of advanced polygeneration systems based on Power-to-X technologies

Relatori:

Prof. Ing. Francesco Calise

Prof. Ing. Massimo Dentice d'Accadia

Candidato:

Luca Cimmino

DOTTORATO DI RICERCA IN INGEGNERIA INDUSTRIALE, CICLO XXXVI

To my family, who made a man out of me.

To my friends, who made a better person out of me.

To my supervisors, who made a researcher out of me.

And to my love, Athena, who made sense out of my life.

“La propria destinazione non è mai un luogo,

ma un nuovo modo di vedere le cose”

Henry Miller

Table of Contents

List of figures

List of tables

List of abbreviations

AD	Anaerobic Digestion
ADM1	Anaerobic Digestion Model n°1
AEC	Alkaline electrolysis cell
CSTR	Continuously-stirred tank reactor
EES	Electric energy storage
CAES	Compressed air energy storage
CCS	Carbon capture and storage
CHP	Cogeneration of heat and power
CNG	Compressed natural gas
CPVT	Concentrating photovoltaic-thermal
D	Diverter
DHC	District heating and cooling
DHW	Domestic hot water
DryC	Dry cooler
EG	Exhaust gases
ESS	Electricity storage system
ETC	Evacuated tubes collector
EU	Europe
EV	Electric vehicle
GDP	Gross domestic product

GHE	Geothermal heat exchanger
GHG	Greenhouse Gas
GHP	Geothermal heat pump
HE	Heat exchanger
HP	Heat pump
HRSG	Heat recovery steam generator
IEA	International Energy Agency
IPCC	International Panel on Climate Change
IRENA	International Renewable Energy Agency
KPI	Key performance indicator
LBM	Liquefied biomethane
LCA	Life cycle assessment
LCOE	Levelized cost of energy
LCOP	Levelized cost of product
LIB	Lithium-ion battery
LNG	Liquefied natural gas
M	Mixer
MCFC	Molten carbonate fuel cell
OFMSW	Organic fraction of municipal solid waste
AFC	Phosphoric acid fuel cell
PCM	Phase change material
PEMF	Proton exchange membrane fuel cell

PV	Photovoltaic
PVT	Photovoltaic thermal
P2C	Power to chemical
P2F	Power to fuel
P2G	Power to gas
P2H	Power to heat
P2L	Power to liquid
P2M	Power to methane
P2X	Power to X
SOEC	Solid oxide electrolysis cell
SOFC	Solid oxide fuel cell
TES	Thermal energy storage
VFA	Volatile Fatty Acids
WT	Wind Turbine
WWHP	Water-water heat pump

Synopsis

During the last 70 years, from the mid-20th century to these days, the world was theatre of an incredible surge in technological growth and exponential increase in global population. This era marked the beginning of what is often referred to as the 'Great Acceleration', a period characterized by rapid industrialization and technological innovation post World War II. Advancements in fields such as computing, telecommunications, and medicine, along with the widespread adoption of automation and digital technology, revolutionized everyday life and industry.

At the same time, the world population began to grow at an unprecedented rate, fuelled by improvements in healthcare and agriculture, leading to longer life expectancies and enhanced food production. This population boom contributed to increased urbanization and a surge in energy demand, setting the stage for the modern globalized society.

This period of rapid technological and population growth, however, came with its own set of challenges. The increased demand for energy, predominantly met by fossil fuels, led to heightened environmental concerns, notably climate change. In the pre-industrialized era, no one would have cared about how much energy was consuming or if their production processes were efficient or eco-friendly. Neither the amount of energy consumed per capita nor the CO_2 emitted were an issue. Nowadays, with an energy consumption per capita four times higher than in that time and a population which is almost ten times larger, these issues have arisen.

Recognizing the unsustainable nature of the existing energy practices, the latter part of the 20th century and early 21st century has seen a concerted push towards an energy transition. This shift aims to reduce the dependence on fossil fuels, mitigate the global warming, and promote the adoption of renewable energy sources. The recent developments in Power-to-X technologies are a testament to these efforts, showcasing innovative ways to harness and utilize the surplus energy generated from renewable sources.

In fact, what is currently known as Power-to-X is nothing else than the most advanced and high technological solution for avoiding wastage, in this case of renewable energy. Power-to-X is indeed the transformation of renewable energy surplus which could be wasted or even hurtful for the existing infrastructures, into useful energy carriers or other products, depending on the diverse needs. This

process signifies a critical advancement in efficiently utilizing excess renewable energy, aligning with the evolving needs of energy consumption and management.

This doctoral dissertation is an overview of a three-year effort in developing models, highlighting issues, and finding solutions for Power-to-X technologies adopted in diverse applications. The methodology adopted roots on the dynamic modelling and simulation of the systems proposed, which is pivotal when intermittent sources of energy are investigated. The first chapter introduces the reader to the current energy framework and delves into the concept of Power-to-X technology. The second chapter encompasses an extensive review of the state-of-the-art of the existing Power-to-X systems, investigating both real plants and scientific purposes. The third chapter deals with the first solution investigated, i.e. Power-to-Heat technology integrated with district heating and cooling systems. The fourth chapter investigates the dynamics of the storage of renewable energy excess in the form of hydrogen, also known as Power-to-Power solution. The fifth chapter performs an in-depth analysis of a Power-to-Gas system entirely based on renewable energy; integrating the anaerobic digestion process for production of biomethane and collection of CO_2. The sixth and last chapter reassumes the main findings of the analyses developed and discussed in the previous chapters.

Chapter 1
Energy framework

This chapter discusses the current energy framework, featured by the urgent imperative of reducing greenhouse gas emissions. Given the necessity of measuring with the always increasing challenges of climate change, renewable energy technologies have rapidly gained worldwide interest. In this realm, here is analyzed the intricate balance between technological advancement and environmental safeguard, highlighting the critical role of renewable energy sources in mitigating the effects of climate change.

Central to the discussion is the concept of 'Power-to-X', an innovative solution designed to maximize the utility of excess renewable energy. The chapter examines how, in an era of abundant technologies for exploiting renewable resources, Power-to-X stands as a headlight of efficiency, preventing the wastage of surplus energy by converting it into various useful forms. This transformation is not just a technical advancement but a necessary evolution in the approach to energy management, aligning renewable energy production with consumption demands.

Through a detailed analysis, it will be first assessed which is the current advancement in the spreading of renewable technologies, with a special focus on solar based systems. Then, the necessity and the complexities of implementing Power-to-X technologies, considering the technical, economic, and regulatory landscapes will be analyzed. The chapter provides a comprehensive understanding of the current state of renewable energy technologies, the pressing need for sustainable climate change actions, and the innovative strategies, like Power-to-X, that are essential to transition towards a more efficient and sustainable energy future.

1.1 A “now or never” call

An existential challenge arises from the CO_2 emissions and their direct correlation with the alarming increase in global temperature. Citing the latest report from the Intergovernmental Panel on Climate Change (IPCC) and statements from UN Secretary-General António Guterres, the humanity is at a pivotal point, facing a "climate time-bomb" [1]. Figure 1 shows the increase in the global surface temperature and the related risks and impact related to all the possible future scenarios.

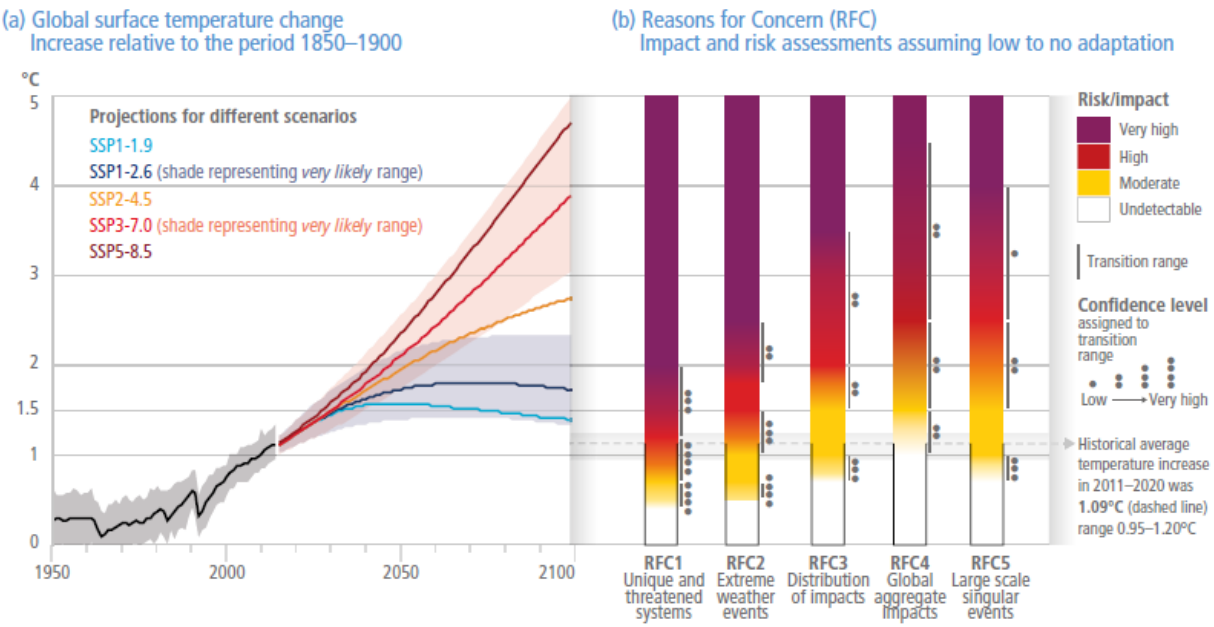

Figure 1. Global surface temperature change (a) and Reason for Concern (b) for all the projections analyzed by the IPCC [1].

The data presented in the IPCC 2022 report lead to a critical analysis, demonstrating how current levels of CO_2 in the atmosphere are the highest in over two million years. In the Shared Socioeconomic Pathways (SSP), shown in Figure 2, different scenarios ranging from sustainable to fossil-fuelled futures are critically analysed, considering the concept of radiative forcing as a key factor in climate dynamics. Through this analysis, it is critically assessed the need for immediate, innovative, and concerted climate action to mitigate the adverse effects of climate change and to steer the global community towards a sustainable trajectory.

Figure 2. Shared socio-economic pathways for the energy transition [1].

According to the US Department of Energy the Gross Domestic Product (GDP) is expected to grow by 1.5 % averagely among the OECD Countries and 3 % on the average among the non-OECD Countries by 2050 [2]. These values are compared in figure3. This growth rate may be significantly high for some developing Countries but it must be mandatorily sustainable for the environment and the humankind. The growth in GDP is strictly related to the increase in the overall primary energy demand, required to support the development. For developed Countries, a limited increase in primary energy demand is expected, due to the recent policies in terms of climate change. Conversely, for developing Countries a dramatic growth in primary energy demand is expected. Therefore, urgent actions must be implemented to prevent a dramatic environmental impact of this growth.

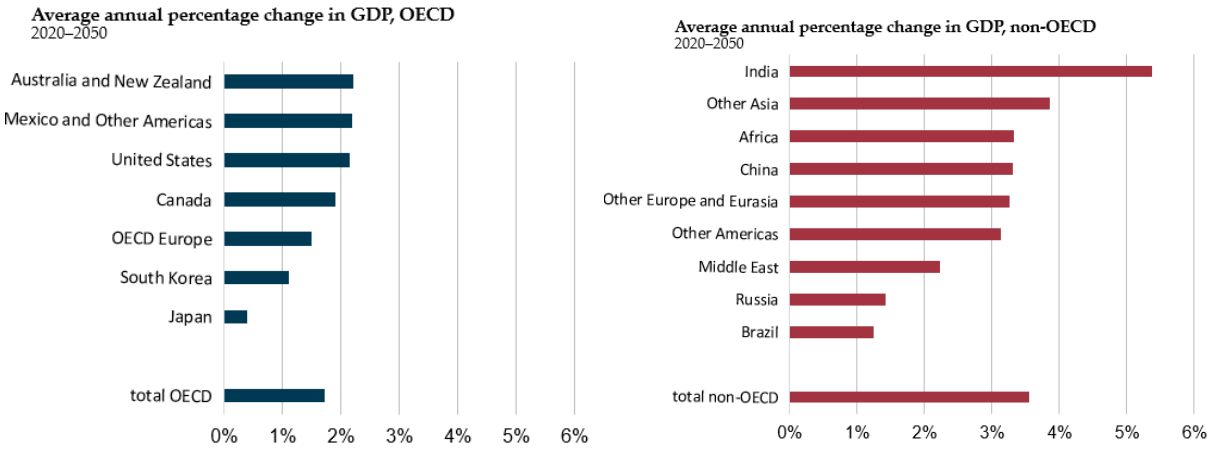

Figure 3. Average annual percentage change in GDP from 2020 to 2050 for OECD Countries (left) and non-OECD Countries (right) [1].

The severe issues related to the climate change are more and more evident with dramatic upsets of macroclimates compromising natural habitats and jeopardizing the life on the planet. After the Paris Agreement all the main global leaders stated that an increase of the average temperature above 1.5 °C would have been extremely life-threatening. Nowadays this threshold is already exceeded and the projections of the global temperature are alarming [3]. As it is well known, the cause of this global warming are greenhouse gas (GHG) emissions due to burning of fossil fuels needed to meet the global energy demand. According to the latest IEA report a peak in fossil fuel consumption will be observed in the year 2030, with a reverse trend below [4]. An unexpected push towards the energy transition is given by recent events such as the pandemic and the Ukrainian war. The latter in particular hastened the necessity of an alternative to the consumption of natural gas [5].

For this reason, an ever increasing effort is being made by Governments to accomplish the energy transition goal and get to the full decarbonisation of the main energy sectors by 2050 [6]. European Countries have already traced a step by step

path by issuing binding laws and regulations to boost the spread of renewable energies and track the CO_2 emissions [7]. In particular, with the Fit for 55 package the target of reducing by 55 % the GHG emissions in 2030 compared to 1990 levels became possible thanks to the introduction of an effective emission trading system (ETS) [8]. United States allocated 391 billion dollars in the Inflation Reduction Act (IRA) also aiming at promoting the investments in clean energy [9]. Canadian Government recently published an Emission Reducing Plan (ERP 2030) including key measures adopted to reduce GHG emissions by 40 % - 45 % below 2005 levels [10]. Japan unveiled a Green Transformation Policy to create a positive cycle of economic growth and environmental protection in Asia with a 1.1 trillion dollars investment [11]. Developing countries, such as Colombia, are included in the Paris Agreement and are participating to the energy transition with initiatives promoting a hydrogen road map (+H2 Colombia) [12].

The global energy scenario is experiencing a remarkable shift toward renewable technologies, with Europe at the vanguard of this transition. The International Energy Agency (IEA) has noted a significant leap in renewable energy capacity, expected to rise by one-third in 2023, with a sustained increase forecasted into 2024. Figure 4 shows the current expected scenario for renewable installation and CO2 emissions.

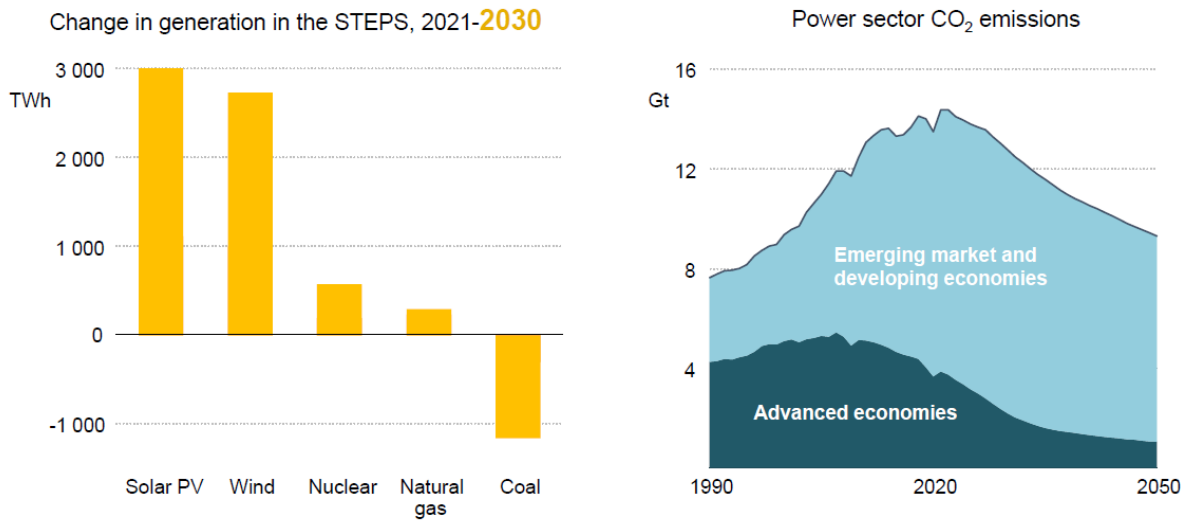

Figure 4. Renewable power installed capacity and CO_2 emissions reduction [1].

Solar photovoltaic (PV) installations are spearheading this growth, making up two-thirds of the overall increase in renewable power capacity for 2023. This acceleration is largely driven by the energy crisis, pushing European countries to expedite the deployment of renewables, particularly solar PV, and wind power, to enhance energy security and reduce dependence on fossil fuels [4].

Solar PV growth trajectory is complemented by wind energy, which is forecasted to experience a robust recovery, growing by almost 70% year-on-year. The rebound is mainly due to the completion of projects delayed by supply chain disruptions and Covid-19 restrictions. However, wind turbine supply chains are struggling to keep pace with the burgeoning demand, attributed to rising commodity prices and lingering supply chain challenges.

The International Renewable Energy Agency (IRENA) reported that the global renewable capacity, spearheaded by solar PV, increased substantially in 2022, with a cumulative installed capacity now exceeding 3'372 gigawatts. This expansion is particularly noteworthy in Europe, whose Countries contributed with 57.3 GW to the growth, thanks to policies aimed at reducing natural gas consumption and enhancing small-scale, rooftop solar PV systems, which have become more financially attractive due to high electricity prices [13].

In addition to solar and wind, Europe is also focusing on District Heating and Cooling (DHC) systems that leverage renewable energy. These systems are essential for reducing emissions from buildings, which are one of the largest energy consumers in urban areas. By integrating renewables, DHC systems can provide efficient heating and cooling solutions that align with the EU decarbonization goals [14]. The advancement of DHC systems is increasingly leveraging renewable energy sources, aiming to provide sustainable heating and cooling solutions in urban areas. These systems are pivotal for reducing the carbon footprint of the building sector, which is among the top energy consumers in Europe. The integration of renewables into DHC is a strategic component of the EU efforts to achieve its climate targets and enhance energy security.

Electric Vehicles (EVs) form another critical component of Europe energy transition, with governments across the continent incentivizing EV adoption through subsidies and investments in charging infrastructure. The shift towards EVs is not just a measure to combat air pollution but also a strategic move to decrease the transport sector reliance on oil [15].

The evolution of electric vehicles (EVs) is another significant aspect of the transition, with Europe investing heavily in EV infrastructure. Government incentives, including subsidies for purchasing EVs and investments in expanding charging networks, are propelling the adoption of electric mobility. This transition to EVs is nonetheless complemented by the integration of vehicles fuelled by bio-fuels and *e*-fuels [16]. EU policies on bio-fuels, i.e. bio-CNG (compressed natural gas), and bio-LNG (liquefied natural gas), vehicles focus on diversifying the transport sector

energy mix and reducing carbon emissions. However, when compared to electric vehicles (EVs) and *e*-fuels, the scale and nature of support differ.

The pathway to Europe energy transition is marked by concerted efforts to integrate a range of renewable technologies, including biogas plants, which convert organic waste into a source of energy. These technologies not only contribute to reducing greenhouse gas emissions but also support the circular economy by valorising waste streams [17].

Bio-CNG and bio-LNG, derivatives of biomethane, are seen as alternatives to natural gas for vehicles. Their expansion is limited, with growth depending on policy support and infrastructure development. The EU aims to increase renewable energy contributions and has directives in place to boost alternative fuel infrastructure, including for bio-CNG and bio-LNG. For instance, the EU commitment to expanding LNG infrastructure is evident in the planned increase of LNG stations, which is expected to grow sixfold by 2030 [18].

The comparison with EVs largely revolves around infrastructure and energy source. EVs benefit from a more straightforward infrastructure (charging stations) and a direct link to renewable energy sources like wind and solar power. The EU has been actively promoting the adoption of EVs through various incentives and targets. For instance, the European Green Deal aims for a 90% reduction in transport emissions by 2050, with EVs playing a significant role [19].

E-fuels, or synthetic fuels, are produced using renewable energy to synthesize fuels from carbon dioxide and water. While they offer potential for decarbonization, especially for sectors where electrification is challenging, their development is still in nascent stages. Policies supporting *e*-fuels are emerging, focusing on research, development, and scaling up production [20].

In terms of numbers, bio-LNG role in heavy-duty transport is significant; its production in the EU is expected to increase tenfold by 2030. This increase can help reduce CO_2 emissions from trucks by 55% with a 40% BioLNG mix. In contrast, the growth of EVs is more rapid and widespread, driven by technological advancements and stronger policy incentives.

In summary, while European policies on bio-fuels, bio-CNG, and bio-LNG focus on sustainable alternatives to conventional fuels, they differ from the approach towards EVs and *e*-fuels. EVs benefit from more direct policy support and infrastructure investment, while the development of *e*-fuels is still in early stages. However, EU has set the stage for increasing the production of *e*-fuels to fully decarbonize several energy sectors by 2050. With the European Green Deal a specific strategy was set for

hydrogen to get to 40 GW of electrolyzers and 10 million tonnes of green hydrogen produced by 2030, mainly for the production of P2X fuels. In the Fit For 55 directive two actions were approved named “FuelEU Maritime” and “ReFuelEU Aviation” [20], voted to increase the production of synthetic fuels as *e*-ammonia and *e*-kerosene. The former is expected to be competitive on the market for blending in marine Diesel engines, the latter to have a large share in the mix of fuels used for sustainable aviation.

The bio-fuel sector, with its need for more complex infrastructure and gradual policy evolution, demonstrates a different trajectory of growth and adoption compared to these alternatives. Unfortunately, the current EU grid infrastructure is not able to bear by itself the huge increasing in the renewable electricity demand and production [18]. As of early 2024, EU large-scale installation of photovoltaic (PV) systems faces several challenges, primarily related to the grid infrastructure and capacity needed to support this rapid expansion. Despite the substantial growth in solar PV installations, with over 41 GW installed across the EU in 2022, the existing transmission networks are not fully equipped for the new, more diverse, and distributed generation mix required for electrification [21].

The traditional model of centralized power plants delivering power through transmission networks is increasingly unsuitable for the current energy landscape. The shift towards distributed generation, including a significant portion of solar energy deployed in small-scale projects, private, and residential rooftop PV deployments, as well as electric vehicles and electric heat pumps, places additional demands on the distribution network. This network is already the source of the majority of grid outages today [22].

Addressing the renewable energy capacity growth requires a significant upgrade in EU grid infrastructure. Furthermore, the energy storage capacity needs a substantial increase, with projections suggesting that storage technologies should reach up to 191 GW by 2030 and potentially 488 GW by 2050. To meet these targets, the grid investment in the EU needs to increase significantly. The investment rule of thumb suggests 0.67 € should be invested in the grid for every 1 € invested in generation capacity, but currently, this figure is closer to 0.30 € [23].

In addition to technical and infrastructural challenges, Europe also confronts issues in competing with large-scale solar manufacturing, which is primarily dominated by imports from China. The European Commission is working on a large-scale rollout of solar energy and aims to rebuild Europe solar manufacturing industry. Initiatives like the "European Solar Rooftops Initiative" aim to help cut gas-fuelled power and

heating in various sectors and install solar energy in all suitable public buildings by 2025 [24].

1.2 The role of Power-to-X

While there is significant momentum and support for the expansion of solar energy in Europe, addressing the grid infrastructure challenges and boosting local manufacturing capacity are critical steps to ensure the successful and sustainable growth of the solar energy sector. To bear the issues of the grid outages and the energy wastage, the most immediate solution is the storage of the renewable power excess. In this realm, the adoption of electricity storage solutions is becoming increasingly crucial in addressing the challenges of grid outages and energy waste associated with the intermittency of renewable energy sources like solar power. Electricity Storage Systems (ESS) play a vital role in stabilizing the grid and ensuring a consistent energy supply [25].

Lithium-ion batteries, a prominent form of ESS, are widely used due to their high energy density, long cycle life, and decreasing cost. According to a study by Schmidt et al. [26], lithium-ion batteries have seen significant advancements in terms of energy density, which enhances their suitability for both grid and residential storage applications. However, there are concerns regarding resource availability for lithium and other critical materials, which could limit the scalability of this technology.

Despite the advantages of lithium-ion batteries, their limitations have led to the exploration of alternative storage solutions, such as power-to-X (P2X) technology. P2X refers to the conversion of electricity into another energy carrier, such as hydrogen or synthetic fuels (Power-to-Gas). This technology is particularly promising for long-term energy storage and can complement the short-term storage capabilities of lithium-ion batteries. A report by (IRENA) highlights the potential of P2X to provide seasonal storage and facilitate the integration of high shares of renewables into the energy system [27].

However, P2X technologies are still in their developmental stages and face challenges related to efficiency, cost, and the need for significant infrastructure development. For instance, the conversion process in Power-to-Gas systems entails energy losses, and the overall efficiency needs improvement [28]. However, while lithium-ion batteries are currently the dominant solution for energy storage, addressing their limitations and the evolving landscape of energy storage technologies, including the development of P2X, is essential. These advancements are critical in ensuring a stable

and sustainable energy supply, especially as the world increasingly relies on intermittent renewable energy sources.

The concept of P2X systems represents a critical advancement in the field of energy, particularly as the world shifts towards more sustainable and renewable energy sources. These systems offer innovative ways to store and utilize surplus energy generated from renewable sources, addressing the intermittency issues associated with solar and wind power.

P2X refers to various processes that convert electricity into other forms of energy, such as hydrogen (Power-to-Gas), heat (power-to-Heat), or liquid fuels (power-to-Liquid). The history of P2X begins with the development of electrolysis, a method used to split water into hydrogen and oxygen using electricity. Over the years, advancements in renewable energy technologies have amplified the significance of P2X systems, especially as a solution to store excess energy generated from renewables.

The evolution of electricity storage systems has been pivotal in advancing P2X technologies. Lithium-ion batteries, as already described, have diverse pros and cons which inhibit the possibility of continuously using them for future applications. Therefore, to address the limitations of conventional storage systems like lithium-ion batteries, the P2X technology has gained prominence. P2X offers an effective way to store surplus renewable energy over longer periods, making it possible to balance supply and demand on the grid. For example, in Power-to-Gas systems, excess electricity is used to produce hydrogen, which can be stored and later reconverted into electricity or used as a clean fuel [29].

Chapter 2
State-of-the-art of the Power-to-X technologies

Multiple definitions have been given of P2X technology. Burre et al. defined it as "the process whose goal is to exploit the environmental and economic potential of renewable electricity" [30]. Michael Sterner, professor of OTH Regensburg University, Germany, defined the P2X as "an umbrella term for different ways of generating energy", referring to all the possible forms of energy previously mentioned, i.e., heat, liquid, chemicals, gas, fuel [31]. The Dansk Energi company, 2020, defined it as "the process converting green electricity into hydrogen" [32], which is similar to the definition given by Lim JY et al. which claimed that "the concept of Power-to-X can be further incorporated to transform the generated renewable electricity into chemical energy stored in the gas form" [33].

All these definitions are correct, but probably each of them needs the others to fully understand the real concept of P2X. This is indeed the technology whose concept arises from the necessity of exploiting the full potential of renewable energy and which translates the issue of surplus into the opportunity of producing energy carriers or products which are of utmost interest to the end user. This term has nowadays the broader meaning here explained but when it had an evolution during the years [34]. The term first appeared in 2014 in a report of the German Aerospace Centre, as a description of the long-term storage of renewable electricity, which is first converted into something – X – and then used again in the form of power. Later on, the same terminology was continuously adopted as a broader extending of large-scale storage systems. This until 2019, when the IRENA used the term for describing the process from which *e*-fuels were obtained, i.e. chemicals produced starting from renewable electricity.

As said, there is a wide spectrum of solutions which go under the cap of the P2X technology, all representing possible solutions for exploiting the renewable energy surplus. These technologies play a crucial role in integrating renewable energy into the broader energy system by addressing issues of intermittency and enabling long-term energy storage. Figure 5 shows an overview of the pathways of the current P2X technologies.

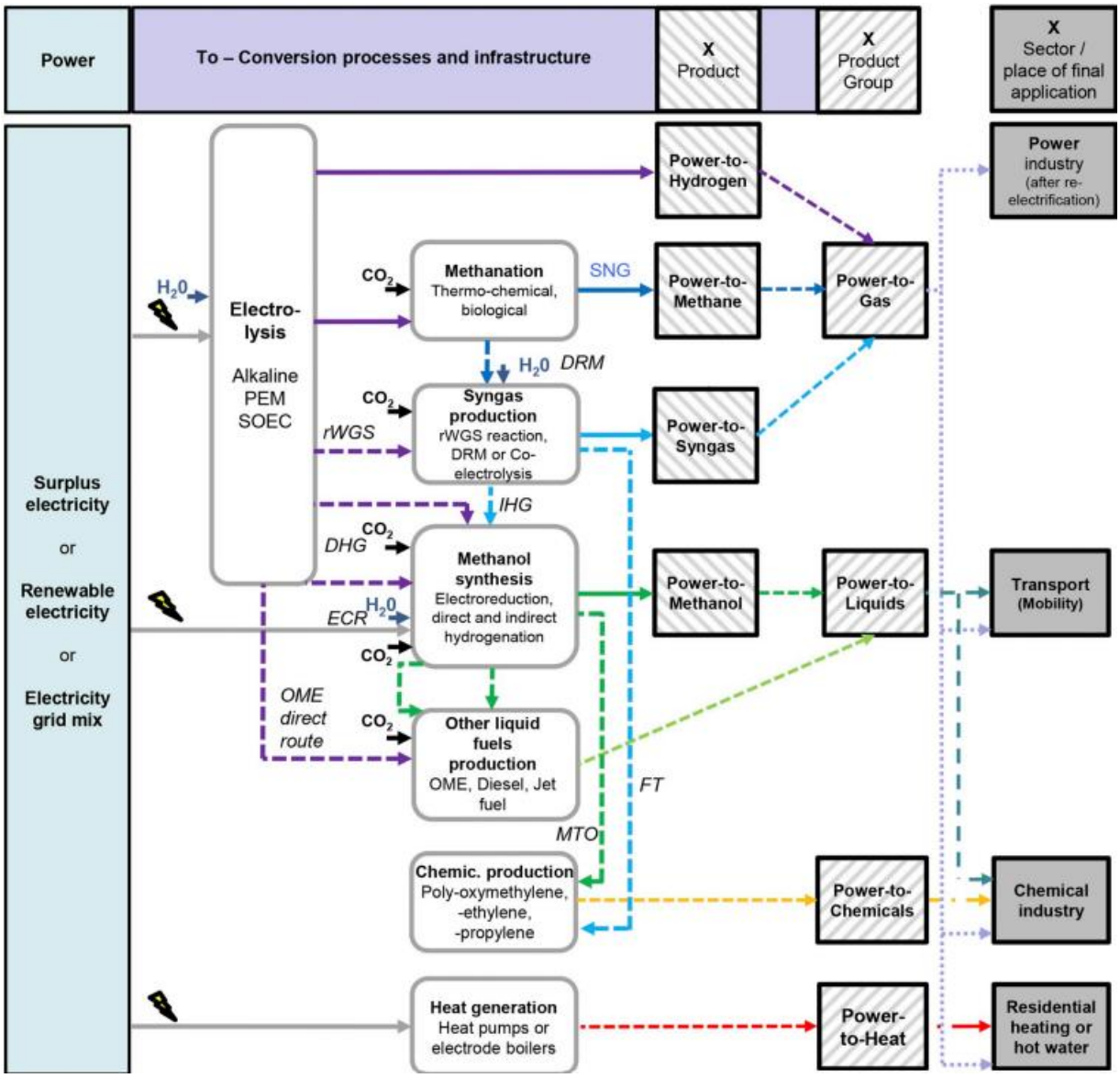

Figure 5. Diverse pathways of Power-to-X technologies [35].

Power-to-Heat: This technology converts electric energy into heat, which can be used for industrial processes or heating buildings. Power-to-Heat systems often involve electric boilers or heat pumps. They are particularly useful in regions with high shares of renewable electricity, providing an alternative to fossil fuel-based heating systems [36].

Power-to-Liquid: Power-to-Liquid involves converting electricity into liquid fuels, such as synthetic gasoline or diesel. This process typically includes electrolysis to produce hydrogen, which is then combined with carbon dioxide to form hydrocarbons. The technology is seen as a way to produce carbon-neutral fuels for sectors that are hard to electrify, like aviation [37].

Power-to-Chemicals: This involves synthesizing chemicals using electricity, often from renewable sources. One common application is the production of hydrogen through water electrolysis. Hydrogen can then be used as a raw material in various

industrial processes, including the production of ammonia for fertilizers. Moreover, the *e*-ammonia can be used as a fuel for maritime engines according to the latest EU directives [20].

Power-to-Gas: This technology converts electric energy into gaseous energy carriers, primarily hydrogen or synthetic natural gas. The process starts with the electrolysis of water to produce hydrogen, which can be used directly or further processed into methane through methanation. Power-to-Gas offers a way to store excess renewable energy and utilize existing gas infrastructure [38]. A subset of Power-to-Gas, power-to-methane involves producing methane by combining hydrogen from electrolysis with carbon dioxide. This methane can be injected into the natural gas grid or used as a renewable fuel, providing a solution for long-term energy storage and carbon utilization [39].

Power-to-Power: Also known as energy storage, Power-to-Power involves storing electricity in a form that can be converted back into power as needed. This can be done through various technologies, including batteries, pumped hydro storage, and chemical storage in form of hydrogen, which is again converted into power, as in the case of electrolyzer-fuel cell coupled systems [40]. It is essential for balancing supply and demand in electricity grids with high shares of intermittent renewable energy sources

In conclusion, P2X technologies are versatile and crucial for the integration of renewable energy into various sectors of the economy. By enabling the conversion of electricity into heat, fuels, chemicals, and other forms of energy, P2X technologies address the intermittency of renewable sources and enhance the flexibility of the energy system. These technologies are a crucial step in the transition towards a more sustainable and renewable-based energy future.

2.1 Power-to-Heat

Power-to-heat (P2H) technology is an emerging and significant area in the realm of renewable energy integration and efficient energy management. As the need for sustainable energy solutions becomes increasingly urgent, P2H technology has gained attention for its potential to bridge the gap between excess electricity generation from renewable sources and thermal energy demand.

In this section the most recent advancements in the technology are discussed to delve into the state of art of these systems and the latest plants developed are analyzed.

2.1.1 State of the art of P2H

The current state of P2H technology is marked by a blend of established methods and innovative approaches. Traditional P2H systems primarily involve the use of electric heaters or heat pumps to convert electric energy into heat. This process is increasingly being utilized to absorb surplus energy from renewable sources such as wind and solar power, thus aiding in grid stabilization and reducing reliance on fossil fuels.

The role of P2H in smart grids in particular has garnered attention, especially in terms of maximizing the value of grid flexibilities and ensuring efficient energy distribution.

According to ref. [41], P2H is a flexible measure helpful to move towards decarbonization of the energy sector and cover 37 % of total heat production by 2050. In this paper, the flexibility issue is addressed by analysing possibility of sector coupling via P2H and P2G applications by using system dynamics approach, and the model is applied to the case of Latvia.

In ref. [42] the flexibility gain provided by P2H in the context of a district heating facility is discussed. It evaluates the impact of adding a P2H unit to the facility and highlights the influence of the regulatory framework on its usage and profitability. The authors evaluate the flexibility gain of a P2H installation using the example of adding it to a district heating facility in Germany and show that the regulatory framework has a crucial influence on usage and profitability of a P2H unit.

A broader analysis on the gain in flexibility provided by P2H systems is made by Gjorgievski et al. [43]. The paper discusses the potential of P2H demand response in improving the flexibility of the energy system. It reviews 34 large-scale projects and classifies them based on location, size, technical implementation, and objective. The paper suggests that P2H demand response has been historically used to address infrastructure capacity limitations and is now being explored for real-time balancing and frequency response. The economic and policy frameworks have a significant effect on the diffusion of power-to-heat demand response.

From the techno-economic aspect, recent studies have explored the economic feasibility and technical viability of P2H systems. This includes analysis of cost structures, efficiency metrics, and long-term financial benefits, especially in the context of large-scale adoption.

In Vannoni et al. [44], the authors explore and compare performance and economic indicators under different installation conditions, considering compression heat pumps employing four different fluids: a traditional HCF (R134a) and three natural

fluids, ammonia (R717), butane (R600), and propane (R290), often preferred nowadays to HCFs due to the lower global warming potential. R717, within its domain of applicability, always results to be the most profitable option. R134a and R290 present very similar results, with the R290 slightly more profitable for HP operating with low temperature heat source. Despite the R600 is the most versatile fluid, when compared against the others it presents the lowest ΔNPV, its gap in profitability is higher when the temperature level of the heat source is lower.

One of the latest technologies investigated in the field of P2H is the catalytic processes for decarbonization. This approach aims to utilize excess renewable energy in chemical processes, contributing to decarbonization efforts in industrial sectors.

Ambrosetti et al. [45] explore P2H technologies in the chemical process industry for decarbonization. The study employs a literature review to analyze four technologies: microwave heating, resistive heating, induction heating, and the RotoDynamic Reactor (RDR), focusing on their potential, energy efficiency, and scalability. Key findings reveal distinct advantages and challenges for each technology. Microwave heating is effective for selective heating but struggles with temperature distribution. Resistive heating offers simplicity but faces uneven heating issues. Induction heating is versatile but less energy efficient, while RDR is promising but still developing. The paper concludes that while P2H technologies hold promise for process intensification and decarbonization, challenges in uniform heating, energy efficiency, and industrial scalability must be addressed for their full potential in reducing the chemical industry carbon footprint.

Bloess et al. [46] provided a deep review of the technologies, the modelling approaches, and the flexibility potential of P2H solutions, particularly focusing on heat pumps and thermal storage. In Figure 6 is shown a simplified scheme of typical interconnections in P2H systems integrating electric and thermal smart network.

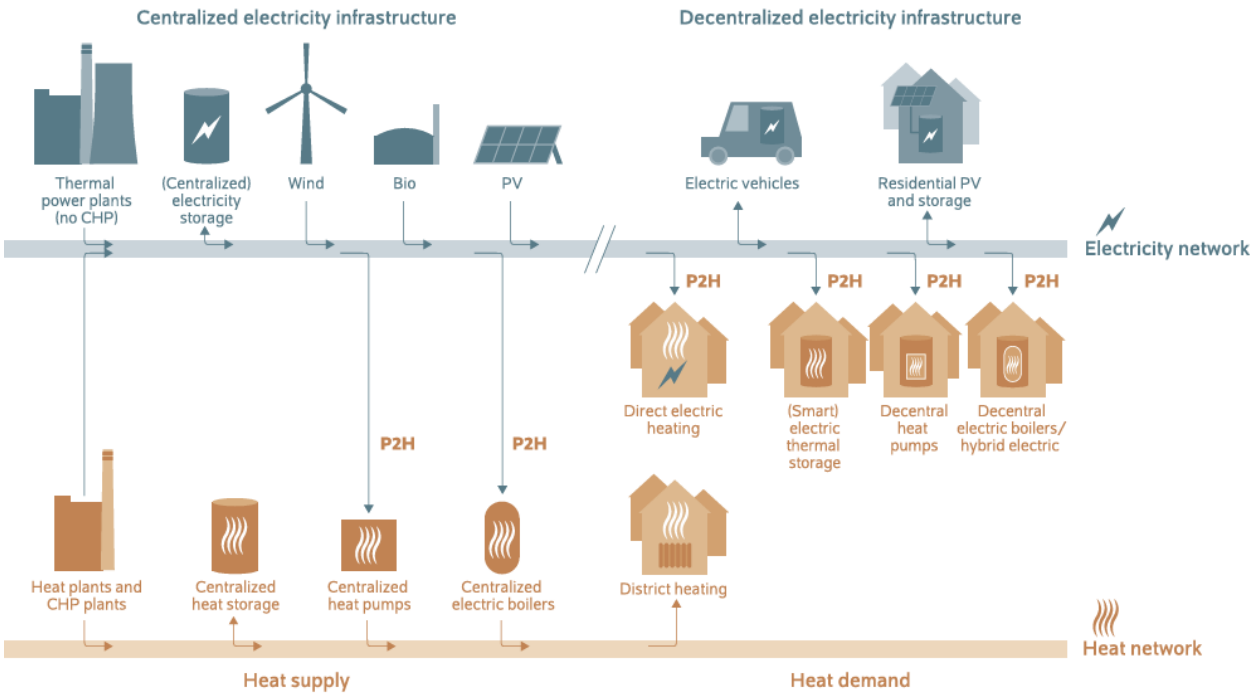

Figure 6. Interconnections of power-to-heat options with electricity and district heating networks [46].

In particular the figure shows how, in general, centralized systems use to withdraw energy from the electric grid to provide heat to the thermal network, by means of large- scale heat pumps or boilers. Conversely, decentralized P2H systems do not make use of heating networks, and also these systems barely integrate thermal storage.

The applications of the P2H technology are diverse and they might depend on several factors, as the end user, the most convenient technologies, or the necessity of storage. Figure 7 categorizes all the possible P2H solutions for residential applications. First, the difference between centralized and decentralized systems is made, and then those with or without thermal energy storage (TES).

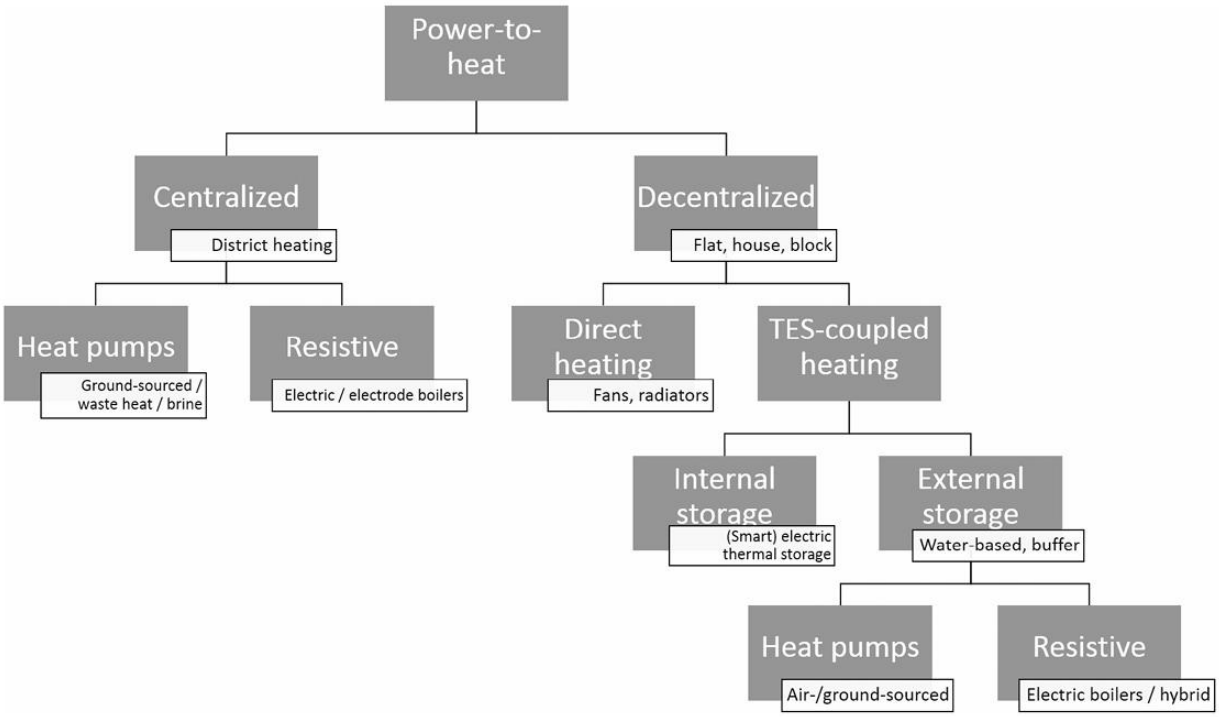

Figure 7. Categorization of residential power-to-heat options [46].

Centralized power-to-heat options convert electricity into heat at a location away from the heat demand, utilizing heating networks for distribution. Decentralized options, however, use electricity directly at or near the heat demand location. The distinction between these two is not always clear-cut; for example, heat might be provided locally for a small group of buildings.

Furthermore, centralized P2H systems inherently have some level of thermal storage due to the thermal capacity of district heating networks. This can be enhanced with dedicated storage facilities, allowing for seasonal storage. Decentralized systems might not include thermal energy storage (TES), known as direct heating, or they might integrate TES, termed storage heating or TES-coupled heating. TES can be internal, like in electric storage heaters with heat stored in insulated materials like ceramic bricks, or external, like hot water storage in residential heating systems.

Advanced systems with TES can be equipped with smart controls. Additionally, there is passive thermal storage, where heat is stored in building structures and released uncontrolled.

The development of advanced thermal storage solutions is a crucial step. This includes innovations in regenerator storage systems, which have significantly improved the thermal storage capacity and overall performance of P2H systems.

In Belik et al. [47], the authors introduce a transient model for electrically heated regenerator storage, enhancing thermal storage capacity and performance through the energy-efficient placement of electric heating elements and optimized designs,

significantly improving thermal storage capacity, cost efficiency, and operational flexibility.

The study employs a simplified two-phase transient and one-dimensional model focusing on axial heat transport for modelling the thermodynamic behaviour of Electric Flow Heater (EFH) and Solid Media Thermal Energy Storage (STES) units under cyclic conditions. Key Performance Indicators (KPIs) like gravimetric energy density, storage material utilization ratio, and the coefficient of uniformity for outlet temperature during discharging were used for technical and economic assessment.

The results are relevant for energy and cost-efficient solutions in converting excess electricity and storing it as high-temperature heat, presenting a significant advancement in the field of thermal energy storage, with implications for increased cost efficiency and operational flexibility.

2.1.2 Scientific literature and real operating P2H plants

The DHC systems are playing a crucial role in the decarbonization of the energy sector, especially when they also include renewable energy sources and are intended as P2H technologies. These networks are well-established in some Countries and, in such cases, they represent the most common technology in this sector. The integration of renewable power into DHC systems is indeed widely investigated in scientific literature.

Bordignon et al. [48] investigated a low-temperature DHC coupled with ground heat pumps and photovoltaic thermal (PVT) panels. Authors considered 3 different weather conditions, typical of cold areas. The system includes centralized ground source heat pumps to control the temperature of the ring and additional heat pumps are installed in the substations. PVT panels are installed on the roof of the buildings, providing a certain amount of electricity to the network. In addition, PVT panels are also cooled by the network, providing additional heat to the ring. The proposed system exhibits excellent results in terms of efficiency and grid independency showing good potential for small residential areas in cold climates.

Aste et al. [49] recently proposed an innovative DHC system located in the city of Milan, north of Italy, integrating several renewable technologies. A 1660 kW PV field meets the electricity demand of the district and an 800 kWt biomass boiler supplies energy for space heating and DHW in winter. Geothermal water heat pumps (GWHP) are also included to manage the thermal energy demand together with the biomass-based CHP unit. The proposed system showed very promising results with a share of renewables higher than 80% in the winter period and higher than 90% in summer.

Peiyuan et al. [50] proposed a new idea for the energy saving of clean DH systems. They modelled a novel layout based on electric boiler, gas boiler and air source heat pump supplied by photovoltaic and thermal panels (PVT) for a residential area of Dalian (China) in order to evaluate the economic performance of this layout. Authors of this paper performed several experimental analyses of a PVT heat pump system during the winter operation. They found that, for an average outdoor temperature ranging from − 0.1 °C to 1.4 C, the average coefficient of performance (COP) ranges from 2.55 to 2.9. The results of the simulation showed that the yearly average COP of PVT heat pump system in Dalian is 3.5, for an average water temperature of 40°C. The achieved payback period of the proposed energy saving strategy is lower than 5 years, showing the feasibility of the proposed layout. Fiorentini et al. [51] analysed the use of a borehole seasonal TES for a DHC network. A case study is performed for a DHC equipped with heat pumps in Switzerland. Authors found that the proposed optimized TES allows one to significantly reduce system CO_2 emissions.

Regarding existing plants, a recent report from IRENA [27] "Renewable Energy in District Heating and Cooling: A Sector Roadmap for REmap," outlines the potential for substantial scale-up of renewable energy in DHC systems globally. It emphasizes the role of renewable energy sources in meeting rising urban energy demands, enhancing efficiency, reducing emissions, and offering cost-effective temperature control. Currently, DHC systems are predominantly fuelled by fossil fuels, therefore these cannot currently be considered as P2H technologies, but there is a significant opportunity to modernize existing infrastructures and develop new networks using biofuels, solar, and geothermal technologies. Moreover, the integration of distributed renewable power generation systems is pivotal to increase the flexibility of these systems and develop zero emission districts, as for the realm of P2H. This could yield major benefits for energy security, human health, and climate change mitigation.

However, renewable DHC is yet to be fully utilized, with only a few countries, mostly in northern Europe, actively promoting it through policy initiatives. The study examines the status and potential of renewable DHC systems in several countries, accounting for about 40% of the global energy used in DHC as of 2015. These countries exhibit a variety of climates, population densities, and energy demand growth patterns, providing a diverse perspective on DHC usage and potential.

The report also draws insights from 21 case studies worldwide. These case studies provide practical experiences of deploying renewable DHC and help identify barriers, policymaking, and development opportunities. It details various existing

plants and their integration of renewable energy sources into DHC systems, which is pivotal to make P2H systems out of them.

Existing P2H systems currently in operation vary widely in scale, application, and geographic distribution, reflecting the versatility and adaptability of this technology to different energy markets and needs. While specific details about each P2H facility can vary based on local energy policies, renewable energy availability, and heating requirements, some remarkable pilot plants illustrate the global application and impact of P2H technologies.

Germany, a leader in the energy transition, has implemented several P2H projects within its district heating networks. For instance, the city of Hamburg operates a large P2H system that utilizes surplus wind energy to generate heat, effectively integrating the electricity and heating sectors and reducing reliance on fossil fuels for heating.

Denmark has been at the forefront of integrating wind energy into its heating sector through P2H solutions. The country has multiple P2H plants that use excess wind power to supply heat to their extensive district heating networks, showcasing an effective use of renewable energy for heating purposes and enhancing grid stability.

Sweden, known for its ambitious climate goals, incorporates large electric boilers and heat pumps into its district heating systems. These P2H solutions are part of Sweden broader strategy to decarbonize its energy system, utilizing the significant renewable energy resources available in the country to provide sustainable heating.

Norway utilizes P2H technology, including large-scale heat pumps, to recover waste heat and supply process heat in industrial applications. This not only improves energy efficiency but also reduces the carbon footprint of industrial operations.

In the Netherlands, P2H systems are being developed to replace natural gas boilers in residential areas, contributing to the efforts to reduce its dependence on natural gas and decrease GHG emissions. These systems often use heat pumps to leverage ambient air or water sources for heating.

These examples demonstrate the practical application and benefits of P2H technologies in operation today. By efficiently using excess renewable energy for heating, P2H systems help reduce carbon emissions, enhance energy security, and promote the integration of renewable energy sources. As countries around the world continue to advance their renewable energy capabilities and seek solutions for decarbonizing heating, the role of P2H technologies is likely to expand, offering a practical tool for achieving energy transition objectives.

2.2 Power-to-Liquid

Power-to-liquid (P2L) technology, a subset of the power-to-X (P2X) strategies, has emerged as a pivotal solution in the transition towards sustainable energy systems. P2L involves the conversion of electrical energy, primarily from renewable sources, into liquid fuels, such as synthetic hydrocarbons or alcohols [52]. This technology is particularly significant due to its potential in addressing the intermittency of renewable energy sources like wind and solar, thereby enabling a more stable and reliable energy supply [52].

In this section the P2L technology is discussed, explaining the reactions at the basis of the processes and the recent advancements of the current technologies.

2.2.1 State of the art of P2L

The integration of P2L technology in energy systems not only promises a reduction in greenhouse gas emissions but also provides a pathway for the storage and transportation of renewable energy over long distances and durations [53]. Moreover, P2L fuels are compatible with existing infrastructure and internal combustion engines, offering a pragmatic approach to decarbonizing sectors that are challenging to electrify, such as aviation and heavy transport [54].

Recent advancements in P2L technology have been focused on improving the efficiency of the conversion processes, specifically in the electrolysis of water to produce hydrogen and the subsequent synthesis of hydrogen with carbon dioxide to form liquid hydrocarbons [55]. These studies underscore the critical role of catalyst development and process optimization in enhancing the overall efficiency and economic viability of P2L systems.

Before getting into the details of the P2L, it is vital to explain that the liquid chemical produced is obtained by means of Fischer-Tropsch synthesis (FTS). FTS, particularly the Low-Temperature Fischer-Tropsch (LTFT) synthesis, is used to convert syngas into a wide range of products. The LTFT synthesis enables flexible production based on market demand, predominantly yielding normal paraffinic hydrocarbons, which can be further processed into chemicals, fuels, and plastics like polypropylene and polyethylene. The main reaction in FTS is highly exothermic, and the process is optimized for different CO conversions and CH_4 selectivity to achieve the desired product distribution [56].

The Fischer-Tropsch synthesis (FTS) is a catalytic reaction for the synthetic production of hydrocarbon fuels and chemicals from a syngas feed, usually

performed on iron- or cobalt-based catalysts. Its reaction mechanism is often described in terms of a simplified, exothermic polymerization equation:

$$nCO + 2nH_2 \rightarrow (\text{-}CH_2\text{-})_n + nH_2O \quad (1)$$

Where (- CH_2 -) is a hydrocarbon monomer of a general length *n* of carbon atoms. In P2L applications, the hydrogen needed to perform the reaction is supplied by means of electrolysis. The electrolyzer is fed with renewable power excess and produces "green" hydrogen, which is then used to produce further chemicals, or is liquefied, depending on the necessity.

The work [57] explores the updated legal framework in the EU concerning P2L, from 2019 to early 2022. It highlights increased interest and market entrance of electrolysis, with a focus still largely on hydrogen as an end fuel. Regulatory revisions and new actions are supporting electrofuels in aviation and marine transport, revealing a shift in the EU and member states approach towards diverse P2X pathways. Through a review of the regulatory framework and analysis of National Energy and Climate Plans (NECPs), hydrogen strategies, and various policy initiatives at the EU level, the study examines specific targets and barriers for P2X pathways and assesses the representation of these fuels in legal frameworks.

In a recent work [58], authors presented a novel layout of a P2L system including a Direct Air Capture (DAC) unit, offshore wind farm, alkaline electrolyser, and a refinery plant (reverse water gas shift coupled with a Fischer-Tropsch reactor). The authors performed a critical analysis of the technical, economic, and environmental performance of the system to investigate the sustainable aviation fuel production. The model was developed on SimaPro to carry out a complete Life Cycle Analysis (LCA) analysis. The main findings of the work are a carbon conversion efficiency of 88%, hydrogen conversion efficiency of 39.16%, power-to-liquids efficiency of 25.6%, and minimum jet fuel selling price (MJSP): £5.16/kg.

Chen et al. [59] analyzed an innovative sustainable energy solution using photovoltaic-driven liquid air energy storage (PV-LAES) to achieve combined cooling, heating, and power (CCHP) for zero-energy buildings. The PV-LAES system can produce 523.93 MWh of electricity, 57.75 GJ of cold energy, and 119.24 GJ of heat energy annually, with an improved round-trip efficiency of 67.05% and a carbon emission reduction of 368.35 tons. The Simple Payback (*SPB*) period is 6.45 years, and the cumulative net present value (*NPV*) reaches 515 k$ throughout the life cycle. The methodology involved the use of Aspen HYSYS software to establish mathematical models for quantifying the thermodynamic performance of the system. The dynamic

process was analyzed using MatLab software, which helped in simulating and analysing the static process of LAES.

Karimian et al. [60] proposed a novel P2L plant integrating CO_2 electroreduction, alkaline water electrolysis, and photovoltaic panel technologies. It found that P2L energy efficiency decreases with the CO_2 electroreduction cell current density, peaking at an alkaline electrolysis cell current density of 0.2 A/cm^2. The plant levelized cost of the product (LCOP) decreases with cell current densities and is reduced by increasing the alkaline electrolyzer operating temperature, while increasing with operating pressure. Energy efficiencies of the alkaline electrolysis and CO_2 electro-reduction cells were 60.80% and 33.80%, respectively, with power-to-liquid energy efficiency and plant LCOP at 37.60% and 22.676 $/kg.

2.2.2 Scientific literature and real operating P2L plants

This section discusses the main types of plants detected for P2L technologies. In [34] an in-depth analysis of P2L technologies is provided, aiming at explaining the differences between the several technologies and highlighting the advantages for each of them.

First, we analyze the case in which the liquid chemical is the hydrogen, whose simplified typical layout is shown in Figure 8. In this case a Claude cycle is used to refrigerate the gaseous hydrogen, which is first compressed and then cooled down to temperature close to 20 K by means of electric driven ammonia chiller. The liquefaction of hydrogen is mostly recommended for long distance transportation and large-scale consumers, where the hydrogen compression is no more feasible. It is also shown the final price in case of green hydrogen and blue hydrogen, i.e. hydrogen produced by fossils but integrated with carbon capture and storage (CCS). The green alternative final price is 7 €/kgLH2 or in a range 2.5–4.5 €/kgLH2 because of the significant difference in electricity price. The price of green liquid hydrogen is approximately two to three times higher than the cost of conventional liquid hydrogen production from fossil fuels, including CCS 1.4–3.4 €/kgLH2. In both cases the production cost is extremely high due to the remarkable energy cost for the liquefaction process.

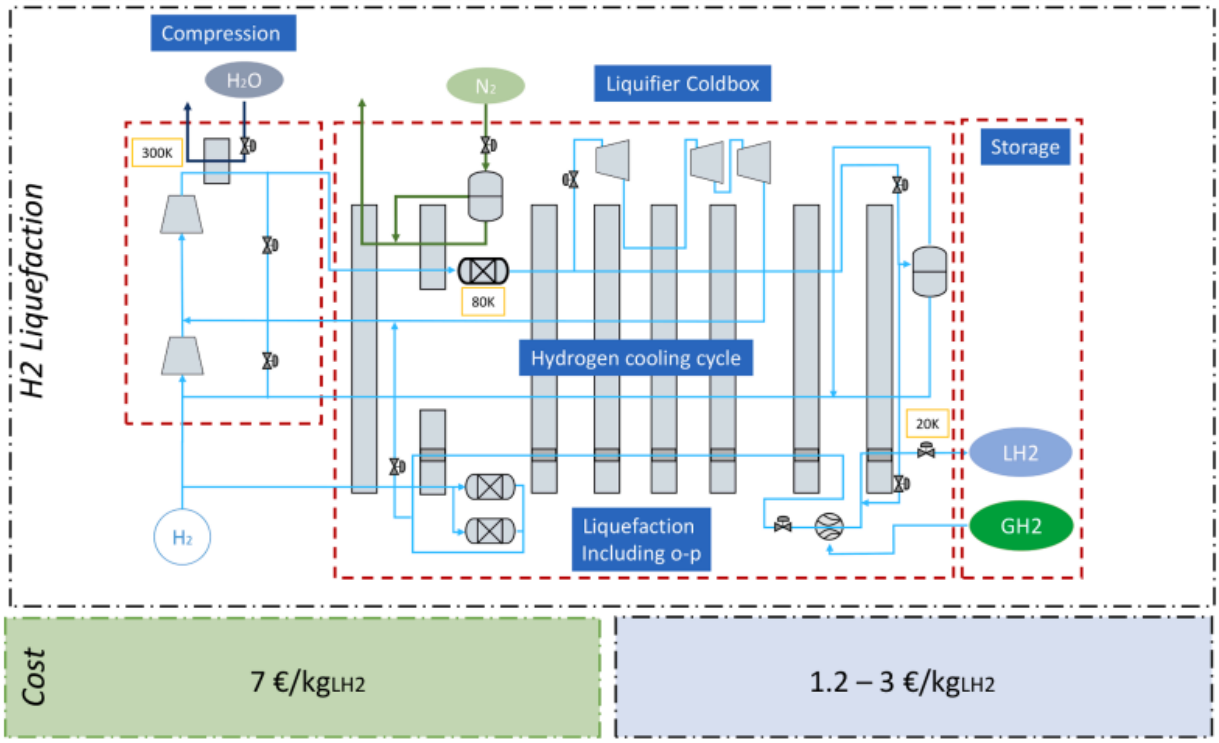

Figure 8. Comparison of the production process and cost of liquid green and liquid blue hydrogen [34].

The overall energy conversion usually lies between 0.35 – 0.45 and the liquid hydrogen stored has a gravimetric density of kgH2/m^3. This means that hydrogen, either in gas or liquid form, can store less hydrogen in the same volume as ammonia or methanol.

Figure 9 shows the layout of a typical ammonia production plant. Ammonia is a potential and promising hydrogen carrier because every molecule of ammonia (NH_3) contains three hydrogen atoms. Ammonia is a gas under atmospheric conditions. It can be efficiently transported in liquid form at a temperature of –33°C and environmental pressure or environmental temperature and a pressure of 8 bar. Ammonia is currently used mainly in the agricultural industry as a fertilizer, but it is also heavily used in the refrigeration industry as a working fluid. The long-distance transportation of hydrogen can be performed in ships powered by clean ammonia, after the development of an ammonia dual-fuel engine (2025). The reaction performing the synthesis of ammonia from hydrogen is the Haber-Bosch synthesis:

$$N_2 + 3H_2 \leftrightarrow 2NH_3, \quad \Delta h_r^{\,o} = -45.9\ kJ / mol \tag{2}$$

The roundtrip efficiency of the ammonia production system is generally between 0.26 – 0.43, slightly lower than hydrogen, but the gravimetric density is 108 kgH2/m^3, meaning that as a hydrogen carrier is more effective. The clean alternative ammonia final price is 0.9 €/kgNH3, whereas the grey alternative is 0.44 €/kgNH3

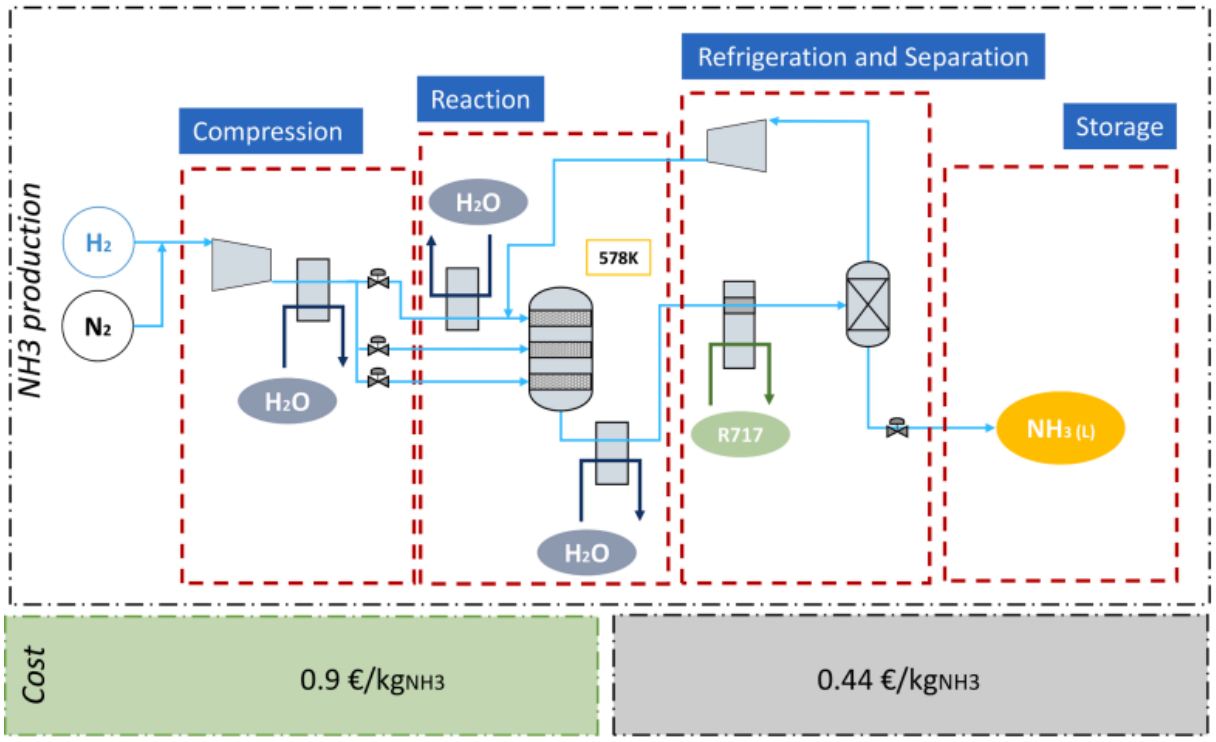

Figure 9. Comparison of the production process and cost of clean and gray ammonia [34].

Another interesting alternative to ammonia is methanol. In 2020, 157 million metric tons of methanol were produced worldwide, making it one of the most highly synthesized chemicals after ammonia, but it is expected to equal ammonia production in 2030. Unfortunately, out of that huge amount, only 0.2 Mt are produced from clean sources. Methanol is mainly synthetized for producing other chemicals, such as formaldehyde, acetic acid, and plastics, but smaller quantities are also used as fuel for vehicles, ships, industrial boilers, and cooking.

Figure 10 shows the two paths for methanol synthesis. H_2 and CO_2 enter the system and are compressed. The process is followed by a reactor where $CuO/ZnO/Al_2O_3$ is used as a catalyst that operates at a pressure of 80 bar and undergoes a maximum temperature increase from 230 °C to 250 °C. The gas phases of two flash evaporators are sent back to the reactor, water is separated in a distillation column, and methanol is stored.

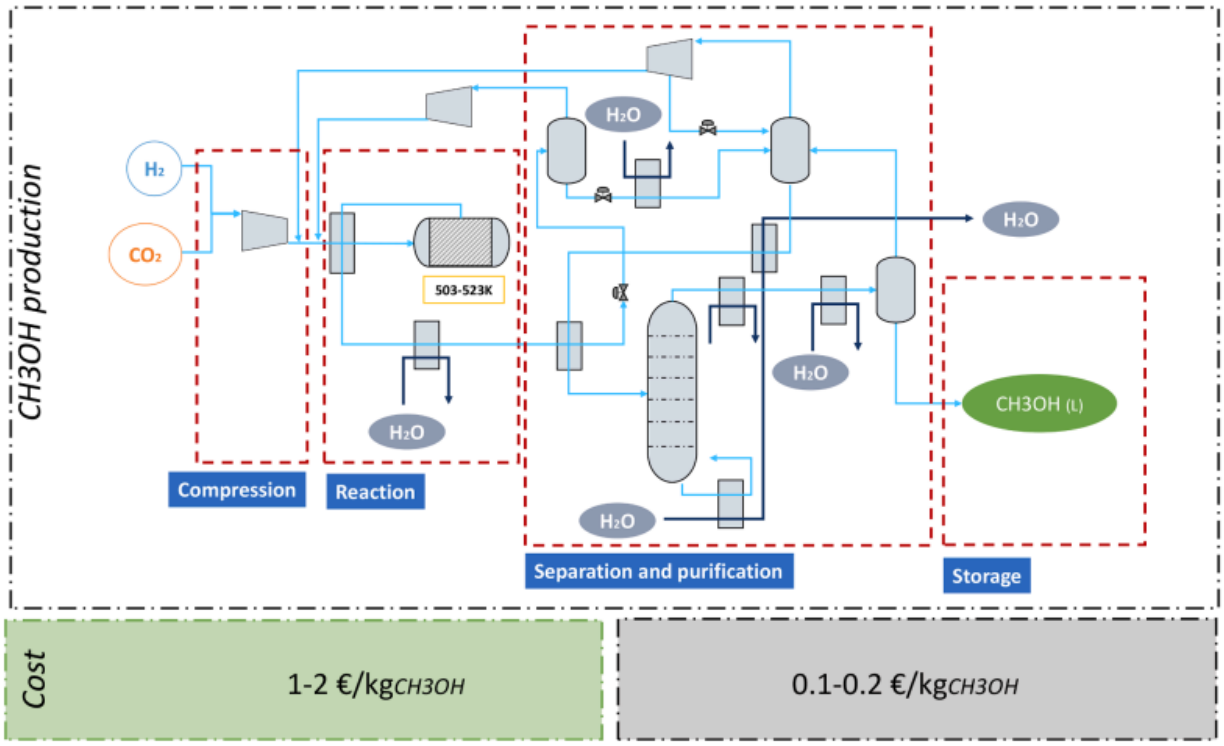

Figure 10. Comparison of the production process and cost of methanol from green and gray hydrogen [34].

The chemical reaction for the synthesis of the methanol is:

$$CO + 2H_2 \leftrightarrow CH_3OH \tag{3}$$

P2L is not going to be discussed in a separate chapter later, because it is not included yet in the spectrum of models developed by the author of this thesis.

2.3 Power-to-Power

This section delves into the state of the art and investigated Power-to-power (P2P) plants. These systems encompass various technologies, including advanced battery systems, supercapacitors, and hydrogen fuel cells. However, here the discussion is mainly focused on hydrogen systems since they are more aligned with the purpose of the work.

2.3.1 State of the art of P2P

P2P systems are at the forefront of modern energy solutions: in fact, this technology is going to replace the widely adopted lithium-ion batteries for power storage. These systems are indeed vital in the context of the smart grid, where the power system is strongly intertwined with information and communication technology infrastructures [61]. Allowing a faster charge and discharge of the storage systems and also exploiting larger storage solutions allow one to increase the flexibility of the modern polygeneration systems.

The integration of these technologies into power systems presents challenges and opportunities. For instance, wireless power transmission (WPT) is an emerging technology with the potential to revolutionize power distribution, particularly for electric vehicles and smart grid applications [62]. Moreover, the development of high-power wind energy conversion systems and solid-state transformers are indicative of the ongoing evolution in power systems.

In the realm of P2P plants, the most interesting technology is the electrolytical conversion of renewable power surplus into hydrogen and, or, chemicals, which then undergo an electrochemical conversion of chemical storage into available power. Gaseous Hydrogen is the most adopted chemical storage option, by means of several technologies [63]. The most efficient technology for performing the electrolytic process is the solid oxide electrolytic cell (SOEC), which is unfortunately still too expensive, as shown in Figure 11.

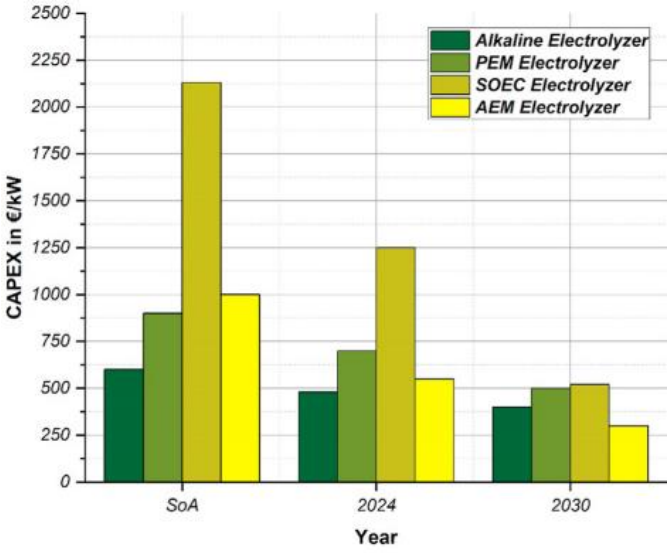

Figure 11. Electrolyzer CAPEX forecast [63].

Reducing the cost of SOEC will likely require a combination of different approaches, including materials development, manufacturing improvements, stack design, energy efficiency, and government policies.

Before discussing the diverse option nowadays investigated for the hydrogen storage, it seems mandatory to make a brief degression on the electrolytic and electrochemical processes. The electrolysis of the water is a well-known process which consists in the splitting of the water molecule into hydrogen and oxygen. When this process is realized by means of renewable power, the hydrogen produced is named "green" hydrogen. The most widespread electrolyzer technologies are currently the alkaline (AEC) and the proton exchange membrane (PEMEC), with an

increasing number of studies on solid oxide electrolysis (SOEC) which is far more efficient than the others [63].

In the case of AEC, the reaction develops continuously thanks to the anionic exchange of OH^- through the diaphragm merged in a KOH solution, the overall efficiency is between 70 % – 80 %. In the case of PEMEC, the same reaction occurs by means of protonic exchange of H^+ through the polymeric membrane used as electrolyte, with an overall efficiency between 50 – 80 %. The solid oxide technology exploits a porous ceramic electrolyte through which the oxide ion O_2^- passes through, with a much higher efficiency between. More details on the technology can be found in ref. [64], here are omitted for the sake of brevity.

Fuel cells operate with a process which is the opposite of the electrolytic process, i.e. the hydrogen is supplied to the cell as a fuel to react with air and produce electricity. In this case the range of technologies studied and adopted is wider, including phosphoric acid cells (PAFC) and molten carbonate cells (MCFC), despite their diffusion reduced with time. Also in this case, the technology featured by the highest efficiency is the solid oxide one (SOFC), but mostly is currently used for demonstrative plants, up to 0.5 MW.

In [64] authors propose an analysis of the energy density of diverse alternatives of hydrogen storage, as the ones discussed in the previous section on P2L. The energy density of the gaseous hydrogen in general is extremely low, even at 300 bar, and only liquid or solid - metal hydrides (MH) - hydrogen storage solution would be competitive with other chemicals. Unfortunately, these processes are highly energy consuming, therefore they are not suitable for large-scale hydrogen storage solutions. In fact, without splitting the compression in more undercooled stages, the compression work increases dramatically, as shown in Figure 12.

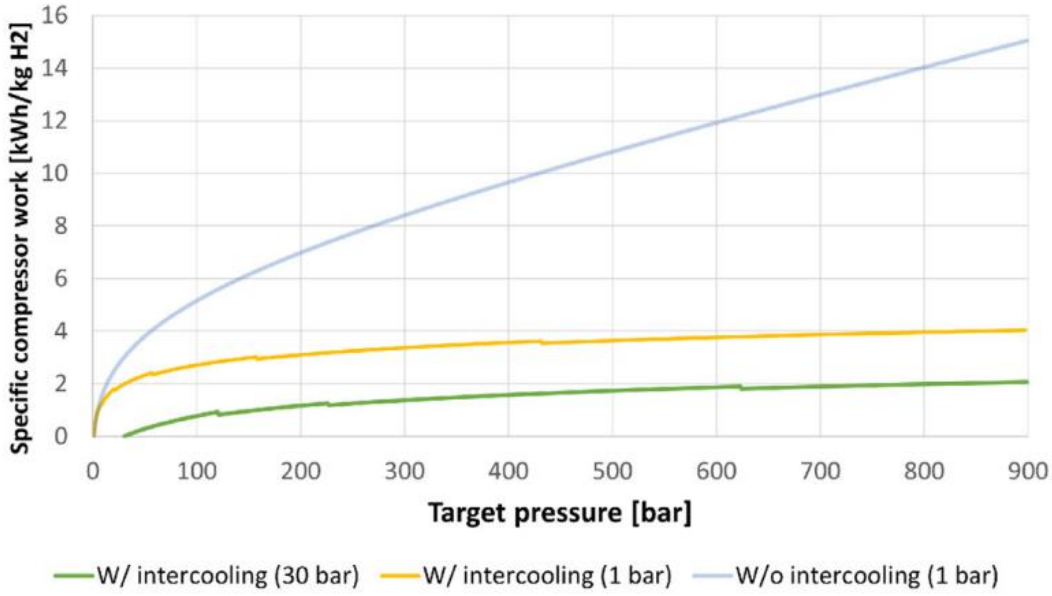

Figure 12. Hydrogen compression work. In brackets, operating pressure of the electrolyzer [64].

The liquefaction of hydrogen occurs by means of the process described in Figure 8, therefore is not discussed again, whereas is of extreme interest to discuss at this stage the storage of hydrogen in solid form as MH. In fact, in the most advanced studies, it is analyzed the combination of metals or alloys with hydrogen which leads to the formation of metal hydrides, with a gravimetric density higher than 115 kgH2/m^3. During the loading phase, hydrogen is adsorbed through an exothermic reaction. Conversely, hydrogen is released (desorbed) when heat is supplied to the metal hydride, according to the equation:

$$M_e + \frac{x}{2} H_2 \leftrightarrow M_e H_x \tag{4}$$

The adsorption/desorption processes make use of cooling and heating sources. These reservoirs are at temperatures of ~10°C for cooling and ~50°C for heating, even though this depends on the specific MH chosen.

2.3.2 Scientific literature and real operating P2P plants

The P2P plants investigated in this section only exist as scientific purpose, since there is no plant of this kind which is actually operating. Nonetheless, the works proposed are useful to highlight the latest findings of plants which can be developed.

Zhao et al. [65] proposed a green hydrogen-electric coupled energy storage system plant managing power in a high-share renewable power system. The system includes a hydrogen-fueled compressed air energy storage (CAES) and a Power-to-Gas-to-power (P2G2P) device, including a PEMFC and a PEMEC. The system is designed to

smooth out long-duration time-scale fluctuation and handle remaining time-scale fluctuations, integrating hydrogen generation and consumption in both CAES and P2G2P devices. The study utilizes assumptions to simplify system modeling and focuses on electrochemical reactions in PEM electrolyzer and PEMFC stacks for hydrogen generation and power generation, respectively. The model is developed in MatLab and it demonstrates a loss of power supply probability (LPSP) of 5.40%, higher than single energy storage systems, and a wind curtailment ratio (WCR) of 8.81%, indicating insufficient storage capacity. It shows the capability of energy shifting on several days scale and seasonal scale.

Escamilla et al. [64] investigated a thermodynamic analysis of hydrogen compression, storage in various forms, and transportation, and proposed a literature review of hydrogen electrolysis systems. The study finds that the round-trip efficiency of the P2P system ranges between 22 % - 29 %. It highlights the potential for efficiency improvements in hydrogen production and power generation, projecting possible efficiencies of around 40 % - 42 % in the future.

In a recent work, Genovese et al. [63] employed a bibliometric analysis using the Web of Science and Scopus databases, focusing on hydrogen technologies from an industrial perspective. It considers the environmental impact of hydrogen production and its potential applications, with a future-oriented view towards 2050. The paper highlights the potential of hydrogen to account for up to 20% of energy needs, especially in transportation (20 % - 50 %) and industrial sectors (5 % - 20 %). It emphasizes hydrogen flexibility as an energy carrier and its role in sector coupling and decarbonization. By 2050, hydrogen could power a significant portion of vehicles, including cars, trucks, and buses, and contribute to electricity generation and heat production. It has indeed a strong potential to be used as storage to be then converted into other useful forms of energy.

2.4 Power-to-Gas

This section presents the state of art and technologies for the last power-to-X option evaluated in this dissertation, i.e. Power-to-Gas (P2G). In the scientific literature there is still not a precise definition of what P2G exactly include as a technology. In the broadest sense, it should include whatever gaseous compound produced by excess of renewable power, also hydrogen or other chemicals which are in gas phase. In this case the author prefers to follow the school of researchers who define P2G the technology that has as final product the natural gas. In some research this is also known as Power-to-Methane (P2M), here both terminologies will be use without distinction.

2.4.1 State of the art of P2G

The methanation process occurs by means of the Sabatier reaction, which is the reaction of conversion of carbon dioxide into methane by means of hydrogen in a catalytic environment. The peculiarity of this technology is that the final energy vector obtained is a high-purity synthetic natural gas which can be injected into the natural gas grid [66]. Such a solution is therefore advantageous for the decarbonization of the residential sector without further affecting the stability of the electric grid. Furthermore, the necessity of independence from the Russian natural gas in many EU Countries became mandatory after the increasing of the natural gas price on the market as a consequence of the war in Ukraine [67].

Modern P2G technology exploits renewable power surplus to produce hydrogen by means of electrolysis, by means of the technologies already discussed. The hydrogen produced by means of the electrolysis of water is then integrated with the CO_2 obtained from other processes or Directly Air Capture (DAC) from the atmosphere [68]. This last option has the relevant constraint of the very low partial pressure of CO_2 which leads to high specific costs. Commonly the CO_2 is captured by means of absorption, adsorption, or membrane processes from cement manufacturing, and iron and steel making industries [69]. As an alternative, the CCS from the process of upgrading of the biogas produced by means of anaerobic digestion (AD) is a suitable measure in order to achieve a fully renewable biomethane production. The H_2 and the CO_2 then undergo a methanation process into a reactor filled of catalytic packed bed usually made of Ni/Al_2O_3 [70], producing CH_4 and steam.

One of the most advanced solutions for production of synthetic methane is biological methanation. Biological methanation is a process that converts hydrogen and carbon dioxide into methane through the action of microorganisms, typically within biogas plants. This process offers a promising approach to renewable energy production and storage. It allows the conversion of carbon dioxide to methane by feeding hydrogen into the reactor, utilizing hydrogenotrophic bacteria already present in the system [71]. It is seen as a crucial method to transform energy from electricity to natural gas, especially using excess energy from fluctuating sources like wind and solar. This approach involves overcoming challenges like gas-liquid mass transfer and managing environmental conditions for microbial biomass.

Biological methanation processes, particularly in the circular economy, can significantly increase methane output of biogas systems. Various system designs have been explored, with a focus on factors like methane evolution rate and gas-liquid transfer coefficients. Catalytic and biological technologies have been compared, with biological methanation showing higher resistance to harmful

impurities. However, catalytic methods are more energy-efficient and require smaller reactors [72]. Thermophilic biological methanation systems have demonstrated high methane production rates and compositions, indicating their potential for biogas upgrading. In-situ and ex-situ biological methanation strategies show promise for biogas upgrading, with the potential for gas grid injection. These strategies involve different operational challenges and benefits [73].

Regarding the state of the art of the methanation reactors, Figure 13 shows the four reactors that are most widespread.

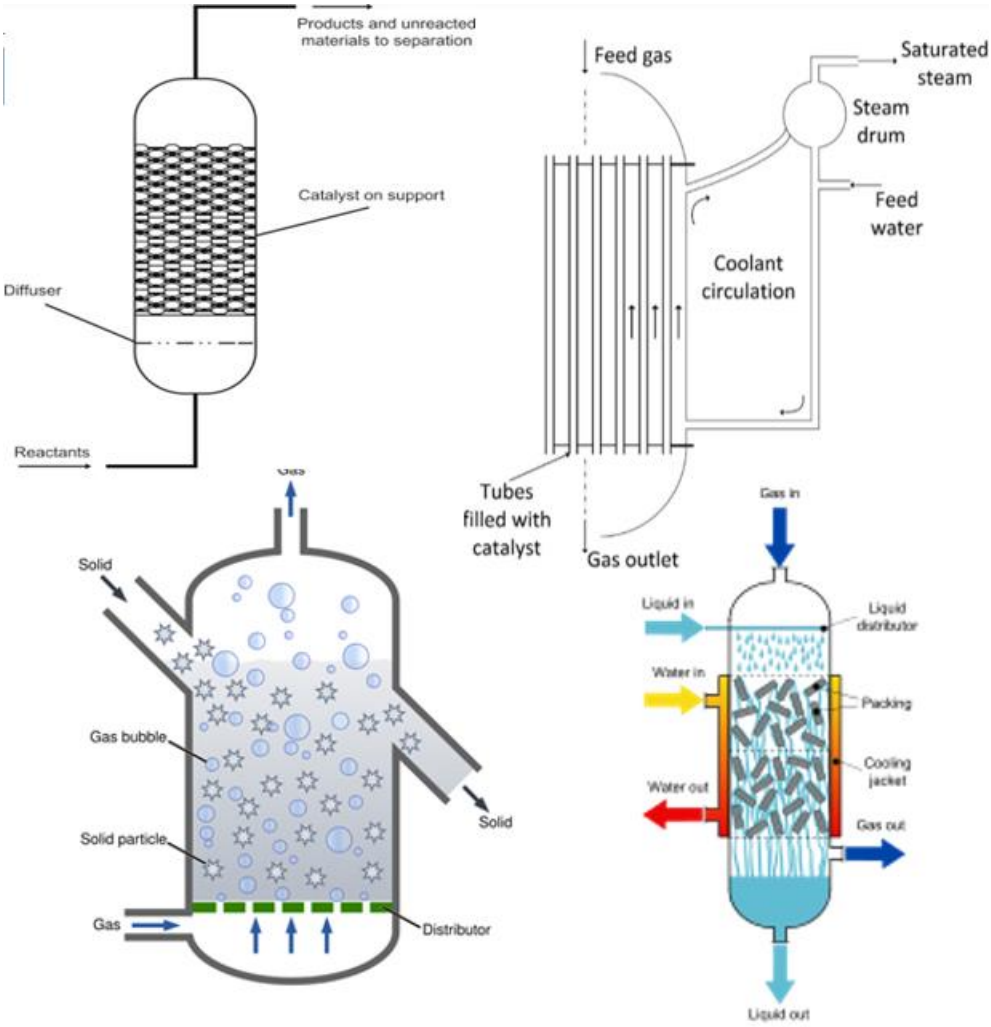

Figure 13. Most diffused methanation reactors, namely: fixed-bed adiabatic reactor (top left), fixed- bed cooled reactor (top right), fluidized-bed reactor (bottom left), and tri-phase reactor (bottom right) [74].

The four types of methanation reactors – fixed-bed adiabatic reactor, fixed-bed cooled reactor, fluidized-bed reactor, and tri-phase reactor – each have unique characteristics and applications in the context of methanation processes.

In adiabatic fixed-bed reactors, the reactor temperature is controlled through product gas recirculation. This type of reactor can operate under a wide range of loads, with

optimal recycling ratios enhancing methane productivity. However, they are sensitive to load changes, requiring careful management of temperature and flow rates [75]. Cooled fixed-bed reactors manage temperature through external cooling mechanisms, allowing for more stable operation under fluctuating feed conditions. They typically require a more complex heat exchanger system for cooling but have a considerably lower startup time compared to adiabatic reactors [74]. Fluidized-bed reactors offer significant advantages in terms of heat and mass transfer efficiency. They show higher CO conversion and selectivity to CH4 compared to fixed-bed reactors, mainly due to better catalyst surface utilization and improved mass transfer characteristics. Fluidized-bed reactors also demonstrate lower carbon deposition on the catalyst, which is crucial for long-term stability [76]. Tri-phase reactors are advanced and less commonly discussed in literature. They generally combine features of both gas and liquid phase reactions, potentially offering enhanced mass transfer and reaction kinetics [77].

2.4.2 Scientific literature and real operating P2G plants

P2G is a topic that collects much more interest, especially from industrials and stakeholders, compared to the other P2X solutions. Clearly the reason is the possibility of producing clean natural gas, perfectly aligned to the standards of the current gas grid infrastructure. Therefore, a large variety of scientific research works deal with the methanation reaction and the P2G.

In [78], the authors proposed the first review of P2G considering real-life projects, economic assessments and systems modelling studies, and comparing these based on scope, assumptions, and outcomes. The review focuses on P2G for injection into the gas grid, as this application has specific economic, technical, and modelling opportunities and challenges. Germany is the leading country in the technology and the most interesting project is the “Element One”. This project is a 100 MW P2G plant being developed by TenneT, Gasunie Deutschland, and Thyssengas in Lower Saxony, Germany. This pilot plant represents a significant step in the integration of renewable energy into the national grid and advancing the energy transition. The primary function of the plant is to convert renewable energy, mainly from offshore wind farms in the North Sea, into green hydrogen or methane. This conversion facilitates the storage and transportation of renewable energy in gas form.

Potential sites for the plant are near the TenneT substations in Diele and Conneforde, which are pivotal in collecting and distributing offshore wind energy. An important aspect of this project is the comprehensive coupling of energy, transport, and industrial sectors. The gas produced from green energy will be transported from the North Sea to the Ruhr region and could be used in hydrogen filling stations for

mobility and by industrial consumers. By converting green energy into gas, the project aims to develop new storage capacities for renewable energies, thereby reducing the future need for grid expansion and stabilizing the electricity grid.

Figure 14 shows a typical layout of a P2G plant. The carbon dioxide in this case is mixed with hydrogen before entering the Sabatier reactor. The methanation reaction is exothermic and its change in moles is negative, therefore the process is promoted at low temperature and high pressure. These plants have round-trip efficiencies ranging between 0.35 – 0.56 and an energy density between 0.40 – 1.20 W/cm^2 as storage.

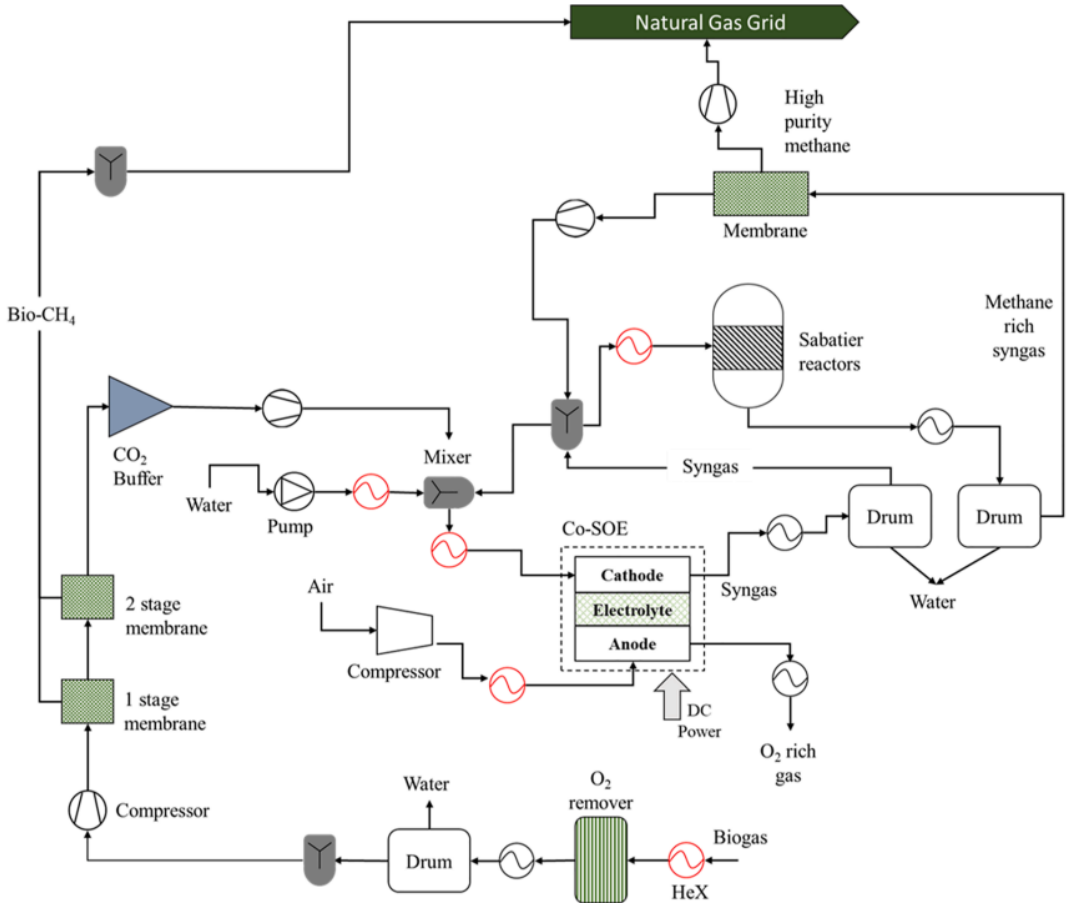

Figure 14. Layout of a P2G plant entirely based on renewable energy sources [34].

The methanation reaction is highly exothermic, thus a suitable heat transfer analysis is pivotal to designing the reactors. In Bolt et al. [79], the authors provided a model for an innovative helical fixed-bed reactor for the methanation of the CO_2. The potential of this reactor in preventing the sharp increasing of temperature, at high conversion efficiency of the reactants, was proved. In fact, several parameters were varied during the analyses, either geometric, as the inner diameter of the tubes, and thermodynamic as the inlet temperature and pressure, or the coolant temperature. For all the cases, the temperature gradient was conveniently steered and the conversion efficiency was kept in a range from 75% to 87%.

Aubin et al. [80] recently investigated the coupling of a water-cooled methanation reactor with a SOEC cell for the optimal design of both units. The system was modelled by means of Aspen Software and an experimental setup was built to validate the model. The steam produced by the methanation unit was used for generating heat for the high temperature electrolyzer which, in turn, provided heat captured by vapor superheated expanded in turbine. Given this setup, the efficiency of the system increased from 83.9% to 87.1%. However, in this case the experimentally observed reactor operating temperature was extremely high, with peaks higher than 700°C. At the same time, several problems of unstable behavior of the SOEC were also observed when a dynamic flow of steam was provided by the methanation unit.

Patcharavorachot et al. [81] recently proposed an Aspen model of a coupled SOEC-methanation technology based on P2G strategy for energy storage and CO_2 utilization. In this study, two alternative options are considered for SOEC operation: water electrolysis and water/carbon dioxide co-electrolysis. In the first case, the green H_2 produced by the SOEC is combined with the CO_2 gathered from a fermentation process for ethanol production. These gases are sent to the methanation unit to produce green natural gas. In the second one, the CO_2 is directly sent to the SOEC, together with the steam, and an output mixture of H_2, H_2O, CO and CO_2 is obtained. After a cooling down phase for storage purpose and a preheating phase, this gaseous compound is sent to the methanation unit for renewable syngas production. The results show a higher methane yield in the second case compared to the first one. The study also provides a pinch analysis of the system in both operating conditions, unfortunately not providing the discussion with any insight on the heat transfer rates and the thermal levels of each heat exchanger considered. The authors claim that the analysis is carried out on Aspen Energy Analysis tool and the electricity comes from renewable source, but no accurate dynamic or thermodynamic analysis is provided. Therefore, there is no study analyzing the dynamics of the system fed by a fluctuating source.

In Zhong et al. [82] a comprehensive framework for investigating the off-design performance of a P2G system combining SOEC with a methanation reactor, using solar energy as the renewable input, is introduced. The study identifies an optimal design condition with a total exergy efficiency ($\eta_{ex,TOT}$) of 11.83% and a levelized cost of exergy (LCOE) of 150.76 $/MWh. Off-design solutions reveal that syngas (SNG) yield increases with solar radiation, while the multi-objective optimization shows hourly SNG yield in the range of 275.06 kW – 946.53 kW, achieving a total annual SNG yield of 1697 MWh/y, and an hourly optimal $\eta_{ex,TOT}$ mainly varying in the range of 10.40 % – 11.40 %. Also in this case, there is no accurate evaluation neither of the

dynamic power production, despite the H_2 produced is described as "green hydrogen" implying a renewable energy source, nor of the thermal load of the SOEC which would be not constant because of the intermittent energy production.

Several types of methanation units can be used, ranging from fixed-bed to fluidized-bed, adiabatic or polytropic, refrigerated and three-phase reactors [75]. Prabhakaran et al. [83] developed a 1-D dynamic numerical model for a three-phase methanation reactor inside which H_2 from electrolysis and CO_2 from DAC flow through a slurry bubble column reactor. The accuracy of the model was tested with experimental data given from the pilot plant designed and developed at the Engler Bunte Institut of KIT, in Germany. Results showed that the model mimics with sufficient accuracy the temperature of the slurry and the CO_2 conversion even under abrupt transitions of the load. The reactor is then coupled to a photovoltaic (PV) system and a PEM electrolyzer to simulate a 100 kW P2G plant but no thermoeconomic analysis is performed in this work.

In Mazza et al. [74], the modelling and simulation of a multi-tubular fixed-bed cooled reactor is performed to analyze the trend of the temperature gradient along the reactor during partial-load operation. Results showed that partial-load operation is safe up to a minimal value of 45%, to avoid hot spot within the reactors and preserve the catalyst from wear and tear.

Salomone et al. [84] developed a model of a P2G system based on renewable power surplus feeding a SOEC for H_2 production coupled to CO_2 capture from AD process. The model was developed in MatLab and an optimization analysis of the size of the plant was performed. Moreover, a pinch point analysis was performed to find the optimal configuration for the heat recovery and a Levelized Cost Of Product (LCOP) was also provided. In conclusion, results showed that the optimal size of the plant allowed the recovery of 70% of renewable surplus from the grid and the solution is feasible with a LCOP ranging from 60.2 €/MWh to 224.9 €/MWh.

Chapter 3
Models developed on Power-to-Heat

Modern District Heating and Cooling (DHC) systems can be considered examples of Power-to-Heat technology due to their ability to utilize electric energy, often generated from renewable sources, to produce heat. This integration aligns with the fundamental concept of Power-to-Heat, which involves converting excess electric power into thermal energy. Modern DHC systems (4th generation and 5th generation of DHC, respectively 4GDHC and 5GDHC) are increasingly being designed to integrate with renewable energy sources like solar, wind, or geothermal energy. Moreover, these systems employ electric heating technologies such as heat pumps or electric boilers and often include thermal energy storage solutions, which allow them to store excess heat generated during periods of high renewable electricity production.

Despite the advancement of the technology, 4GDHC systems show some drawbacks due to the centralized heat generation system which may affect the reliability of the network [85]. The latest advancements of this technology led to the development of low-temperature district heating and cooling networks, also known as fifth-generation district heating and cooling (5GDHC) networks [86]. The temperature of the main ring ranges between 15°C and 25°C, for this reason this loop is also called "neutral" ring [87]. Note that the temperature of the neutral ring is very similar to the ground temperature, reducing the heat losses and allowing this system to exploit the ground as low enthalpy source of energy [88].

In the scientific literature there are diverse works performing a comprehensive overview of the main pros and cons of both the systems. In the work presented in ref. [89-91] similarities and differences between 4GDHC and 5GDHC are summarized. Results show that both 4GDHC and 5GDHC networks can reach the goal of decarbonization. A SWOT (strengths, weaknesses, opportunities, and threats) is also useful to compare 4GDHC and 5GDHC networks. To clarify and shorten the discussion on the differences and the similarities between the two technologies, Figure 15 and Figure 16 show, respectively, a SWOT analysis for the 4th and 5th generation districts.

In this chapter, the scientific works proposed within this framework are presented and discussed. The first one regards an optimal layout for an innovative 5GDHC system, the second one proposes a thermoeconomic comparison of a 4GDHC and a 5GDHC.

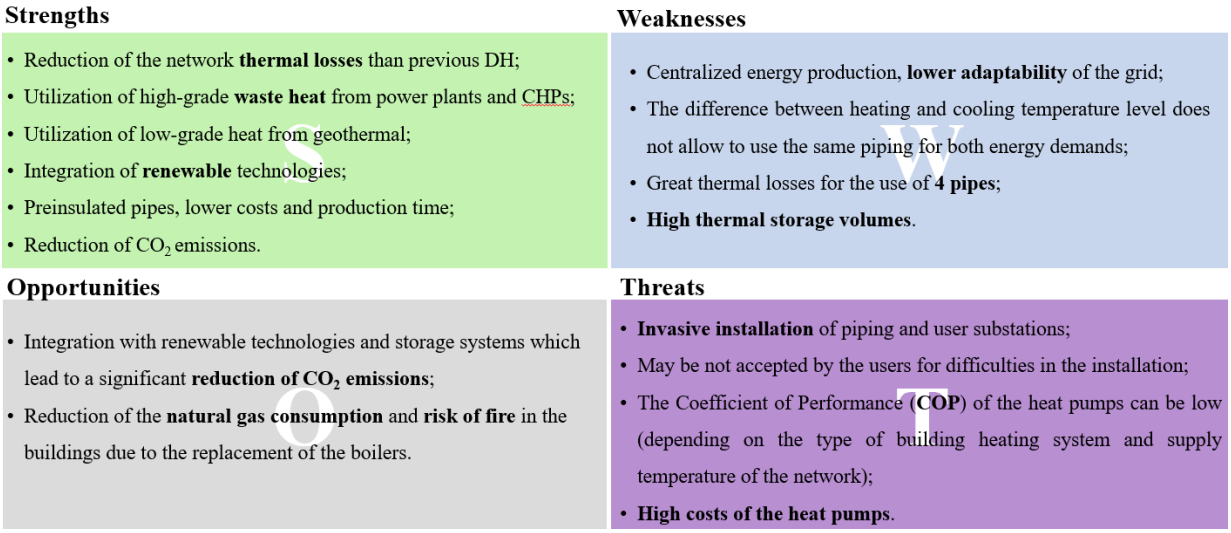

Figure 15. SWOT analysis of the 4GDHC.

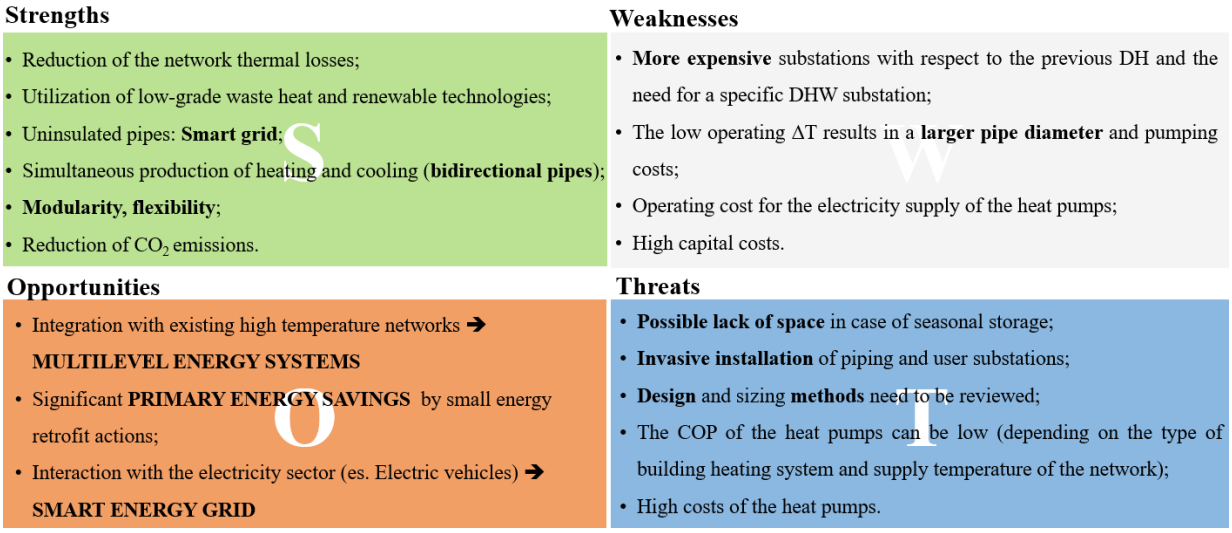

Figure 16. SWOT analysis of the 5GDHC.

3.1 Optimal design of a 5th generation district heating and cooling network based on seawater heat pumps

The present work aims at presenting significant novelties with respect to the findings available in literature in this research area. The main innovation lies in the method used for the calculations. In fact, to the best of authors' knowledge, the energy, economic and environmental advantages of this technologies are usually calculated using simplified approaches. According to the literature review discussed in ref. [92], very few papers address the energy, environmental and economic analysis of 5GDHC networks, implementing a dynamic simulation approach. This detailed approach based on dynamic simulations is implemented in the present paper, including suitable models for all the components of the system and for the system as a whole.

In addition, from the literature review, it was also found that the majority of the available papers only focus on the space heating demand of DH networks, neglecting the contribution of domestic hot water demand of buildings [93] and space cooling. Conversely, in the present work, a detailed calculation of all the energy demands of the buildings (space heating and cooling, domestic hot water, electric appliances) is performed, based on the dynamic simulations of the building. Furthermore, some significant innovations are also introduced in terms of system layout. The proposed system also includes the integration with a plurality of technologies: heat pumps with seawater heat exchangers, PV, wind, and it is based on the use of neutral rings of the district network.

3.1.1 System Layout

The layout of the novel 5GDHC system integrated by diverse renewables is displayed in Figure 17. The 5GDHC network consists of a network of two rings, in a water loop arrangement, namely water loop 1 (RING1 in Figure 17) and water loop 2 (RING2 in Figure 17), which respectively match the user heating and cooling demands. RING1 and RING2 represent the distribution system, the primary network of pipes, and are distributed along the urban surface. These are connected to a secondary network, the transmission system, on which the end users heat pumps are connected. 14 water-to-water heat pumps (HP_{R1}) supply the water loop 1 (RING1) in heating mode, whereas 10 water-to-water heat pumps (HP_{R2}) supply the water loop 2 (RING2) in cooling mode.

RING1 (R1) operates at temperatures ranging from 16°C to 19°C, whereas RING2 (R2) operates at temperatures ranging from 18°C to 25°C. Both water loops are connected by means of a crossflow heat exchanger, HE_{R1vsR2}. The heat transfer with the users occurs through 14 reversible water-to-water heat pumps (HP_{DHC} in Figure 17), which provide thermal energy for space heating, in winter, and cooling energy for space cooling, in summer, and 2 water-to-water heat pumps (HP_{DHW}) for the production of DHW. All the heat pumps HP_{DHC} and HP_{DHW} are installed in the substations of the buildings. In particular, the heat exchanged with the water of the secondary network is used for producing the thermal energy needed for space heating, space cooling and domestic hot water (DHW).

The set point temperatures of HP_{DHC} for space heating and cooling are 50°C and 10°C, respectively. The set point temperature of HP_{DHW} for the DHW production is 55°C. To manage properly the operation and activation of the pumps (P), diverters (D) and mixers (M) included in the system, several specific control strategies are implemented.

During the wintertime, only R1 operates, by carrying the inlet water flow rates to the HP_{DHC} (equal to the flow rate circulating through the pump P_{DHC1}), in heating mode, and to the HP_{DHW} (equal to the flow rate circulating through the pump P_{DHW1}). The outlet flow rates from HP_{DHC} (around 13 °C – 16 °C) and from HP_{DHW} (at roughly 13 °C - 17°C) are mixed by means of the mixer M1, returning to the R1. During the summertime, the water flows inside the pipes of both R1 and R2. In particular, the outlet water flow rate from R1, matches the DHW energy demand by supplying heat to the pump HP_{DHW}. The outlet water flow rate from R2 meets the space cooling energy demand by supplying heat to the heat pumps HP_{DHC}.

After the heat exchange, the water leaving HP_{DHC} (at roughly 23 °C - 25 °C) returns to R2. During the summer season, a simultaneous demand of cooling and heating energy may occur. This circumstance is managed by the heat exchanger HE_{R1vsR2}, which allows the heat transfer rate between R1 and R2. In particular, the heat transfer goes from R2, which is warmer, to R1, which is colder. This heat transfer may occur only if the temperature of the R1 is lower than 17 °C and the temperature of the R2 is higher than 22 °C. The whole system is supplied and balanced by the heat pumps HP_{R1} and HP_{R2}, exchanging heat with the seawater heat exchangers $HE_{sea,R1}$ and $HE_{sea,R2}$.

When R1 is operating, the seawater flow rate enters $HE_{sea,R1}$, at an average temperature of 15 °C, heating the flow rate on the other side of the heat exchanger (Close Loop Water), from about 8 °C to 11 °C, and returns to the sea at roughly 9 °C. When R2 is operating, the seawater flow rate enters $HE_{sea,R2}$, averagely at the same temperature, cools the flow rate on the other side of the heat exchanger (Close Loop Water) from roughly 20°C to 11°C, and returns to the sea at about 20°C.

Two control strategies on the temperature are implemented for R1 and R2, so that the heat pumps HP_{R1} and HP_{R2} operate within their operating temperature range. In particular, an on/off differential controller manages the flow rates of the pumps P_{seaR1}, $P_{R1,1}$ and $P_{R1,2}$, so that the R1 water temperature ranges between 16 °C and 19 °C. Similarly, a further on/off differential controller switches on the pumps P_{seaR2}, $P_{R2,1}$ and $P_{R2,2}$, when the R2 water temperature is higher than 21 °C. Another important control strategy is set for the loop including the heat exchanger HE_{R1vsR2}, operating in the summer season, when the simultaneous energy demand for heating and cooling occurs. This strategy works by means of a feedback controller which varies the inlet water flow rate to HE_{R1vsR2} in RING1 (ICW loop) so that after the heat exchange with the inlet hot water flow rate (IHW loop), the outlet cold water temperature (OCW loop) is equal to 18.5 °C. Finally, the temperatures of the DHC and DHW loops are managed by further on/off differential controllers.

In particular, during the heating season, a controller manages the on/off of the pumps P_{DHC1} and P_{DHC2} in order to guarantee a user setpoint temperature between 42 °C and 50 °C. During the cooling season, the controller manages the on/off operation of the pumps P_{DHC1} and P_{DHC2} in order to guarantee a user setpoint temperature between 15 °C and 10 °C. As for the DHW loop, a controller activates or deactivates the pumps P_{DHW1} and P_{DHW2} so that the user temperature ranges from 45 °C to 55 °C.

The layout proposed includes a renewable power production plant, consisting of wind turbines and PV panels, meeting the electric energy demand of the buildings and the DHC system. In particular, the capacity of the PV field and the number of wind turbines are selected with the aim of limiting high excesses of electricity to the grid and maximizing the electricity self-consumption, according to the Power-to-Heat strategy. The electricity produced by the PV panels and the WTs is indeed used to also match the electric energy demand of all the heat pumps and circulation pumps. The district is grid-connected in order to manage the further excesses of electricity or supply the necessary integrations.

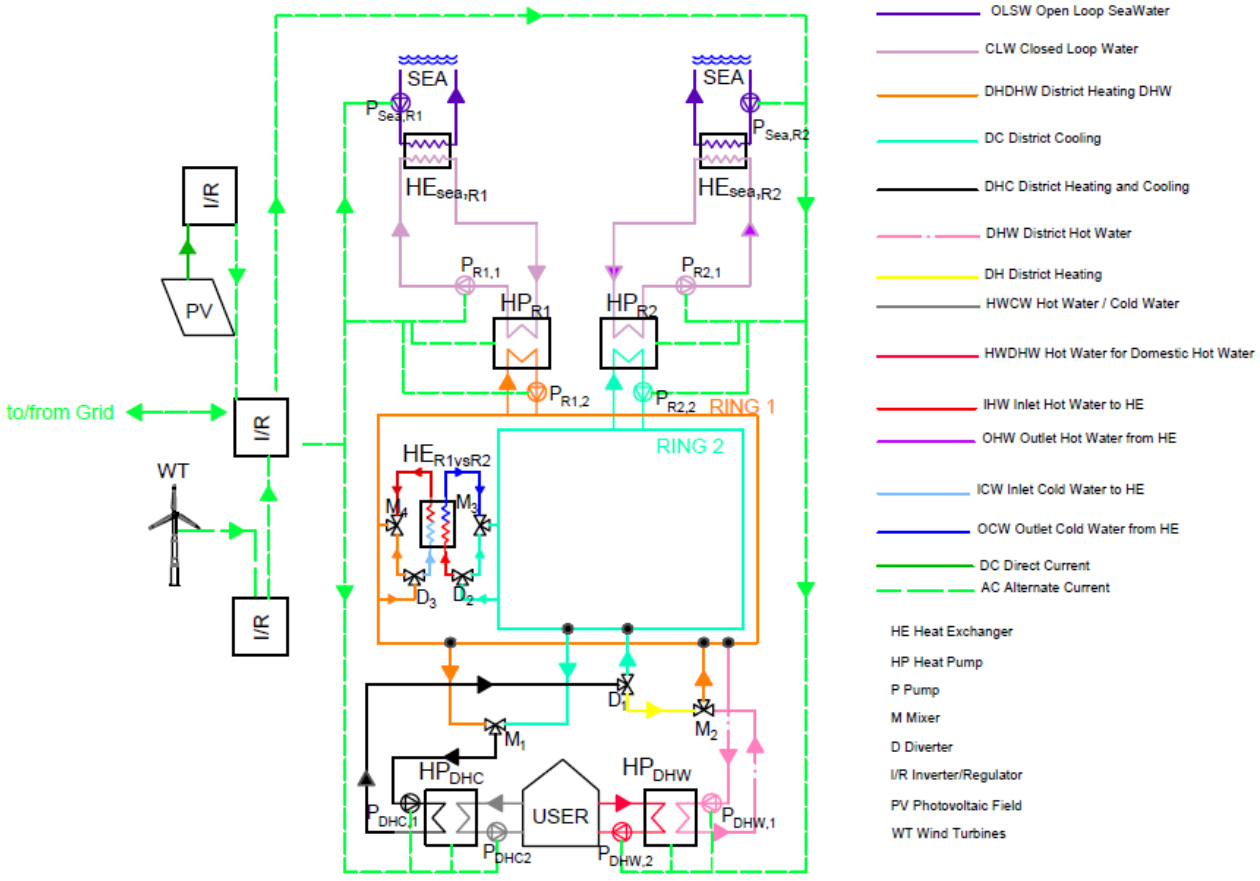

Figure 17. Layout of the 5GDHC system based on a plurality of renewable technologies.

3.1.2 System Model

The investigated districts, as well as all the included technologies are modelled and dynamically simulated by using the TRNSYS software, where a detailed method for

the assessments of building loads is also implemented. In particular, the space heating, cooling and electricity loads of the DHC buildings are evaluated on the basis of the work performed by Calise et al. [94].

The dynamic load for DHW is predicted according to the conventional assumptions concerning the Mediterranean islands communities, considering that an increased number of people inhabits the district during the summer seasons, according to the increasing of the touristic activity of the island. This assumption, made in this work, was implemented in a previous study [95], performed by the authors of this paper, in order to define the dynamic load for DHW purposes for users of Mediterranean islands. The design of the system is carried out considering the power peak of the user demand both for the electric requests of the network and buildings and for the thermal requests for space heating, cooling and DHW.

In order to model the developed 5GDHC network, TRNSYS software is used. TRNSYS is well known in the academic community mainly when it is used to assess both the building energy demand and dynamic energy performance of energy systems [96]. Further details regarding the types used and the models behind them are discussed in the work [92], together with the thermoeconomic model developed.

Wind turbines

Type 90 is used to calculate the power produced by WT, by considering the Betz theory. The produced power is calculated according to:

$$P = \frac{1}{2}\rho_{air} c_p A_r v^3 = \frac{1}{2}\rho_{air} 4a(1-a)^2 A_r v^3 \quad (5)$$

where c_p [−] is the power coefficient of WT, A_r [m^2] is the rotor area, ρ_{Air} [kg/m^3] is the air density and v [m/s] is the wind speed.

Type 90 is coupled with an external file (provided by the manufacturer, that must be provided to the Type, reporting the curve of power as a function of the wind speed for each operating condition The model also considers the variations of the air density and the increase of wind speed v with the height above the ground of the site where the WT is placed.

Photovoltaic field model

PV panels are modelled by means of Type 94: this library simulates the electric performance of the poly-crystalline/crystalline silicon cells adopting the so-called "four parameters" model. The slope of the current-voltage (IV) curve is null at the short-circuit condition:

$$\left(\frac{dI}{dV}\right)_{v=0} = 0 \tag{6}$$

The model is based on the following for parameters: i) R_s (module series resistance); ii) γ (empirical PV curve-fitting parameter); iii) $I_{o,ref}$ (diode reverse saturation current at reference conditions); iv) $I_{L,ref}$ (module photocurrent at reference conditions). These values are assessed from manufacturers' data for providing the *IV* curve at each time step. The current-voltage equation is:

$$I = I_{L,ref}\frac{G_{tot}}{G_{tot,ref}} - I_o\left[exp\left(\frac{q}{\gamma k T_c}\left(v + IR_s\right)\right) - 1\right] \tag{7}$$

The diode reverse saturation current I_o depends on the cell temperature and its value is calculated by mean of eq.(4):

$$\frac{I_0}{I_{0,ref}} = \left(\frac{T_C}{T_{C,ref}}\right)^3 \tag{8}$$

The PV operating current is evaluated by using the method of Newton, starting from the value of I_o, assessed by means of eq.(3).

Once I_o is obtained, the Newton's method is employed to calculate the PV current (I_{mp}) and voltage (v_{mp}) at the maximum power point along the IV curve by means of an iterative routine.

The current and voltage are then replaced into eq. (3) at the maximum power point, short circuit, and open-circuit conditions. Then, after a rearrangement, the following equation are added, as a function of $I_{L,ref}$, $I_{o,ref}$, γ:

$$\boldsymbol{I_{L,ref} \approx I_{sc,ref}} \tag{9}$$

$$\gamma = \frac{q\left(v_{mp,ref} - v_{oc,ref} + I_{mp,ref}R_s\right)}{kT_{c,ref}ln\left(1 - \frac{I_{mp,ref}}{I_{sc,ref}}\right)} \tag{10}$$

$$I_{o,ref} = \frac{I_{sc,ref}}{exp\left(\frac{qv_{oc,ref}}{\gamma kT_{c,ref}}\right)} \tag{11}$$

A fourth equation is provided to close the model. This equation is assessed by considering the analytical derivative of voltage with respect to temperature at the reference open-circuit condition.

$$\frac{\partial v_{oc}}{\partial T_c} = \mu_{voc} = \frac{\gamma k}{q}\left[ln\left(\frac{I_{sc,ref}}{I_{o,ref}}\right) + \frac{T_c\mu_{isc}}{I_{sc,ref}} - \left(3 + \frac{q\varepsilon}{\frac{\gamma}{N_s}kT_{c,ref}}\right)\right] \tag{12}$$

Finally, by means of the iterative routine the equivalent circuit characteristics are evaluated.

3.1.3 Case Study

The case study selected is a residential district of 800 buildings, located in Pantelleria island (South Italy, latitude 36°39′ N, longitude 11°58′ E) in the Mediterranean Sea .The procedure for the estimation of the energy loads for electricity, and space heating and cooling energy is reported in detail in ref. [94], as well as all the main features of the buildings and their envelope features. Pantelleria is characterized by 717 heating degree-days and according to the Presidential Decree 412/L73 [97], Pantelleria falls in climatic zone B. For this climatic zone, the heating system can be activated from December 1st to March 31st. The same Decree assesses that for climatic zone B the heating system is activated for a maximum of 8 hours per day and the indoor temperature must be set at 20°C.

The detailed description of the case study together with the data for the definition of the case study and the loads obtained are omitted here for the sake of brevity but can be found in ref. [92]. Table 1 summarizes the main thermoeconomic assumption regarding the reference and proposed system. In particular, the efficiency of the conventional gas-fired boilers (η_{boiler}) is assumed equal to 80 %, while the efficiency of the electric grid (η_{el}) is assumed equal to 46 %. The electric energy purchasing cost

($j_{el,fromGRID}$) is assumed equal to 0.16 €/kWh, while the natural gas purchasing cost (j_{NG}) is assume equal to 0.80 €/Sm^3.

Table 1. Thermoeconomic assumptions of the 5th generation DHC layout reference system.

Parameter	Description	Value	Unit
COP	Air to air heat pumps (RS)	3	
$j_{el,fromGRID}$	Electric energy purchasing unit cost	0.16	€/kWh
$j_{el,toGRID}$	Electric energy selling unit cost	0.05	€/kWh
j_{NG}	Natural gas unit cost	0.80	€/Sm^3
m_{WT}	ORC machine maintenance yearly cost	1.5	%/year
m_{PV}	PV field maintenance yearly cost	2	%/year
m_{pump}	Pumps maintenance cost	1	%/year
LHV_{NG}	Natural gas lower heating value	9.59	kWh/Sm^3
η_{el}	Conventional thermo-electric power plant efficiency	46	%
η_{boiler}	Natural gas-fired heater efficiency.	80	%
F_{el}	Electric energy equivalent CO_2 emission factor	0.48	kgCO_2/kWh
F_{NG}	Natural gas equivalent CO_2 emission factor	0.20	kgCO_2/kWh

3.1.4 Results

Simulations are carried out by means of TRNSYS over one year of operation using the weather data of Pantelleria, included in METEONORM database. The results obtained are analyzed and discussed considering different time bases (hours, weeks, months, year). In fact, thermal, cooling, and power can be integrated in order to calculate the related energy, considering any integration period higher than the simulation time-step. In this work, a time step of 2.4 minutes was selected, as a trade-off between computational time and accuracy. The following subsections present the dynamic results of the model for a random winter day. Then, the results are integrated on a monthly and yearly basis in order to illustrate the overall energy and economic performance of the proposed system more effectively.

The dynamic results refer to a representative winter day. Figure 18 and Figure 19 show some of the main parameters related to the thermal loop of the district. In particular, Figure 18 shows the trend of the following parameters: space heating load Q_{heat}, heat transferred to the load-side fluid by the heat pumps $Q_{load,HPDHC}$, heat transferred from the source fluid by the heat pumps $Q_{source,HPDHC}$, i.e. by the DHC network.

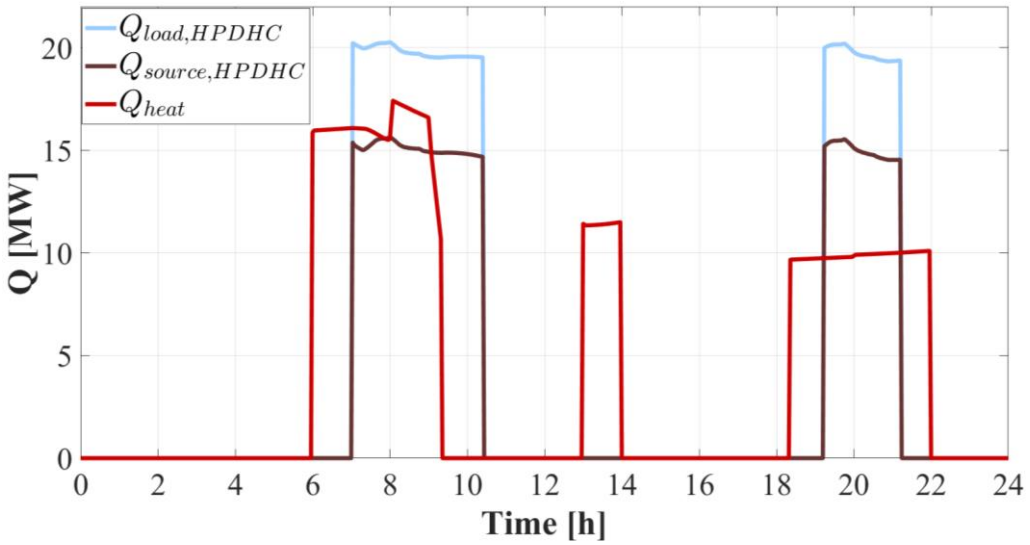

Figure 18. Winter day: thermal flow rates of heat pumps, HP_{DHC}.

For a typical winter day, the total space heating load Q_{heat} reaches its maximum value equal to 17.4 MW_{th} at 8:15 AM, whereas $Q_{load,HPDHC}$ reaches the maximum value of 2.07 MW_{th} at 8:00 AM. The peak of the heat transferred to the network $Q_{source,HPDHC}$ occurs at 8:00 AM, equal to 15.6 MW_{th}. This means that the thermal demand is not simultaneous with the HP_{DHC} heat rate production, mainly due to thermal inertia of the piping network as well as to the implemented control strategies. In particular, the continuous and instantaneous activation of heat pumps HP_{R1} on the network side can be better observed in Figure 19. Here, the heat transferred to the load-side fluid by the heat pumps $Q_{load,HPR1}$, i.e. to the RING1, the heat transferred from the source fluid by the heat pumps $Q_{source,HPR1}$, i.e. from the technical water passing through the seawater heat exchanger $HE_{sea,R1}$ are reported. In Figure 19, the control strategy, implemented to obtain a low temperature on RING1, is shown, observing the intermittent activation of the heat pumps HP_{R1}, which operate to maintain the supply temperature below 19°C on the source side of HP_{R1} (user side), with a return temperature higher than 16°C on the load side of HP_{R1}. The narrow temperature range implies the intermittent operation represented in Figure 19, that is typical during the dynamic simulation of district.

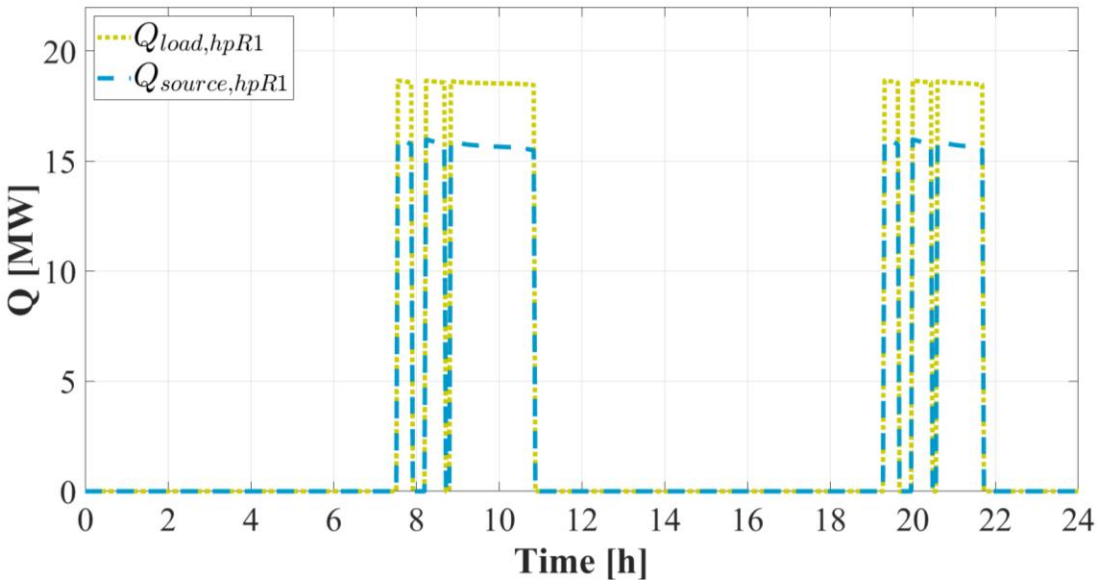

Figure 19. Winter day: thermal flow rates of heat pumps HPR1, RING1.

Figure 20 shows the electric powers of the subsystems, including the PV field and wind turbines, connected to the DHC network. In particular, Figure 20 shows the trend of the following parameters: the power production of the PV field $P_{el,PV}$ and WTs $P_{el,WT,}$ their sum $P_{el,PV\&WT,tot}$, the power required by the whole district $P_{el,district,tot}$, including the electric load of buildings, water-to-water heat pumps and circulation pumps, the power delivered to the grid $P_{el,toGRID}$ and withdrawn from the grid $P_{el,fromGRID}$. For a typical winter day, wind production is greater than PV field production. In particular, the electricity production of PV field occurs from 08:00 AM to 05:00 PM, with a peak power of 1.2 MW at 01:30 PM. WTs production occurs during all hours of the day, reaching the rated value equal to 4 MW, from 04:00 PM. At 02:00 PM a minimum value of $P_{el,WT}$ of about 2 MW is detected.

The electric energy integration from the grid, $P_{el,fromGRID}$, mainly occurs during the activation of the heat pumps. The electricity excesses $P_{el,toGRID}$ are also significant during the night hours due to the extra production of WTs with respect to the user electric demand $P_{el,district,tot}$. Note that $P_{el,district,tot}$ is significantly higher than $P_{el,PV\&WT,tot}$. This is due to the fact that the electric capacities of PV field and WTs are selected with the aim of maximizing the amount of electric energy self-consumed and minimizing the excesses. This determines that a certain amount of the electricity demands will be covered by the national grid. The intermittent trend of electricity demand is due to the heat pumps operation. The maximum value of $P_{el,district,tot}$ equal to 9 MW is reached at 10:00 AM.

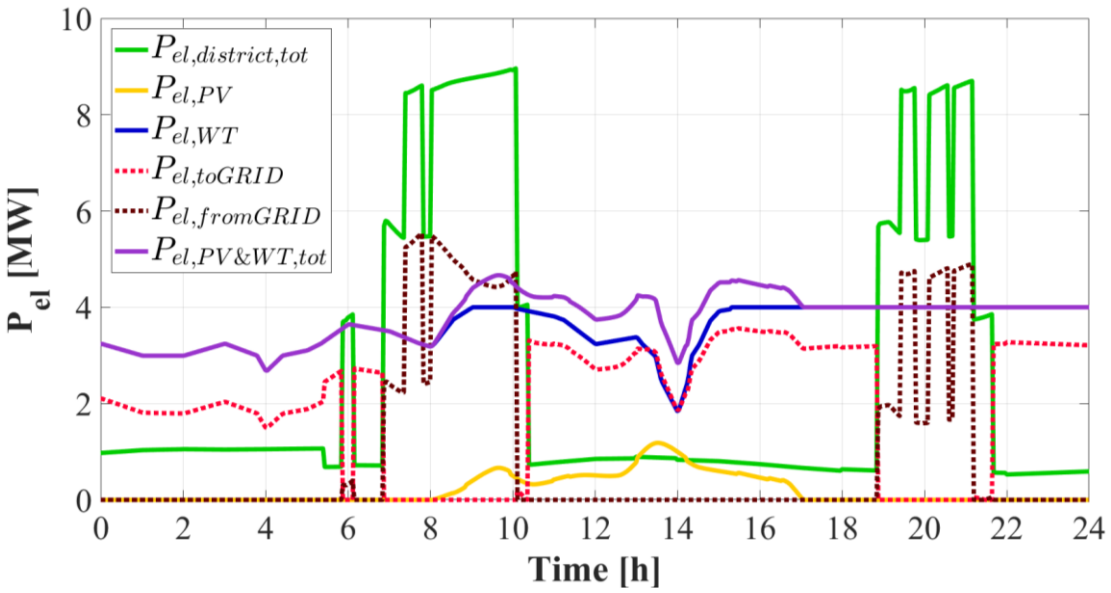

Figure 20. Winter Day: Powers.

Figure 21 shows the monthly performance of heat pumps HP_{DHC} in heating and cooling modes, and the monthly performance of heat pumps HP_{DHW} employed to match DHW energy demand. In particular, $E_{th,heat,HPDHC}$ and $E_{th,cool,HPDHC}$ are the total thermal energy supplied by heat pumps HP_{DHC} on the load side to the users, $E_{th,heat,HPDHW}$ is the thermal energy supplied by heat pumps HP_{DHW}. EE_{HPDHC} and EE_{HPDHW} are the electric energies required by heat pumps HP_{DHC} and HP_{DHW}, respectively and COP_{HPDHC} and COP_{HPDHW} are the corresponding Coefficients Of Performance. COP_{HPDHW} is stably close to 3.7 all year long, whereas COP_{HPDHC} is about 6.4 during the summer months and 4.1 during the winter ones. COP_{HPDHW} is lower than COP_{HPDHC} due to the higher DHW set point temperature considered for the user side, equal to 55°C.

In January, the thermal energy production of HP_{DHC}, $E_{th,heat,HPDHC}$, for space heating purpose is maximum. As for the cooling energy production $E_{th,cool,HPDHC}$, the maximum is achieved during the month of August. The same trend is detected for the electric energy demand of the heat pumps HP_{DHC}. During the spring and autumn months, since the energy demand for space heating and cooling is zero, the heat pumps do not operate. Therefore, the related electric energy demand is also zero. It is clearly shown that the seasonal trend of $E_{th,heat,HPDHW}$ can be justified by the dramatic increase of population for touristic activity. In fact, $E_{th,heat,HPDHW}$ passes from 202 MWh/month on February to 432 MWh/month on July and August. As shown, the simultaneity between the cooling and energy demand occurs only during the summer months, when the whole plant matches both the space cooling and DHW energy demands of the buildings.

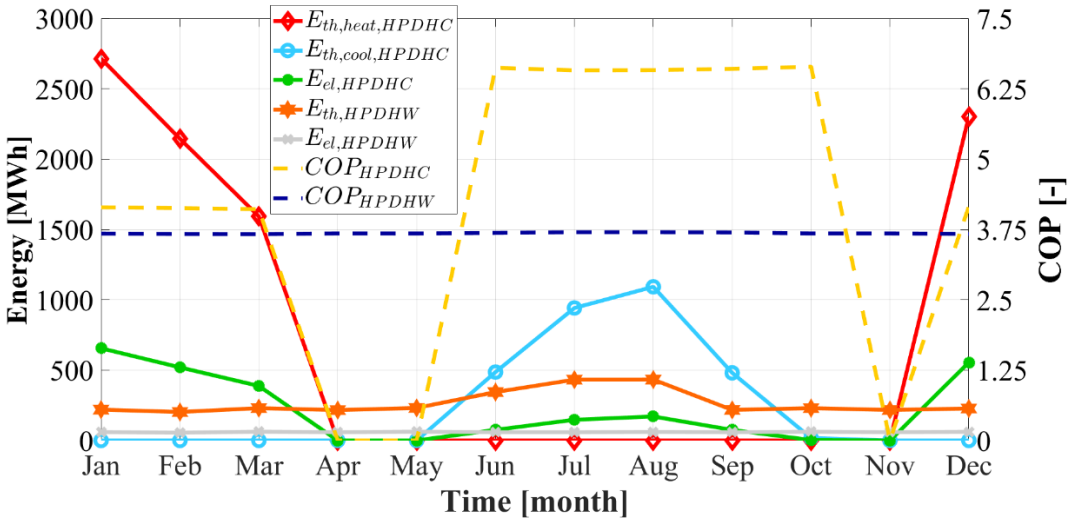

Figure 21. Thermal and electric energy of heat pumps of DHC network and DHW production (left), COP (right).

The yearly results of the carried out dynamic simulations are summarized in Figure 22, Figure 23 and in Table 2. The high COP values of the heat pumps on the two RINGs, HP_{R1} and HP_{R2}, equal to 6.7 and 7.7, respectively (Figure 22), are due to the use of heat exchangers operating with seawater as energy source. In fact, during the winter operation the seawater is a source of energy for the heat exchanger supplying the RING1, while during the summer operation the RING2 releases thermal energy to the seawater. This allows the heat pumps HP_{R1} and HP_{R2} to operate between optimal supply temperature ranges on the source side, capable of improving the units performance.

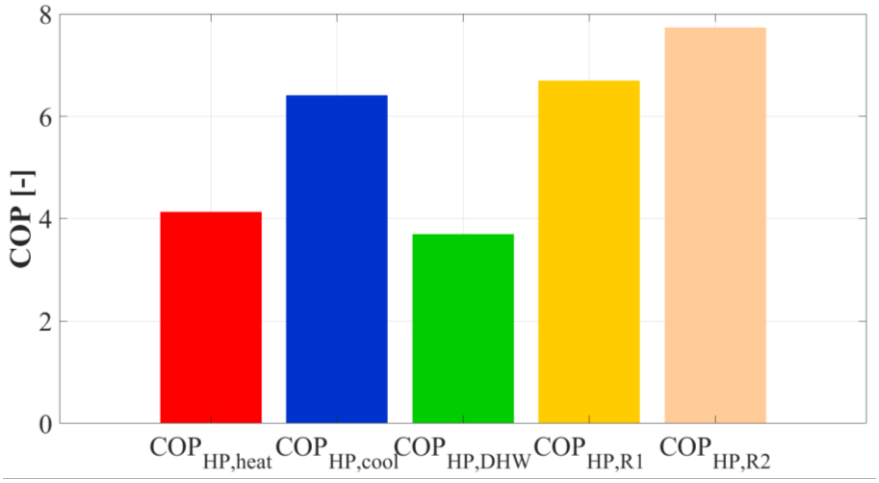

Figure 22. Heat pumps: Coefficient of Performance.

In Figure 23, the energy ratios between the main electric fluxes of the plant are reported. More specifically, EE_{PV} is the electric energy production of the PV field, EE_{WT} is the electric energy production of WTs, $EE_{renewable}$ is the total electric energy production by both the included renewable technologies, $EE_{self\text{-}consumed}$ is the self-consumed electric energy, EE_{user} is the total electric energy demand required by the

buildings of the district, electric components of the DHC system, such as pumps and heat pumps, EE_{toGRID} is the electric energy delivered to the grid and $EE_{fromGRID}$ is the electric energy withdrawn from the grid.

In particular, less than half of the electric energy production of the plant is self-consumed, i.e. 37%, due to the phase shift between the peak of renewable power production and the corresponding peak of power demand (see Figure 20). Despite the similar rated powers of WTs and PV panels, i.e. 4000 kW WTs and 3744 kW PV, WTs electric energy is much higher than the one produced by PV panels, due to the higher number of operating hours. The yearly ratios $EE_{WT}/EE_{renewable}$ and $EE_{PV}/EE_{renewable}$ are equal to 36% and 64%, respectively. The selected user equipped with the proposed renewable 5th generation district is able to meet more than half of the electricity demand. This means that the energy withdrawn from the grid is remarkably lower, with the $EE_{fromGRID}/EE_{user}$ ratio equal to 46%.

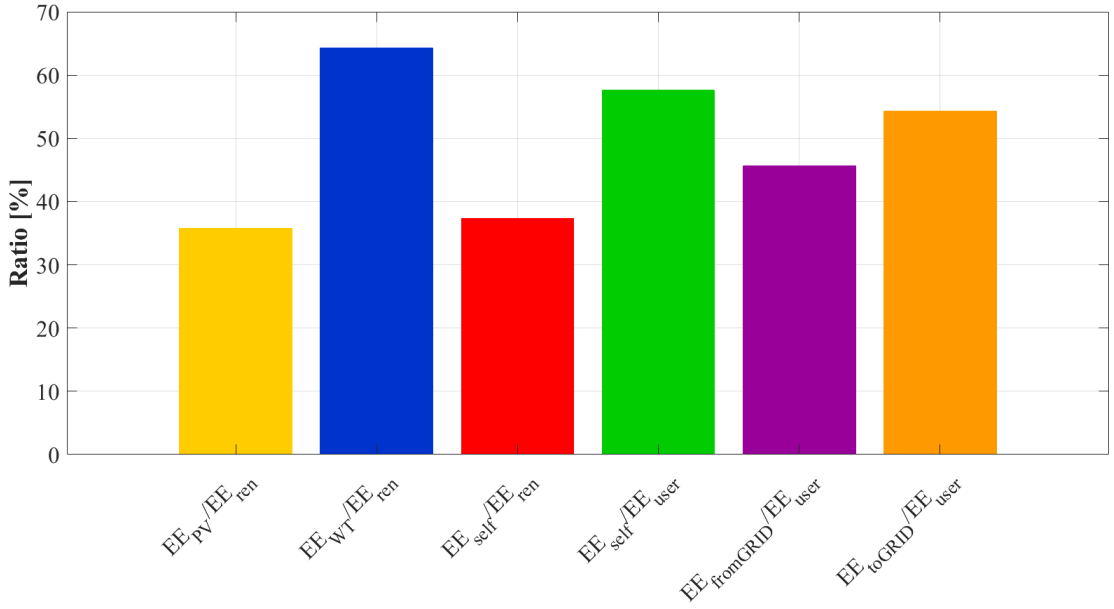

Figure 23. Electric energy ratios.

When the proposed system is compared to the reference system, in which the energy demands are matched by conventional energy technologies (gas boiler, electric chiller, and national electricity grid), the following environmental, economic and energy results are achieved, Table 2.

The proposed 5GDHC network is able to zero the primary energy consumption and CO_2 emissions of the district, considering that the *PES* and difference of CO_2 emissions between the reference and proposed system ΔCO_2 are equal to 133% and 134%. This is also due to the remarkable amount of the primary energy produced by renewable energy technologies delivered to the grid with respect to the primary energy withdrawn from the grid.

Although the yearly economic savings are relevant, roughly 72%, the *SPB* is quite high, equal to 14.7 years, due to the high capital cost of the plant *I*, including the cost of pumps C_{pumps}, heat exchangers C_{HE}, piping C_{piping}, heat pumps C_{HP}, WTs C_{WT} and PV panels C_{PV}. The high capital cost is mainly due to the cost heat pumps and WTs, equal to 28.7% and 23.4% of the total cost *I*, respectively (Figure 24).

The piping cost also significantly impacts on the total cost of the plant (21.1% of I). Due to the high capital cost of the system proposed, the Net Present Value (*NPV*) and Profit Index (*PI*) turned out to be negative. Furthermore, the Discounted Pay-Back (*DPB*) is extremely high and equal to 27.2 years.

All these key performance indicators suggest that the system is featured by poor economic profitability.

Table 2. Environmental, economic and energy results.

Parameter	Description	Value	Unit
PES	Primary Energy Saving	133	[%]
I	Total Capital Cost	25.6	[M€]
ΔC	Operating Costs Difference	1.75	[M€/year]
ΔC	Operating Costs Difference	72	[%]
ΔCO_2	CO2 Emissions Saving	134	[%]
SPB	Simple Pay-Back	14.7	[years]
DPB	Discounted Pay-Back	27.2	[years]
NPV	Net Present Value	-3.79	[M€]
PI	Profit Index	-0.15	[-]

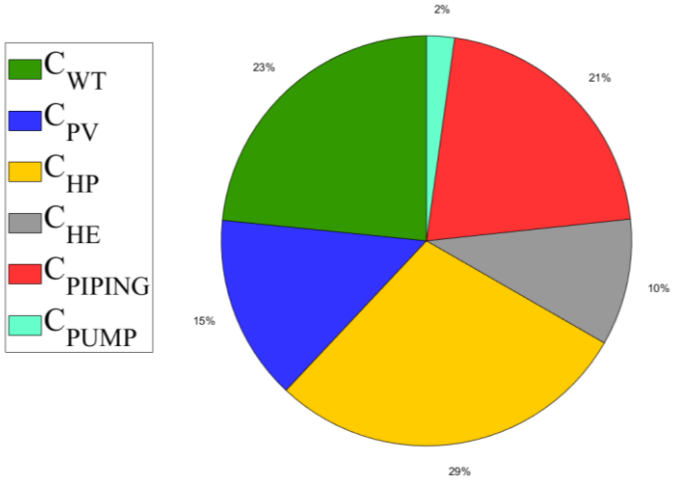

Figure 24. Percentages on the total cost *I*.

The results are also integrated by a sensitivity analysis aiming at evaluating the optimal capacities of renewable technologies. The analysis was performed by varying the rated power of the PV field, P_{PV}, as well as the rated capacity of wind turbines, P_{WT}. In particular, P_{PV} varied from 0 (no solar field) to 500 MW, whereas P_{WT} varied considering 1, 2, and 3 wind turbines corresponding to 2, 4 and 6 MW rated power.

Figure 25 shows how the variation of these parameters affect the *SPB* of the proposed system. With the same value of P_{WT}, in the initial part of the graph, i.e. for low values of P_{PV} and up to P_{PV} values of approximately 60 MW, *SPB* rapidly decreases. Considering the range of P_{PV} between 0 and 20 MW, *SPB* minimum can be easily identified. For values of P_{PV} higher than 60 MW, *SPB* exhibits an asymptotic trend. This means that a remarkable increase of *SPB* values is obtained only for significantly high values of installed PV power, corresponding to solar field featured by millions of m². In fact, for extremely large solar field capacities, PV capital costs become relevant for the overall plant capital cost. In particular, from P_{WT} =2 MW to P_{WT} =6 MW, *SPB* slightly decreases from 13.9 to 13.7 years for P_{PV} decreasing from 74.8 MW to 29.9 MW, respectively. Therefore, it is clear that according to the P_{WT} value, in order to obtain the minimum *SPB* value, considerable areas of PV field, between 200'000 and 500'000 m², are required.

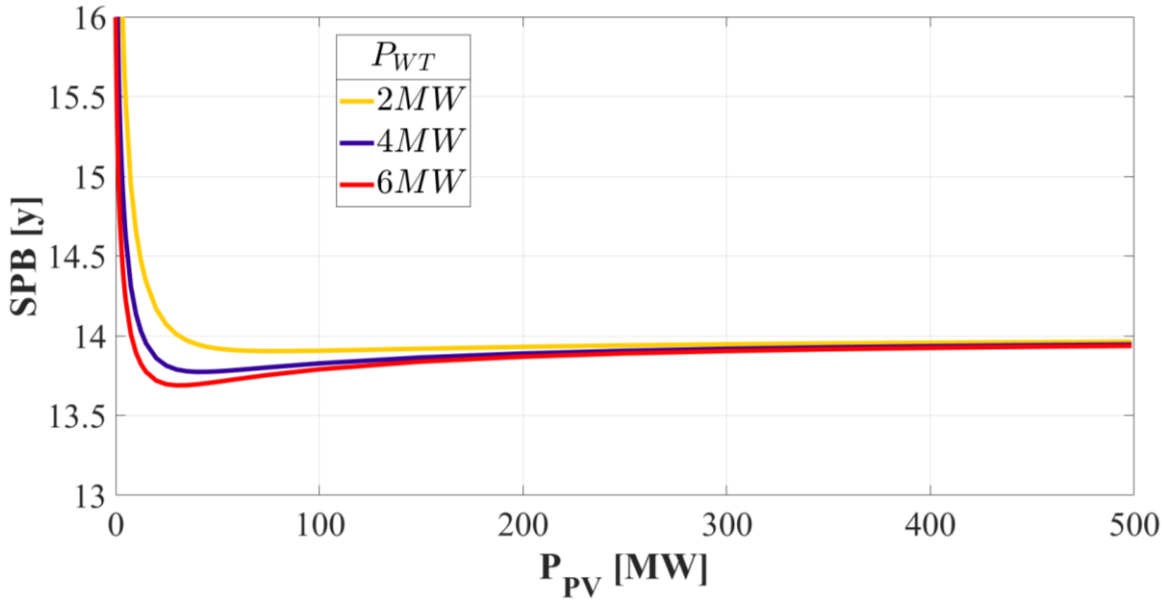

Figure 25. *SPB* vs P_{PV} for P_{WT} equal to 2 MW, 4 MW and 6 MW.

Figure 26 shows the trend of primary energy saving *PES* varying P_{PV} and P_{WT}. Obviously, increasing the rated power of both renewable energy sources, *PES* significantly increases over 350% for P_{PV} equal to 20 MW and P_{WT} equal to 6 MW.

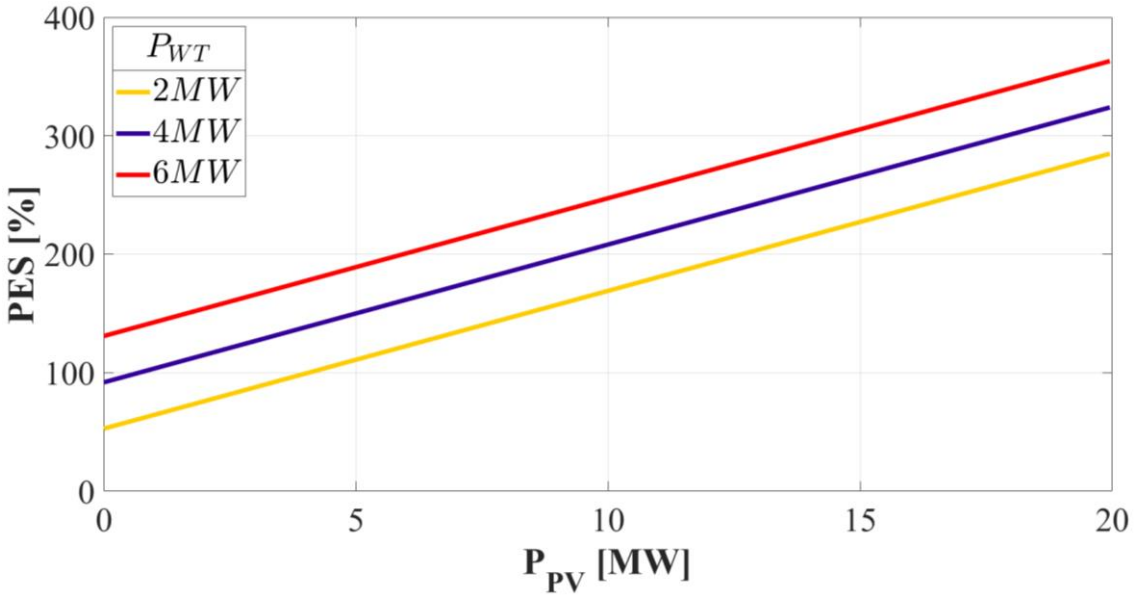

Figure 26. *PES* vs P_{PV} for P_{WT} equal to 2 MW, 4 MW and 6 MW.

In Figure 27 shows the trends of the ratios $EE_{self\text{-}consumed}/EE_{renewable}$ (the self-consumed electric energy/the total electric energy production by PV field and wind turbines), $EE_{toGRID}/EE_{renewable}$ (the electric energy delivered to the grid/the total electric energy production by PV field and wind turbines) and $EE_{self\text{-}consumed}/EE_{user}$ (the self-consumed electric energy/the total electric energy demand) as a function of P_{PV} and P_{WT} . With the same value of P_{PV} , the ratio $EE_{self\text{-}consumed}/EE_{renewable}$ increases when the number of installed wind turbines decreases. With the same value of P_{WT}, the ratio $EE_{self\text{-}consumed}/EE_{renewable}$ increases when the rated power of PV field decreases. This means that for high values of P_{PV} and P_{WT}, high electric energy excesses to the grid are obtained. The maximum value of $EE_{self\text{-}consumed}/EE_{renewable}$, equal to 64%, is reached for P_{WT} equal to 2 MW and P_{PV} equal to 0.15 MW.

These trends are consistent with the results discussed in the section *Dynamic Results*. In fact, a significant misalignment between power production and power demand has been detected. Therefore, the increase of the renewable power park capacity leads to a limited increase in the self-consumed energy (see ratio $EE_{self\text{-}consumed}/EE_{user}$) and a huge increase in electricity exported to the grid (see ratio $EE_{self\text{-}consumed}/EE_{renewable}$). For example, for the layout equipped with 3 WTs, i.e. 6 MW, and a PV field of 20 MW, the self-consumed energy matches almost 58% of the district electric energy demand, but 73% of the produced renewable electricity is exported to the grid.

The higher the P_{PV} and P_{WT} values, the higher the ratio $EE_{self\text{-}consumed}/EE_{user}$ due to the greater production of the installed renewable energy sources, able to match the user energy demand.

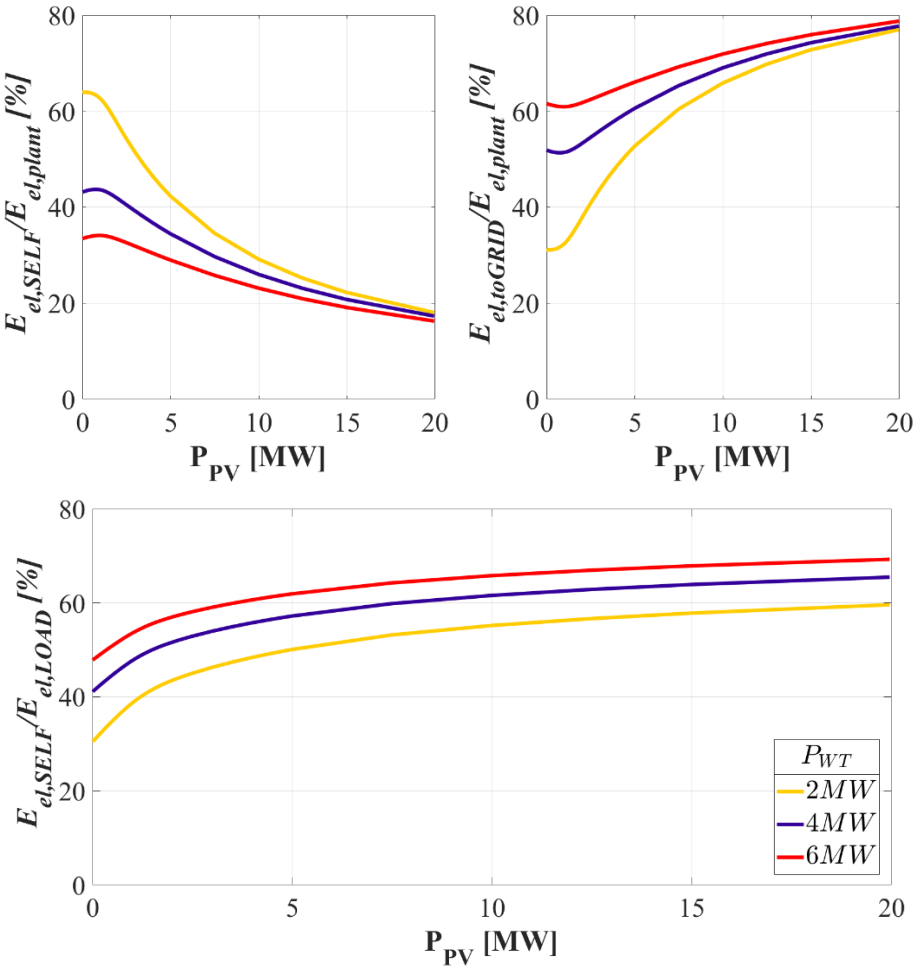

Figure 27. *PES* vs P_{PV} for P_{WT} equal to 2 MW, 4 MW and 6 MW.

3.2 A Comparative thermoeconomic analysis of fourth generation and fifth generation district heating and cooling networks

According to the literature review presented and discussed in [98], a relevant number of papers is available comparing 4GDHC and 5GDHC systems. However, to the best of the authors' knowledge, none of them presented a numerical comparative analysis of the two systems based on dynamic simulations and thermoeconomic analyses. There are only a few works which perform separately a dynamic simulation of a fourth-generation district network, as well as for the fifth-generation one, as the one previously discussed. However, no numerical comparative analysis is reported. In summary, the main novelties of the present work can be summarized as follows:

- Development of a dynamic simulation tool for both 4GDHC and 5GDHC systems based on detailed models implemented in TRNSYS environment, also including an efficient novel control strategy and a comparative thermoeconomic analysis.

- Detailed characterization of the dynamic thermal and electric loads of the district of Leganès, in Madrid, in case of 4th generation and 5th generation districts.
- Development of a detailed analysis with a critical approach to dig into the differences between the 4th and 5th generation districts with the aim of providing useful suggestions for academics and professionals when selecting the topology of a district heating and cooling network, in particular for residential application.

3.2.1 System Layout

In this work two layouts are analysed, namely 4GDHC network and 5GDHC network. The layout of the 4th generation DHC is shown in Figure 28.

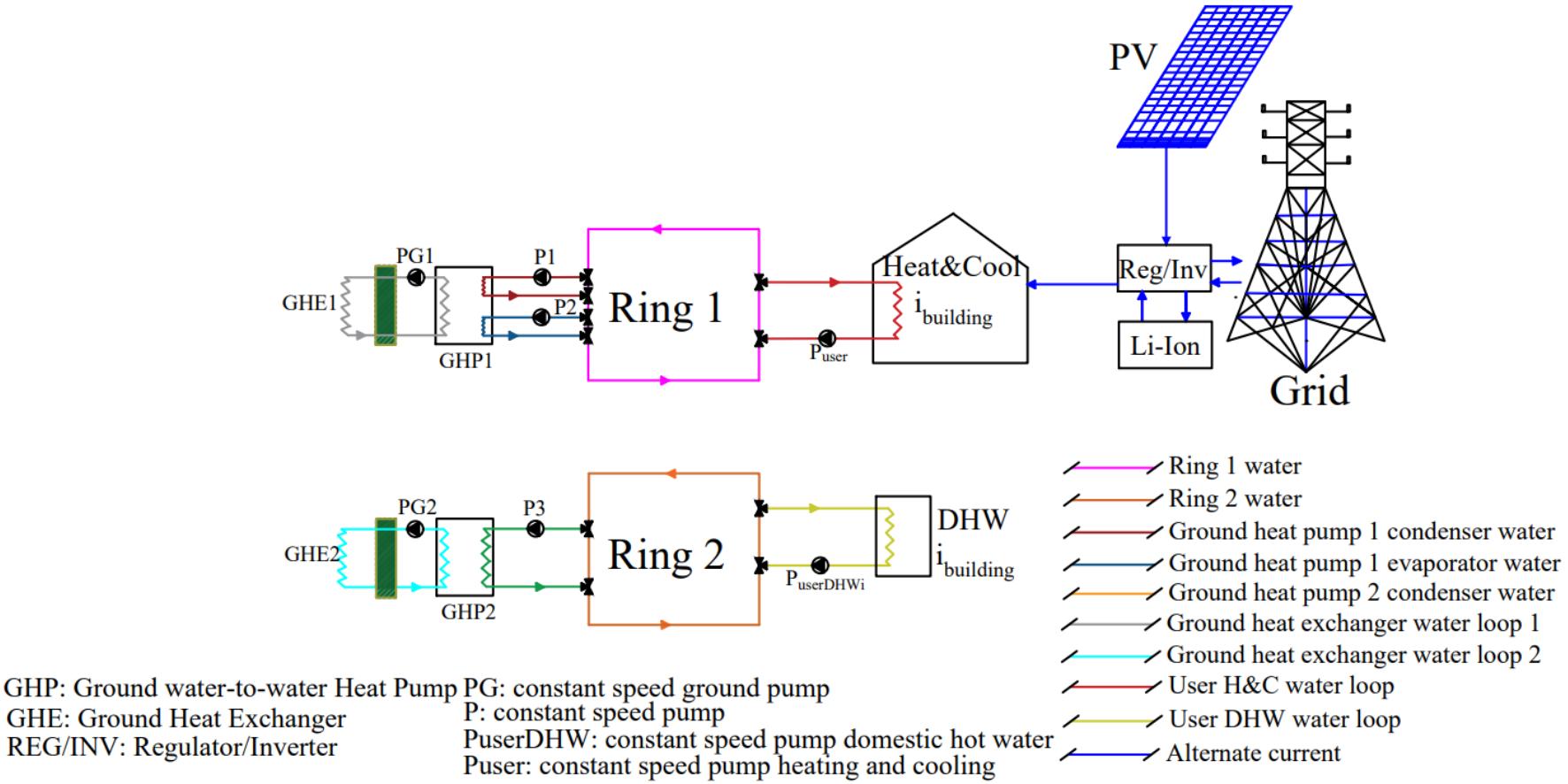

Figure 28. Layout of the 4GDHC system.

The 4GDHC system designed for this case study includes two rings, namely RING 1 (R1) and RING 2 (R2). R1 meets the energy demand for building space heating and cooling of the selected residential district. R2 meets the thermal load for DHW. R1 is equipped with a group of 6 reversible GHPs (GHP1) of 1.25 MWth/HP. The R2 is equipped with a group of 3 high-temperature GHPs (GHP2).

In case of 4GDHC, the same ring is used for both space heating and cooling purposes. This specific layout is selected considering that the residential users are equipped with fan-coils. Thus, the same plant (R1, Figure 28) may be used for supplying both building space cooling and heating. In addition, according to Legislation, the heating and the cooling seasons are strictly separated. Therefore, no simultaneous space heating and cooling demand ever occurs.

In this case, a different ring (R2, Figure 28) is used for matching the thermal energy demand for domestic hot water. This specific arrangement is selected considering two aspects. First, the DHW ring (R2, Figure 28) has a higher supply temperature, i.e. 60°C-70°C, to avoid the Legionella bacteria formation in the heat exchanger. Conversely, the district heating ring (R1, Figure 28) is featured by a lower temperature, i.e. 40°C-50°C. Using the same ring for building space heating and domestic hot water would significantly worsen the performance of the heat pumps, balancing this ring. In fact, the higher the condensing temperature, the lower the COP of the heat pumps. Second, such arrangement allows the proposed plant to simultaneously match the domestic hot water demand (via R2) and the building space cooling demand (via R1).

According to the data available in literature [99], R1 operating temperature (T_{R1}) ranges between 50°C and 60°C in heating mode, i.e. during the winter period. When T_{R1} decreases below 50°C, the thermal energy is supplied by the GHP1 condenser water loop (GHPCW) to the R1. In particular, the pump P1 is turned on allowing the group GHP1 to heat the R1 loop water. Heat is collected from the group of ground heat exchangers GHE1s that supply thermal energy to the evaporator of GHP1 by means of a water loop. Using the ground as hot energy source, the performance of the heat transfer system may be significantly enhanced. The temperature of the ground is much more stable and higher with respect to the one of the outdoor air. This leads to higher values of the COP of the GHP1s. The GHP1s are turned off when T_{R1} reaches the threshold value of 60°C.

The water of R1 is delivered to the fan coils installed in the buildings of the residential district, to keep the indoor temperature equal to 20±1°C. During the

summer period, R1 operates in cooling mode. Then, T_{R1} ranges from 6°C to 12°C. When T_{R1} rises over 12°C, the pump P2 is activated, supplying thermal energy from R1 to the evaporators of the GHP1s. The heat is transferred to the GHE1s by means of the ground heat exchanger water loop activating the pump PG1. In this case, the condenser of the GHP1s supply heat to the water loop, which rejects it to the ground through the GHE1s.

In summer, the temperature of the ground is more stable and lower than the one of the outdoor air. Therefore, in summer period the average COP is also higher with respect to the case of air-to-water HPs. The rated capacity of each of the HPs in cooling mode is 1.14 MW. When T_{R1} reaches the threshold value of 6°C, the GHP1s are turned off. During the summer period, R1 delivers the chilled water to the fan coils installed into the building of the district, to keep the indoor temperature equal to 26±1°C.

R2 loop operates according to a similar strategy, with T_{R2} ranging between 60°C and 70°C. R2 is equipped with the group GHP2, supplying the ring when T_{R2} decreases below 60°C. In fact, in this case, pump P3 is activated to provide thermal energy from the condenser water loop of the GHP2s. Then, P3 is turned off again when the threshold value of 70°C is reached. The water of this ring is delivered to the substations installed in the buildings which exchange heat to deliver DHW.

The layout includes a 3 MW PV field equipped with a 15 MWh lithium-ion battery for storage purpose. This system is able to meet a relevant amount of the electricity demand of the district. Note that the electricity demand of the district includes the baseload of the residential buildings due to the electric appliances of each apartment, the electricity supplied to the ground heat pumps, and to the auxiliary pumps.

The network is equipped with an internal electric grid where all the buildings, GHPs and auxiliary devices are connected, together with the PV field. Moreover, this grid is grid-connected to the national electric grid for power exchange both in case of excess or integration. In Figure 2, such internal connections are omitted and only one substation is shown despite the relevant number of end users which are connected to the grid. More details regarding the end user are discussed in the Case Study section. The same approach is used for the layout of the 5GDHC network.

The layout of the 5th generation district is shown in Figure 29.

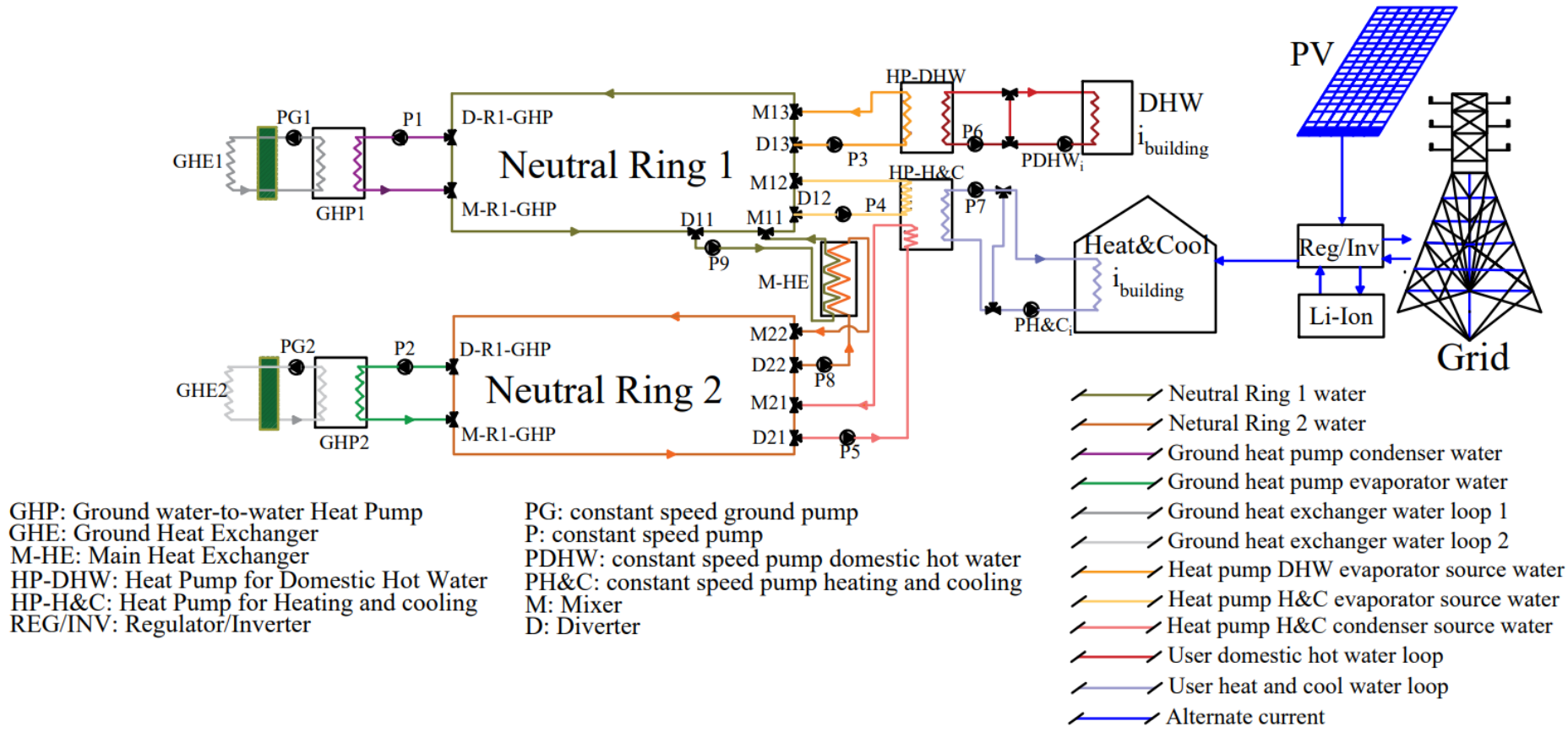

Figure 29. Layout of the 5GDHC system.

In this case, the system is based on two neutral rings in a double-ring bidirectional arrangement, namely Neutral Ring 1 (NR1) and Neutral Ring 2 (NR2). NR1 delivers heat to the evaporators of the WWHPs for DHW (HPs-DHW) and for building space heating (HPs-H&C). The temperature level of NR1 (T_{NR1}) ranges between 15.5 °C and 19.0 °C. When T_{NR1} decreases below the minimum value, the pump P1 is turned on. The condenser water loop of the group of 4 HPs, GHP1, supplies heat to NR1 to achieve the ring set point temperature of 19.0 °C.

NR2 provides cooling energy to the condensers of the HPs-H&C, working at temperatures ranging between 20.0 °C and 23.5 °C. Cooling energy is provided to the NR2 by means of the group of two GHP2s, used to decrease the temperature of the ring. In fact, in summer, the GHE2 rejects heat to the ground which is at lower temperature with respect to the outdoor air temperature. Then, HPs-DHW uses NR1 as thermal source. HPs-DHW consists of 4 WWHPs, which deliver thermal energy to the users for producing DHW (UDHWL). This secondary ring operates between 46 °C and 55 °C.

Pump P3 is switched on when the temperature decreases below the minimum value to deliver the water of NR1 to the HPs-DHW. At the same time, HP-H&C operates to meet the heating and cooling demand of the buildings of the residential district, by means of 4 WWHPs H&C (see UHCW). In heating mode, the HPs-H&C are fed by the water of NR1. In cooling mode, the HPs-H&C are fed from the water of NR2.The temperature ranges from 10 °C to 15 °C.

During the summer period, the heat exchanger M-HE is activated, allowing heat exchange from the NR2 to the NR1. In fact, during the summer period, NR1 must provide thermal energy for DHW, at the same time the NR2 must address the energy demand for space cooling. As well as the 4GDHC network, also the 5GDHC network is equipped with a 3 MWe PV field coupled with a 15 MWh lithium-ion battery. Moreover, the configuration of the internal smart grid is the same for both the layouts proposed. Further details regarding the functioning of the 5GDHC network are discussed in the previous work [89].

3.2.2 System Model

Both the district heating systems are developed in TRNSYS environment

Several components are included in the proposed systems, namely: ground heat exchangers, heat pumps, photovoltaic modules, electric battery, hydronic pumps, thermal storage, building load, and other minor components. For sake of brevity, the discussion related to the models is here omitted, since they are presented in detail in a previous work of the authors [89]. The most important thing to know is that the

thermal inertia of the district was accurately considered in TRNSYS by means of mixed tanks. In fact, these are needed to model the capacitive effect of the ring which would not be otherwise possible with this software. Note that, both networks (4GDHC and 5GDHC) are modelled following the same approach, thus both networks are featured by similar thermal inertia and thermal capacity.

Thermoeconomic model

The thermoeconomic model aims to compare the energy, environmental and economic results obtained comparing the 4GDHC system and the 5GDHC system. Both systems are compared to a reference system where the thermal load is met by conventional boilers and conventional electric chillers. Furthermore, the electric load of the district is only met by the national electric grid. The primary energy (*PE*) consumed by the reference system (RS) and the proposed systems (PS) are calculated, respectively, as:

$$PE_{,RS} = \sum_{i=1}^{n} \left[\frac{E_{th,H} + E_{th,DHW}}{\eta_b} + \frac{E_{th,C}}{\eta_{el,grid} \cdot COP_{ref}} + \frac{E_{el,LOAD}}{\eta_{el,grid}} \right]_i \tag{13}$$

$$PE_{,PS} = \sum_{i=1}^{n} \left[\frac{E_{el,\ fromGRID} - E_{el,\ toGRID}}{\eta_{el,\ grid}} \right]_i \tag{14}$$

The primary energy of proposed system ($PE_{,PS}$) is only due to the electricity withdrawn from the grid minus the energy sent to the grid. This equation is the same for both the 4GDHC system and 5GDHC system which are the alternative solutions proposed and compared in this work. Clearly, the values adopted in the equation are different basing on the case. The primary energy saving (*PES*) of the solution proposed is:

$$PES = \frac{PE_{RS} - PE_{PS}}{PE_{RS}} \tag{15}$$

In order to assess the performance of the adopted DHC technology, a primary energy saving index referred only to the thermal energy demand of the district is evaluated.

$$PES_{DHC} = 1 - \frac{\left(E_{el,\ HPs} + E_{el,\ pumps} \right) / \eta_{el,\ grid}}{\frac{E_{th,H} + E_{th,DHW}}{\eta_b} + \frac{E_{th,C}}{\eta_{el,grid} \cdot COP_{ref}}} \tag{16}$$

The environmental analysis in terms of avoided CO_2 emissions is performed according to the following equations.

$$MCO_{2,RS} = \sum_{i=1}^{n} \left[\frac{E_{th,H} + E_{th,DHW}}{\eta_b} \cdot f_{NG} + \left(\frac{E_{th,C}}{COP_{ref}} + E_{el,LOAD} \right) \cdot f_{EE} \right]_i \quad (17)$$

$$MCO_{2,PS} = \sum_{i=1}^{n} \left[\left(E_{el,\ fromGRID} - E_{el,\ toGRID} \right) \cdot f_{EE} \right]_i \quad (18)$$

The economic feasibility of both the solutions is calculated in the same way, according to the equations reported in [89]. The Simple Pay Back (*SPB*), Net Present Value (*NPV*), and Profit Index (*PI*) of the systems are also evaluated. Furthermore, a Demand Overlap Coefficient (*DOC*) is also considered in this case study for the 4GDHC and the 5GDHC. This parameter was first introduced by [100], it ranges from 0 to 1, and it is useful in understanding how much heating and cooling demands overlap during the year.

$$\Phi = \frac{2 \cdot \sum_t min \left\{ \sum_{i=1}^{n} P_{th,H,i} , \sum_{i=1}^{n} P_{th,C,i} \right\}}{\sum_t \left[\sum_{i=1}^{n} \left(P_{th,H,i} + P_{th,C,i} \right) \right]_t} \quad (19)$$

Table 3 shows the values of the parameters adopted for the thermoeconomic analysis.

Table 3. main parameters used for the thermoeconomic analysis.

Parameter	Description	Value	Unit
$\eta_{el,grid}$	Electric efficiency of national grid	0.498	-
η_b	Conventional boiler efficiency	0.750	-
COP_{ref}	Reference electric chiller coefficient of performance	3.00	-
LHV_{NG}	Natural gas lower heating value	9.590	kWh/Sm^3
f_{EE}	Unit emission of CO_2 per kWhe	0.182 [101]	kg$_{CO2,el}$/kWhe
f_{NG}	Unit emission of CO_2 per kWh of natural gas consumed	0.190	kg$_{CO2,NG}$/kWhp
$Cu_{,PV}$	Unit cost of PV modules per peak power	1000 [102]	€/kWp
$Cu_{,sto}$	Unit cost of lithium-ion storage	200 [102]	€/kWh
$Cu_{,HP}$	Unit cost of the heat pump	150	€/kW
$Cu_{,piping}$	Unit cost of the piping for the network	33	€/m
$Cu_{,excavation}$	Unit excavation cost	5	€/m^3
j_{NG}	Unit cost of natural gas	0.689	€/ Sm^3
$j_{el,fromGRID}$	Purchasing unit cost of electric energy	0.223	€/kWh
$j_{el,toGRID}$	Selling unit cost of electric energy	0.050	€/kWh

3.2.3 Case Study

For the case proposed study, the residential district of Leganès, in Madrid, was again selected. In addition to the previous work, this one also presents the approach adopted for modelling the residential district and for validating this model. In particular, the district includes 50 buildings occupied by 2490 inhabitants. In order to assess the building energy demand a clustering approach was used with 4

representative buildings selected as the most commonly diffused in the district. The buildings were selected according to the data available in literature and direct inspections of the district. Inhabitants of the district were selected basing on a statistical report [103] and thus divided into families (FAM), old people (OP), and young people (YP) according to the data obtained.

The occupancy profiles of the users for both winter and summer periods are shown in Figure 30 and Figure 31, respectively. As previously specified in the "system model" section, the thermal load of the buildings was accurately characterized by means of a 3D model. Note that the thermal load was assessed also considering the heat gains due to the electric appliances installed into the apartments and due to the activities of the building users. In this framework, this occupancy profiles are also useful to characterize the heat gain of the building.

The buildings of the district were built between the 50s and the 70s, so it can be assumed that they are made of brick walls [104]. In Table 4 the main thermophysical characteristics of the buildings are shown. The seasonal heating period ranges from September 16th to April 30th, while the seasonal cooling period occurs from May 1st to September 15th [105]. Furthermore, the indoor set point temperature is set at 20°C for the heating period and 26°C for the cooling period.

The electric load of the building was assessed according to the approach described in [89]. The UNI-EN-ISO-13790 regulation was adopted to predict the domestic hot water demand [106].

Figure 32 displays the monthly thermal load of the 4 clusters of buildings selected for modelling the residential district. It can be noticed that the district has a peak of thermal energy demand greater than 800 MWh during December and January, and a much lower peak for cooling in July, nearly 200 MWh. Considering that the district covers an area of almost 0.37 km^2, with a total pipe length of roughly 6 km, the energy density of the district is roughly 600 kWh/m^2 for building space heating demand and 90 kWh/m^2 for building space cooling, Table 5.

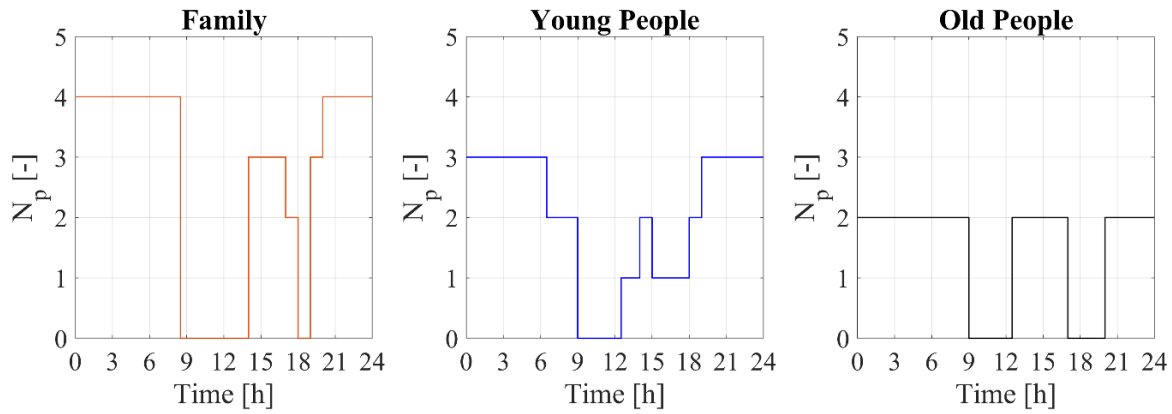

Figure 30. Occupancy profile in the winter period.

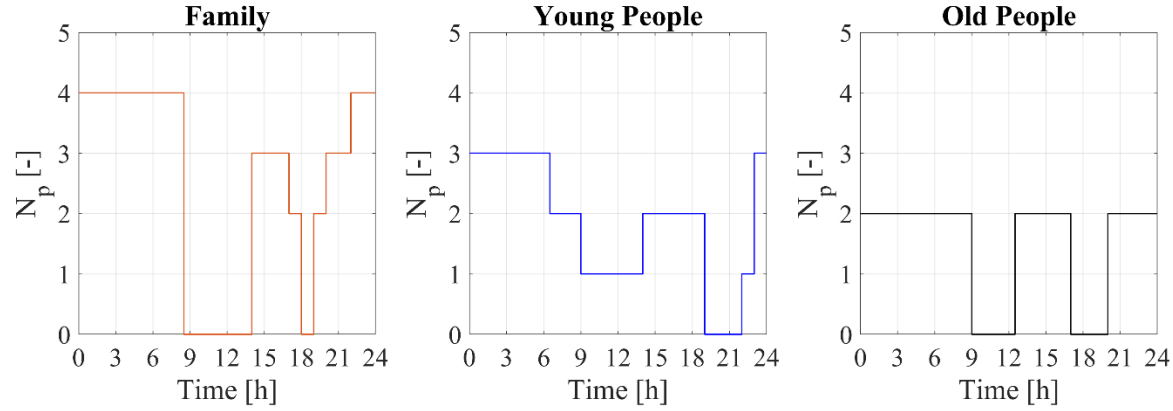

Figure 31. Occupancy profile in the summer period.

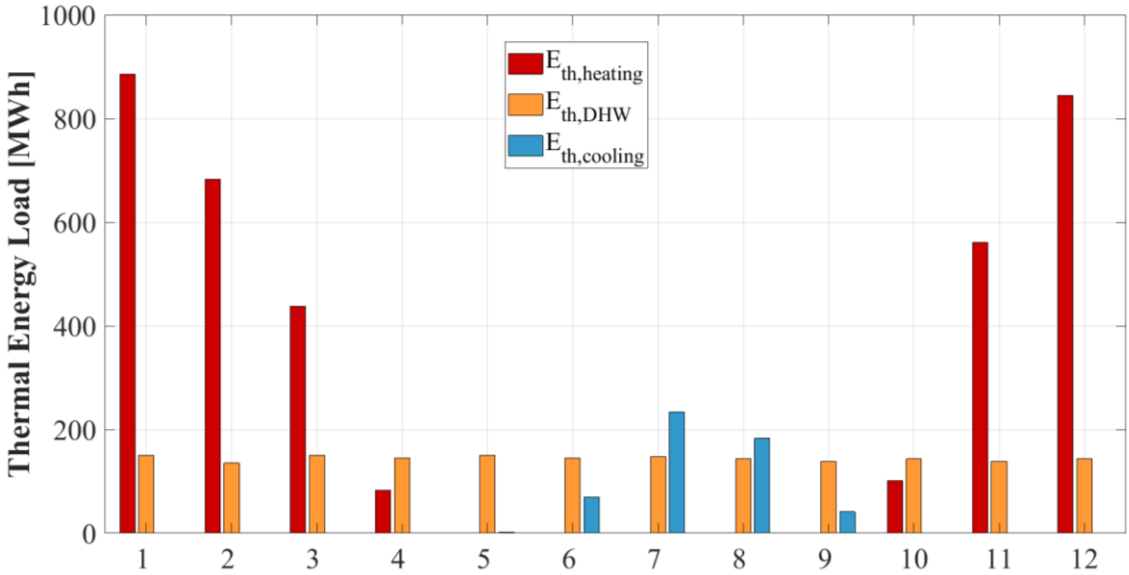

Figure 32. Thermal energy for Heating, Cooling, and Domestic Hot Water demanded by the district per each month of the year.

Table 4. Thermophysical features of the buildings considered.

Element	Thermal transmittance U [W/m²K]	Thickness [m]	ϱ_s [-]	ε [-]
Roof	0.949	0.27	0.4	0.9
Façades	1.20 - 1.26	0.33-0.35	-	-
Ground floor	1.12	0.40	-	-

Adjacent ceiling	1.75	0.29	-	-
Window glass	2.89	0.004/0.016/0.004	0.13	0.18

Table 5. Energy Density of the District.

Parameter	Space Heating	Domestic Hot Water	Space Cooling
Energy density [kWh/m²]	599.66	288.68	88.40
Linear density [kWh/m]	10.68	5.14	1.57

The reference system (RS) is the above-described residential district where the electric load is met by the electric national grid and the building space heating and DHW demand are met by conventional boilers. Furthermore, the cooling demand is matched by electrically driven air-to-air HPs.

The proposed system 1 (PS1) consists of the selected residential district where a 4th generation DHC network is considered to meet the building space heating and cooling demands and the DHW thermal energy demand. In addition, a 3 MW PV field is partially integrated to meet the electricity demand, coupled with a 15 MWh lithium-ion battery.

The proposed system 2 (PS2) includes a 5th generation DHC network for matching the residential district building space heating/cooling and DHW energy demand. A 3 MW PV field of is also included in such layout, equipped with the same battery of the PS1. Details of the 5GDHC are shown in the previous work [89].

In this section only the main features of 4GDHC are discussed. The 4th generation district is based on 6 HWFG6412 AERMEC [92] WWHPs for the R1 and 3 HWFG6412 AERMEC for the R2 (see Table 6). The ground heat exchangers are designed according to the guidelines provided in Ref. [107]. The GHEs peak power is calculated according to the maximum thermal energy demand of the ground coupled heat pumps. The rated specific heat transfer rate for the clay ground is 20 W/m^2 [107]. Thermal features of the GHEs are shown in Table 7. The maximum depth of the GHEs pipes is 9 m, since the ground temperature is sufficiently stable and allows the HPs evaporators to suitably work in the desired range of temperatures [89]. The length of the ring is estimated to be of 3 km, for both R1 and R2.

In the proposed system PS1 and PS2 the PV renewable power production is managed according to the energy community agreement. In fact, according to this approach the renewable production is shared among the users of the district. This strategy maximizes the renewable power self-consumption.

Table 6. Technical features of the HWFG6412 AERMEC heat pump.

Parameter	Description	Value	Unit
$P_{th,H}$	Rated thermal power in heating mode	1.254	MW
$P_{th,C}$	Rated thermal power in cooling mode	1.143	MW
COP	Coefficient of Performance in rated conditions	4.66	-
EER	Energy Efficiency Ratio in rated conditions	5.11	-
$m_{water,L}$	Water flow rate load side	217.84	m^3/h
$m_{water,S}$	Water flow rate source side	288.37	m^3/h

Table 7. Thermal features of the GHEs.

	Q_{gr} [MW]	A_{exch} [m^2]	A_{exch} [km^2]
GHE1	5.402	270´112	0.27
GHE2	2.541	127´050	0.13

3.2.4 Results

One-year simulations are performed using a time step of 1.5 minutes. Results are analysed on daily, monthly, and yearly bases. In particular, the results are mainly focused on the comparison between the electricity demands of the two proposed systems. The parametric analysis is here omitted for the sake of brevity but it can be found in ref. [98].

Figure 5 shows the electricity consumption and production for a typical day in the winter period for both the 4GDHC and 5GDHC systems.

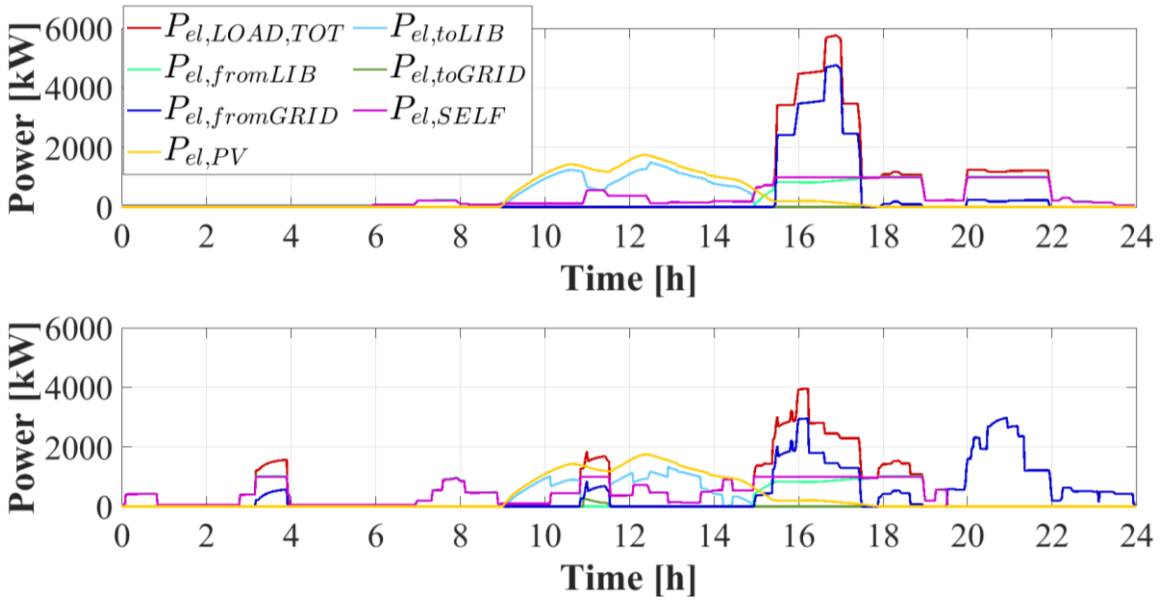

Figure 33. Power flows for the 4GDHC system (top) and the 5GDHC system (bottom) in a typical winter day.

5GDHC is characterized by a more stable energy consumption ($P_{el,LOAD,TOT}$) during the day. The peak demand is higher for 4GDHC, but the overall consumption of the

5GDHC is greater. This difference is due to the features of 4GDHC and 5GDHC systems. In fact, in 4GDHC arrangement the building space heating demand is directly matched by the thermal network balanced by means of a group of ground heat pumps GHPs. A peak of the demand is detected when these GHPs are activated, i.e. from 3:45 PM to 5:50 PM, $P_{el,LOAD,TOT}$ ranges between 3500 kW to 5800 kW.

Conversely, for 5GDHC the thermal energy demand is matched by the HPs installed in the substations, which exploit the neutral ring NR1 as thermal energy sink. This neutral ring (NR1) is balanced by means of the GHPs1 (Figure 29). Therefore, the heat demand of the district is split among several heat pumps, which are activated during the day in different periods of the day. Therefore, several peaks of power demand ($P_{el,LOAD,TOT}$) are detected during the day. As a consequence, the magnitude of the peaks is lower than the one achieved by 4GDHC, due to its centralized energy production. The peak for space heating demand occurs in the afternoon, Figure 33, when people come back home. Therefore, a dramatic mismatching between power demand and power production ($P_{el,PV}$) is detected. This mismatching is partially balanced by the electric storage, improving the self-consumption ($P_{el,SELF}$).

Figure 6 shows the electric consumption of the 4GDHC during the year along with some useful energy ratios. The electricity delivered to the heat pumps ($E_{el,HPs}$) of the DHC accounts for the majority of the residential district load. According to the results discussed in literature, crowded residential districts are featured by a higher building space heating demand. This trend is due to the buildings self-shadings, reducing the solar radiation incident on the buildings. Thus, the cooling energy demand is lower whereas the heating energy demand is higher, comparing to the case of an isolated building. The self-consumption of electric energy ($E_{el,SELF}$) is relevant, with an average around 300 MWh/month and a coverage of roughly 70% during the year. Only in the winter period the self-consumption is lower, $E_{el,SELF}/E_{el,LOAD}$ around 0.4, because of the dramatic increase of the load.

The ratio $E_{el,SELF}/E_{el,PV}$ ranges widely, with an average of 0.4 in summer period and 0.8 in winter period. This trend is clearly explained by the dynamic trends, see Figure 33. In fact, the peak of power production occurs in the central part of the day, whereas the peak of power demand occurs in the late afternoon and evening. Therefore, only a limited share of renewable electricity meets the district electricity demand. Thus, $E_{el,fromGRID}$ is extremely high during the winter period, being constantly greater than 400 MWh/month. The opposite occurs for $E_{el,toGRID}$ which is still relevant with an average value above 300 MWh/month in the summer period. This occurs despite the fact that the PV system is equipped with a 15 MWh lithium-ion battery. This fact can be also explained with the high charge/discharge limit imposed to guarantee a longer

lifetime of the battery. In fact, $E_{el,toLIB}/E_{el,PV}$ is roughly 0.25 in the summer period. Nevertheless, the ratio $E_{el,fromLIB}/E_{el,LOAD}$ shows that the battery remarkably affects the performance of the grid. This value is indeed roughly 0.35 during large part of the year.

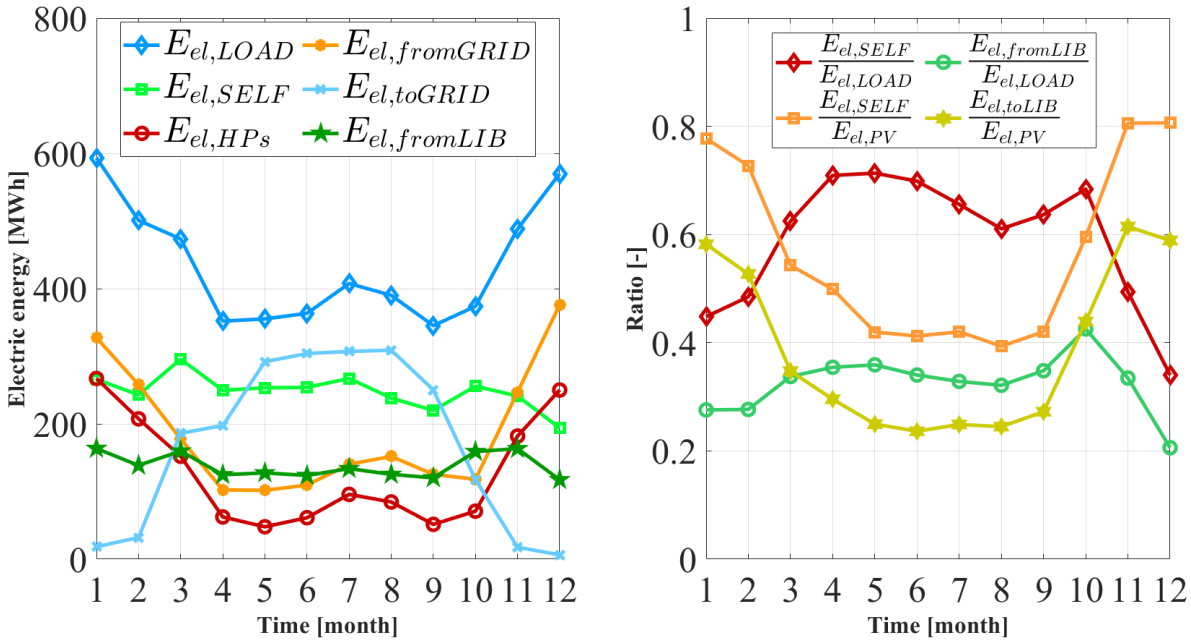

Figure 34. Electric energy flows on monthly scale for the 4GDHC system.

Figure 35 displays the monthly performance for 5GDHC. For 5GDHC, similar trends as 4GDHC are detected. Then, for the sake of brevity, only the main differences are discussed. 5GDHC is featured by higher electricity demand with respect to 4GDHC, due to the extensive use of HPs and hydronic pumps. In fact, 5GDHC uses a larger number of heat pumps and hydronic pumps for meeting the thermal energy demand of the district. The activation of the GHP1 and GHP2 would be limited in 5GDHC, when a simultaneous heating and cooling demand occurs. In fact, the heat exchange between the two neutral rings (NR1 and NR2) by means of the main heat exchanger would reduce the activation of such heat pumps.

Thus, the overlapping of the demands for heating and cooling is crucial to make the 5GDHC networks competitive with respect to the 4GDHC one. Given the considered case study this heat exchange occurs only during the summer period, when the buildings of the district require thermal energy for domestic hot water and for space cooling. Unfortunately, this heat exchange results quite negligible. This result is consistent with the results provided in the previous work[89, 102].

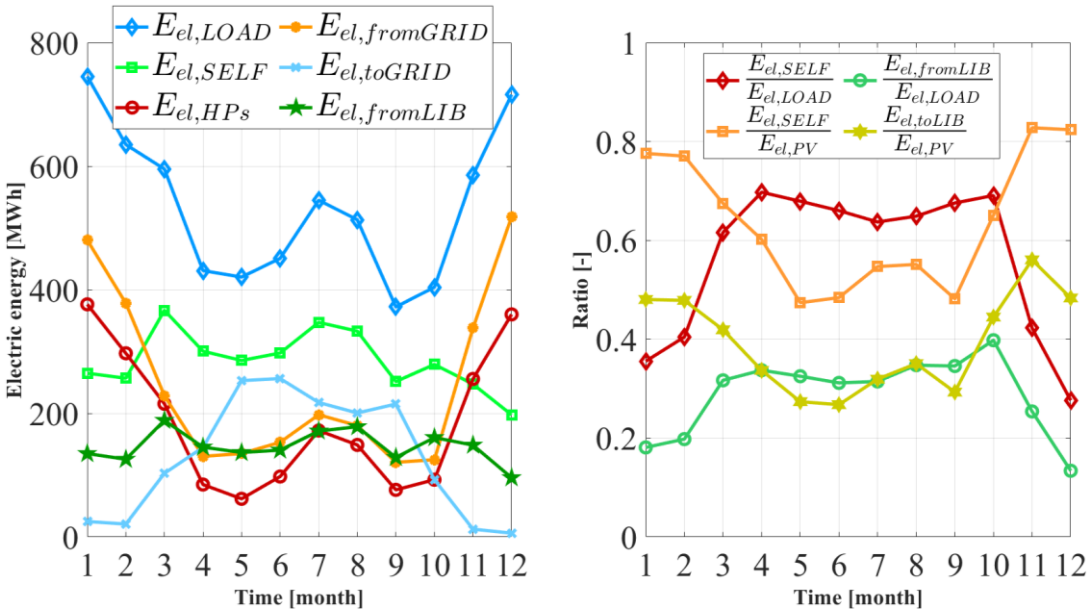

Figure 35. Electric energy flows on monthly scale for the 5GDHC system.

The yearly analysis (Table 8 and Table 9) comparatively shows the results in terms of energy, environmental, and economic impact of the proposed solutions. Both the PSs can significantly reduce the primary energy consumption and the CO_2 emissions related to the building energy demand. In fact, PS1 achieves a *PES* of 97%, whereas PS2 achieves a *PES* of 81%. This difference is mainly related to the fact that 5GDHC adopts a larger number of HPs and hydronic pumps, as explained before. In addition, for the case study selected the thermal energy exchanged between the two rings resulted almost negligible, i.e. 0.017 GWh/year.

As a consequence, the potential advantages of 5GDHC, in terms of heat recovery, are also negligible. In fact, the internal heat exchange would be crucial to reduce the activation of GHP1 and GHP2, reducing the system electricity demand and improving PS2 performance. In fact, the electricity supplied to the heat pumps ($E_{el,HPs}$) in 4GDHC is lower with respect to the case of 5GDHC. Therefore, 5GDHC is featured by a higher electricity demand, i.e. $E_{el,LOAD}$ equal to 5.21 GWh/years (4GDHC) vs 6.41 GWh/years (5GDHC).

Unfortunately, a pure residential district is characterized by a limited period of simultaneous heating and cooling demands. In fact, such simultaneous heating and cooling demand only occurs during the summer period. In that season, the residential district simultaneously requires building space cooling energy and heating energy for domestic hot water. In fact, for the selected residential district an overlap ratio Φ of 0.04 is detected.

These trends are furtherly confirmed by the PES_{DHC} value, that represents the energy savings due to the adoption of the DHC network. PES_{DHC} is equal to 56% for 4GDHC,

whereas PES_{DHC} is equal to 25% for 5GDHC. In conclusion, 5GDHC for a user featured by a very limited time window of simultaneous heating and cooling demands, achieves limited energy results compared with 4GDHC. However, the fact that 5GDHC achieves a PES_{DHC} of 25% means that despite the scarce contemporaneity between heating and cooling demand such technology is more efficient than the conventional technologies installed into the residential buildings, i.e. individual natural gas boilers and individual air-to-air heat pumps (see section 3.2.3).

The photovoltaic field can only match a limited share of the district electricity demand, i.e. $E_{el,SELF}/E_{el,LOAD}$ equal to 57% (4GDHC) vs 53% (5GDHC). This trend is because the adoption of the DHC network driven by HPs shifts the thermal load of the residential district into electric load. But this load mainly occurs in the late afternoon and evening when the PV production is limited or null. This mismatch is partially balanced with the electric storage, mainly for the 5GDHC.

From the economic point of view, such technologies are featured by a very high capital cost, mainly due to the high costs of the GHEs. 5GDHC is featured by a greater capital cost due to the higher number of heat pumps and hydronic pumps installed. In addition, as explained before 4GDHC achieves better results, leading to a lower electric load. For these reasons, 4GDHC reaches better economic results. i.e. *SPB* of roughly 16 years (4GDHC) vs *SPB* of 21 years (5GDHC).

In addition, a further reason for the low profitability of the investigated 5GDHC for such a case study, is due to the fact that the space cooling energy demand is lower than the space heating demand. Therefore, the installation of a proper ring for balancing the heat pumps operating in chiller mode (NR2) leads to an increase of the plant capital cost. This increase in capital cost is not balanced because of the negligible thermal energy recovered by means of the heat exchange between NR1 and NR2. Conversely, for the case of 4th DC, this does not involve any additional cost with respect to DH, since it uses the same piping network. In conclusion, both the proposed plants achieve limited economic results due to the high capital cost of such technologies.

Table 8. Annual results from thermoeconomic and environmental analysis.

Parameter	Description	Value			Unit
		RS	PS1	PS2	
$E_{th,H}$	Thermal energy required for heating	3.63	3.63	3.63	GWh/year
$E_{th,C}$	Thermal energy required for cooling	0.90	0.90	0.90	GWh/year
$E_{th,DHW}$	Thermal energy required for domestic hot water	1.81	1.81	1.81	GWh/year
$E_{th,HE}$	Thermal energy recovered between the rings	-	-	0.017	GWh/year
$E_{el,LOAD}$	Electric energy required from the building load	3.48	3.48	3.48	GWh/year
$E_{el,fromGRID}$	Electric energy withdrawn from the grid	3.78	2.24	2.99	GWh/year

$E_{el,toGRID}$	Electric energy sent to the grid	-	2.04	1.55	GWh/year
$E_{el,HPs}$	Electric energy consumption for the HPs	-	1.53	2.24	GWh/year
$E_{el,pumps}$	Electric energy consumption for the pumps	-	0.20	0.69	GWh/year
$E_{el,TOT}$	Electric energy consumption of the district	3.78	5.21	6.41	GWh/year
V_{NG}	Natural gas consumption	756´343	-	-	Sm^3/year
PE	Primary energy consumption	14.84	0.40	2.89	GWh/year
MCO_2	CO_2 equivalent emissions	2066	38	274	t_{CO2eq}/year
C	Operative costs of the system	1.36	0.47	0.66	M€/year

Table 9. Yearly performance indexes.

Parameter	Description	Value		Unit
		PS1	PS2	
$E_{el,SELF}/E_{el,LOAD}$	Electricity self-consumed by the district	57.1	53.5	%
ΔCO_2	CO_2 equivalent emission savings	98	87	%
ΔC	Yearly operative costs difference	0.89	0.70	M€/year
PES	Primary energy saving	97	81	%
PES_{DHC}	Primary energy saving of DHC system	56	25	%
C_{TOT}	Capital cost of the system proposed	14.09	14.77	M€
SPB	Simple payback	15.8	21.1	years
NPV	Net present value	-1.63	-4.97	M€
PI	Profit Index	-0.12	-0.34	-
Φ	Demand overlap coefficient	0.04		-

Chapter 4
Models developed on Power-to-Power

Electric energy storage systems (EESs) can balance the electric grid, shaving the peaks of power demand and renewable power production, reducing at the same time the electricity exchanged with the grid [108]. Several EESs technologies are analysed in the open literature [109], namely: electrochemical, mechanical, flywheel, compressed air, gravity, super capacitor, chemical, etc. In this framework, the vast majority of EESs are based on electrochemical batteries (lead acid, lithium ions, vanadium, etc.). At the same time, some innovative EES are also under investigation, aiming at improving power density and reducing capital cost and environmental impact, with respect to the case of electrochemical batteries.

Lithium-ion Battery, (LIB), that is a special case of the electrochemical energy storage technology, is the most common technology as electric energy storage system [110]. LIBs are featured by small size, good capacity (up to 85 kWh per single unit), low self-discharge rate, no memory effect and a specific energy density ranging from 0.60 kWh/kg to 3.00 kWh/kg [111]. However, even though LIBs have gained very wide acceptance and use in various applications (electrical, electronics and automobile industries), several issues limit the LIB diffusion as EESs. For instance, some technical issues are related to the maximum charging/discharging rate, which is directly proportional to the increase of the operating temperature of the battery, favouring the wear and tear of the device.

The aging mechanism is a dramatic problem for the user, since the degradation of LIB components results in the loss of residual capacity and increase of internal impedance, causing the decrease of the overall performance of LIBs [112]. In some cases, this overheating is also responsible for accidents. Conversely, Hydrogen storage systems (HSS) are increasing their awareness as an advanced solution for storage of renewable energy excess thanks to their low environmental impact on the whole life cycle. In fact, HSS systems based on electrolysis and fuel cell can be used to store electric energy in the form of hydrogen chemical energy.

The efficiency of chemical energy storage systems based on hydrogen mainly depends on the energy conversion efficiency of hydrogen production from electrolysis: the highest conversion efficiency can be even higher than 90% [113]. This route of conversion, from power to hydrogen ad, again, to power is also known as Power-to-H2-to-Power, or shortly Power-to-Power. Given the low overall energy efficiency of the process, in this framework the Reversible Solid Oxide Fuel Cell

(rSOFC) has become a worldwide benchmark for its high efficiency, low environmental impact and high market conversion rate [114]. RSOFCs can operate as solid oxide fuel cells (SOFC) and solid oxide electrolysis cells (SOEC), respectively. In SOEC mode, the exceeding renewable electric energy can be used to convert water into hydrogen with high efficiency. In SOFC mode, the chemical energy of the hydrogen can be converted into electricity and heat [115].

rSOFCs are extremely interesting since they can provide load shifting, managing, and controlling the hourly power load according to the following operation strategy. rSOFC operates in SOFC mode for high electric energy demand, converting the chemical energy of the fuel into electricity. rSOFC operates in SOEC mode when the electric energy demand is low and the renewable electricity is higher than user demand.

In this chapter, two works are proposed which fall within the realm of Power-to-Power, always adopting the same dynamic approach that was already presented in the chapter on Power-to-Heat. The first work regards a thermoeconomic analysis of a building using a rSOFC for renewable electricity excess storage purpose. The second work compares, on a thermoeconomic basis, the storage of renewable electricity surplus made by means of a LIB with the Power-to-Power technology.

4.1 Dynamic simulation and thermoeconomic analysis of a hybrid renewable system based on photovoltaic and fuel cell coupled with hydrogen storage

The aim of this analysis is to present a dynamic analysis of a hybrid renewable plant that exploits the electricity provided by a PV field to match the power demand of a dwelling. The surplus electricity is supplied to a SOEC system to convert it into hydrogen and store it inside a carbonium-fiber tank. The energy storage allows one to avoid overloads of the electric grid at the local level during the most irradiated hours. Furthermore, the energy stored can be exploited when a deficit of PV production occurs. In that case, hydrogen is withdrawn from the tank and sent to a SOFC system to furnish the needed energy.

As discussed in [116], there is a lack of studies in the literature dealing with the dynamic simulation of PV systems coupled with SOFC. The novelty of this work can be summarized by the following points: (i) The dynamic analysis of a hybrid renewable system for hydrogen production and storage carried out by means of a reversible SOC model validated in MATLAB®; (ii) Several control strategies

implemented and discussed both for the operation of the fuel cell and hydrogen storage; furthermore, temperature operating conditions of the cell are managed; (iii) A well-developed thermoeconomic analysis proposed to evaluate the energy and environmental savings along with the economic feasibility; (iv) A thermoeconomic analysis focused on the hydrogen storage made to select the optimal size of the H_2 storage for the proposed system; (v) The analysis of the power exchanged with the grid is carried out to investigate how the local grid overloading conditions are avoided by means of the proposed technology.

4.1.1 System Layout

The layout of the proposed hybrid renewable plant is omitted for the sake of brevity, it can be found in ref. [116]. However, a similar layout and control strategy can be found also in the Section 4.2.1.

4.1.2 System Model

The reversible SOFC (rSOFC) mathematical model proposed in this work is a lumped-parameter model, based on the model proposed by Wang et al. [117]. Although several rSOFC models are available in the open literature, only a few of them are suitable for being integrated into a dynamic simulation model. The necessity of developing an in-house simulation model of the reversible solid-oxide cell comes from the lack of models available in the TRNSYS built-in library. In fact, other components are suitably modelled in TRNSYS, as it will be shown in the next section, but no model is available for the rSOFC.

The mathematical modelling of the rSOFC is an interdisciplinary task because it involves different research areas. In fact, a well-structured model must include an electrochemical model, a thermodynamic model, and a chemical reaction model [118]. Several phenomena have to be considered, such as transport and diffusion, heat and mass transfer, and chemical kinetics. Obviously, the more comprehensive the model, the more accurate the simulation is.

The accuracy of the rSOFC model out of the ordinary operating conditions is not the main concern for the aim of the proposed work. The model of the rSOFC must be integrated in a more general dynamic system useful for a one-year simulation. To avoid excessive computational efforts, a 0D quasi-steady state model was selected because a more complex one would determine unacceptable computational times.

The model considered in this work was validated by experimental studies, and it allows one to calculate the efficiency, voltage, and operating temperature of the cell starting from the input current. These parameters affect the polarization curve of the

cell, which correlates the voltage to the current density. The polarization curve also depends on several design parameters such as geometry, pressure, fuel utilization factor, etc.

In SOFC mode, the cell operating voltage can be calculated subtracting from the reversible potential of the cell the activation, ohmic, and concentration losses terms:

$$V_{cell} = V_{rev} - V_{act} - V_{ohm} - V_{conc} \tag{20}$$

Conversely, in SOEC mode, the mentioned losses represent an overvoltage that must be overcome to start the electrolysis process. Therefore, losses terms must be added to the reversible potential:

$$V_{cell} = V_{rev} + V_{act} + V_{ohm} + V_{conc} \tag{21}$$

The cells can then be arranged in series to form a stack, whose voltage would be the sum of the voltages of each cell. More stacks can be arranged in series to increase the power of the SOFC field.

The reversible voltage (V_{rev}) is calculated starting from the Gibbs free energy of the reaction at standard conditions, which is a known parameter, according to the Nernst' equation:

$$V_{rev} = \frac{-\Delta G_0}{2F} + \frac{RT}{2F} ln\left(\frac{p_{H_2} \cdot {p_{O_2}}^{0.5}}{p_{H_2O}} \right) \tag{22}$$

where ΔG_0 is the Gibbs free energy at standard conditions (T = 25°C, p = 1 bar) and F is the Faraday constant. Moreover, to calculate V_{rev} at the cell operating conditions, the operating temperature and the partial pressures of the gases must be also considered.

The activation losses are due to the charge transfer between electronic and ionic conductors and represent an energy barrier that must be overcome to activate the electrolysis process. This term is calculated by means of the semiempirical Butler–Volmer equation:

$$i = i_0 \left[exp\left(\frac{\alpha F V_{act}}{RT} \right) - exp\left(\frac{-(1-\alpha) F V_{act}}{RT} \right) \right] \tag{23}$$

where i is the density current, α is the symmetry factor, and i_0 is the exchange current, calculated as:

$$i_0 = \gamma \cdot exp\left(-\frac{E_{act}}{RT} \right) \tag{24}$$

where E_{act} is the activation energy. The ohmic losses depend on the ohmic resistance of the electrons and ions flows through the components and the connectors. It can be calculated as:

$$V_{ohm} = i \cdot ASR_{ohm} \tag{25}$$

Where ASR_{ohm} is the area-specific ohmic resistance, which is function of the materials adopted and the operating temperature, empirically correlated.

The concentration losses depend on the concentration gradient between the bulk flow and the reaction sites. In fact, since the electrochemical reactions occur at the "three phases boundary", a mass transport phenomenon within the electrodes takes place. To model the diffusion losses that are caused by this phenomenon, the Fick's law was selected, which implies less computational effort. According to this law, the concentration losses are calculated as follows:

$$V_{conc} = \frac{RT}{zF} ln\left(1 - \frac{i}{i_L} \right) \tag{26}$$

where i_L is the limiting current density, given from the cell datasheet.

The operating current I is instead obtained by means of the fuel utilization factor Uf, and it is calculated as $2 \cdot Uf \cdot n_{H2}$. The current is an input to the model, whether it is supplied or withdrawn, whereas the hydrogen flow rate is one of the output of the equation. The oxygen flow rate is calculated by means of the air utilization factor Ua, and it is equal to $Uf \cdot n_{H2}/(2 \cdot Ua)$.

Once the cell voltage and the molar fluxes are calculated, the operating temperature is obtained as a function of the equilibrium constant

$$K\left(T_{cell}\right) = \frac{n_{H_2O}^{out}}{n_{O_2}^{out} \cdot n_{H_2}^{out}} \tag{27}$$

The electro-chemical model is coupled with a thermodynamic model which allows to calculate the operating temperature of the cell at each condition, by means of an energy balance. The equation is the following:

$$C_S M_S \frac{dT_C}{dt} = \dot{m}_{in,i} h_{in,i} - \dot{m}_{out,i} h_{out,i} + \varphi \dot{m}_{chem,i} h_{out,i} - \dot{W} + \frac{jNA_{cell}}{2F} \dot{Q}_{react} + \dot{Q}_{ext} + \dot{Q}_{int} \quad (28)$$

All the terms are discussed and explained in ref. [116], here omitted for the sake of brevity.

The overall efficiency of the process is defined as the ratio between the electric energy provided by the SOFC, $E_{el,SOFC}$, and the electric energy supplied to the SOEC, $E_{el,SOEC}$

$$\eta_{glob} = \frac{E_{el,SOFC}}{E_{el,SOEC}} \quad (29)$$

4.1.3 Case Study

The system is designed to meet the electricity demand of a dwelling located in Fuorigrotta (Naples, south of Italy). The electric load of the selected building is evaluated according to the approach described in detail in [119]. Figure 36 shows the building model developed with the Sketchup plug-in of the TRNSYS software.

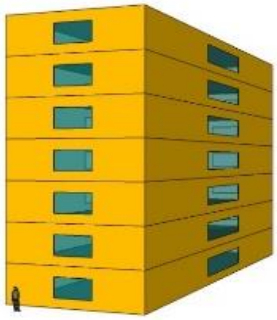

Figure 36. 3D representation of the building model.

The result is a daily load profile that shows three peaks between 8 AM and 10 AM, between 11 AM and 12 PM, and between 4 PM and 6 PM. The first and the second peak are about 40 kW, whereas the last peak reaches 60 kW, which is the maximum value of the load. Figure 37 shows the electric load.

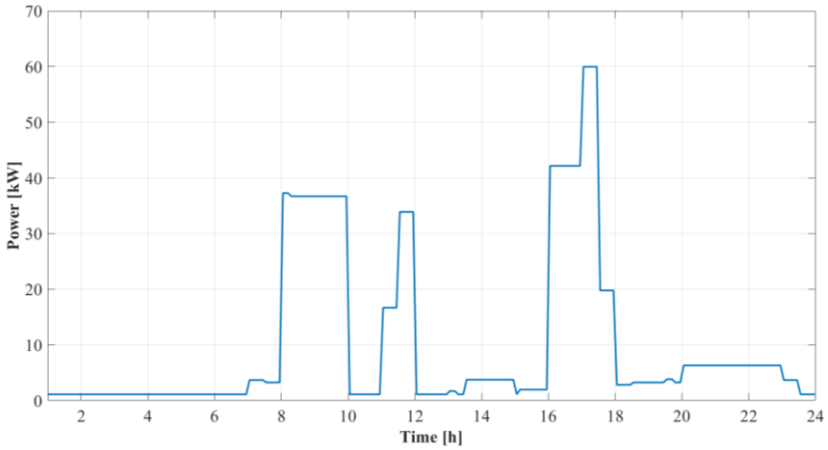

Figure 37. Dynamic load simulated for the building considered as a case study.

The reference system (RS) is the above-described dwelling, whose power load is met by the grid. The proposed system (PS) is the one described in the section 4.1.1.

Further design parameters of the model proposed are listed in Table 10.

Table 10. Main design parameters of the model proposed.

Component	Parameter	Description	Value	Unit
PV PANEL	$A_{module,PV}$	PV module area	1.609	m^2
	$P_{el,PV}$	PV field rated power	50	kW
	N_{series}	Number of modules in series	2	-
	$N_{paralel}$	Number of modules in parallel	100	-
	$I_{sc,ref}$	Modules short-circuit current at reference conditions	8.94	A
	$v_{oc,\ ref}$	Module open-circuit voltage at reference conditions	37.3	V
	$T_{c,\ ref}$	Reference temperature	298	K
	$G_{tot,ref}$	Reference solar radiation	1000	W/m^2
	$v_{mp,ref}$	Module voltage at max power point and reference conditions	30.1	V
	$I_{mp,ref}$	Module current at max power point and reference conditions	8.64	A
	μ_{Isc}	Temperature coefficient of Isc at (ref. condition)	0.0004	1/K
	μ_{voc}	Temperature coefficient of V_{OC} (ref. condition)	−0.003	1/K
	$T_{c,\ NOCT}$	Module temperature at NOCT	319	K
	$T_{c,\ ref}$	Ambient temperature at NOCT	293	K
Electrolyzer-Fuel Cell	Pr_{cell}	Cell operative pressure	1	bar
	A_{cell}	Cell area	87.7	cm^2
	n_{cell}	Number of cells in series	8	-
	n_{stack}	Number of stacks in parallel	50	-
	$P_{el,EC,min}$	Minimum power allowed to SOEC	13.15	kW
	$P_{el,EC,max}$	Maximum power allowed to SOEC	48.23	kW
	$P_{el,FC,min}$	Minimum power allowed from SOFC	10.52	kW
	$P_{el,FC,max}$	Maximum power allowed from SOFC	36.83	kW
	$P_{el,FC}/P_{el,EC}$	Rated fuel cell/electrolyzer capacity	45/50	kW
H_2 storage	V	Tank volume	1	m^3
	$Pr_{TK,max}$	Maximum tank pressure	200	bar
Compressor	η_{IS}	Compressor isentropic efficiency	0.80	-
Inverter	η_I	Inverter/Regulator efficiency	0.96	-

4.1.4 Results

This section presents and discusses the validation of the rSOFC model through comparison with experimental data, as well as the dynamic simulation of the hybrid system. Following this, a parametric analysis on the H_2 tank capacity is proposed, along with a discussion on the optimal configuration.

The developed model was successfully validated by means of experimental data provided in [117]. In particular, the model proposes the simulation of a 50-stack planar cell designed and produced by Topsøe in 2014 made of Nickel/Yttria stabilized Zirconia (Ni/YSZ). Boundary operating conditions are reported in Table 11.

Table 11. Feeding condition for the experimental fuel cell [117].

Component	**Feeding Gas**	**Flow Rate**	**Temperature**
-	**-**	**[sccm/cm²]**	**[K]**
Anode	H_2/H_2O (50–50%)	12.44	1033
Cathode	O_2 (100%)	5.70	1033

When the cell operates in SOFC mode, the anode is fed by a 50/50 mixture of hydrogen and steam whereas the cathode is fed by pure O_2.

Figure 38 shows the comparison between the simulated *I–V* curve of the cell and the experimental operating data, both for the electrolyzer and the fuel cell.

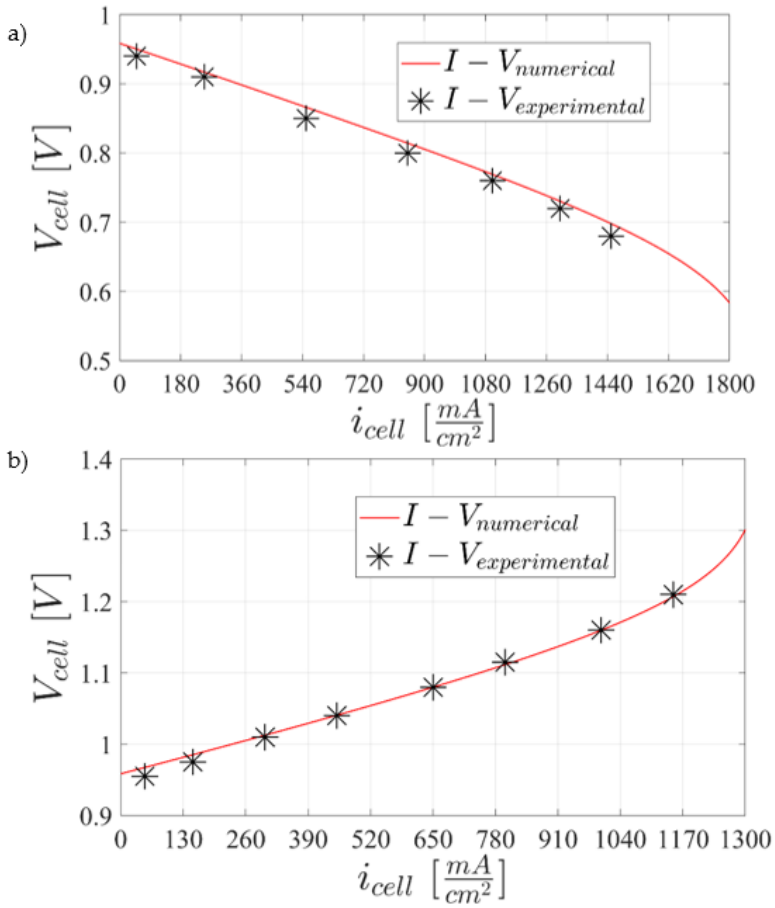

Figure 38. Comparison between numerical and experimental data for the fuel cell mode (a) and the electrolyzer mode (b).

The experimental data closely align with the polarization curves obtained from the model for both cell configurations, with deviations between simulations and experiments remaining below 2 %. More specifically, in the fuel cell mode, voltage decreases with increasing current densities, whereas in the electrolyzer mode, the opposite trend is observed.

Figure 6 depicts the relationship between cell temperature and current density (i_{cell}), for various fuel utilization factor values. In fuel cell operation, an increase in the fuel utilization factor leads to a corresponding increase in cell temperature, regardless of the operating current density. This can be explained by examining the energy balance. Essentially, a higher fuel utilization factor results in more H_2 reacting, which in turn releases more heat due to the exothermic nature of the process.. As a consequence, in this case, a higher amount of heat is also released by the exothermic process.

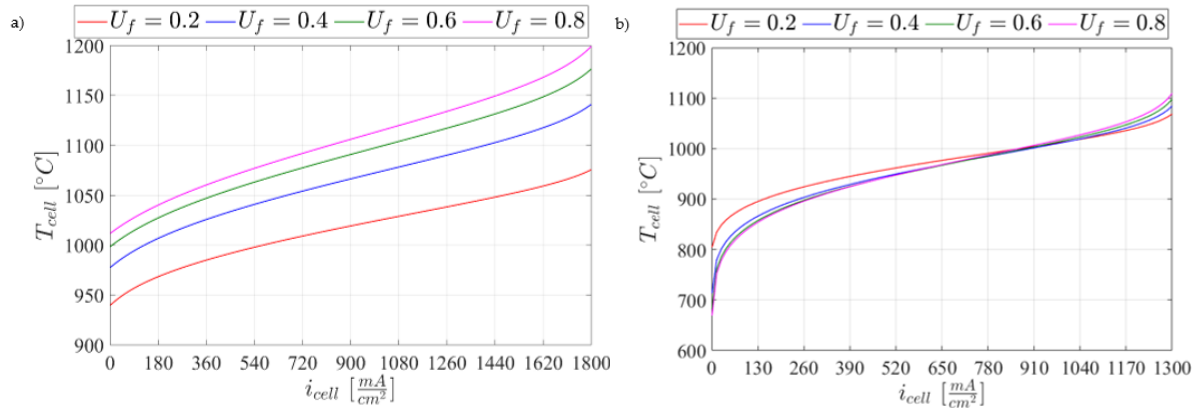

Figure 39. Temperature of the cell as a function of density current for different fuel utilization factors for the fuel cell mode (a) and the electrolyzer mode (b).

Conversely, when the cell operates as an electrolyzer, a reverse trend is detected as far as the density current is below a value of 854 mA/cm^2. In fact, the greater the steam flow, the lower the cell temperature is. This trend is due to the fact that these electrochemical reactions are endothermic. The temperature difference in this case is lower than the previous case, and it decreases to 0 when a value of current density of about 854 mA/cm^2 is reached. For higher values of the current density, the opposite trend occurs. The reason is that, in this case, the efficiency of the cell rapidly decreases due to the high operating temperature. Once the threshold value of current density is exceeded, the increasing of H_2 production can no longer compensate for the increasing of absorbed power.

As a consequence, the cell should always operate in a specific range of current density to achieve an optimal operation. For values of this parameter out of the linear field of the polarization curve, the conversion efficiency is very low. Moreover, when the temperature of the cell is too high, the degradation of the cell occurs much faster. The selected current density range for the SOFC is between 400 and 1400 mA/cm^2, whereas for the SOEC, it is 300–1100 mA/cm^2. By means of the design parameters of the cell, it is possible to determine in which range electric power can be supplied to the electrolyzer or withdrawn from the cell.

For the sake of brevity only the results for the parametric analysis are discussed, all the details regarding the dynamic, monthly and yearly results can be found in ref. [116].

The thermoeconomic analysis shows that the economic profitability of the system is not encouraging. This is also due to an unoptimized selection of components capacities, mainly for the case of the storage tank. As a matter of fact, a tank of 1 m^3 volume and 200 bar of maximum pressure can store the energy produced by the SOEC for 13 h of nominal operating conditions.

Figure 40 shows the results from the parametric analysis of the tank size, ranging from 25 bar to 200 bar of maximum pressure. The curves are referred to three different volumes of the storage, that are 0.50, 0.75, and 1 m^3.

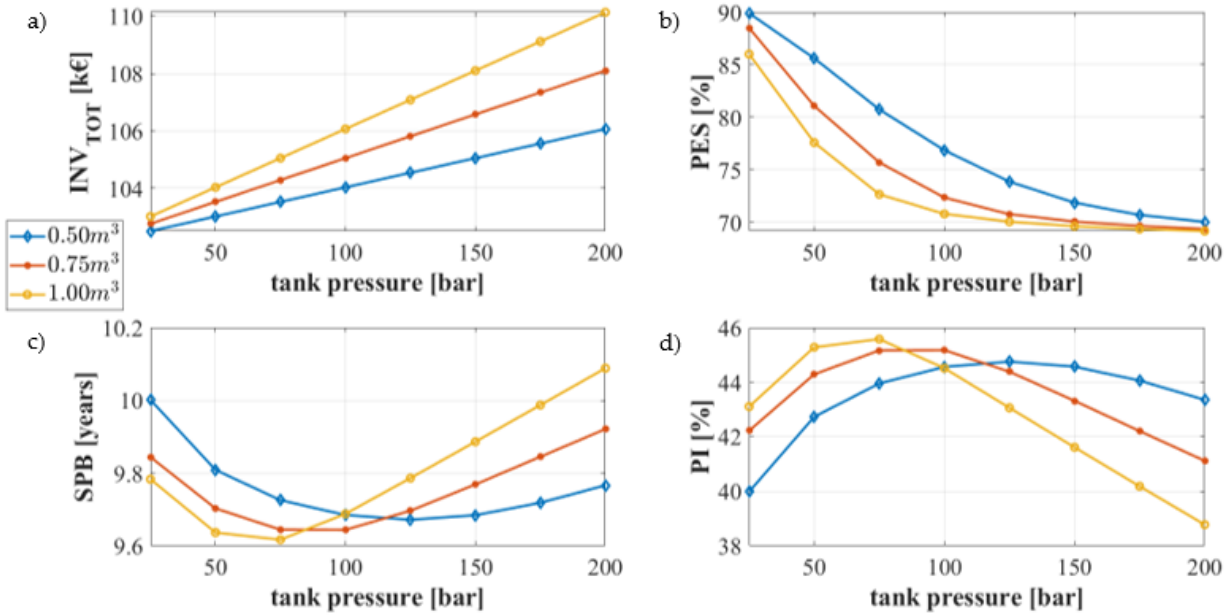

Figure 40. Parametric analysis of the hydrogen storage system: a) total capital costs, b) primary energy saving, c) simple payback, d) profit index, as a function of the maximum storage pressure.

The capital cost of the system is the sum of two terms, one is constant and the other one is linear. The constant term is represented by the plant capital costs, mostly PV and rSOFC systems. The linearly increasing term is the cost for the storage, which is proportional to the maximum capacity.

The higher the tank capacity and pressure, the higher the amount of energy that can be stored and the greater the energy self-consumed by the plant is. At the same time, the increase of the tank capacity causes a reduction of the surplus electricity exported to the grid. Note that 1 kWh produced by the PV field and delivered to the grid corresponds to 0.96 kWh exported to the grid, due to the regulator/inverter efficiency. Conversely, 1 kWh produced by the PV field and delivered to the SOEC and stored into the tank corresponds to about 0.80 kWh self-consumed by the plant, because of the efficiency of the electrolyzer, fuel cell, and compressor.

These figures justify the reduction of the *PES* as the tank capacity increases.

From the economic point of view, the self-consumed electricity plays a significant role, much more than the one played by the electricity exported to the grid: $j_{el,fromGRID}$ = 0.20 €/kWh vs $j_{el,toGRID}$ = 0.05 €/kWh. As mentioned before, the higher the tank capacity and maximum pressure, the higher the amount of energy stored in the tank.

However, *SPB* curves in Figure 40 exhibit a minimum that represents a threshold value. Expanding the tank capacity beyond a certain point would not enhance the energy self-consumption, as the system reaches its limit in filling the tank. For instance, with a 1 m^3 tank, optimum profitability is achieved at a maximum pressure of 75 bar. Increasing the tank maximum pressure beyond this point only adds to the storage capital cost without improving its charge/discharge utilization.

This pattern is similarly observed in the Profitability Index (*PI*) graph. Selecting a tank capacity of 1 m^3 and a maximum pressure of 75 bar, any further increase in storage capacity results in decreased system profitability. The impact here is notable; the optimal setup yields to a *PI* of 46%, and any increase in capacity could reduce this figure to below 40%.

4.2 Renewable smart energy network: a thermoeconomic comparison between conventional lithium-ion batteries and reversible solid oxide fuel cells

According to the literature review presented in ref. [120], lithium-ion batteries and reversible fuel cells are both considered suitable technological solutions in the field of electric energy storage systems for increasing the penetration of renewables. However, very few works presented a comprehensive comparison between these two technologies, as a suitable device for balancing complex energy grids, unfortunately without considering a customized residential district including electric vehicles [29].

Conversely, the research proposed in the present paper presents a dynamic technoeconomic comparison between two renewable plants designed for meeting the energy demand of a residential district, including the energy demand for building space heating/cooling and domestic hot water, building electric load and electric energy demand for electric vehicles. The two renewable layouts are based on a PV field, integrated with: i) a reversible solid oxide fuel cell (L1, see System layout) and ii) a lithium-ion battery (L2, see System layout). In particular, the present paper investigates the capability of reversible SOFCs (L1) and LIBs (L2) to shave both the peaks of surplus renewable power and the peaks of user power demand, reducing the stress for the local electric grid. Therefore, this research aims at assessing which technology will represent the most profitable selection for integration in fully renewable smart energy networks. In conclusion, the main novelties provided by the study presented in this paper can be summarized as follows:

- The development of a detailed model of a residential district, including air-to-air heat pumps for space heating and cooling purposes; air-to-water heat pumps for domestic hot water production; electrical appliances in the apartments and electric vehicles.
- The development of detailed dynamic simulation model of two different renewable based smart energy networks, to compare the performance of SOFCs and LIBs under dynamic conditions. In particular, the layout based on reversible SOFC was carefully modelled taking also into account the thermal management of the reversible SOFC, operating both in electrolyzer and fuel cell modes.
- The development of a sensitivity analysis regarding the specific cost of reversible SOFC and LIB in order to assess the future feasibility of the proposed renewable smart energy networks. In fact, as mentioned before, the LIB purchasing cost may increase due to the increase in lithium demand. Conversely the growing in interest into hydrogen related technologies may lead to a reduction of the capital cost of the devices/technologies involved in hydrogen plant.

4.2.1 System Layout

Figure 41 and Figure 42 display the two layouts investigated in this research. Figure 41, shows a system where a photovoltaic (PV) field powers a residential district and electric vehicles. Excess energy from the PV field is converted to hydrogen via a reversible SOFC operating as an electrolyzer. This process involves heating water to 800°C using waste heat from the cell, both in electrolyzer and fuel cell modes, and storing it in a diathermic oil tank with Therminol 66. The water is preheated and converted to steam through heat recovery steam generators (HRSG-1, HRSG-2, and HRSG-3), then mixed to achieve the required temperature for electrolysis. The hydrogen-steam mix from HRSG-2 is cooled in a dry cooler (DryA) to separate water from hydrogen, which is then compressed in a four-stage compressor (C1) and stored in a 51 m^3 tank at 200 bar. The oxygen byproduct, cooled in DryB, is also compressed, and potentially sold.

When electric vehicle charging demand exceeds PV output, the stored hydrogen is used in the fuel cell to generate electricity, producing heat and steam. Both hydrogen and air inlet streams are preheated using waste heat from the cell. The gas at the outlet of the anode and the exhaust air mix in a post-combustion chamber (PC-C) for catalytic combustion, generating further heat. The exhaust gas (EG) from PC-C preheats incoming air and hydrogen and also heats diathermic oil in TK-Oil for

further system use. A bypass valve (D4) controls the oil temperature to prevent overheating.

Figure 28 introduces a second layout, identical to the first except for using a lithium-ion battery storage system (D-LIB) instead of hydrogen storage. Here, surplus power is stored in D-LIB and used to meet electric vehicle charging demands when they are lower than the PV field output. This comparative analysis aims to assess the efficiency and effectiveness of these two distinct energy storage solutions. Further details on the layout can be found in ref. [120].

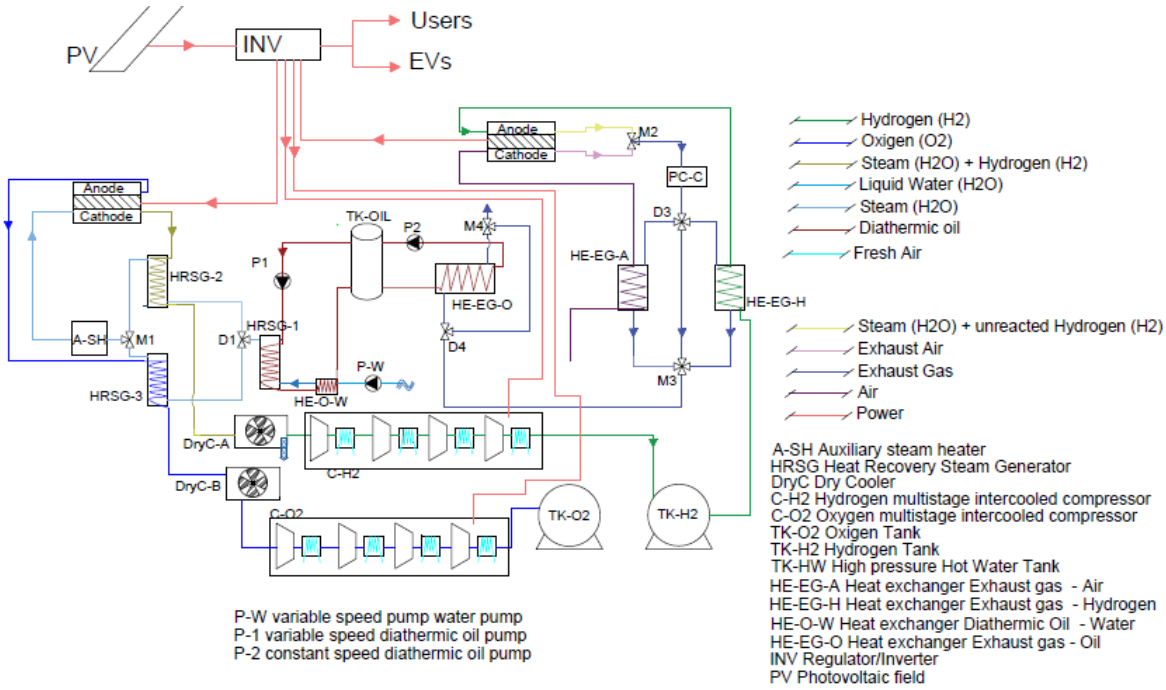

Figure 41. Layout of the plant adopting hydrogen as electric energy storage.

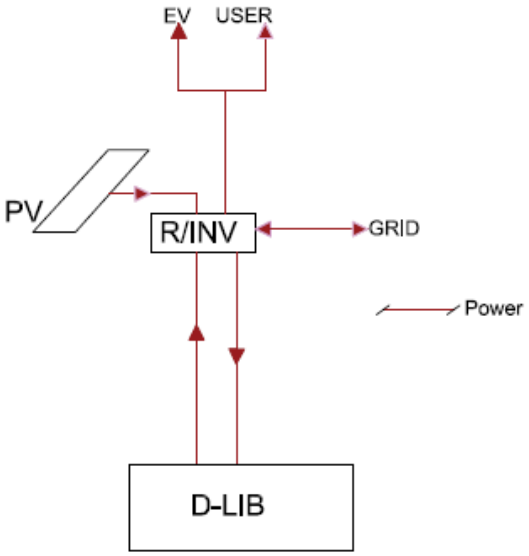

Figure 42. Layout of the plant adopting lithium-ion battery as electric energy storage.

Table 12.Technical data of diathermic oil [121].

Diathermic oil	Boiling point (1.01 bar)	Density	Heat Capacity	Dynamic viscosity	Kinematic viscosity
	[°C]	[kg/m^3]	[kJ/kgK]	[mPa*s]	[mm^2/s]
Therminol 66	359	885	2.195	0.86	0.97

4.2.2 System Model

The dynamic simulation model of the two layouts analysed is developed in TRNSYS 18 environment. The main components employed in this work are resumed below.

- The EV model and the district electric energy storage system (D-LIB) are modelled by means of Type 47. Type 47 is based on Shepard mathematical model. The parameters of Type 47 are customized, aiming at fitting the performance of commercial lithium-ion batteries. In particular, Nissan Leaf [122] and Renault Zoe [123, 124] battery data are selected. A detailed description of Type 47 is available in Ref. [125].
- Type 94 is modelled for simulating the PV panel performance, considering the electric performance of the poly-crystalline/crystalline silicon cell.
- Type 56 is used for modelling the buildings of the district. In particular, the geometry of such buildings is developed by means of Google SketchUp TRNSYS3d plug-in and linked to TRNSYS18 by means of Type 56. Note that type 56 is able to simulate the building energy performance considering the thermophysical property of the envelope, the weather condition, the heat gains due to electrical appliance and people inside the building, the solar radiation affecting the building and the features of the HVAC system. Furter details about this type are provided in Ref. [126].

The rSOFC model is the one described in section 4.1.2; therefore, it is not discussed again for the sake of brevity.

Figure 43 and Figure 44 summarize the operating strategies assumed for managing the electric vehicles charging and the reversible fuel cell operation. In particular, when the electric vehicles are connected to the charging stations and their *SoC* is greater than the threshold value of 40%, these EVs are charged exploiting the available surplus power, i.e. $P_{el,surplus}$, Figure 43. When the state of charge of EVs connected to the charging stations is lower than 40%, a minimum guaranteed power ($P_{el,guaranteed}$, Figure 43) is delivered to such EVs until the state of charge of these EVs achieves the assumed threshold value of 40%. Note that $P_{el,guaranteed}$ is assumed equal to 3 kW/EV, according to Ref. [102, 127]. If the hydrogen tank (TK-H2) energy storage capacity is not null, i.e. Ψ>15%, H_2 is withdrawn from TK-H2 for driving the SOFC and producing electricity for charging EVs.

The available surplus power is first exploited for charging EVs. However, when the EVs are not connected to the charging stations, $P_{el,surplus}$ is delivered to the reversible fuel cell for producing H_2, see Figure 44. Note that the net power delivered to the fuel cell is evaluated according to the following equation (Figure 44).

$$P_{el,toSOEC} = P_{el,PV} - P_{el,LOAD} - \left(P_{el,C1} + P_{el,C2} + P_{el,A\text{-}SH} - P_{el,DryA} - P_{el,DryB}\right) \quad (30)$$

Where, $P_{el,A\text{-}SH}$ is the power delivered to the auxiliary steam heater (A-SH, Figure 41), $P_{el,C1}$ and $P_{el,C2}$ are the power delivered to the hydrogen and oxygen compressors, respectively and $P_{el,DryA}$ and $P_{el,DryB}$ are the power demand of the fans of the dry coolers.

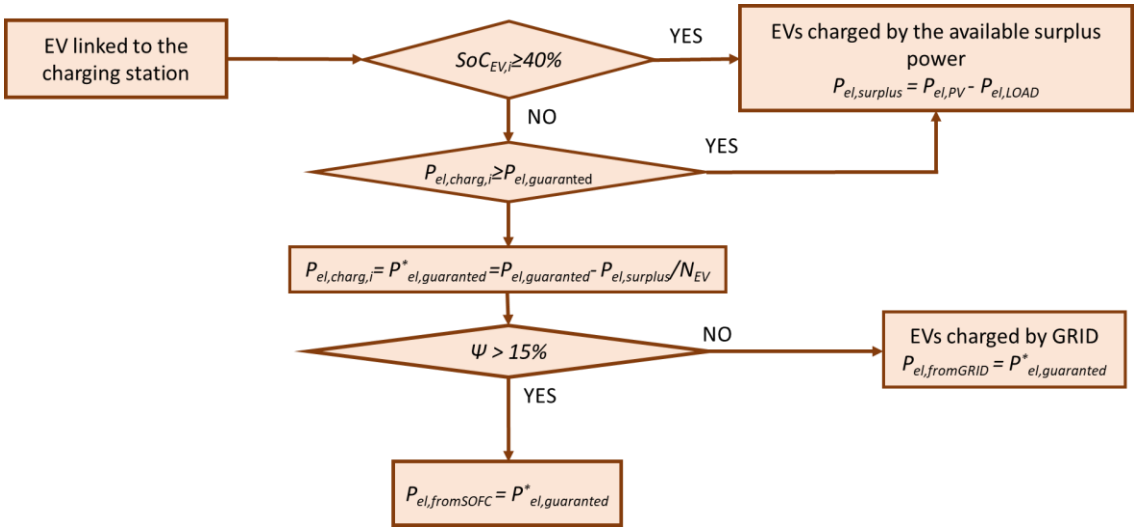

Figure 43. Electric vehicle charging model for Layout 1.

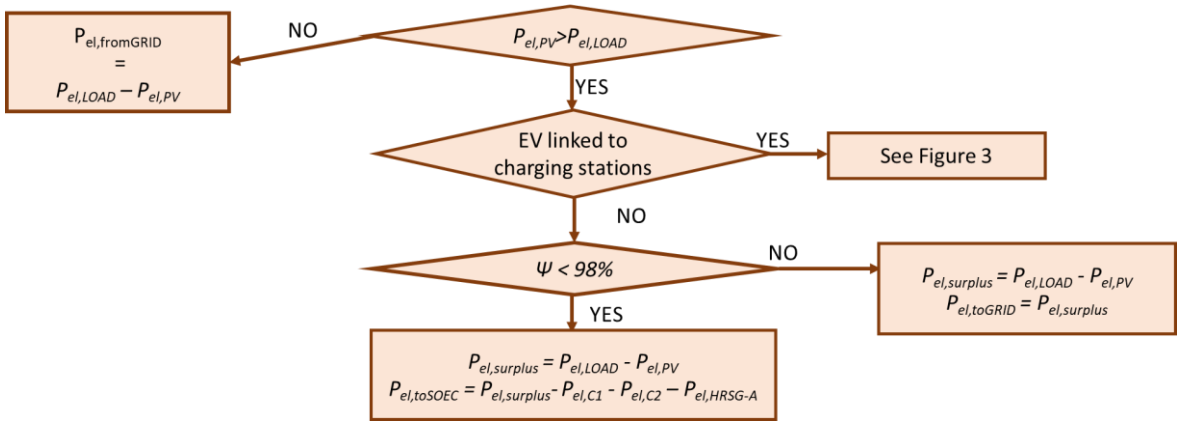

Figure 44. Reversible fuel cell charging model for Layout 1.

When the district lithium-ion battery *SoC* is greater than 5%, the guaranteed power for charging EVs ($P_{el,guaranteed}$, Figure 45) is first withdrawn from D-LIB, according to Figure 45. Conversely, when the power production is greater than the power demand, the surplus power is stored in D-LIB, according to Figure 46.

Note that, $P_{el,D\text{-}LIB,lim,disch}$ and $P_{el,D\text{-}LIB,lim,ch}$ are the maximum allowed discharging and charging powers, respectively. These values are selected with the aim of limiting the battery ageing and degradation.

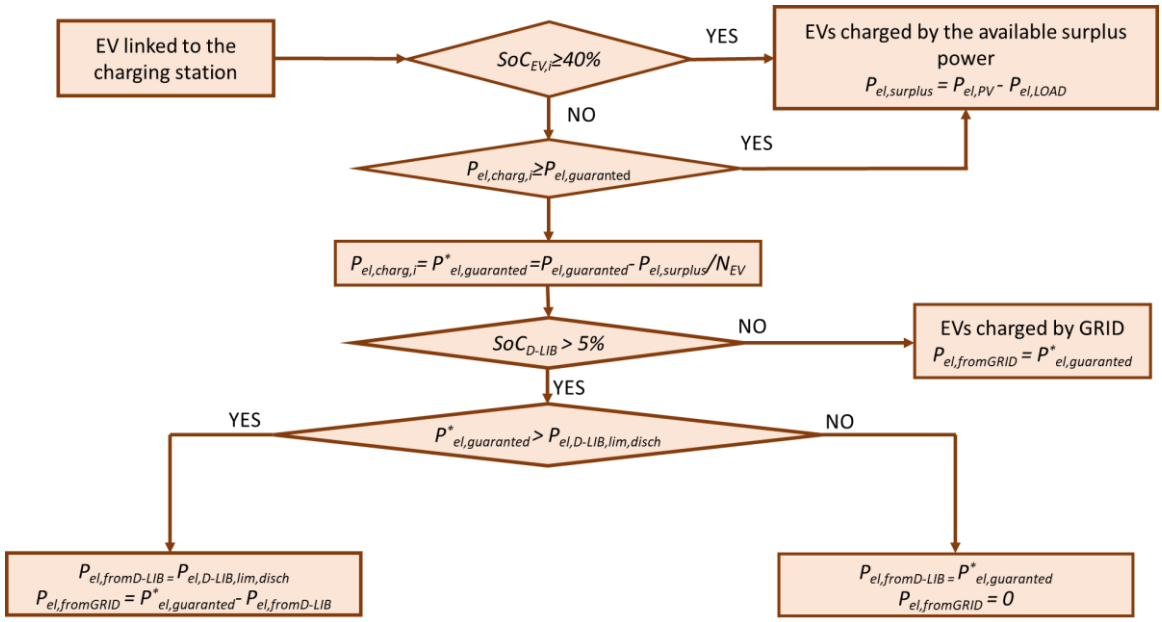

Figure 45. Electric vehicle charging model for Layout 2.

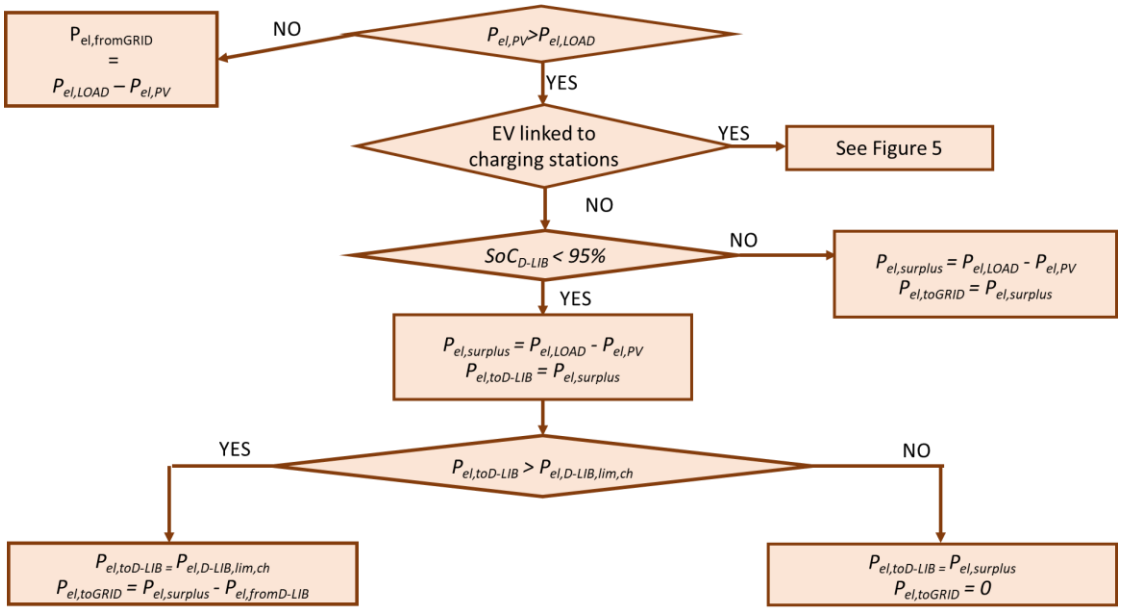

Figure 46. Reversible fuel cell charging model for Layout 2.

The diverter D1 (Figure 41) is managed according to the following equations:

$$\varphi_2 = \frac{\dot{m}_{cathode} C_{cathode}}{\dot{m}_{anode} C_{anode} + \dot{m}_{cathode} C_{cathode}}$$
$$\varphi_3 = \frac{\dot{m}_{anode} C_{anode}}{\dot{m}_{anode} C_{anode} + \dot{m}_{cathode} C_{cathode}}$$
$$\dot{m}_{steam,toHRSG\text{-}2} = \varphi_2 \cdot \dot{m}_{steam} \tag{31}$$
$$\dot{m}_{steam,toHRSG\text{-}3} = \varphi_3 \cdot \dot{m}_{steam}$$
$$\dot{m}_{steam} = \dot{m}_{steam,toHRSG\text{-}2} + \dot{m}_{steam,toHRSG\text{-}3}$$

The flow rate of steam delivered to HRSG-2($\dot{m}_{steam,toHRSG-2}$) is evaluated according to the thermal capacity flow($C_{chatode}\dot{m}_{chatode}$) of the hot stream feeding HRSG-2. Note that, $C_{chatode}$ is the thermal capacity of the stream exiting the cathode of the cell operating in electrolyzer mode, and $\dot{m}_{chatode}$ is the mass flow rate of such stream. A the same time the amount of steam delivered to HRSG-3 ($\dot{m}_{steam,toHRSG-3}$) is evaluated on the basis of the thermal capacity flow ($\dot{m}_{anode}C_{anode}$) of the steam exiting from the anode of the cell operating in electrolyzer mode, see also Figure 41.

The primary energy (*PE*) of the considered reference system, i.e. a residential district including internal combustion engine vehicles (see next section *Case Study*), is evaluated as follows.

$$PE_{RS} = PE_{district,RS} + PE_{vehicle,RS}$$
$$PE_{district,RS} = \sum_t \left[\left(E_{el,LOAD} + \frac{E_{th,cool}}{COP_n} \right) \frac{1}{\eta_{el}} + \left(\frac{E_{th,heat}}{\eta_B} + \frac{E_{th,DHW}}{\eta_B} \right) \right]_t \tag{32}$$
$$PE_{vehicle,RS} = \left[\sum_i N_i \frac{1}{1000} \left(\frac{L_{year,i}}{\Gamma_{diesel,i}} \right) \rho_{diesel} LHV_{diesel} \right] + \left[\sum_j N_j \frac{1}{1000} \left(\frac{L_{petrol,j}}{\Gamma_{petrol,j}} \right) \rho_{petrol} LHV_{petrol} \right]$$

The primary energy of the two analyzed layouts (L1 and L2) is evaluated according to the following equation.

$$PE = \sum_t \left[\frac{\left(E_{el,fromGRID} - E_{el,toGRID} \right)}{\eta_{el}} \right]_t \tag{33}$$

In order to evaluate the reduction of conventional fuel for PS, the following index is also evaluated.

$$R_{ren} = 1 - \frac{PE_{PS,consumed}}{PE_{RS}} \tag{34}$$

where $PE_{PS,consumed}$ is the fraction of primary energy consumed by the proposed system.

In order to assess the performance of the reversible fuel cell operating in electrolyzer mode, the rated cell efficiency ($\eta_{SOEC,rated}$) and the actual efficiency are evaluated (η_{SOEC}). $\eta_{SOEC,rated}$ is evaluated as the ratio between the mass of hydrogen stored into the tank ($M_{H2\text{-}inTK\text{-}H2}$) and energy delivered to the electrolyzer. Note that $E_{th,SOEC}$ is the thermal energy demand for producing the steam at 800°C delivered to the electrolyzer, while η_{SG} is the efficiency of the steam generator. η_{SOEC} represents the electrolyzer efficiency also considering the waste heat recovery systems. In fact, in this case, only the thermal energy provided by the auxiliary steam heater is considered $E_{th,A\text{-}SH}$.

$$\eta_{SOEC,rated} = \frac{M_{H2,inTK\text{-}H2} LHV_{H2}}{E_{el,toSOEC} + E_{th,SOEC} / \eta_{SG}}$$
$$\eta_{SOEC} = \frac{M_{H2,inTK\text{-}H2} LHV_{H2}}{E_{el,toSOEC} + E_{th,A\text{-}SH} / \eta_{A\text{-}SH}} \quad (35)$$

The performances of the solid oxide fuel cell are assessed evaluating the following efficiencies.

$$\eta_{el,SOFC} = \frac{E_{el,fromSOFC}}{M_{H2,outTK\text{-}H2} LHV_{H2}}$$
$$\eta_{th,usefulSOFC} = \frac{E_{th,useful}}{M_{H2,outTK\text{-}H2} LHV_{H2}} \quad (36)$$
$$\eta_{th,ratedSOFC} = \frac{E_{th,useful} + E_{th,exhaust}}{M_{H2,outTK\text{-}H2} LHV_{H2}}$$
$$\eta_{ttotSOFC} = \eta_{el,SOFC} + \eta_{th,usefulSOFC}$$

Where $M_{H2,outTK\text{-}H2}$ is the mass of hydrogen withdrawn from the hydrogen tank, $E_{el,fromSOFC}$ is the electricity provided by the SOFC, $E_{th,useful}$ is the thermal energy delivered by the SOFC and exploited by the plant, whereas $E_{th,exhaust}$ is the thermal provided the SOFC and rejected.

Finally, the round trip efficiency is evaluated as follows:

$$\eta_{roundtrip} = \frac{E_{el,fromSOFC}}{E_{el,toSOEC} + E_{th,A\text{-}SH} / \eta_{A\text{-}SH}} \quad (37)$$

The operating costs of the reference system (C) are evaluated according to the following equation.

$$C_{RS} = C_{disrict,RS} + C_{vehicles,RS}$$

$$C_{disrict,RS} = \sum_t \left[\left(E_{el,LOAD} + \frac{E_{th,cool}}{COP_n} \right) J_{el,fromGRID} + \left(\frac{\left(E_{th,heat} + E_{th,DHW} \right) / \eta_B}{LHV_{NG}} \right) J_{NG} \right]_t \quad (38)$$

$$C_{vehicles,RS} = \left[\sum_i N_i \left(\frac{L_{year,i}}{\Gamma_{diesel,i}} \right) J_{diesel} \right] + \left[\sum_i N_i \left(\frac{L_{petrol,i}}{\Gamma_{petrol,i}} \right) J_{pretrol} \right]$$

The operating costs of the proposed plants are evaluated as follows:

$$C_{L1} = \sum_t \left[E_{el,fromGRID} j_{el,fromGRID} - E_{el,toGRID} j_{el,toGRID} + m_{L1} - M_{O2} j_{O2} \right]_t$$
$$C_{L2} = \sum_t \left[E_{el,fromGRID} j_{el,fromGRID} - E_{el,toGRID} j_{el,toGRID} + m_{L2} \right]_t \quad (39)$$

Where m_{L1} and m_{L2} are the maintenance of plant L1 and L2, respectively. The profits for pure oxygen exporting are also considered. In fact, the oxygen produced by means of water electrolysis may be employed for industrial or medical purposes. An exporting price (j_{O2}) of 2 €/kg is assumed according to data available in open literature [120].

The capital cost of L1 and L2 are evaluated according to the following equations:

$$C_{tot,L1} = I_{PV} + I_{SOFC} + I_{TK\text{-}H2} + I_{C1} + I_{C2} + I_{TK\text{-}Oil} + I_{HEs} + I_{HRSG} + I_{EVs} + I_{pumps} + I_{dryCs} + I_{A\text{-}SH} \quad (40)$$

$$C_{tot,L2} = I_{PV} + I_{D\text{-}LIB} + I_{EVs} \quad (41)$$

The main terms of the above displayed equations are reported in Table 13.

Table 13. Design and operating parameters.

Parameter	Description	Value	Unit
$j_{el,fromGRID}$	Electricity purchasing cost	0.18	€/kWh
$j_{el,toGRID}$	Electricity energy exporting cost	0.06	€/kWh
j_{NG}	Natural-Gas purchasing price	0.18	€/Sm^3
j_{O2}	Oxygen purchasing price	2	€/kg
j_{diesel}	Diesel purchasing cost	1.859	€/l
j_{petrol}	Petrol purchasing cost	1.99	€/l
LHV_{H2}	Hydrogen lower heating value	3.00	kWh/Sm^3
		120.00	MJ/kg
LHV_{CH4}	Natural gas lower heating value	9.59	kWh/Sm^3
LHV_{diesel}	Diesel fuel lower heating value	11.86	kWh/kg
LVH_{petrol}	Petrol lower heating value	12.21	kWh/kg
ρ_{diesel}	Diesel fuel density	833	kg/m^3
ρ_{petrol}	Petrol fuel density	714	kg/m^3

Γ_{diesel}	Average consumption ratio diesel ICE vehicle	18	km/l
Γ_{petrol}	Average consumption ratio petrol ICE vehicle	12	km/l
J_{PV}	PV cost	1000	€/kW
J_{SOCF}	Reversible SOCF cost	3000	€/kW
$J_{TK\text{-}H2}$	Hydrogen tank cost	500	€/kg
J_{oil}	Therminol 66 cost	5.65	€/kg
I_C	Compressor capital cost	$C_{comp} = 5840 \cdot (P_{el,comp,rated})^{0.82}$	€/compr
I_{HE}	Heat exchanger capital cost	$C_{HE} = 130 \cdot 1.4 \cdot [(A_{HE}/0.093)^{0.78}]$	€/HE
$I_{TK\text{-}O}$	Oil tank capital cost	$C_{TK} = 494.9 + 0.808\ V_{TK}$	€
J_{HRSG}	Heat recovery steam generator	0.368	M€/HRSG
$JdryC$	Dry cooler specific cost	200	€/kW
$J_{A\text{-}SH}$	Auxiliary steam heater specific cost	125	€/kW
$J_{D\text{-}LIB}$	Lithium-ion battery cost	200	€/kWh
C_{EV}	Electric vehicle capital cost	$CEV = N_{Leaf}C_{Leaf} + N_{Zoe}C_{Zoe} - N_{ICE}C_{ICE}$	€
C_{Leaf}	Nissan Leaf capital cost	39.00	k€/vehicle
C_{Zoe}	Renault Zoe capital cost	29.00	k€/vehicle
η_{el}	Conventional thermo-electric power plant efficiency	46	%
η_B	Boiler efficiency	75	%
η_{SG}	Steam generator efficiency	98	%
$\eta_{A\text{-}SH}$	Steam heater efficiency	98	%
η_{inv}	District Inverter efficiency	95	%

4.2.3 Case Study

The considered user consists of a residential district of 50 buildings. The main features of this residential district are reported in ref. [120]. Moreover, these works also present in detail the approach used for harvesting the data about the residential district. Table 14 summarizes the main characteristics of the residential district. Buildings space heating and domestic hot water demands are met by independent boilers, with an average efficiency of 75 %. The thermal energy demand for building space cooling is matched by means of independent electric driven air-to-air heat pumps. The power load of the district, due to the electrical appliances installed in each apartment and due to the air-to-air HPs is met by electricity withdrawn from the grid.

This residential district includes 47073 inhabits and 2598 internal combustion engine vehicles. Table 15 displays the main data concerning vehicles and drivers.

The above-described district is considered as the reference system (RS). On the other hand, the proposed system consists of the above considered district, where the existing boilers are dismissed and the existing air-to-air heat pumps are used for matching the thermal energy demand for both building space heating and cooling,

while the thermal energy demand for domestic hot water is met by means of ANK-050 Aermec electric driven air-to-water heat pumps [128], Table 16. Moreover, all the internal combustion engine vehicles are replaced by electric vehicles, namely Nissan Leaf and Renault Zoe, [127] Table 15. Thus, this district is fully powered by electricity.

In this framework two layouts are considered and compared, see System Layout Figure 41 and Figure 42.

The first considered layout (L1 Figure 41) consists of the above described fully electric district integrated with a renewable plant based on a reversible solid oxide fuel cell and a photovoltaic field. In particular, the electricity demand is matched by the electricity produced by a PV field of 10.04 MW (Table 16). The surplus electricity is delivered to a 5 MW reversible SOFC and stored in a 51 m^3pressurized tank. When the production is not sufficient for meeting the district load, the 5 MW reversible fuel cell is activated, consuming the stored hydrogen.

The second considered layout (L2 Figure 42) consists of the above described fully electric district, integrated with 10.04 MW PV field and a 12.53 MWh lithium-ion battery, Table 16.

Table 14. Residential district, including internal combustion engine vehicles features [119].

Parameter	Value	Unit
$E_{th,heat}$	4.00	GWh/y
$E_{th,DHW}$	2.47	GWh/y
$E_{th,cool}$	0.50	GWh/y
$E_{el,LOAD}$	3.89	GWh/y
$PE_{district}$	17.04	GWh/y
PE	56.91	GWh/y
$C_{district}$	1.67	M€/y
C	14.97	M€/y
$CO_{2\ district}$	3.65	10^6 $kgCO_2/y$
$CO_{2\ total}$	11.60	10^6 $kgCO_2/y$

Table 15. Vehicles summary [127].

Type of Vehicle	Number [-]	l_{day} [km/day]	v_{mean} [km/h]	Type of user	Scheduling	ICE	EV
A	932	60	90	family	00:00-07:00; 19:00-24:00	petrol	Renault Zoe
B	932	50	50	family	00:00-08:00; 10:00-14:30 19:00-24:00	diesel	Nissan Leaf
C	330	20	50	old people	00:00:09:00; 11:00-16:00 18:00-24:00	petrol	Renault Zoe
D	312	80	50	young people	00:00-09:00; 14:00-15:00; 22:00-24:00	diesel	Nissan Leaf
E	83	70	60	smart worker/single person	09:00-22:00	petrol	Renault Zoe

Table 16. Plant main components data.

Component	Parameter	Value	Unit
EVs	Charging efficiency	0.9	-
	High limit on State of Charge ($SoC_{lim,max}$)	0.95	
	Minimum limit on State of Charge ($SoC_{lim,min}$)	0.15	
	Guaranteed limit on State of Charge ($SoC_{lim,min}$)	0.4	
	$P_{el,ch,guaranteed}$	3	kW
PV Field	Module efficiency	0.18	-
	PV panel rated power	10.04	MW
	PV field area	55779	m^2
D-LIB	Capacity	12.53	MWh
	Battery charging efficiency	90	%
	Maximum allowed discharging/charging power	4.17	MW
Reversible SOFC	Cell operative pressure	1	
	Number of cells in series	8	
	Number of stacks in parallel	5555	
	Rated fuel cell/electrolyzer capacity	5.00	MW
Tank TK-H2	Tank Volume	28	m^3
	Max tank pressure	200	bar
Compressor H_2	Compressor isentropic efficiency	80	%
	Number of stages	4	-
	Compression ratio	3.75	-
	Rated pressure	200	bar
Compressor O_2	Compressor isentropic efficiency	80	%
	Number of stages	4	-
	Compression ratio	3.50	-
	Rated pressure	150	bar
HP DHW (ANK-050, [128])	Rated heat transfer ratee	15.2	kW
	Rated power demand	4.4	kW
	Rated coefficient of performance (COP)	3.45	-
	Rated water flow rate (load side)	2659	kg/h
	Rated air flow rate (source side)	7000	m^3/h
	Rated load temperature	55	°C

4.2.4 Results

Table 17 summarizes the main results of the two layouts proposed. Both the analyzed layouts achieve very similar energy, economic and environmental performance indexes, i.e. a *PES* equal to 83% (L1) vs 90% (L2) and a *SPB* equal to 4.4 years (L1) vs 3.5 years (L2).

The layout L2 (including Lithium-ion batteries as district EES) achieves a slightly lower share of self-consumed energy ($E_{el,SELF}$), i.e. $E_{el,SELF}$ equal to 11.62 GWh/y (L2) vs 12.43 GWh/y (L1). This difference is mainly due to the performances of the reversible SOFC and of D-LIB. In fact, the activation of the reversible solid oxide fuel cell in electrolyzer mode leads to the operation of a number of ancillary systems, namely,

auxiliary electric steam boiler, pumps, and compressors. These devices are mainly driven by the surplus of renewable power provided by the PV field. Therefore, the activation of the SOEC causes an increase of the electric load of the district met by renewable power, also increasing the share of self-consumed energy. As a consequence, the electric load ($E_{el,LOAD}$) of L1 is greater than $E_{el,LOAD}$ of L2, i.e. 19.19 GWh/year vs 17.75 GWh/year.

Despite the electricity delivered to the D-LIB ($E_{el,toDLIB}$) is almost equal to that delivered to the reversible SOFC ($E_{el,toSOEC}$), i.e. 4.74 GWh/y (L2) vs 4.51 GWh/y (L1), D-LIB provides a higher amount of electricity with respect to the SOFC. In particular, the electricity provided by the reversible SOFC ($E_{el,fromSOFC}$) is approximately equal to 2.24 GWh/y, while the electricity withdrawn from D-LIB ($E_{el,fromDLIB}$) accounts for 2.81 GWh/y. This difference can be justified by the higher D-LIB roundtrip efficiency, i.e. 62%, compared with the reversible SOFC, i.e. roughly 43%. These trends can be better understood with the dynamic trends shown in ref.[120], here omitted for the sake of brevity.

The electricity exported to the grid is higher for L2 with respect to L1, 2.22 GWh/y (L1) vs 3.40 GWh/y (L2). In order to avoid battery degradation and overheating, an upper value of charging power is selected. When the surplus power is higher than this value, a fixed power equal to $P_{el,D\text{-}LIB,lim,ch}$ is delivered to the battery, while the residual power is exported to the grid. Conversely, the reversible SOFC is able to handle a higher maximum power (see $P_{el,toSOEC}$) dramatically reducing the electricity exported to the grid ($P_{el,toGRID}$).

It is worth noting that the above discussed results are also affected by the selection of the capacities of the hydrogen tank and the lithium-ion battery. In fact, for a more consistent comparison, LIB and TK-H2 are designed with the same capacity in terms of electric energy storage. Thus, considering the higher efficiency of the reversible SOFC in electrolyzer mode with respect to the fuel cell mode, i.e. 73% (electrolyzer mode) vs 49% (fuel cell mode), L1 stores an amount of electricity significantly higher than the provided electricity.

Both the proposed layouts achieve the goals of reducing the surplus electricity exported to the grid and the dependence of the residential district from conventional fuels. In fact, less than 20% of PV electricity production is exported to the grid, $E_{el,toGRID}$ (Table 17), and the fraction of renewable energy matching the residential district load is the majority, i.e. R_{ren} = 74% (L1) and R_{ren} = 76%, Table 17.

From the economic point of view, the layout based on reversible SOFC plant has a significantly higher capital cost, due to the high cost of the technologies involved in

such plant. Despite this significant difference, the layouts achieve similar economic results because of a huge difference also in the operating costs savings.

Table 18 displays the main results concerning the thermal energy performance of the waste heat recovery system (WH-RS) included in the layout L1. The thermal energy provided by the WH-RS, consisting of the heat supplied by the recovery steam generator HRSG-1 and the economizer HE-O-W, matches roughly 22% of the thermal energy demand of the reversible SOFC operating in electrolyzer mode ($E_{th,SOEC}$), accounting for about 0.40 GWh/year. Figure 47 and Figure 48 show the dynamics of the thermal recovery system.

When the SOFC is in operation, from 7 PM to 9:50 PM, the available heat ($\Phi_{available}$) is roughly equal to 2.89 MW, but the system is able to store less than 20% of this thermal energy available. In fact, the useful thermal energy ($P_{th,useful}$), i.e. the thermal energy stored in the oil tank (Tk-Oil), rapidly decreases. Therefore, the share of the available thermal energy rejected is very high ($\Phi_{exhaust}$). From 9:20 PM to 10 PM, all the available thermal energy is rejected, i.e. 2.89 MW, since the tank is not able to store additional thermal energy, i.e. the temperature of the tank is close to the maximum acceptable operating temperature of the diathermic oil selected.

Figure 48 is consistent with the above discussed trends. The thermal efficiency of the SOFC is minimum in the summer months, i.e. $\eta_{SOFC,th}$ equal to roughly 7.90 %, and maximum during the winter months, i.e. $\eta_{SOFC,th}$ equal to roughly 11.20 %. This trend is due to the fact that, during the summer day, the share of thermal energy rejected is greater. In fact, the higher the number of hours of SOFC operation, the higher the amount of thermal energy rejected. For the same reason, the WH-RS matches a higher share of the electrolyzer thermal energy demand during the winter period, i.e. 23-26 %. In fact, during the summer period the SOEC operates more hours, then the WH-RS is only able to match a limited share of the SOEC thermal energy demand.

The higher the hours of SOEC operation, the lower the amount of thermal energy met by WH-RS. It is worth nothing that this system is able to improve the efficiency of the cell operating in electrolyzer mode, which achieves a yearly efficiency of 93% compared with an efficiency of 73% achieved without the WH-RS.

Table 17. Yearly results for the two layouts analyzed: L1 and L2.

Parameter	Value (L1)	Value (L2)	Unit
$E_{el,LOAD}$	19.19	17.75	GWh/year
$E_{el,aux}$	1.15	-	GWh/year
$E_{el,PV}$	17.23	17.23	GWh/year
$E_{el,toSOEC}$	4.74	-	GWh/year
$E_{el,fromSOFC}$	2.24	-	GWh/year

$E_{el,toDLIB}$	-	4.51	GWh/year
$E_{el,fromDLIB}$	-	2.81	GWh/year
$E_{el,toGRID}$	2.22	3.40	GWh/year
$E_{el,fromGRID}$	6.76	6.13	GWh/year
$E_{el,self}$	12.43	11.62	GWh/year
$\eta_{SOEC,rated*}$	73.30	-	GWh/year
η_{SOEC}	93.37		%
ηel_{SOFC}	49.28		%
$\eta_{th,usefulSOFC}$	8.37	-	%
$\eta_{th,ratedSOFC}$	46.43	-	%
$\eta_{SOFC,tot}$	57.64	-	
$\eta_{roundtrip}$	43.58	62.24	%
PE	9.85	5.92	%
PES	82.69	89.60	%
R_{ren}	74.19	76.60	%
ΔCO_2	81.81	88.74	%
$E_{el,self}/E_{el,LOAD}$	64.79	65.48	%
$E_{el,fromSOFC}/E_{el,LOAD}$	11.67	-	%
$E_{el,frommDLIB}/E_{el,LOAD}$	-	15.82	%
$E_{el,toGRID}/E_{el,PV}$	12.90	19.75	%
C_{TOT}	67.56	48.64	M€
M_{O2}	803.52	-	10^3 Sm^3/year
S_{O2}	2.30	-	M€/year
C	-0.48	1.21	M€/year
ΔC	15.45	13.76	M€/year
SPB	4.37	3.53	years
NPV	125.53	123.40	M€
PI	1.86	2.54	

Table 18. Yearly results: thermal energy performance of L1.

Parameter	Value	Unit
$E_{th,HE-O-W}$	0.08	GWh/year
$E_{th,HRSG-1}$	0.32	GWh/year
$E_{th,HRSG-2}$	0.83	GWh/year
$E_{th,HRSG-3}$	0.18	GWh/year
$E_{th,A-SH}$	0.39	GWh/year
$E_{th,SOEC}$	1.80	GWh/year
$E_{th,WH-RS}/E_{th,SOEC}$	22.11	%
$E_{th,HRSG-2}/E_{th,SOEC}$	45.81	%
$E_{th,HRSG-3}/E_{th,SOEC}$	10.21	%
$E_{th,A-SH}/E_{th,SOEC}$	21.88	%

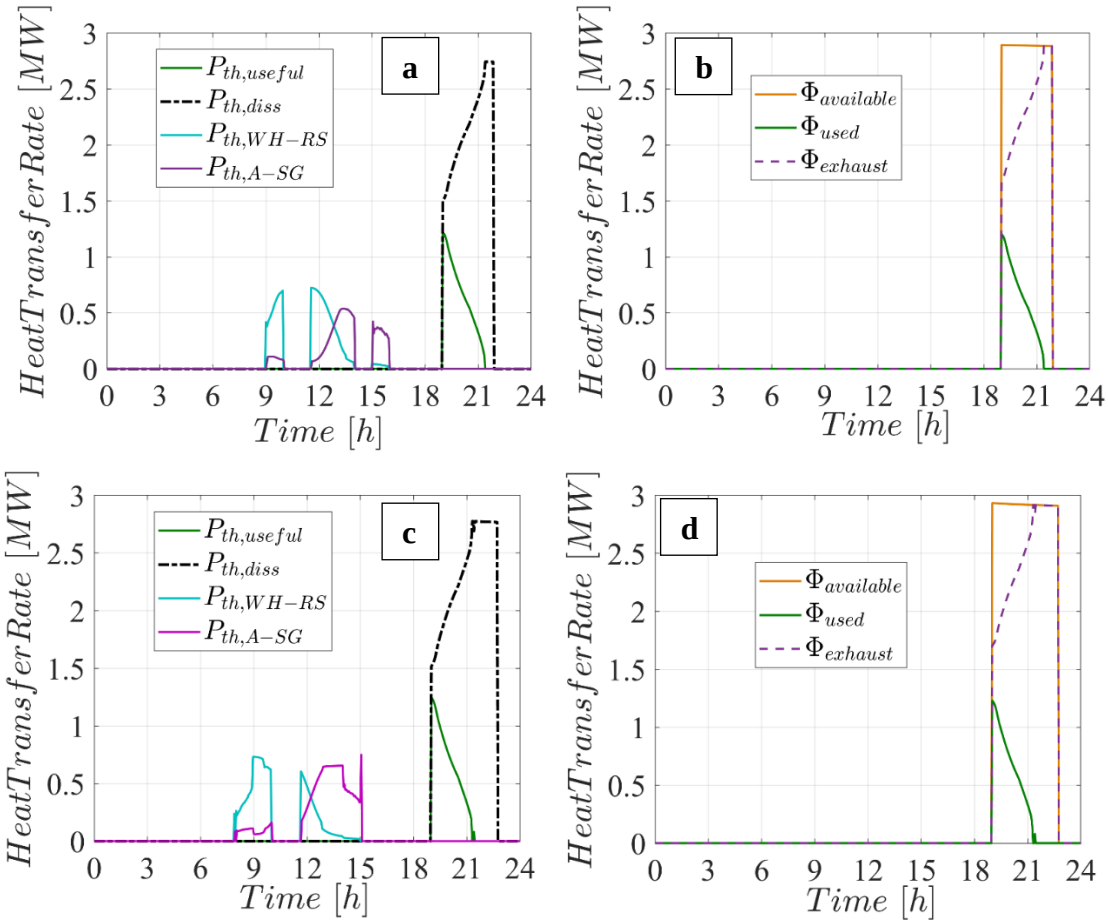

Figure 47. Dynamic performance of the waste heat recover system above and a typical summer day below: a) thermal energy trends of WH-RS for a typical winter day; b) thermal energy performance of the SOFC for a typical winter day; a) thermal energy trends of WH-RS for a typical summer day; b) thermal energy performance of the SOFC for a typical summer day.

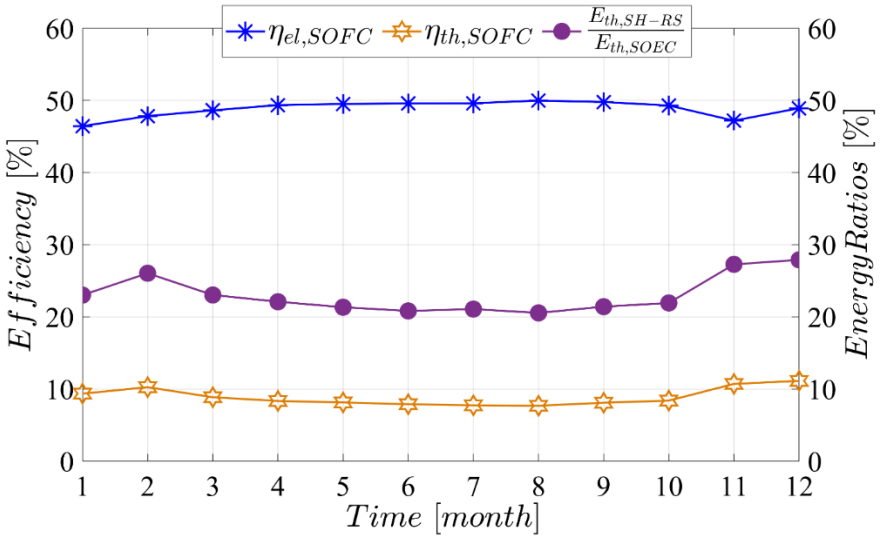

Figure 48. Electric and thermal performance of the SOFC and thermal energy performance of the WH-RS.

The discussion regarding the dynamic and monthly results from the electric side of the system is thoroughly discussed in ref. [120]. Furthermore, in the same reference, parametric and sensitivity analyses on electric vehicles performance, oxygen price and storage systems capital costs are provided.

Chapter 5
Models developed on Power-to-Gas

As discussed in the chapter 2, Power-to-Gas (P2G) technology is a pivotal aspect of modern renewable energy systems, offering a valid solution for storing excess electrical energy produced from renewable sources. Among its various applications, the power-to-methane (P2M) is catching the eye most because not only it aids in balancing the electric grid but also contributes to the production of renewable natural gas, which can be integrated into existing natural gas infrastructures.

In this chapter, we delve into several studies that pave the way for the development of models dedicated to producing entirely renewable natural gas. A cornerstone of this exploration is the development, simulation, and analysis of an anaerobic digestion (AD) model. This model allows to evaluate the yield of biogas from the organic fraction of municipal solid waste, a substantial step in utilizing waste for energy production. The biogas thus produced is further upgraded, with the resultant biomethane being fully renewable because the AD plant operation is driven by solar energy, ensuring a sustainable and green energy source.

Moreover, an innovative aspect of this process is the utilization of carbon dioxide, separated from methane during the upgrading process. This CO_2 is then combined with green hydrogen, produced via solid oxide electrolysis powered by photovoltaic (PV) systems, in a methanation reactor. The outcome of this reaction is the formation of renewable synthetic methane. This '*e*-fuel' is utterly renewable and represents a significant stride in the advancement of green energy solutions.

This approach, encompassing the AD model and the following steps, embodies the essence of circular economy principles. By exploiting both organic waste and solar energy, it enhances the potential of renewable resources in creating sustainable fuel alternatives. The integration of these technologies – solar-powered AD, electrolysis using PV energy, and methanation – not only demonstrates the feasibility of producing renewable natural gas but also exemplifies a closed-loop energy system which minimizes waste and maximizes resource efficiency.

In the following of this chapter, each of these components and their interplay in creating a sustainable energy ecosystem will be explored in detail. The pioneering works presented will highlight both the technological advancements and the potential challenges in realizing the full potential of power-to-methane within the broader Power-to-Gas framework.

5.1 Integration of photovoltaic panels and solar collectors into a plant producing biomethane for the transport sector: dynamic simulation and case study

The first study presented discusses a technical and economic feasibility analysis for a fully renewable biomethane production plant proposed for a city in the region of Campania, in the south of Italy, where the issues of waste disposal and road transport sector pollution are predominant. Furthermore, the high solar radiation of this area makes the renewable technologies considered particularly appealing. Therefore, this work proposes a novel paradigm for the green public transport, where a residential district is served by a fleet of buses fed by the biomethane produced by the organic urban wastes. A deep literature review is provided in ref. [129] on the novelty of the solution and the methodology proposed by this work. Here, the novelty is summarized by the following points:

- A fully-renewable biomethane plant is proposed and analysed under dynamic operating conditions, based on the integration of Photovoltaics (PV) and Evacuated Tube Collectors (ETC) into the process.
- A multiparametric analysis is carried out to investigate the profitability of the system by ranging the unit costs of the electricity and gas. Different scenarios are evaluated to understand how the market variability influences the economic return.
- A sensitivity analysis is performed, to point out the best configuration of renewables integration and other components sizing. The optimal size of PV and ETC fields are evaluated, along with the optimal capacity of both thermal and electric energy storage systems.
- A thermoeconomic analysis of the biomethane production plant is proposed to investigate the feasibility of a solution for the road transport sector decarbonisation. Advanced biomethane production, which means biomethane production from OFMSW, is strongly supported in Italy. The influence of such incentives on the feasibility of the system is analysed.

5.1.1 System Layout

Figure 49 shows the layout of the system proposed. Two main loops are detected in this plant, the solar loop (SL) and the digester loop (DL). The SL connects the evacuated tube collector (ETC) field to the thermal tank (TK). The water in the SL is pumped by the variable speed pump P2 from the tank to the ETC solar field. The ETC collector is used to provide heat transfer rate to the water by solar energy. The mismatch between solar radiation and the anaerobic digester (AD) thermal demand

is mitigated by the TK. In the SL, solar energy is used to increase the fluid temperature up to the set point of 60°C. A feedback controller manages P2 functioning. In particular, if the bottom temperature of the tank is greater than the temperature of the water outgoing the collector ($T_{b,tank} > T_{out,coll}$) or the solar radiation G < 10 W/m^2, the controller switches the pump off to prevent thermal energy dissipation.

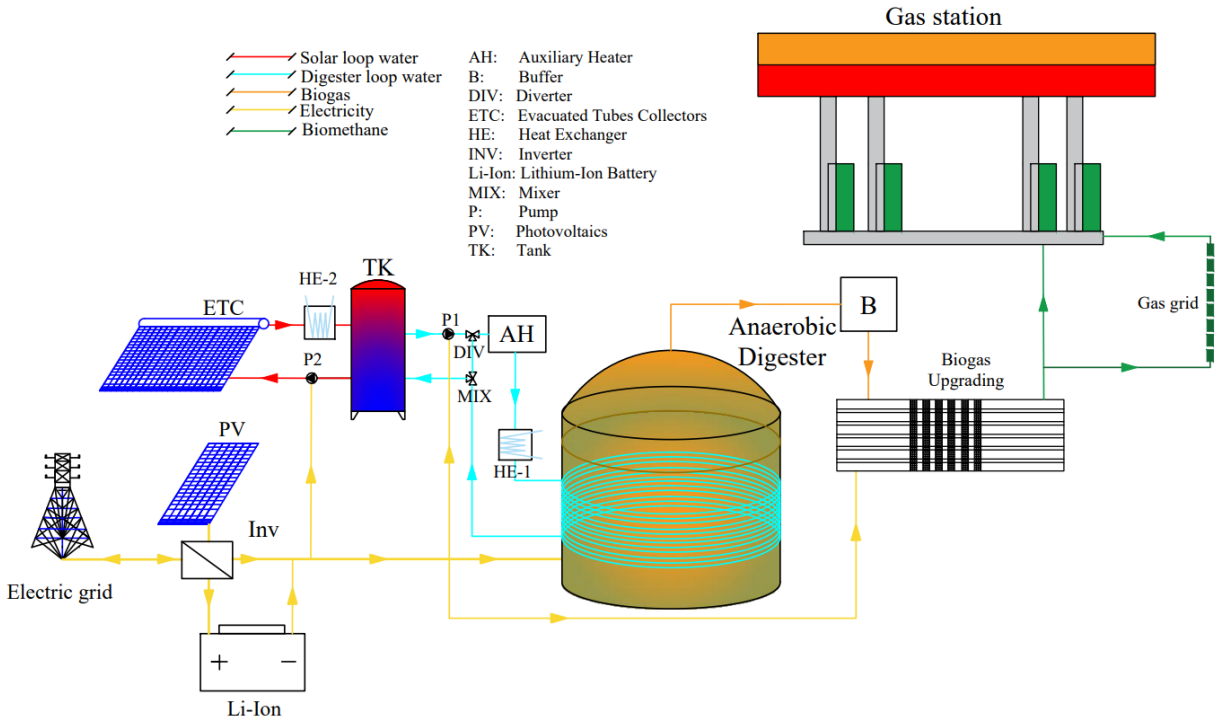

Figure 49. Layout of the plant.

In addition, the SL is also equipped with the heat dissipator HE-2, in case the regulation with the P2 is not sufficient. In case $T_{out,coll}$ > 60°C, the surplus heat is dissipated by means of thermal exchange with a counterflow water at lower temperature. Conversely, when $T_{out,coll}$ < 60°C, no thermal dissipation occurs. That measure is proposed in order to avoid tank overheating, thus the inlet temperature set point is 60°C.

On the other side of the tank, the DL provides to the AD the thermal energy collected and stored in the TK. The hot water is delivered to the digester by means of a constant speed pump P1. This loop is equipped with an auxiliary biomass heater (AH), whose setpoint temperature ($T_{set,AH}$) is equal to 50°C. A PID controller manages this loop, through the diverter DIV, based on the temperature inside the digester. If the fluid temperature (T_{DL}) is below the set point, equal to 50°C, the water delivered to the digester is heated up to $T_{set,AH}$ by the AH. When T_{DL} is greater than 50°C, the PID controller proportionally diverts a suitable amount of water by means of D1, allowing such flow to bypass the digester. Therefore, only a limited share of hot

water is provided to the digester, to avoid overheating and sharp temperature variations. When T_{DL} is higher than 52°C, some heat is rejected to the environment by means of HE-1, reducing such temperature below the rated limit.

These controls are designed to keep the digester temperature to roughly 38°C and to avoid digester overheating. In fact, the digester produces biomethane by means of mesophilic reaction. Sharp variations of its temperature may cause inhibition of biochemical processes, due to the death of mesophilic bacteria. A PV field is used to drive the auxiliary devices, such as the pumps, the mixing, and the biogas upgrading unit. The system is also equipped with a 1000 kWh lithium-ion battery storage, to maximize the self-consumption of electricity provided by the PV.

5.1.2 System Model

To perform the dynamic simulation of the hybrid renewable energy system proposed in this work, several models were integrated. For simulating the anaerobic digestion process, the biological and thermal model of the reactor were developed in MatLab, as well as the membrane separation for the biogas upgrading. Such models were integrated in TRNSYS (version 17), to exploit a large library of mathematical models for different components ("Types").

The anaerobic digestion (AD) model developed in this work is the ADM1, widely adopted for the simulation of the biogas production from low total solid content biomass. In this work, the biogas production from OFMSW is investigated by means of a modified version of the ADM1, due to its reliability and robustness for this specific case. More specifically, this version of ADM1 just considers 13 out of the 19 components of the standard model, sufficient to provide accurate results for this application. Therefore, this model is based on 13 differential equations, considering mass balances for each biological component. More details regarding this model can be found in [130].

The AD mechanism is a sequence of several biochemical processes which lead to the production of methane starting from complex organic matter. To analyse the process is crucial to know the concentration of chemical species in the biomass; such concentrations are expressed as kg_{COD}/m^3, where the chemical oxygen demand (COD) refers to the milligrams of oxygen required to chemically oxidize organic and inorganic substances in 1 L of H_2O. Thus, the model includes 10 processes and 13 components, including the Monod's first-order kinetics for the extracellular processes and the Michaelis-Menten kinetics for the intracellular biochemical reactions. These assumptions lead to the system of equations:

$$\frac{dS_{waste,\,i}}{dt} = \frac{q_{in}}{V_{waste}} S_{waste,i,in} - \frac{q_{out}}{V_{waste}} S_{waste,i} + \sum_{j=1}^{10} \varphi_j \alpha_{i,\,j} \tag{42}$$

Eq.(38) represents a system of differential equations considered for a continuously stirred tank reactor (CSTR), i.e. a reactor with one temperature node, where the subscripts *i* and *j* refer, respectively, to the component and the process. $S_{waste,i,in}$ is the input concentration of the substrate *i* in the liquid biomass, q_{in} and q_{out} are the input and output OFMSW flow rates, is the concentration of the substrate within the reactor, $\varphi_{i,j}$ is the kinetic term and $\alpha_{i,j}$ is the biochemical coefficient of the substrate *i* during the process *j*.

The temperature of the digester T_{dig} dramatically affects the AD process. Steering the temperature inside the reactor is crucial to enhance bacteria operation. The dynamic calculation of T_{dig} can be performed considering the heat transfer occurring in the AD. Eq. (39) is the equation of thermal equilibrium applied to the control volume of the digester and eq. (40) is the project equation of the heat exchanger HE:

$$\begin{aligned} &\dot{m}_{OFMSW} c_{p,OFMSW} T_{in,OFMSW} + \dot{m}_W c_{p,W} T_{in,W} = \dot{m}_{digestate} c_{p,digestate} T_{dig} + \dot{m}_{biogas} c_{p,biogas} T_{dig} \\ &+\dot{m}_W c_{p,W} T_{out,W} + U_{dig} A_{dig} \left(T_{dig} - T_{amb} \right) + U_f A_f \left(T_{dig} - T_{ground} \right) + U_{cov} A_{cov} \left(T_{dig} - T_{amb} \right) \end{aligned} \tag{43}$$

$$\dot{m}_{HW} c_{p,HW} \left(T_{in,HW} - T_{out,HW} \right) = n U_{HE,n} A_{HE,n} \Delta T_{lm} \tag{44}$$

$m_{digestate}$ and $m_{biomass}$ can be calculated by means of the biological model. Conversely, T_{dig} and the water outlet temperature, $T_{out,water}$ are the unknown quantities to be calculated through the system of equations (Eq.(39) and Eq.(40)). Once that T_{dig} is known, the biological model evaluates the microbial species evolution calculating the kinetic rates at that precise temperature level, predicting the biogas yield.

The model here proposed by the authors is an integration of already widely analysed and validated models proposed in literature. In fact, the ADM1 model is the most widespread model for the estimation of the biogas yield from the anaerobic digestion process applied to several biomasses. At the same time, the logarithmic-mean temperature model is used in many heat transfer problems. Thus, the coupling of these models is considered an intrinsically validated model.

Unfortunately, the validation of the model as a whole is not possible, since the plant designed in this study is not available and the cost of the possible experimental setup is extremely high. Nevertheless, the models of all the components and processes included in the system were previously validated vs experimental or literature data. Therefore, according to the method widely used in literature, the model as a whole is considered validated too.

Most of the models used in this work were taken from the TRNSYS library; some other models were specifically developed for the scope of the work and/or based on manufacturers' data. In particular, a suitable model was developed for the simulation of the anaerobic digester (AD), whose model was not available in the TRNSYS library.

As previously mentioned, the anaerobic digestion biological model was developed in MatLab. Together with this model, thermal balance equation were integrated to calculate iteratively the value of the reactor temperature according to the different inlet water temperature and ambient temperature values. The model developed in MatLab was then integrated in TRNSYS environment by means of the *type581a* which allows one to recall the results of the MatLab file at each iteration. The strength of this integration is that the model can be recalled at each time step with different boundary conditions, preserving the evolution of the biochemical species. The main design parameters of the digester are summarized in Table 19.

Table 19. Main design parameters of the digester.

Parameter	Description	Value	Unit
m_{OFMSW}	mass flow rate of OFMSW	2016	kg/h
ρ_{OFMSW}	Density of OFMSW	750	kg/m^3
$C_{p,OFMSW}$	Specific heat of OFMSW	2.72	kJ/(kg K)
$m_{w,in}$	mass flow rate of the inlet hot water range	1400÷9000	kg/h
T_{amb}	ambient temperature range	-2 ÷ 35	°C
$T_{w,in}$	inlet hot water temperature range	40 ÷ 60	°C
HRT	hydraulic retention time	30	d
T_{dig}	digester temperature	38	°C
H_{react}	height of digester	10	m
n	Number of heat exchanger coils	3	-

To couple the AD model with TRNSYS, a map of data obtained from the simulation in MatLab was integrated into the TRNSYS project. The combined biological-thermal model operated with different values of ambient temperature, flow rate and temperature of the water incoming the digester, and flow rate of biomass. The outputs are the operating temperature of the reactor, the temperature of the outgoing water, the heat transfer rate within the digester through the pipes, and the mass flow rate of biogas. The results achieved for a set of input data were interpolated in TRNSYS to obtain the values for different operating conditions. In this way, it was possible to calculate the biogas production in dynamic conditions. More details about that model are available in [130].

The upgrading unit consists of a three-stage selective membrane system (Figure 50). It was simulated by an in-house model, since this component was not available in TRNSYS.

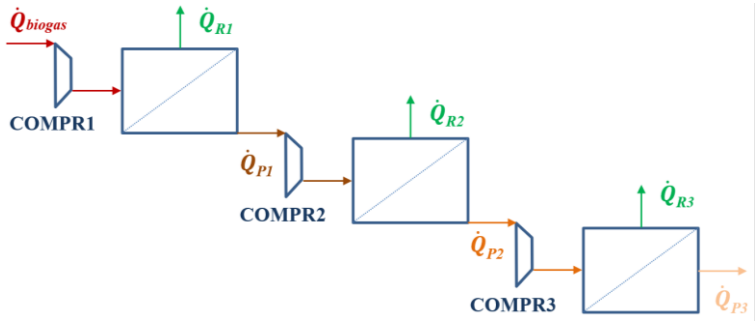

Figure 50. Three phases of the upgrading process.

A detailed description of this model is in the section 5.3, where both the membrane separation and water scrubbing upgrading processes are explained with detail. For the other components of the plant, built-in models from TRNSYS libraries were adopted. Since there are no dedicated models for ETC in TRNSYS, the flat plate collector model was used. For adapting to the ETC model, the incident angle modifier (IAM) was managed. Type 71 is the one used in this TRNSYS version and the efficiency of both ETC and flat plate collectors (FPC) is calculated with the same equations.

The tank was modelled by the TRNSYS 4d type, considering a multi-layer system where each layer is perfectly mixed, and all the layers have the same dimensions. The equilibrium between adjacent layers is ruled by the energy balance equations:

$$M_i C_p \frac{dT_i}{dt} = \alpha_i \dot{m}_h C_p (T_h - T_i) + \beta_i \dot{m}_l C_p (T_l - T_i) + UA_i (T_{amb} - T_i) \quad (45)$$

Here, subscript "*i*" refers to the layer on which the energy balance is considered, whereas "*h*" and "*l*" refer to the higher and the lower layer, respectively. The tank volume design value linearly depends on the ETC total area and on the volumetric flow rate of the pump, which is of 150 kg/(h m^2):

$$V_{TANK} = Q_P \cdot A_{ETC} / 1000 \quad (46)$$

The performance of the proposed system (PS) was evaluated by comparison with a Reference System (RS), where it is assumed that a fleet of conventional buses, whose operating conditions will be explained later, are only fuelled by diesel.

The Primary Energy Saving (*PES*) is calculated as:

$$PES = \frac{PE_{RS} - PE_{PS}}{PE_{RS}} \quad (47)$$

$$PE_{RS} = \frac{V_{diesel} \cdot LHV_{diesel}}{3.6} \quad (48)$$

$$PE_{PS} = \frac{E_{el,fromGRID} - E_{el,toGRID}}{\eta_{el,GRID}} - V_{CH_4,surplus} \cdot LHV_{NG} \quad (49)$$

Where PE_{RS} is related to the diesel used for road transport, whereas PE_{PS} is due to the difference between the primary energy related to the electricity withdrawn from the national electric grid and the primary energy saved thanks to the surplus biomethane. $V_{CH4,surplus}$ is the difference between the volume of biomethane yearly produced by the digester and the annual demand of biomethane of the fleet of buses; this surplus is injected into the natural gas grid, allowing to save natural gas produced by fossil sources.

Similarly, the savings in terms CO_2 equivalent emissions are calculated according to:

$$MCO_{2,RS} = f_{CO_2,diesel} \cdot \delta \cdot 365 \quad (50)$$

$$MCO_{2,PS} = E_{el,fromGRID} \cdot f_{CO_2,EE} - V_{CH_4,surplus} \cdot f_{CO_2,NG} \quad (51)$$

Where $f_{CO2,diesel}$ is expressed in g/km and δ is the distance, in km/day, covered by the buses. Capital costs include expenditure for PV modules, auxiliary heater, solar collectors, storage systems, digester and biomethane plant, with corresponding auxiliary devices. In addition, it is assumed that a full refurbishment of the existing diesel buses is needed; therefore, assuming that the difference in costs between gas and diesel buses is negligible, no extra investments were considered for the replacement of the fleet. The feasibility analysis of the proposed system is assessed by calculating the Simple Payback (*SPB*) and Discounted Payback (*DPB*) period:

$$SPB = \frac{INV_{TOT}}{\Delta C} \quad (52)$$

$$DPB = -\frac{log(1 - SPB \times a)}{(1+a)} \quad (53)$$

Where ΔC is the difference between yearly operating costs for the Reference System (RS) and the Proposed System (PS), INV_{TOT} the total investment, or Capital Expenditure (CAPEX) and *a* is the discount rate.

In the RS, buses run with diesel engines and all the operating costs are related to the cost of diesel. In the PS, the diesel is replaced by the biomethane; investment,

maintenance and operating costs include the digester, the PV collectors, the tank, and the battery.

The operating costs are due to the energy and maintenance costs, *M;* this latter term was assumed equal to 1% of total investment costs. Therefore, the *SPB* is equal to:

$$SPB = \frac{P_{p,PV} \cdot C_{u,PV} + E_{el,storage} \cdot C_{u,storage} + INV_{AH} + A_{ETC} \cdot C_{u,ETC} + INV_{dig}}{V_{diesel} \cdot j_{diesel} - E_{el,fromGRID} \cdot j_{EE} + \frac{Q_{th}}{\eta_{th,ref}} \cdot \frac{j_{wc}}{LHV_{wc}} - V_{CH_4,surplus} \cdot j_{NG} + M} \quad (54)$$

In Table 20, the data used for the thermoeconomic analysis are shown.

Table 20. Technical parameters of the thermoeconomic study.

Parameter	Description	Value	Unit
$\eta_{el,grid}$	Rated efficiency of the power grid	0.46	-
η_{AH}	Rated efficiency of conventional boiler	0.95	-
LHV_{NG}	Natural gas lower heating value	9.59	kWh/Sm^3
LHV_{wc}	Woodchip lower heating value	3.7	kWh/kg
LHV_{diesel}	diesel lower heating value	36	MJ/L
ρ_{NG}	Natural gas density	0.705	kg/m^3
ρ_{diesel}	Diesel density	480	kg/m^3
$f_{CO2,EE}$	Unit emission of CO_2 per kWh$_{el}$	0.48	kg$_{CO2,el}$/kWh$_{el}$
$f_{CO2,NG}$	CO_2 emissions per kWh of natural gas	0.20	kg$_{CO2,NG}$/kWh$_p$
$f_{CO2,NG}$	CO_2 emissions per km driven by natural gas	1.23	kg$_{CO2,eq}$/km
$f_{CO2,diesel}$	CO_2 emissions per km driven by Diesel fuel	1.57	kg$_{CO2,eq}$/km
j_{EE}	Unit cost of electric energy	0.18	€/kWh
j_{NG}	Unit cost of natural gas	1.72	€/Sm^3
j_{wc}	Unit cost of woodchip	0.06	€/kg
j_{diesel}	Unit cost of diesel	1.26	€/L
$Cu_{,PV}$	Unit cost of PV modules per peak power	1000	€/kW$_p$
$Cu_{,ETC}$	Unit cost of ETC	300	€/m^2
$Cu_{,storage}$	Unit cost of electric storage	200	€/kWh

Some specific incentives were also considered. In Italy, the use of biomethane in transports is subsidized by means of the "Certificates of release for consumption" ("CIC"), acknowledged to fuel companies who release biomethane to end users. A CIC corresponds to about 1231 m^3 of CH_4 used in the transport sector; biomethane producers are acknowledged a public subsidy of 375 €/CIC; however, in case of "advanced biomethane production" (as in case of OFMSW used as feeding biomass), their value is doubled.

5.1.3 Case Study

The case study refers to a plant under construction near Napoli, in the region of Campania, south of Italy. The selection of this region is due to the dual problem of

the waste disposal and public transport sector underdevelopment. The plant was designed to digest 40´000 tons/year of OFMSW supplied by nearby cities, operating 24/7 for 365 days/year. Given a volume of the digester V_{dig} = 2586.7 m^3, a production of 7.46 tons/day of biogas is calculated. The total amount of biogas produced in one-year is V_{biogas} = 968´035.85 Sm^3. The biomethane produced from this amount of biogas is used to match the natural gas demand of a fleet of buses, evaluated according to [131]. The optimal area of the ETC collectors was calculated as a result of a parametric analysis, considering both energy and economic objective functions. The ETC system is used to preheat the water up to 50°C (set point value), before entering the digester. In case of scarce solar availability, the set point temperature is guaranteed by a 100-kW auxiliary biomass heater. Clearly, auxiliary heat will be required mainly during the winter season. As shown in Figure 51, with a 200 m^2 solar field area, the auxiliary heat is strongly reduced in summer (less than 20%). The ETC field matches roughly 40% of total heat request on a yearly basis.

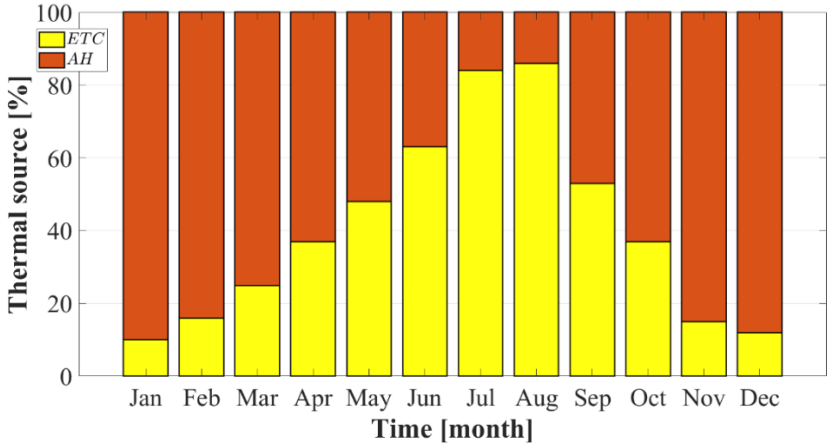

Figure 51. Auxiliary Heater and ETC fraction of heat demand.

The tank capacity was designed for storing the maximum heat produced by ETCs for 1 hour. The corresponding volume of the tank is thus 30 m^3. The plant is equipped with a lithium-ion battery (LIB) of 1800 kWh, calculated by assuming a ratio battery/PV rated capacity equal to 5 kWh/kW.

The PV capacity was selected varying the PV field area from 2000 m^2 to 4000 m^2 and performing a parametric analysis; an optimal value of 2000 m^2 was found, corresponding to a LIB of 1800 kWh. The analysis is carried out by considering both the Profitability Index (PI) and primary energy saving (ΔPE) functions, depending on the PV field and the storage capacity. The solution adopted is a trade-off between these aspects, as shown in Figure 52.

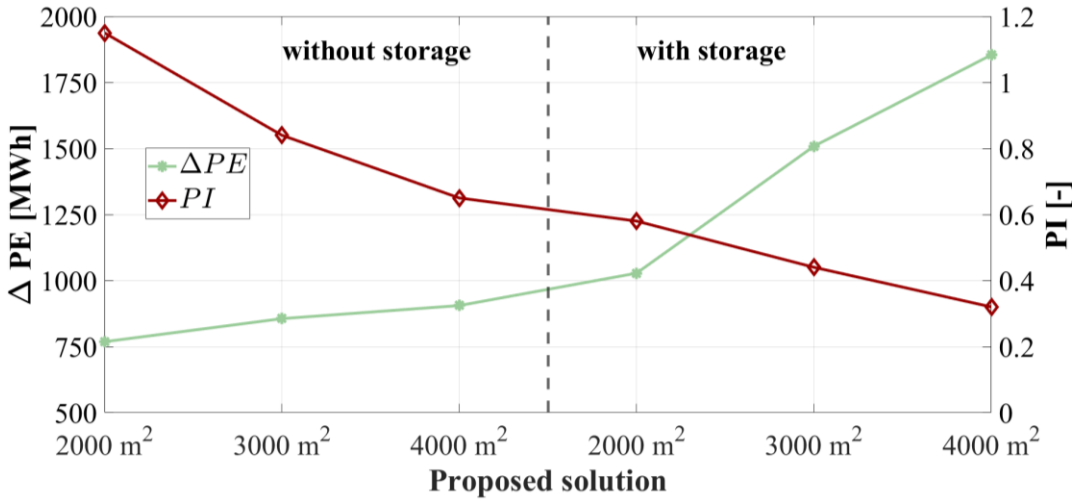

Figure 52. Energy savings (ΔPE) and Profitability Index (PI) of PV plant and Electric Storage solutions.

5.1.4 Results

In this section, the results provided by the simulation model for the case study proposed are shown and discussed, considering hourly, monthly, and yearly bases, in order to provide a comprehensive overview of the system performance. A parametric analysis is also shown, to investigate the most important factors who influence the feasibility of the system. Finally, an optimization of the layout is presented.

Figure 53 shows the dynamic results in terms of heat transfer rates for a typical winter (a) and summer (b) day. Figure 54 shows the dynamic trends of the temperatures, for both summer (a) and winter (b) typical day.

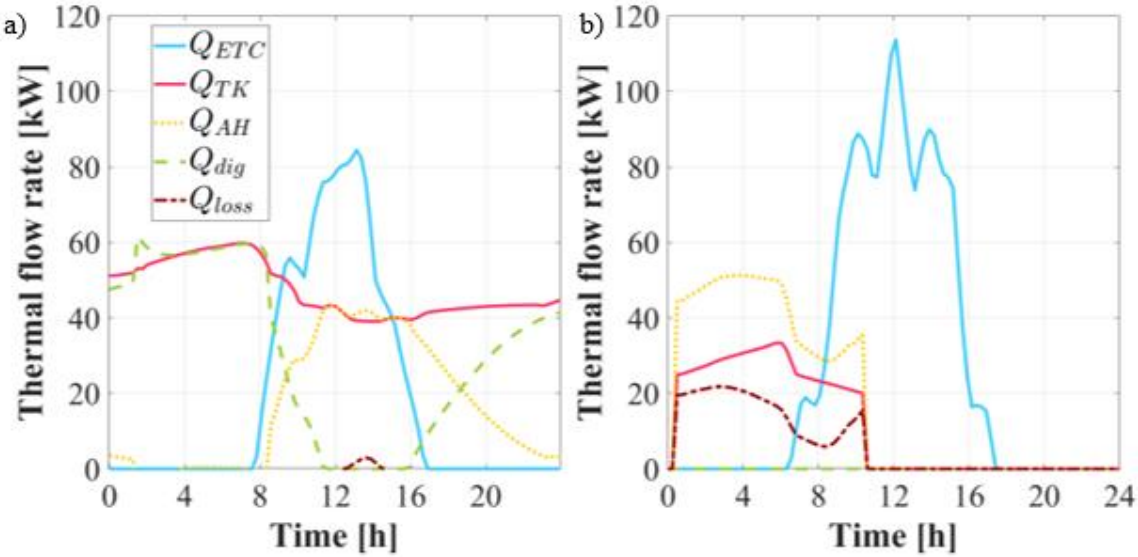

Figure 53. Dynamic results for thermal flow rates in typical winter day (a) and typical summer day (b).

The digester heat demand (Q_{dig}) mainly depends on the ambient temperature, which determines the heat loss toward the environment. Therefore, solar thermal systems are ineffective in reducing GHG emissions, especially during the summer period, in absence of a proper storage.

In fact, during the winter period the tank provides heat constantly during the day, see Figure 53 (a), with small oscillations. Conversely, in summer period, Figure 53(b), the heat collected is sufficient to meet the thermal energy demand being activated until 11 AM. ETCs provide greater heat production during the summer, when the heat demand of the digester is low. In fact, during the summer, the auxiliary heater is rarely turned on, and some heat dissipation is required during the hottest hours. In this period, the collector temperature rises almost up to 70°C, keeping the T_{tank} at its set point of 60°C (Figure 54(b)).

Conversely, the AH is often activated during the winter. In fact, in the winter period, the collector temperature (T_{coll}) and tank top temperature (T_{tank}) are constantly lower than 50°C (Figure 54(a)). The trend of the collector temperature is perfectly matched with the pattern of the thermal energy provided by the ETC field. During the winter, the auxiliary heater is averagely turned off only from 12 PM to 4 PM.

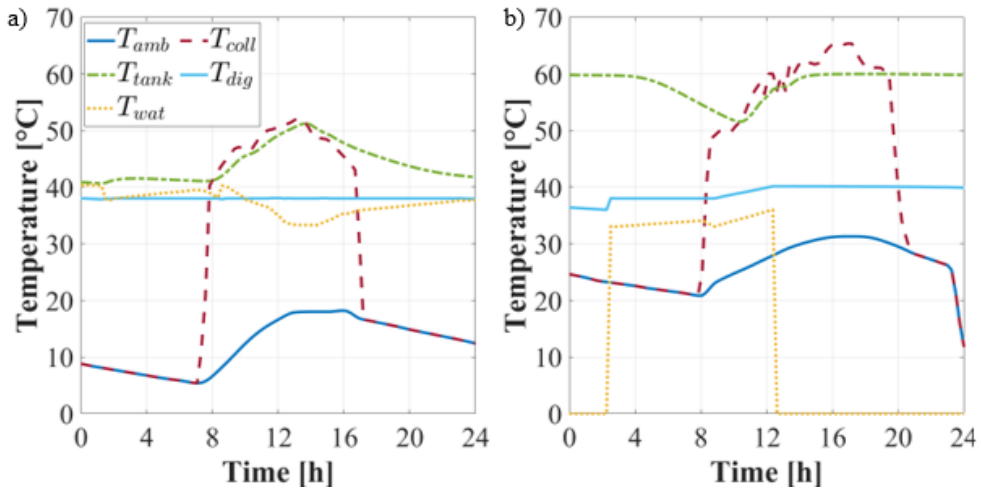

Figure 54. Temperature data for a typical winter day (a) and a typical summer day (b).

Figure 55 shows the dynamic results in terms of power flows for a typical summer (a) and winter (b) day. The power load of the plant ($P_{el,LOAD}$) is almost constant and equal to 120 kW, since the upgrading unit accounts for the major share of power demand and operates at full load for almost for the whole day.

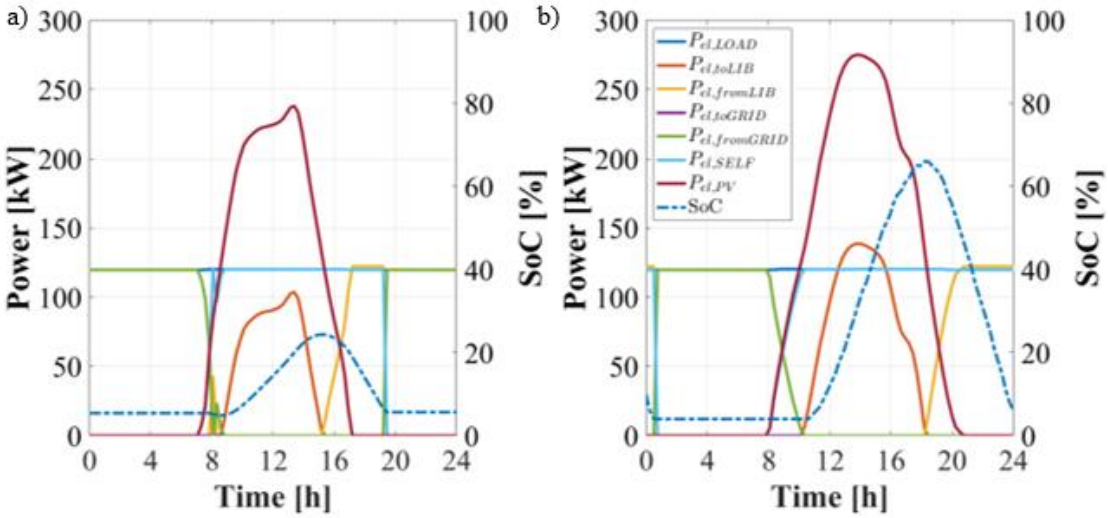

Figure 55. Dynamic results for electric powers in typical winter day (a) and typical summer day (b).

In winter, the power produced by PV ($P_{el,PV}$) matches the plant power demand only during the hours of high solar radiation, roughly from 10 AM to 3 PM, see Figure 55(a). Consequently, during the remaining hours of the day, the power demand of the plant is matched by the energy withdrawn from the public grid ($P_{el,fromGRID}$) and from the battery, ($P_{el,fromLIB}$).

For the typical summer day considered in Figure 55(b), the PV peak power production ($P_{el,PV}$ 238 kW) is such that the plant is not able to exploit the charge-discharge depth of the battery, being the maximum *SoC* roughly equal to 25%. However, the LIB allows the system to be self-sufficient for about 3 hours after the PV power drops below the load. In the summer, the *SoC* rises up to 70%. Because of the higher PV production, auxiliary power is withdrawn from the grid only during the night hours. In fact, the PV, coupled to the LIB, is able to match the load for 16 hours in a row.

In Figure 56(a), the monthly thermal energies are shown, to assess the effectiveness of integrating the ETCs into the biomethane plant. As expected, the major production of thermal energy from the ETC ($E_{t,ETC}$) field occurs in the summer; the maximum monthly production is equal to 18.6 MWh (August). In the same season, the thermal energy required from the digester ($E_{t,dig}$) is obviously minimum (14.25 MWh). In fact, the thermal demand of the AD consists of two main terms: i) the thermal losses to the environment, and ii) the thermal energy required for heating the waste entering the digester. Of course, the higher the ambient temperature, the lower these two terms.

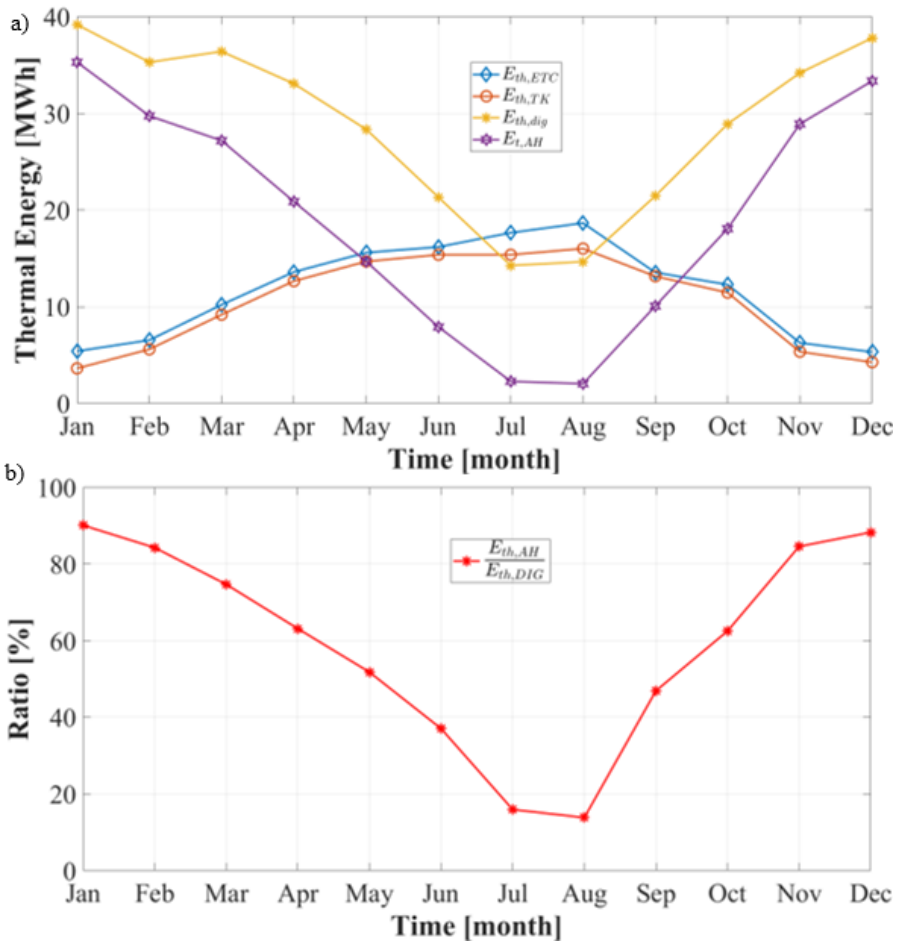

Figure 56. Monthly thermal energy (a) and AH/DIG thermal ratio (b).

The ratio of the thermal energy supplied form the auxiliary heater to the total heat demand of the digester is shown in the lower part of Figure 56(b). It is clear that the ETC system is more efficient during the summer. However, the AH integration is always nonzero, even in the summer, since the tank is not able to store all the thermal energy produced by ETC. Therefore, the tank is not able to match the digester thermal energy demand during the night-time . Figure 57(a) shows the monthly results for the electric energy flows.

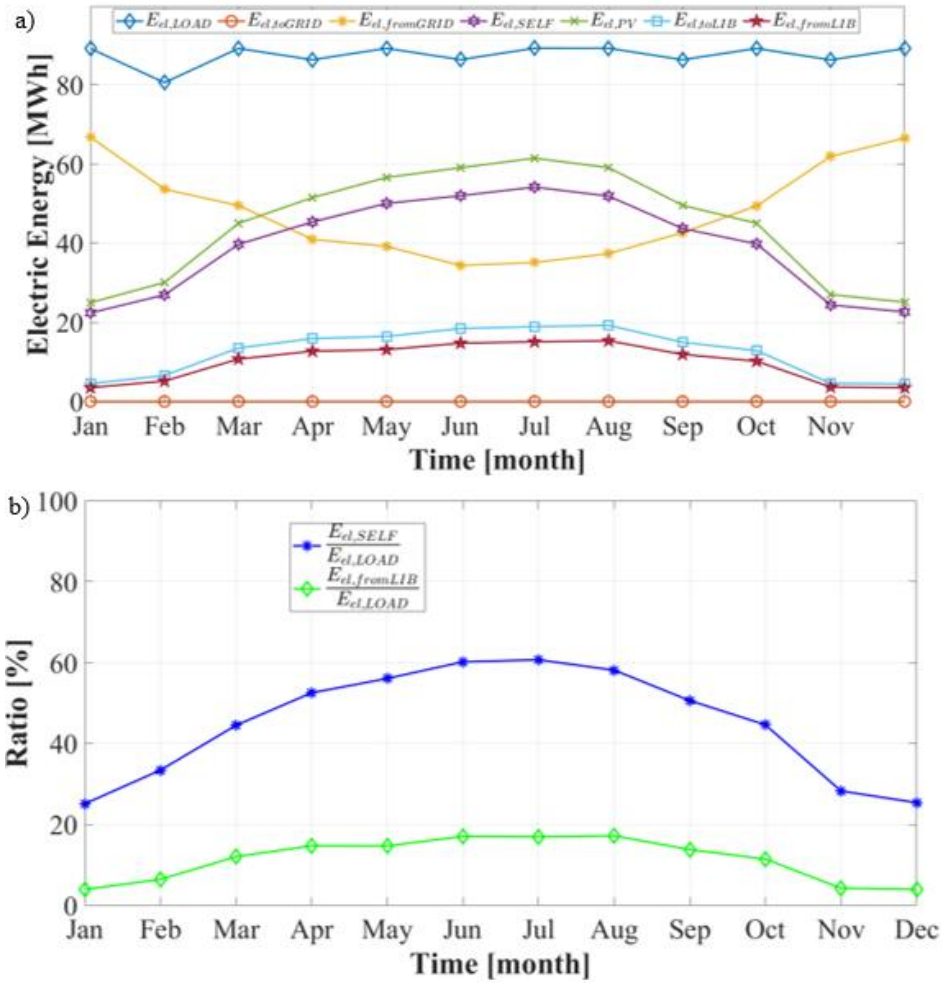

Figure 57. Monthly electric energy (a) and electric energy ratios (b).

The electricity exported to the grid is always null, thanks to the sizing of the LIB. The power demand of the plant is mainly due to the upgrading unit, which operates at full load during the whole year; therefore, the overall monthly consumption ($E_{el,LOAD}$) is almost constant during the year, with an average value of 87.5 MWh. The maximum value reached by the PV production is 61 MWh (July). The electricity withdrawn from the grid is remarkable, but the contribution of solar energy is significant. In fact, the ratio between the self-consumed electricity and the total load ($E_{el,SELF}/E_{el,LOAD}$) ranges from 23% (in winter) to 60% (in summer), see Figure 57(b). This is also due to the presence of the LIB, which can meet up to almost 20% of the $E_{el,LOAD}$.

These results suggest that a greater PV capacity should be considered, to meet a larger share of the electric energy demand of the plant, better exploiting the battery charge-discharge depth. However, a too large PV field may introduce issues related with the area available for installing the modules.

The yearly results are summarized in Table 21 and Table 22.

Table 21. Annual results: fuel consumption.

Parameter	Description	Value	Unit
$V_{bioCH4,r}$	Annual volume of biomethane required by the fleet of bus	333282.19	Sm^3/y
$V_{bioCH4,p}$	Annual volume of biomethane produced by the digester	651080.53	Sm^3/y
$V_{bioCH4,s}$	Annual volume of surplus biomethane	317798.33	Sm^3/y
$V_{diesel,r}$	Annual volume of diesel required by the fleet of bus	678900.00	L/y

Table 22. Annual results: primary energy, CO_2, and costs.

Parameter	Description	Value		Unit
		RS	PS	
PE_{diesel}	Primary energy consumed by diesel vehicles	6789.00	-	MWh/year
PE_{grid}	Primary energy consumed by withdrawn from gird	-	577.37	MWh/year
PE_{AH}	Primary energy consumed by the auxiliary heater	-	-	MWh/year
$PE_{bioCH4,s}$	Primary energy saved by selling biomethane surplus	-	3565.20	MWh/year
$M_{CO2,diesel}$	CO_2 emissions produced by diesel fuelled vehicles	2288.55	-	tons/year
$M_{CO2,grid}$	CO_2 emissions produced by withdrawn from grid	-	278.86	tons/year
$M_{CO2,AH}$	CO_2 emissions produced by the auxiliary heater	-	47.21	tons/year
$M_{CO2,bioCH4,s}$	CO_2 emissions saved by selling biomethane surplus	-	713.04	tons/year
F_{diesel}	Annual cost of diesel	856.37	-	k€/year
F_{grid}	Annual cost of electric energy withdrawn from grid	-	103.93	k€/year
F_{wc}	Annual cost of woodchip	-	3.93	k€/year
F_{bioCH4}	Annual economic return from surplus biomethane	-	544.88	k€/year
M	Total maintenance costs for the plant	-	131.28	k€/year
PE_{tot}	Total primary energy consumed by the system	6789.00	-1792.19	MWh/year
M_{tot}	Total CO_2 emissions produced by the system	2288.55	-283.39	tons/year
F_{tot}	Yearly operating cost of the system	856.37	-696.51	k€/year

Table 8 shows that the total amount of primary energy, produced CO_2 and operating costs for the proposed system have negative values, due to the savings in terms of avoided use of diesel for the buses, but also to the surplus biomethane exported to the gas grid. These results highlight the feasibility of the proposed solution. Table 23 shows the main performance indexes obtained from the yearly analysis.

Table 23. Yearly performance indexes.

Parameter	Description	Value	Unit
ΔPE	Annual primary energy difference	8587.11	MWh/year
ΔCO_2	Total amount of CO_2 savings	2573.25	tons/year
ΔOC	Difference of total yearly operating costs	1.96	M€/year
PES	Primary Energy Saving	126	%
INV_{ETC}	ETC capital cost	0.06	M€
INV_{PV}	PV capital cost	0.72	M€
INV_{DIG}	Digester capital cost	12.50	M€
INV_{AH}	Auxiliary heater capital cost	0.009	M€
INV_{TOT}	Total capital cost	13.28	M€
SPB	Simple Payback period	11.40	years
DPB	Discounted Payback period	16.37	years

NPV	Net Present Value	3.03	M€
PI	Profitability Index	0.23	-
CIC	Incentives	0.79	M€
***SPB*$_{CIC}$**	Simple Payback period with incentives	6.82	years
***DPB*$_{CIC}$**	Discounted Payback period with incentives	8.51	years
***NPV*$_{CIC}$**	Net Present Value with incentives	14.13	M€
***PI*$_{CIC}$**	Profitability Index with incentives	1.06	-

An overall *PES* equal to 1.26 was calculated, with a 112 % reduction of CO_2 equivalent emissions Unfortunately, the overall capital cost of the plant is extremely relevant (INV_{TOT} = 13.28 M€), mainly due to the digester, involving a low profitability, in spite of high economic savings. A *SPB* of 11 years was calculated and a *DPB* of 16 years, leading to a *NPV* of 3.2 M€/year and a *PI* of 0.23. However, considering the incentives for the production of advanced biomethane, the economic indexes improve remarkably (*SPB* = 6.8 years, *DPB* = 8.5 years, *NPV* = 14.13 M€/year, *PI* = 1.06).

For brevity, this section does not include the sensitivity analysis, which explores more results under various price ranges for Diesel, natural gas, and electricity, as well as the parametric analysis concerning the sizes of the system main components. Readers interested in these details can refer to them in ref. [129]. Nonetheless, the key findings from these analyses are discussed comprehensively in Section 5.1.5.

5.2 Dynamic analysis and investigation of the thermal transient effects in a continuously stirred tank reactor producing biogas

While the literature features numerous studies on biological models for biogas production [132], there is a notable scarcity of research addressing the issue of providing to the digester the thermal energy required to maintain the desired temperature in the digester. Previous studies have indeed conducted thermal balances to analyze the heat exchange between the digester and its environment, and some have even integrated heat balance equations with solar thermal modules to meet the energy requirements. However, there appears to be a gap of research that simultaneously address thermal transient phenomena and biological processes within the digester. Furthermore, no existing study, to our knowledge, combines such a detailed transient thermal model with integration of solar thermal collectors.

In this work, a transient thermal model that describes the heat transfer between the water flow in the heat exchanger tubes and the biomass within the digester is proposed, integrated with the digester biological model. Therefore, with respect to

the previous study the thermal model now considers the thermal transient due to the thermal inertia of the biomass. Furthermore, a Concentrated Photovoltaic Thermal (CPVT) field is considered to partially meet the thermal and energy demand. MATLAB® simulations reveal that internal thermal transients in the reactor impact microbial growth, leading to a delayed biogas production. These dynamic analysis results are invaluable for understanding the compatibility of the CPVT solution with both the digester's requirements and the energy needs of the upgrading unit.

5.2.1 System Layout

The digester modelled in MATLAB® is combined with a case study simulated in TRNSYS, where the energy demand of the end user and a CPVT field are implemented for dynamically assessing the energy performance of the proposed plant based on renewables . The layout of the proposed system is shown in Figure 58.

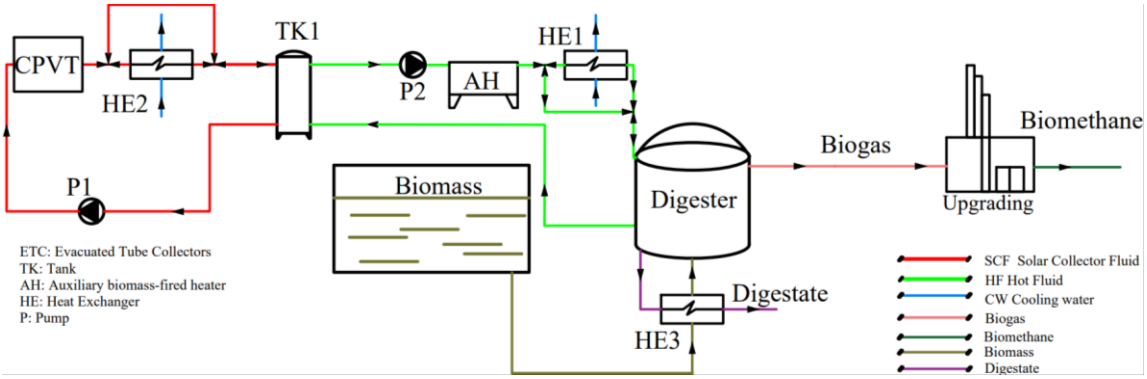

Figure 58. Layout of the proposed biomethane hybrid plant.

The discussion of the layout is the same provided for the previous work, with the only difference that the CPVT field is also providing electricity to the units of the system, without the contribution of the PV field. The thermal control strategy is the same applied to the STC field.

5.2.2 System Model

The digester considered in this work is the same CSTR previously described inside which the OFMSW is converted into biogas, by means of the biological process of Anaerobic Digestion (AD). The anaerobic digestion model No. 1 (ADM1) is the one already described in section 5.1.2, therefore is here omitted for the sake of brevity.

The thermal model considered here includes two thermal balances for the two main components, namely the digester and the heat exchanger. In the former development the heat balance was performed using the logarithmic mean temperature method. Furthermore, this previous model assumes the steady state conditions. Consequently,

both the thermal inertia of the digester and the temperature transient due to the heat transfer between the heat exchanger tubes and the biomass were not considered. The model proposed here removes the steady state assumption, considering the transient phenomena in terms of mass and energy. The thermal balance on the digester control volume can be written as:

$$\dot{m}_{OFMSW}C_{p,OFMSW}T_{in,OFMSW} + \dot{m}_{w}C_{p,w}T_{in,w} - \dot{m}_{dig}C_{p,dig}T_{react} - \dot{m}_{biogas}C_{p,biogas}T_{react} - \dot{m}_{w}C_{p,w}T_{out,w} - \dot{Q}_{loss} = \rho_{OFMSW}V_{OFMSW}C_{p,OFMSW}\frac{dT_{react}}{d\vartheta} \quad (55)$$

In this equation, the first two positive terms on the left side are the inlet enthalpy flows due, respectively, to the inlet OFMSW flow rate and the water flow rate, while the negative terms are the outlet thermal flows due to: i) the outgoing digestate flow rate, and ii) the biogas flow rate, which are assumed to be at the same temperature of the reactor; iii) the output water flow rate; iv) heat losses toward the environment. These terms, at any time, must be equal to the variation rate of the internal energy of the reactor content, assumed as control volume. The term on the right refers only to the volume of the biomass because the density of the biogas is much lower than that of the biomass and therefore its term is negligible in the thermal balance. In this case, ϑ is the time.

The equation is a first-order ODE so only one initial condition is required to solve the problem, that is the temperature of the reactor at $\vartheta = 0$, which is supposed to be equal to the ambient temperature. The thermal balance on the heat exchanger is based on the ε-NTU method, where ε is the effectiveness of the heat exchanger and NTU is the Number of Thermal Units, calculated by means of the well-known equation:

$$NTU = \frac{UA}{\dot{C}_{min}} \quad (56)$$

U is the global heat transfer coefficient of the heat exchanger and A is the total heat exchange area. $\dot{C}_{min}$ is the lower heat capacity rate between the biomass one and the water one. Here, the heat capacity rate of the biomass is supposed to be much higher than the water one. This assumption is based on the fact that the thermal capacity of the OFMSW involved in the heat exchange process is significantly higher than the one of water. The biomass in the CSTR reactor is considered as fully mixed with stationary behavior due to the slow motion of the mass in random directions. In this case the ratio:

$$\omega = \frac{\dot{C}min}{\dot{C}max} \quad (57)$$

is approximately zero. Therefore, the effectiveness of the heat exchange can be calculated with the general analytic form for the heat exchangers $\varepsilon = 1\text{-}e^{(-NTU)}$. The energy balance on the heat exchanger is:

$$\dot{C}_w(T_{w,in} - T_{w,out}) = \varepsilon \dot{C}_{min}(T_{w,in} - T_{react}) \quad (58)$$

Where the heat capacities are equal in this case. This model allows one to calculate the output temperature water $T_{w,out}$, with a lower calculation time with respect to the logarithmic mean temperature method. Values of the main parameters used are shown in Table 24.

Table 24. Main parameters used in the thermoeconomic model.

Parameter	Description	Value	Unit
N_{CPVT}	Number of CPVT collectors	4	-
Au_{CPVT}	Unit area of CPVT collectors	12	m^2
$\eta_{el,CPVT}$	CPVT electric efficiency	0.205	-
$\eta_{t,CPVT}$	CPVT thermal efficiency	0.529	-
$A_{CPVT,TOT}$	Total area of CPVT collectors	48	m^2
V_{TK1}	Specific volume of the tank	50	l/m^2
$V_{TK1,TOT}$	Tank volume	2.2	m^3
$T_{set,CPVT}$	Set point temperature of the CPVT collectors	80	°C
$T_{set,HE1}$	Set point temperature of the HE1	55	°C
$T_{set,HE2}$	Set point temperature of the HE2	60	°C
$T_{set,dig}$	Set point temperature of the digester	38	°C
m_{OFMSW}	OFMSW inlet flow rate	626.4	kg/h
$x_{CH4,biogas}$	Volumetric fraction of methane in biogas flow rate	50	%
η_{CH4}	Methane recovery	98.3	%
$x_{CH4,biometh}$	Biomethane purity at the end of the upgrading process	95	%

The digester operating temperature is set at 38°C. This value is selected according to the works available in literature suggesting the mesophilic conditions as the optimal ones for AD process. Several conditions must be considered during the process and this temperature level is also considered as optimal for several input biomasses. This selection is also forced by the need to compare the present results with the ones presented in the previous work, considering this specific value of digester set point temperature. Nevertheless, an optimization could be also performed in order to calculate a time-dependent optimal value of the digester operating temperature. This optimal value should be a trade-off between digester thermal losses and biogas production rate. The thermoeconomic model is omitted since it is developed according to the previous work.

5.2.3 Case Study

The system proposed in this paper includes a CSTR digester coupled to a CPVT field for the request of electricity and thermal energy and an auxiliary heater in case of low solar radiation. The system is expected to be installed in the suburbs of Naples, a city in Southern Italy, and the biogas produced is converted into biomethane for road transport. Details of the design parameters can be found in ref. [132].

5.2.4 Results

This section shows the results of the analysis of the thermal transient of the digester, the simulations and the results carried out in TRNSYS are omitted for the sake of brevity.

Figure 59 shows the trend of temperatures provided by the thermal transient simulation. The ambient temperature T_{amb} is set as a constant input to the model, as well as the inlet water temperature $T_{w,in}$. These values are set as constant in the MATLAB® simulation since the interest is to verify the thermal transient behaviour for some given boundary and initial conditions.

As expected, both the reactor temperature T_{react} and the outlet water temperature $T_{w,out}$ show the typical temperature slope due to the initial transient. At steady state condition, the water temperature difference is below 10 °C. This trend is consistent with the design specifications for this kind of component. At the same time, at steady condition, the water outlet temperature is about 5 °C higher than the reactor one. Once again, this result is in accordance with the common practice.

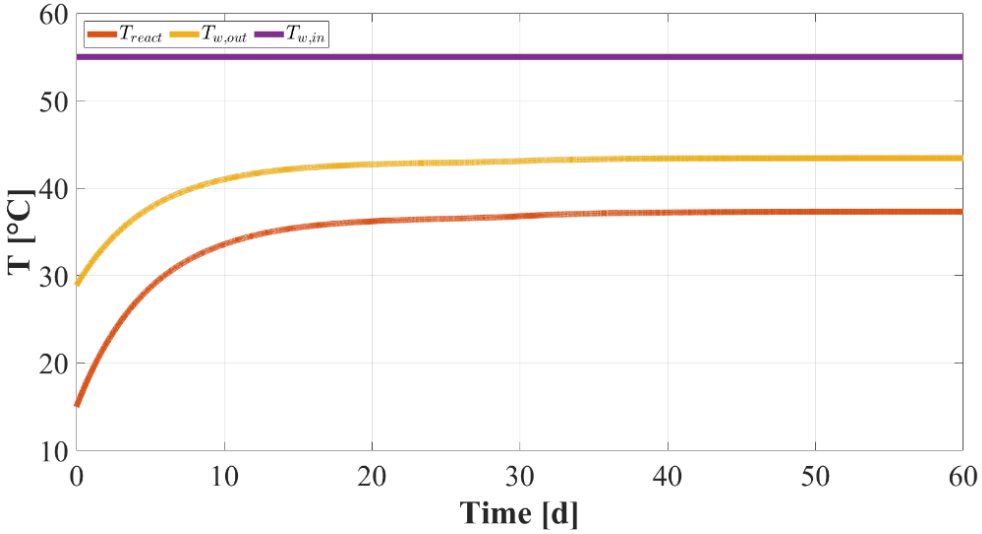

Figure 59. Dynamic pattern of the main temperature involved in the process.

Figure 60 shows the different results obtained in terms of flow rates. Such graph presents a comparison between the production of biogas, and CO_2 and CH_4 fractions,

considering or neglecting the thermal transient. In both cases, the models of biological processes include time-dependent terms.

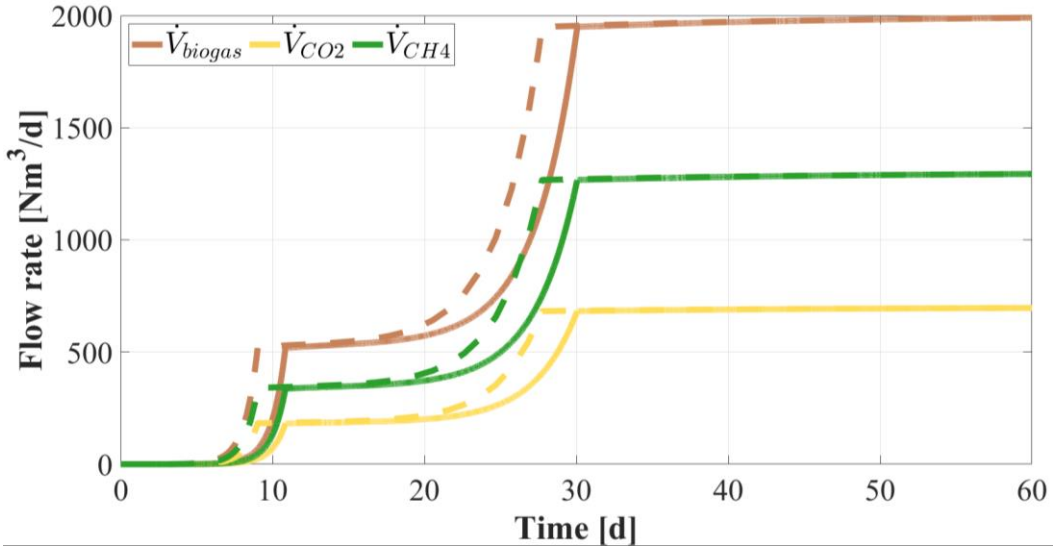

Figure 60. Biogas volumetric flow rate calculated neglecting (dashed line) and considering (continuous line) the thermal transient effect.

This comparison clearly shows that the model including thermal transient provides a more detailed evaluation of the time-dependent biogas production. In fact, the reaction rates of the biochemical species strongly depend on the temperature of the reactions. This parameter is not accurately estimated when the thermal inertia of the biomass is neglected, affecting in turn the estimation of the biogas production. Therefore, the time-dependent biological model is not sufficient to predict in detail the biogas yield. This model must be mandatorily coupled with a transient heat transfer model in order to achieve more detailed results.

The analysis without the thermal transient shows that the first exponential growth of biogas production is completed within 8 days, while the thermal transient analysis shows that this growth starts later and ends in about 12 days. The total production of biogas is not affected by the transient temperatures and the maximum biogas flow rate for the proposed digester is in any case equal to roughly 2000 Nm^3/day. This is due to the fact that the AD model includes the time-dependent terms in the differential equation.

Thus, it considers the dynamic evolution of the biochemical species. This model is based on a system of differential equations which considers the reaction kinetics of all the species of interest. However, these terms depend on the temperature of the reactor which is obviously below the set point of 38 °C in the first operating days. This difference leads to a time delay of the kinetic rates growth and so of the biogas production.

The reason why the trend of biogas production shows a double exponential growth is due to the different microbial families that operate in the production of biogas. In fact, after the first phases of hydrolysis and acidogenesis, two complementary and concurrent processes lead to the formation of methane. The first process is the hydrogenotrophic methanogenesis which occurs from the reduction of CO_2 due to the presence of H_2. The second process takes place later, because it requires a preliminary phase which is the acetogenesis, that is the production of acetate from volatile fatty acids (VFA).

Then, acetoclastic methanogenesis becomes the predominant process during which the anaerobic degradation of acetate produces methane. Figure 61 shows the trend of the hydrogen and acetate concentrations for the carried out transient analysis. Figure 61 proves why the acetoclastic methanogenesis process is predominant over the hydrogenotrophic one. In fact, the hydrogen concentration in this case study reaches a maximum at about 10^{-5} kgCOD/m^3 while the acetate concentration stabilizes at over 100 kgCOD/m^3. In particular, the specific combinations of these steps is due to the different acidity of the environment in which the different species grow. Furthermore, it is well known that the acetoclastic methanogenesis is by far predominant with respect to the hydrogenotrophic one when the AD process occurs at mesophilic or thermophilic conditions.

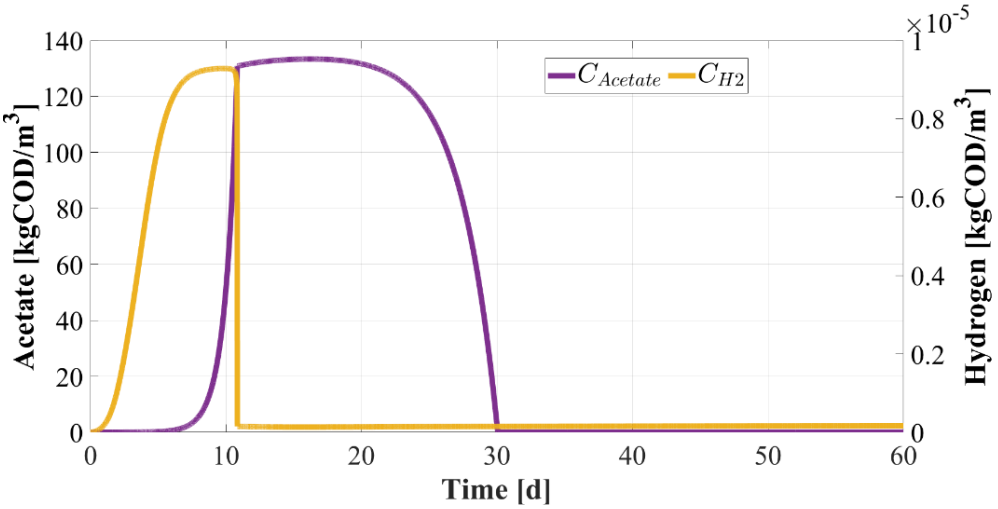

Figure 61. Dynamic evolution of acetoclastic and hydrogenotrophic methanogenesis phases.

For the sake of completeness, the thermal flow rates involved in the transient simulation are shown in Figure 62. In particular, $Q_{exchanged}$ refers to the heat delivered to the digester by means of the water heat exchanger. Q_{loss} is the sum of all the thermal losses due to the heat transfer to the environment and to the ground together with the total outgoing enthalpy flow. In particular, this includes the thermal energy outgoing flow related to the biogas and digestate mass flows. The biogas leaves the digester at the temperature of the digester, collecting into the dome. The digestate

leaves the digester at a temperature equal to the one of the digester, whereas the preheated waste enters at a lower temperature with respect to the digester. At the equilibrium point, $Q_{exchanged}$ and Q_{loss} reach the same constant value, close to 30 kW.

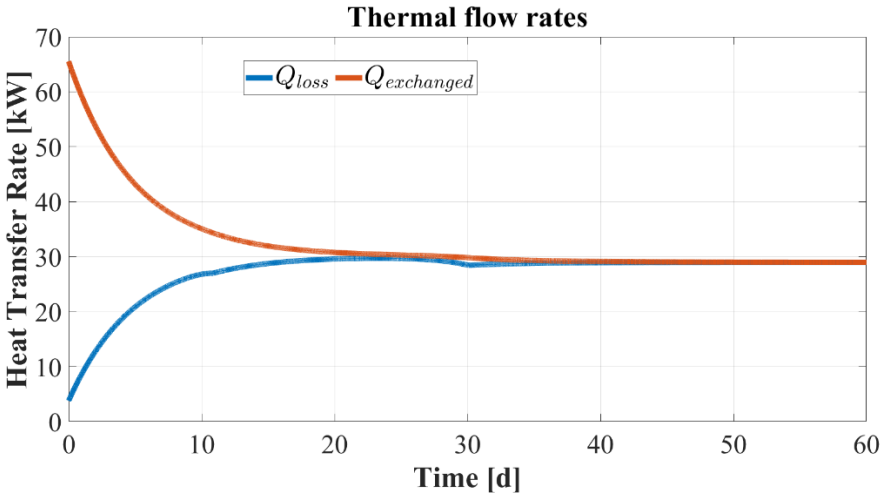

Figure 62. Thermal flow rates on the digester control volume.

The results shown here prove the accuracy of the proposed thermal transient model. Therefore, the digester model developed in MATLAB® is implemented in TRNSYS to evaluate the dynamic performance of the system. The integration of a CPVT field is considered along with the biogas upgrading unit. The model also evaluates the dynamic behaviour of the auxiliary components and shows the correct functioning of the controllers. The following results are provided by the TRNSYS dynamic simulation with the integration of the digester model.

5.3 Thermoeconomic analysis of biomethane production plants: a dynamic approach

This work starts from the necessity of developing a detailed comparative thermo-economic analysis of biogas upgrading technologies operating in dynamic conditions coupled with photovoltaic and electric energy storage system. In particular, the novelties of this work can be listed as follows: i) The development of a comprehensive dynamic simulation model for the renewable biomethane production based on photovoltaic and lithium-ion battery; ii) The coupling of PV panels and a lithium-ion storage system to increase the self-consumed energy and sustainability of the biomethane production; iii) A thermoeconomic comparison of the water scrubbing and membrane separation technologies in order to assess which achieves a more sustainable biomethane production; iv) A detailed analysis in order to assess the optimal capacity mix of the considered technologies, i.e. PV capacity, battery capacity, water scrubber operating pressure, membrane separation operating

pressure and membrane separation number of stages, for detecting the optimal layout.

5.3.1 System Layout

The proposed plant aims at integrating renewable sources of energy, i.e. a photovoltaic field, into a biogas upgrading plant. Three layouts are studied and compared in this work. These layouts differ only for the biogas upgrading theconology, namely water scrubbing, 2 stage membrane separation and 3 stage membrane separation.

The electricity produced by the PV field is used for matching the electric energy demand of the biogas upgraing plant, consitsting of the biogas upgrading unit and its auxiliary components. This plant is also equipped with an electric energy storage system, that contists of a lithium-ion battery (LIB).

In case of scarce or null solar production, the electric energy is firstly withdrawn from the LIB. Note that the battery discharge is allowed only if the battery state of charge (SoC) ranges from 5 % to 90 %. Conversely, in case of solar production higher than plant energy demand, the surplus electric production is delivered to the LIB, until its SoC reaches the maximum allowed value of 90 %. When the battery SoC is higher than the upper treshold, i.e. SoC = 90 %, the electric energy is delivered to the grid. The electric energy storage is used both to increase the energy self-sufficiency of the system proposed and to shave the peaks of electricity injection into the grid during the most irradiated periods.

In the plants proposed, the biogas flow rate provided to the upgrading unit is assumed to be constant, thanks to a tank buffer at the downstream of the anaerobic digester. This solution is commonly applied in the design of biogas upgrading plants. In fact, such approach is able to avoid sharp variations of the biogas flow rate that may worsen the performance and the security of the plant.

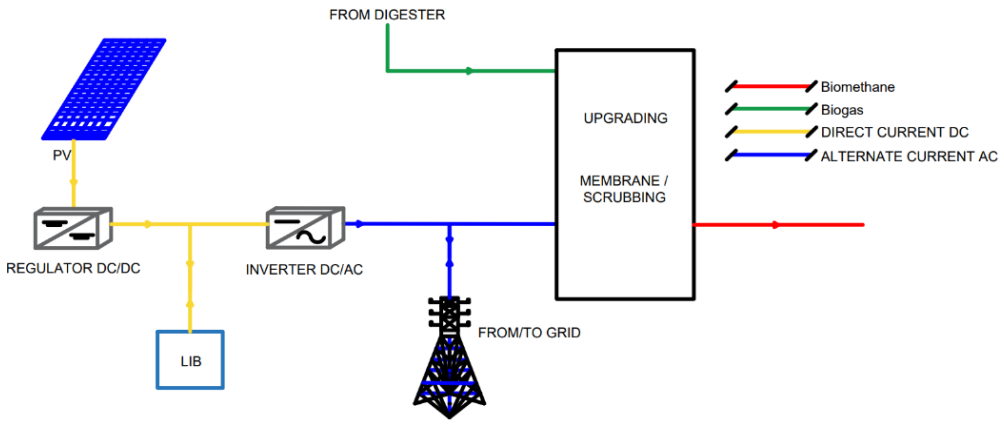

Figure 63. Layout of the studied renewable driven biogas upgrading plant.

5.3.2 System Model

Regarding the membrane separation (MS) biogas upgrading thecnology, compressors and membranes play a crucial role. The components of the systems are:

- Compressors, which compress the inlet gas to the rated operating pressure, providing the driving force for the whole process
- Spiral wound membrane modules, where the separation between CO_2 and CH_4 occurs.

Several configurations may be developed considering a variable number of membranes and compressors. As mentioned before, this work addresses two stage MS and three stage MS. An example of a layout of a three-stage MS biogas upgrading unit is shown in Figure *64*.

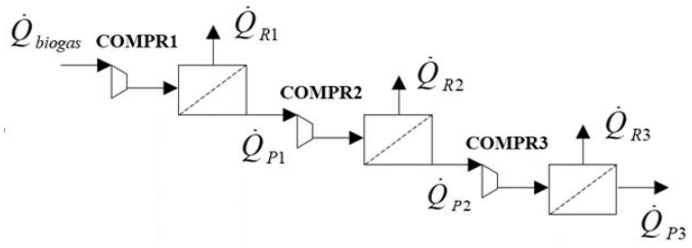

Figure 64. Three stage membrane separation upgrading system configuration.

The model used for the simulation of the membrane system is based on the principle that a gaseous mixture can be fractionated as a function of the different permeability of its components in polymeric films membranes. In particular, when the compressed gas is supplied to a module, the pressure difference across the membrane generates a permeate, rich in permeable compound (i.e. CO_2), and a residual flow, defined as retentate, rich in non permeable components, i.e. CH_4. Further details of this model are discussed in reference [133]. The presented model also includes the assessment of the CH_4 recovery η_{CH4} and the average composition of the permeate y_{ave}:

$$\eta_{CH4} = (1-\theta)\frac{1-x_R}{1-x_F} \tag{59}$$

$$y_{ave} = \frac{x_F - (1-\theta)x_R}{\theta} \tag{60}$$

where θ is the permeated supply fraction

The simplified layout of the plant related to the pressure water scrubbing technology is represented in Figure 65. The system consists of the following components:

- Absorption column (scrubber): a tower where the biogas and water are fed in counter flow arrangement.

- Compressors: a first compressor is used to increase the pressure of the biogas entering the column; a second compressor is used to increase the pressure of the outlet biomethane up to the low pressure network, about 7 bar.
- Pump: a circulation pump is needed for the water supplying the top of the scrubber at the operating pressure.
- Cooler: it cools down the outlet gas exiting from the compressor. In fact, due to the pressure increase the gas temperature increases, decreasing its solubility. Therefore, a cooling process is needed to control the gas outlet temperature.
- Filter: this device filters the impurities in the water entering the scrubber.
- Dryer: it removes water from the biomethane gas mixture in order to avoid any reduction of its heating value.

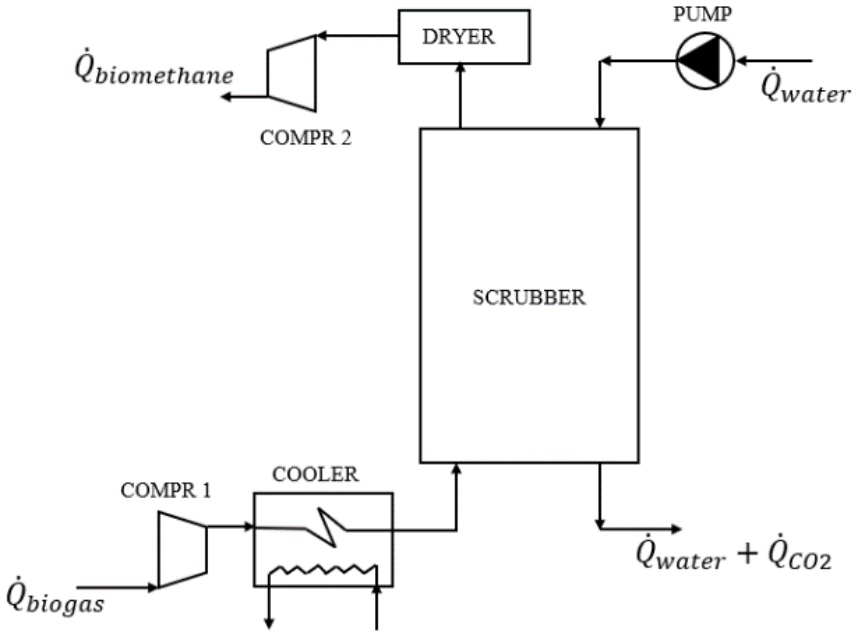

Figure 65. Water scrubbing plant configuration.

The model is derived by the algorithm provided by Ref. [134], which was validated against experimental results (i.e. data available in Ref. [135]). The simulation model of the water scrubber technology allows one to evaluate the performance of the system according to the one-dimensional mass balances of the species involved for an element of the column of infinitesimal height, in both the liquid and gaseous phases.

$$\frac{dx_{CO_2,G}}{dz} = \frac{-\tau_{CO_2}(1-x_{CO_2,G}) + \tau_{CH_4} x_{CO_2,G}}{Q_G}$$

$$\frac{dx_{CH_4,G}}{dz} = \frac{-\tau_{CH_4}(1-x_{CH_4,G}) + \tau_{CO_2} x_{CH_4,G}}{Q_G}$$

$$\frac{dx_{CO_2,L}}{dz} = \frac{-\tau_{CO_2}(1-x_{CO_2,L}) + \tau_{CH_4} x_{CO_2,L}}{Q_L} \quad (61)$$

$$\frac{dx_{CH_4,L}}{dz} = \frac{-\tau_{CH_4}(1-x_{CH_4,L}) + \tau_{CO_2} x_{CH_4,L}}{Q_L}$$

The partial pressure of each gas in the gaseous phase is assumed to be directly derived from its mole fraction, which is related to the mass fraction according to the Raoult Law. Boundary conditions and assumptions of the model are furtherly discussed in Ref. [134] where all the packing characteristics are explained. Furthermore, the most widely used semi-empirical correlations for the calculation of the Henry coefficients, Diffusive coefficients, Equilibrium constants, and Mass Transfer parameters are shown. The system of equation (57) was implemented in MatLab environment and using *ode15s* solver specifying the initial conditions, i.e. the mass fractions of CO_2 and CH_4 in the inlet gas and in the outlet liquid from the scrubber, and the integration interval, i.e. from the basis to the top of the scrubber. The calculation procedure involves iterating the integration interval, i.e. the height of the scrubber, until the desired outlet conditions are reached. The models of the auxiliary units are reported in ref. [132], here omitted for the sake of brevity.

The model includes the assessment of the capital cost of the upgrading unit and auxiliaries as well as the operating costs due to the maintenance and replacement of components and electric energy consumption. The revenues due to the sale of the biomethane produced are evaluated according to the Italian feed-in tariff policies. The capital cost of the scrubber system is a function of the treated biogas volumetric flow rate. Considering a specific cost of 5'400 €/Nm³/h, the total capital cost $I_{scrubber}$ is 427.50 k€. The capital cost of PV panels and electric energy storage system are equal to 1000 €/kW and 200 €/kWh, respectively. For the membrane system, the total capital cost $I_{membrane}$ considers the cost of pumps, compressors and the membranes area A. The membranes area A depends on the compression ratio of the various stages and the specific cost per m² of the selected membrane. A polymide membrane is selected, featured by a specific cost $c_{membrane}$ of 50 €/m² . The designed area considers that the outlet biomethane only includes CO_2 at 2 % and considering the inlet biogas flow rate F_{feed} (Nm³/s), the pressure difference ΔP (Pa) between the inlet and outlet sections of the mebrane and the average permeability of the biogas Q_{av} (GPU, gas permeance

unit) (weighted according to the fractions of biogas components $x_{i,feed}$ and the related permeability Q_i)[136]. The equation for the calculation of the membrane area cost is reported as follows :

$$c_{membrane} A_{membrane} = c_{membrane} \frac{F_{feed}}{7.501 \times 10^{-12} \cdot \Delta P \cdot Q_{av}} = c_{membrane} \frac{F_{feed}}{7.501 \times 10^{-12} \cdot \Delta P \cdot \sum_{i=1}^{Cn} Q_i x_{i,feed} / \sum_{i=1}^{Cn} Q_i} \quad (62)$$

The pumps and the compressors are selected according to the pressure drop and the flow rate of biogas. Therefore, these devices are selected from the "Fini" and "Salmson" data sheed and price lists [137]. The maintenance cost of the scrubber system is assumed equal to 9 % of the total capital cost $I_{scrubber}$, whereas for the membrane systems, the membrane replacement cost (*MRC*) is considered according to a yearly replacement rate (ν), equal to 0.25, and a membrane replacement price (K_{mr}) equal to 25 €/m^2 :

$$MRC = \sum_s A_{membrane,s} \nu K_{mr} \quad (63)$$

The yearly maintenance costs of pumps and compressors are assumed to be 1% of the capital cost. The selling price of the biomethane produced is calculated considering a selling price ranging from 0.25 – 0.70 €/Sm^3. In addition, energy saving certificates for biomethane production are considered, as for the previous work. *NPV* index is evaluated considering a lifetime of 10 years and a discount factor of 5%. The yearly maintenance cost of the CHP is equal to 2% of the capital cost (357.5 k€/y).

It is assumed a selling price for the produced thermal energy equal to 0.05 €/kWh, however three reference scenarios are evaluated considering different fractions of recovered thermal energy with respect to the total produced thermal energy, i.e. 0 %, 50 % and 100 %. To consider this variation of the thermal recovery from the cogenerator, a sensitivity analysis is carried out, varying the thermal fraction as follows:

$$E_{th,CHP} = \alpha \cdot E_{th,CHP,max} \quad (64)$$

The selling price of the electric energy produced by the CHP is considered variable from 0.06 to 0.17 €/kWh, as well as the selling price of the biomethane in proposed systems from 0.20 to 0.40 €/Sm^3, in order to estimate the economic feasibility of the

proposed systems according to several feed-in tariff policies. Table 25 shows all the parameters adopted in the thermoeconomic analysis discussed above.

Table 25. Parameters selected for the thermoeconomic analysis.

Parameter	Description	Value	Unit
$\eta_{el,GRID}$	Electric efficiency of the public power grid	0.46	-
$\eta_{th,BOILER}$	Thermal efficiency of the auxiliary heater	0.95	-
$\eta_{el,CHP}$	Rated electric efficiency of the cogenerator	0.43	-
$\eta_{th,CHP}$	Rated thermal efficiency of the cogenerator	0.449	-
LHV_{CH4}	Natural gas lower heating value	9.59	kWh/Sm^3
LHV_{biogas}	Biogas lower heating value	5.86	kWh/Sm^3
j_{th}	Thermal energy selling unit cost	0.05	€/kWh
$j_{el,fromGRID}$	Electric energy purchasing unit cost	0.20	€/kWh
$j_{el,toGRID}$	Electric energy selling unit cost	0.07	€/kWh
C_{PV}	Unit cost of PV modules per peak power	1000	€/kW$_p$
C_{LIB}	Unit cost of lithium-ion battery	200	€/kWh
C_{SCR}	Unit cost of scrubber	5400	€/Nm^3/h
C_{MEM}	Unit cost of membrane	50	€/m^2
MRC	Membrane replacement cost	25	€/m^2
C_{CHP}	Unit cost of cogenerator	1700	€/kW
ESC	Biomethane energy saving certificates	0.609	€/Sm^3

5.3.3 Case Study

As shown in the section 5.3.2, three different biogas upgrading plants are studied and compared. Such plants are coupled with a sewage sludge treatment plant located in Stuttgard (Baden-Wuttemberg, Germany). This plant is equipped with an anaerobic digester producing biogas from sewage sludge. In particular, such plant pruduces rougly 83.46 Sm^3/h of biogas, which consist of 62% of CH_4 and 38% of CO_2. Despite the variability of the biogas flow rate, it is assumed that the investigated upgrading systems are supplied by a fixed flow rate of biogas. This assumption is consistent with the use of a gasometer and a buffer tank included between the digester and the upgrading unit as buffer.

The performances of the proposed layouts, discussed in section 5.3.2, are compared against the current state of the art of biogas power plants, that consists of cogeneration by means of an ICE fed with biogas. The cogenerator has a rated power of 210.3 kW and produces 1'842.25 MWh/year of electric energy and 1'923.65 MWh/year of thermal energy, which are delivered to the electric grid and to local facilities, respectively. Table 26 lists the main design data of the units.

Table 26. Design parameters of the main units of the upgrading plants.

Component	Parameter	Definition	Value	Unit
LIB	C_{cell}	Cell energy capacity	63.27	Ah
	$V_{battery}$	Battery voltage	360	V
	η_{LIB}	Battery efficiency	0.90	-

	SoC_{min}	Minimum allowed State of Charge	5	%
	SoC_{max}	Maximum allowed State of Charge	90	%
	m_{LIB}	Wight of the battery	305	kg
	Vol_{LIB}	Volume of battery	0.13	m^3
PV	P_{max}	Maximum power	260	W_p
	V_{oc}	Open-circuit voltage	37.7	V
	I_{sc}	Short-circuit current	9.01	A
	V_{mpp}	Voltage at point of MPP	30.5	V
	I_{mpp}	Current at point of MPP	8.51	A
	N_s	Number of modules in series	2	-
	N_p	Number of modules in parallel	50	
	A	PV module area	1.6	m^2
	η_{PV}	Module efficiency	18	%
AD	V_{biogas}	Biogas produced by the digester	83.46	Sm^3/h
	$T_{digester}$	Digester Temperature	36.2	°C
	x_{CO2}	Percentage of CO_2 in the biogas mixture	38	%
	x_{CH4}	Percentage of CH_4 in the biogas mixture	62	%
CHP	$P_{el,rated}$	Rated Power	210	kW
	$\eta_{el,CHP}$	Rated electric efficiency of the cogenerator	0.43	-
	$\eta_{th,CHP}$	Rated thermal efficiency of the cogenerator	0.45	-

5.3.4 Results

This section is divided into two subsections. In the first one, the optimal response surfaces for all the considered upgrading plants are evaluated and discussed. In the second one, the optimal layouts are compared against the current state of the art in biogas power plant, i.e. a cogenerator burning biogas for producing thermal energy and electricity. The electricity and the thermal energy produced are exported.

To detect the optimal response surface of the proposed renewable layout based on water scrubbing upgrading technology (water scrubbing plant WSP), the operating pressure of the scrubber (see *System Model* and *System Layout*) is varied from 1.20 bar to 20 bar, the photovoltaic field capacity is varied from 10 kW to 400 kW and the battery capacity is varied from 91 kWh to 569 kWh.

Figure 66 shows the optimal response surface of the objective functions investigated, namely costs (*C*) and primary energy (*PE*). The operating costs are negative because the savings due to the biomethane exporting and energy saving certificates overcome the plant operating costs due to maintenance and electric energy purchasing. *PE* is negative because the primary energy linked to the volume of biomethane exported is significantly higher than the primary energy consumption due to the electricity withdrawn from the grid.

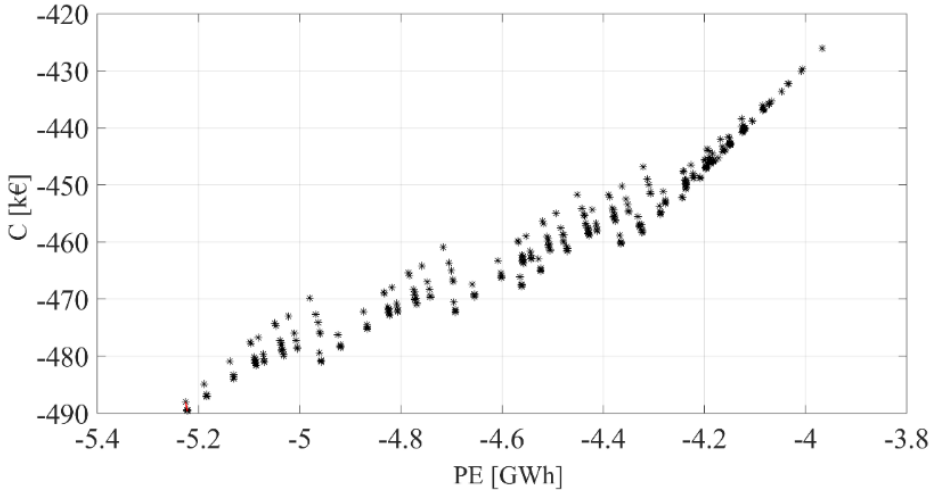

Figure 66. Optimal response surface and Pareto frontier: water scrubbing plant.

The optimal layout achieves a *C* of -488 k€/y and a *PE* of – 5.22 GWh/y, it consists of a rated operative pressure of 1.20 bar, a PV field of a capacity of about 200 kW and a lithium-ion battery of a capacity roughly 182 kWh. In particular, this layout is featured by the lower bound of the operative pressure. In fact, the plant performance worsens as the scrubber operating pressure increases.

This trend is related with the fact that the increase of the scrubber operating pressure leads to a negligible enhancement in biomethane quality (i.e. percentage of CO_2) and a negligible increase of biomethane production. The increase of the operating pressure reduces the height of the scrubber column: the desired purity of biomethane (i.e. CO_2 concentration less equal to 2%) is achieved with a shorter scrubber column. However, the investment cost of the plant does not depend on the height of the scrubber column, but it depends only on the volume of biogas processed by the plant. At the same time, the increase of operating pressure leads to a significant increase of the plant power demand.

The fact that the optimal layout is featured by a PV field capacity of 200 kW and a battery capacity of 182 kWh is clearly shown in Figure 67. In particular, it is shown the energy performance of the WSP when the PV field capacity and battery capacity are simultaneously varied, and the operating pressure is equal to 1.20 bar.

The best layout maximizes the share of the plant electricity demand ($E_{el,LOAD}$) matched by the self-consumed energy ($E_{el,self}$), almost limiting the surplus electricity exported to the grid ($E_{el,toGRID}$). In fact, for such configuration, the self-consumed energy meets roughly 92% of the plant load, while 64% of the produced renewable electricity ($E_{el,PV}$) is exported to the grid. In particular, such layout resulted almost grid-independent, being the battery ($P_{el,fromLIB}$) able to match the plant power demand ($P_{el,LOAD}$) throughout the day. This is clearly shown in Figure 68, which displays dynamic and

monthly results for the water scrubbing plant. According to these results, the battery is crucial to achieve the grid-independence: the share of plant electricity demand matched by the battery ranges from 50% to 60% averagely every month.

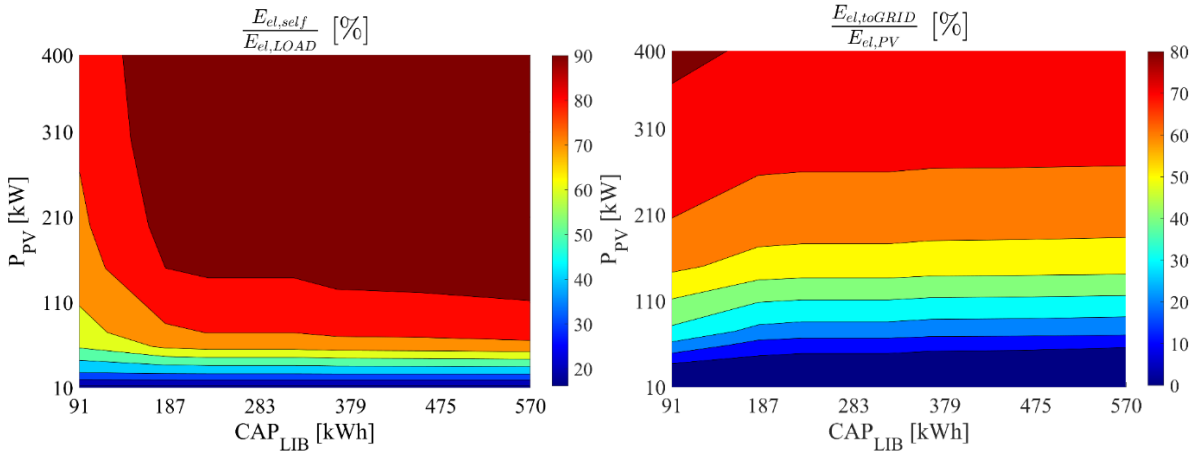

Figure 67. Optimal layout research for water scrubbing plant operating at 1.20 bar: energy performance.

A larger PV field further increases the surplus electricity without significantly reducing the electricity withdrawn from the grid. This trend worsens the economic performance of the renewable plant. In fact, the increase of the PV field capacity increases the maintenance costs, which overcome the gains due to electricity exporting for larger PV field capacity. In fact, the battery would not be able to store further share of photovoltaic electricity. Concerning the electric energy storage system, the plant is not able to exploit the discharge depth of high-capacity LIB, because of the low rated power demand of the WSP using 1.20 bar as operating pressure.

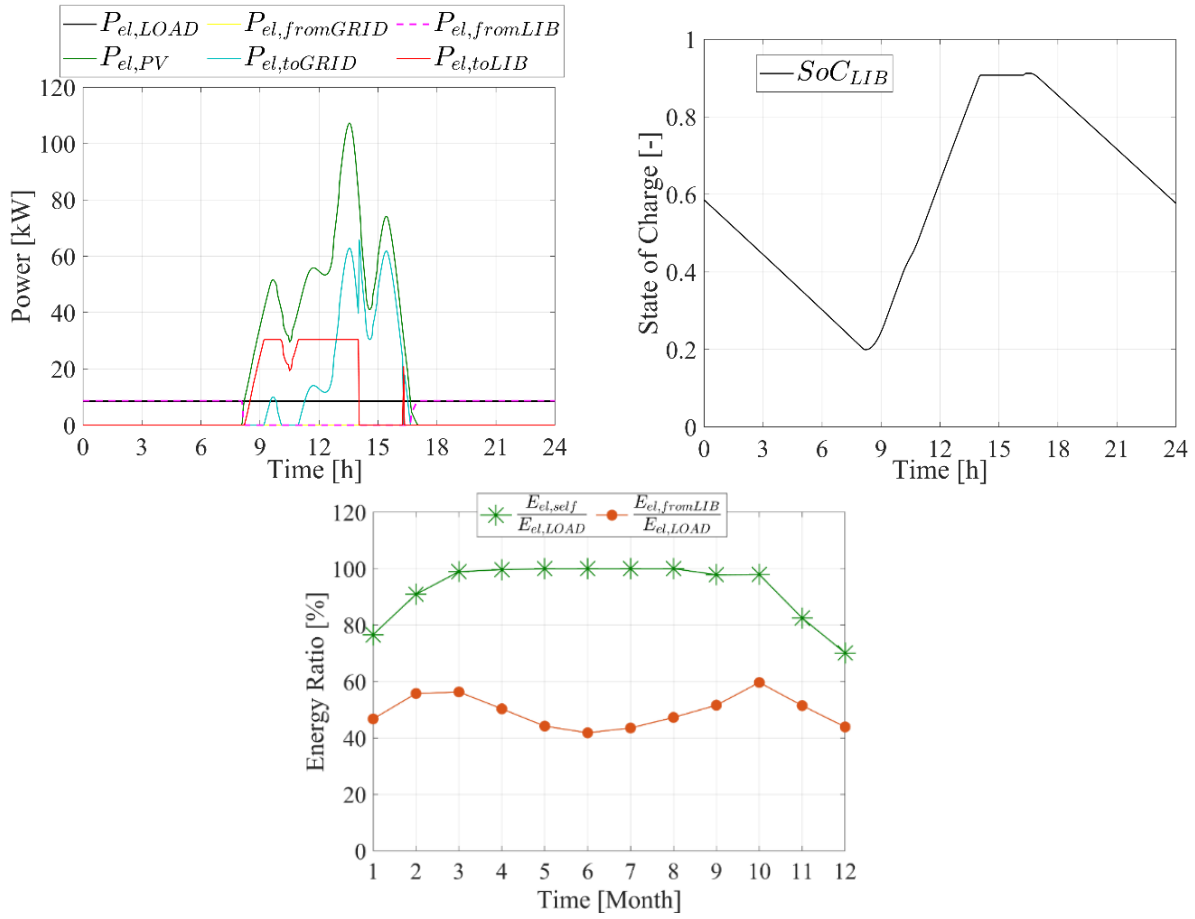

Figure 68. Dynamic and monthly energy results for water scrubbing plant operating at 1.20 bar with a PV field capacity of 200 kW and battery capacity of 182 kWh.

Figure 69 displays the optimal response surface for the renewable plant adopting 2 stage and 3 stage membrane separation upgrading technology (2SMP and 3SMP). The layouts featured by the highest operating pressure and the highest battery and PV capacity achieve the best results for 2SMP, i.e. a *PE* of roughly -5.02 GWh/y and a *C* of about 483 k€/y. This result is related with the fact that the increase of the operating pressure improves the amount of biomethane produced by the plant. In fact, the higher the pressure the higher the driving force of the membrane separation process is. This allows the membrane to separate a higher fraction of CH_4 from the biogas mixture.

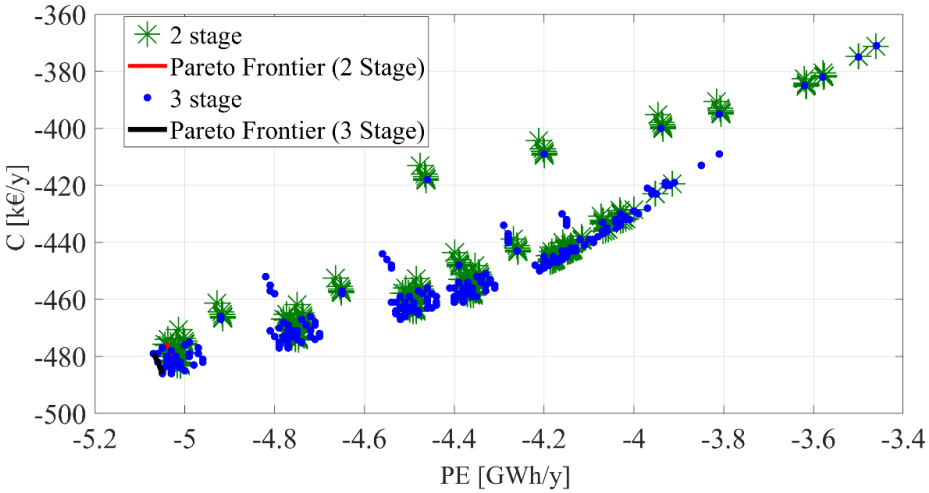

Figure 69. Optimal response surface and Pareto frontier: membrane separation upgrading plants.

Higher operating pressures lead to higher power demand for plant compressors. Therefore, the plant operating at higher pressure also exploits a higher share of the renewable power produced. In fact, as clearly displayed in Figure 70, the plant operating at 20 bar, with a PV field capacity of 400 kW and a battery capacity of 365 kWh is able to self-consume almost 50% of the electricity produced. At the same time, roughly 90% of plant electricity demand is met by the self-consumed electricity ($E_{el,self}$).

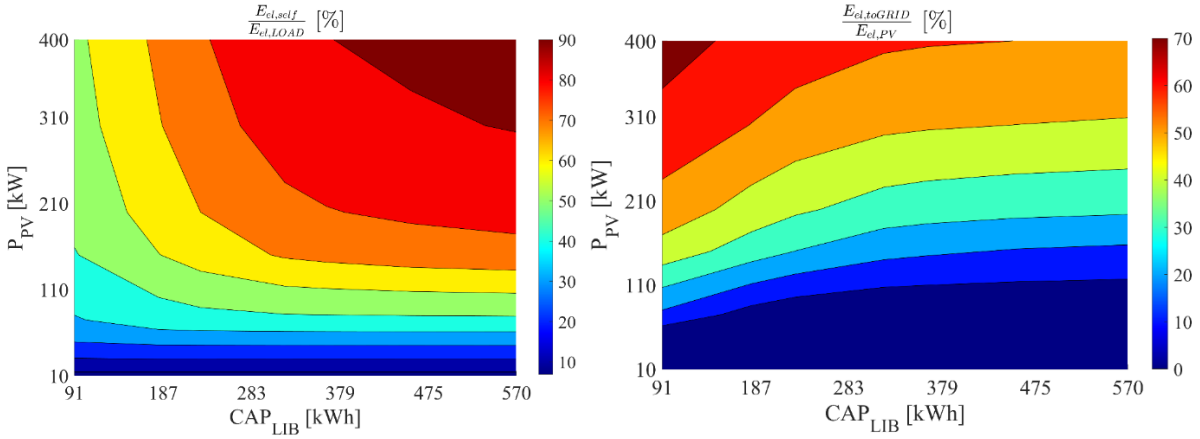

Figure 70. Optimal layout research for 2 stage membrane separation upgrading plant operating at 20 bar: energy performance.

This point is clearly displayed in Figure 71. In fact, the photovoltaic field ($P_{el,PV}$) with the lithium-ion battery ($P_{el,fromLIB}$) meets the power load ($P_{el,LOAD}$) throughout the day, without withdrawing electricity from the grid ($P_{el,fromGRID}$). According to the above described trends, the plant is almost grid independent from February to October. The battery plays a crucial role in such plant, matching around 40÷60% of $E_{el,LOAD}$.

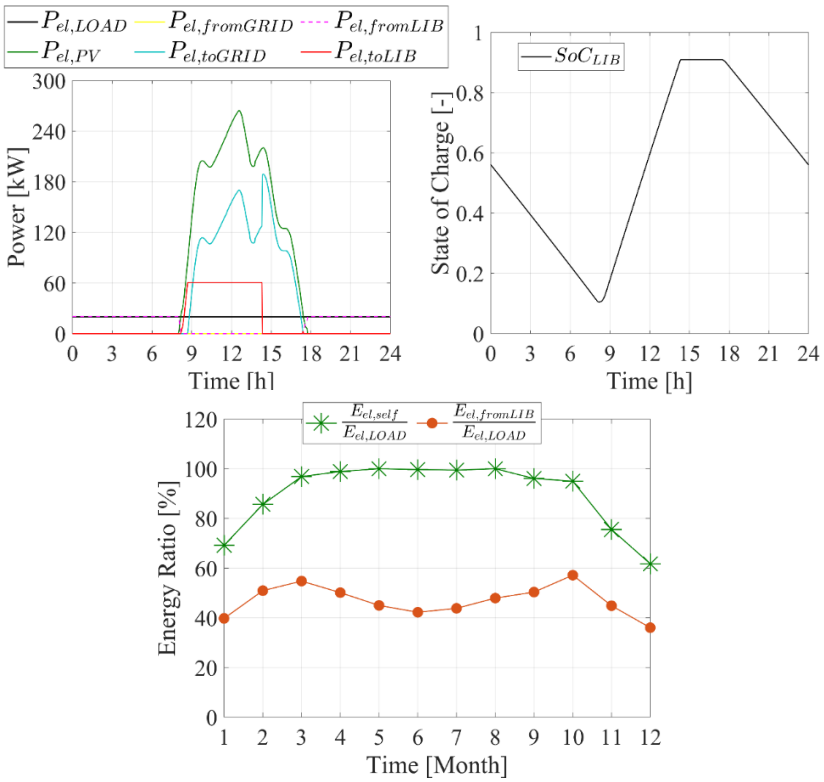

Figure 71. Dynamic and monthly energy results for 2 stage membrane separation upgrading plant operating at 20 bar with a PV field capacity of 400 kW and battery capacity of 364 kWh.

Figure 72 displays the energy performance of the proposed renewable plant adopting 2 stage membrane biogas upgrading process, for a storage system capacity of 364 kWh and simultaneously varying system rated pressure and photovoltaic capacity. This figure is consistent with the above described trends. In fact, as explained before, the increase of the rated operating pressure comes with the increasing of the plant power demand, allowing the plant to exploit more of the energy produced. Therefore, for higher operating pressure and higher PV field, the electricity exported to the grid ($E_{el,toGRID}$) is limited, but the self-produced electricity ($E_{el,self}$) matches roughly 90% of plant electricity demand.

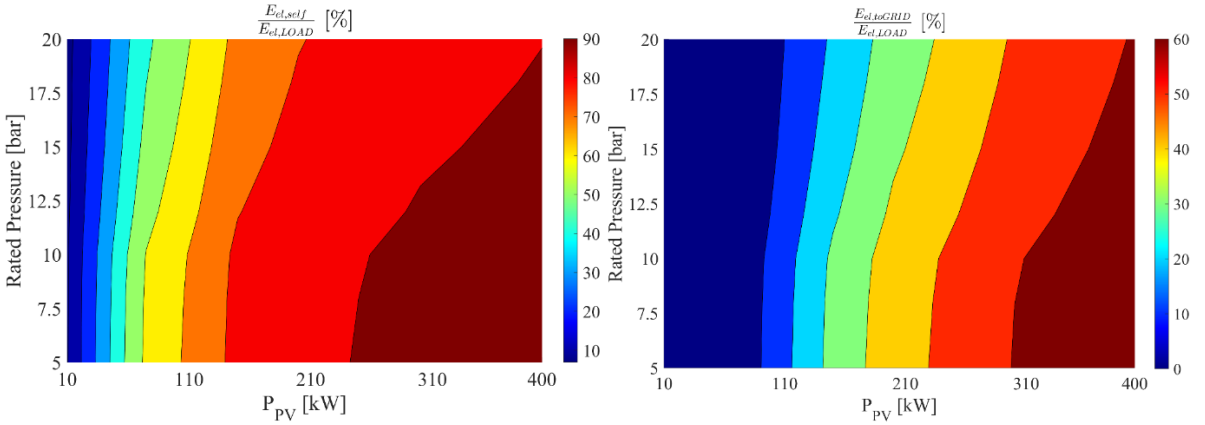

Figure 72. Optimal layout research for 2 stage membrane separation upgrading plant adopting a battery of 364 kWh: energy performance.

The optimal response surface and the Pareto Frontier for 3SMP is displayed in Figure 69. The optimal 3SMP operates at a rated pressure of 10 bar, with a PV field of 400 kW and a battery capacity of 365 kWh. The operating costs (C) of such plant are around -486 k€/y, while the primary energy (PE) is around -5.06 GWh/y. The increase of the operating pressure leads to a decrease of the plant overall performance, because the operative pressure significantly increases the power demand of the plant, due to the compressors. At the same time, this increase causes a very limited enhancement in biomethane production and quality. In other words, the marginal electric cost of biomethane production rapidly increases beyond 10 bar.

The fact that the 3SMP with an operative pressure of 10 bar achieves better results with respect to 2SMP adopting an operative pressure of 20 bar (the optimal 2 stage membrane separation layout) is related with the fact that such 3SMP uses less electricity for producing more biomethane. In fact, 2SMP is featured by rated specific production ratio of 0.38 kWh/Sm^3, whereas 3SMP is featured by a specific production ratio of 0.36 kWh/Sm^3.

Moreover, since the increase in the number of stages leads to an enhancement in purity of the biomethane, the 3SMP achieves better results with respect to 2SMP, adopting a lower operating pressure, i.e. 10 bar vs 20 bar. Further increasing the number of stages would not be beneficial because the more the stages, the greater the technological complexity of the plant is, due to higher number of compressors and sensors. Therefore, in this framework, 3SMP may be considered the optimal trade off, among the biomethane purity and plant complexity.

The same results discussed for the 2SMP system are analyzed for the 3SMP in ref. [132] here omitted for the sake of brevity.

The optimal layouts assessed in the previous section are compared with the conventional state of art in biogas power plant, which consists of a reciprocating engine burning the produced biogas (CHP). The electricity produced by the engine is exported to the electric national grid, getting fees that may range from 0.06 €/kWh to 0.22 €/kWh. The thermal energy recovered from the engine is purchased to local facilities, with a selling price of 0.05 €/kWh. The ratio of thermal energy exported is varied according to the parameter α, see section 5.3.2.

Figure 73 shows the primary energy of each scenario varying the share of thermal energy exported in the reference system. As expected, the increase of the parameter α leads to a significant enhancement of the reference system, i.e. cogeneration plant, letting CHP to achieve better results with respect to the proposed optimal scenarios. In fact, for value of α greater than 0.50, the PES becomes negative, meaning that the

avoided primary energy of CHP is greater than the proposed scenarios. Therefore, the ratio of thermal energy exported to local users is crucial, in fact such point is able to make the conventional approach of burning biogas into a CHP plant more energy convenient with respect to every biogas upgrading strategy. This result is deeply related with the fact that the biogas upgrading process is remarkably energy demanding. Note that the surplus electricity exported to the grid is limited, accounting for less than 13% of the avoided primary energy for all the proposed scenarios. Finally, Figure 73 confirms that the water scrubbing process reaches better results from the energy point of view.

Figure 74 summarizes the economic performance of the proposed optimal scenarios compared with CHP. In particular, the electricity and natural gas selling costs are mutually varied. The economic performance of the analyzed scenarios is dramatically affected by the natural gas selling price (j_{NG}). In fact, for value of j_{NG} greater than 0.55 €/Sm^3 all the scenarios achieve a *SPB* lower than 10 years, regardless the electric energy selling cost and the share of thermal energy exported.

However, when the thermal energy exported increases and j_{el} increases, the RS is much more convenient than the proposed scenarios, achieving higher value of savings. Moreover, water scrubbing biomethane upgrading technology achieves better results with respect to membrane separation, since it is less energy demanding. Therefore, the water scrubbing plant purchases less electricity from the grid. Moreover, water scrubbing is featured by lower costs for maintenance. Moreover, membrane separation process is featured by very high maintenance costs.

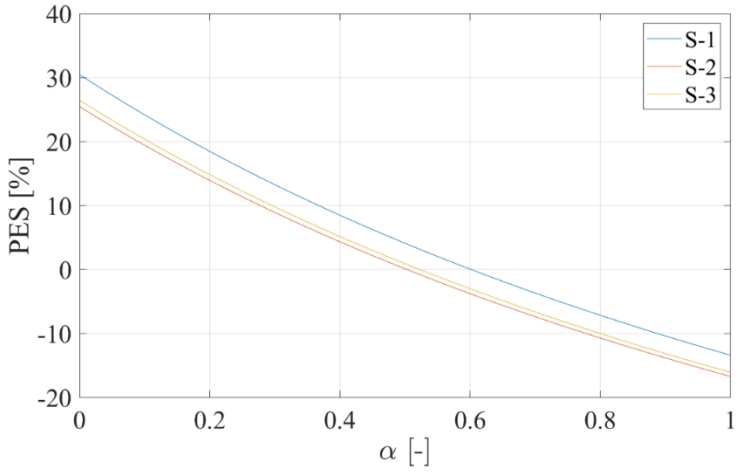

Figure 73. Primary energy of each scenario varying the share of thermal energy exported by the reference system.

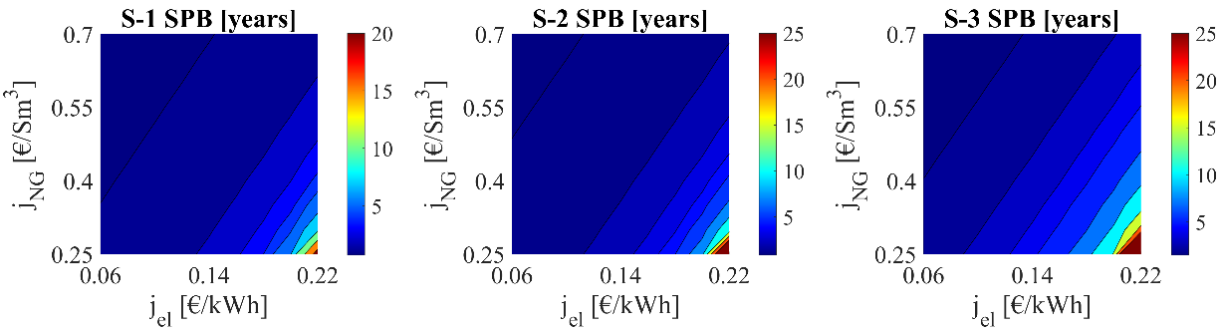

Figure 74. Simple Payback of each scenario varying the electric energy incentives (RS) and the natural gas purchasing cost: A $E_{th,CHP,useful}/E_{th,CHP}$ = 0% exported.

5.4 Dynamic heat recovery analysis and thermoeconomic optimization of a Power-to-Gas system driven by solar energy

In the current chapter, we have delved into the intricate dynamics of anaerobic digestion and biogas upgrading processes. This exploration is crucial in understanding the complexities involved in transforming organic waste into biomethane, a renewable energy source. Previously, in the previous chapter, our focus was on the dynamics of solid oxide electrolysis, a pivotal technology for green hydrogen production. By analysing these two distinct technologies, we set the stage for an innovative coupling: the integration of green hydrogen production through solid oxide electrolysis with biomethane production from anaerobic digestion.

This combination paves the way for the creation of fully renewable synthetic natural gas (SNG), marking a significant leap forward in our quest for sustainable and environmentally friendly energy solutions. The production of biomethane comes with the separation of the carbon dioxide present in the biogas, which can be therefore exploited for further usage. When combined with green hydrogen through catalytic process, this carbon dioxide obtained starting from biomass is converted into methane entirely produced by renewable sources of energy.

The literature review discussed in [39] focused on the existing works in scientific literature dealing with the P2G strategy for storage of renewable energy surplus. There are plenty of works in literature in which the P2G concept is commonly considered as the conversion of electricity into gas of whatever type. This mistaken approach is misleading compared to the real meaning of the P2X concept in general, whose aim is to exploit renewable power surplus that would be sent to the grid causing relevant issues or even wasted.

Within the works which consider this option to perform analyses of P2G plants, only a few of them analyze the issues arising when it comes to the coupling of

methanation reactors with a fluctuating energy source. In fact, several works discuss a fully renewable layout in steady-state operating conditions whereas some other ones focus on the analysis of the reactor neglecting the coupling with other components. It is also clear that literature still lacks a detailed thermoeconomic analysis of such a system. Moreover, the issue of the thermal coupling between the electrolyzer and the methanation reactor, when it comes to dynamic operating conditions, is still far from being solved. In fact, most of the works analyzed model and simulated the whole plant using Aspen, which uses a steady state approach. The dynamic operation occurring into the plant is indeed neglected.

Moreover, such works assume that the steam produced by the methanation reactor can be fully used to feed the solid oxide electrolyzer. Unfortunately, for the most common available technologies the gap of the thermal levels, i.e. the temperature difference, is such that full heat recovery is not possible. Furthermore, considering the optimal operating conditions of both units, simultaneous operation is not guaranteed, given the fluctuation of the power source. The aim of this work is to fill up this gap by proposing a thermoeconomic analysis for a P2G system fully based on renewables, where the heat recovery aspect is accurately modelled and simulated. The main novelty of this work can be then summed up as following:

- The dynamic modelling of a fully renewable-based P2G system, considering heat transfer rates and the different thermal levels.
- The comprehensive heat transfer dynamic analysis, which shows the cumbersome issues related to the dynamic operation of the electrolyzer and the methanation reactor when it comes to the heat recovery of the units. In fact, with the existing technologies the combined heat integration is not a solution, especially when renewable power excesses are used to drive the system operation.
- The analysis of a specific control strategy developed in order to minimize the compression work and maximize the efficiency of the system, also guaranteeing safe operating conditions of the methanation reactor.
- The computer-based design of experiment (DoE) analysis performed to detect the optimal configuration of the P2G system from the thermoeconomic perspective. Several variables are considered in the system proposed to detect the most influencing factors affecting the optimal solution both in terms of energy and economic results.

5.4.1 System Layout

The layout of the proposed P2G system is shown in Figure 75.

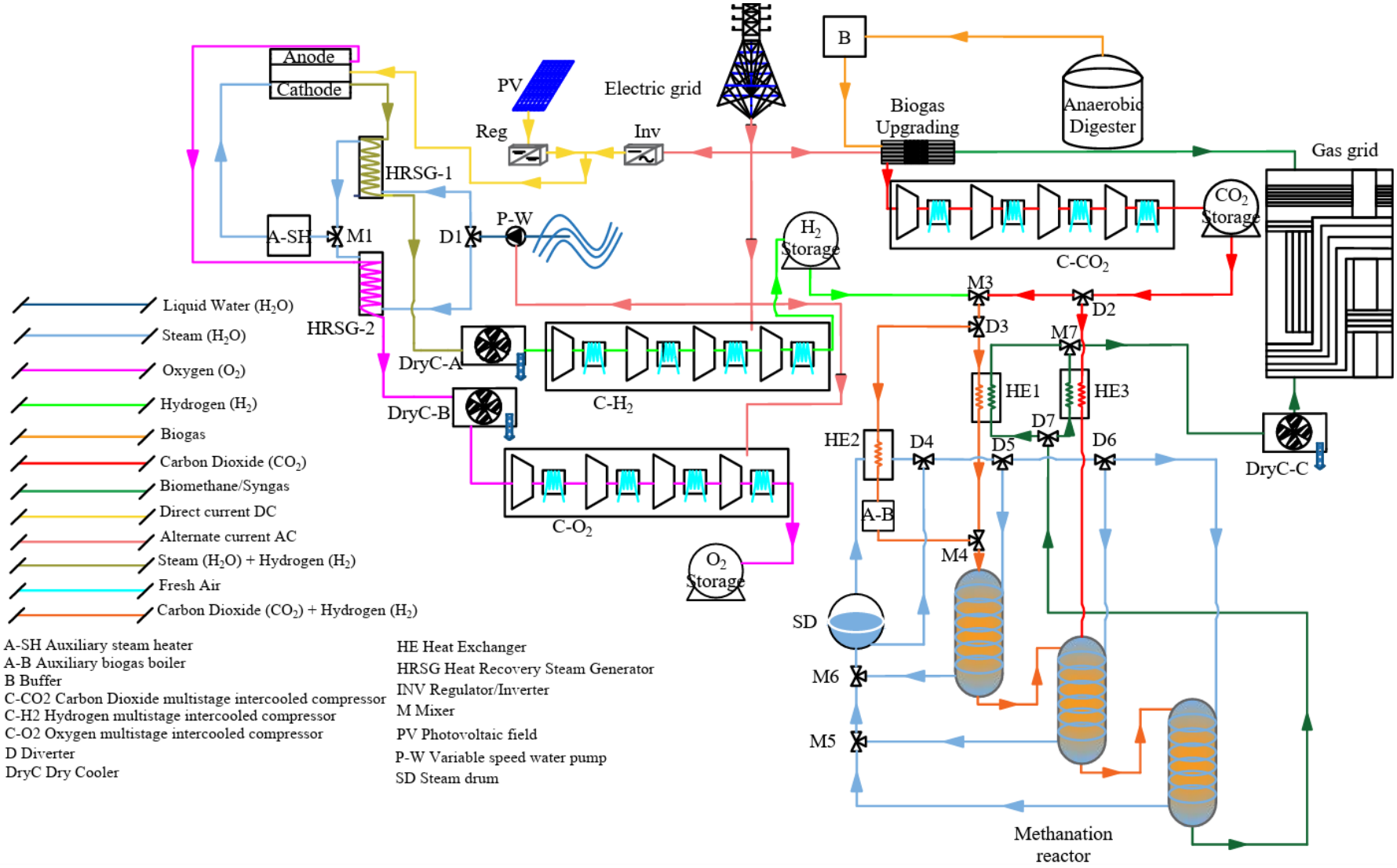

Figure 75. Layout of the P2G plant proposed.

The proposed plant is based on the hydrogen production from the excess of renewable energy produced by photovoltaic. The photovoltaic field first meets the electricity demand of the biogas upgrading unit and the auxiliary components, then the surplus is supplied to the solid oxide electrolyzer (SOEC) for producing hydrogen. The SOEC is activated only when excess renewable power is available, according to the P2X concept. The electrolyzer produces a gaseous flow rate of hydrogen and steam at the outlet of the cathode (H_2O + H_2) and an oxygen gaseous flow at the anode (O_2). The inlet temperature of the supply steam is 800°C, whereas the operating temperature of the cell oscillates between 650° and 800°C. Therefore, the streams leaving the electrolyzer are used for increasing the enthalpy of the water steam entering the cell. In fact, the waste heat coming with the flows leaving the cell is used for producing high temperature steam. In particular, these flows are used in internal recovery heat exchangers, which pre-heat the incoming water up to 445°C. The incoming water mass flow rate is split to get preheated by the streams leaving the anode and the cathode of the electrolyzer. One fraction of the water is heated by means of the flow of H_2 and steam leaving the cathode in the heat recovery steam generator (HRSG-1). The other fraction is heated by means of the O_2 flowing from the anode in HRSG-2. The water flow rate splitting occurs according to a specific control strategy. In order to maximize the gain by both the heat exchangers, the inlet water mass flow rate is divided according to the thermal capacity of the two hot streams leaving the electrolyzer [39]. Thus, on both sides, the water outlet temperature is the same. The inlet steam flows coming from HRSG-1 and HRSG-2 are then collected by means of M1 mixer and supplied to the auxiliary electric heater (A-SH). The A-SH unit, run by the renewable power, increases the temperature of the steam entering the cell up to the design value of 800°C.

As for the hot streams leaving the heat recovery steam generators HRSG-1 and HRSG-2, these flows, i.e. O_2 and mixture of H_2 and steam, are cooled down to ambient temperature by means of dry coolers (DryC-A and DryC-B). The dry cooling process is designed both for reducing the temperature of these flows before entering the compressors (C-H2 and C-O2), and for separating the water from the cathodic stream before delivering it to the compressor (C-H2).

The compression stages are intercooled to reduce the electricity demand of the compressors. Finally, a further cooling is performed in order to deliver the compressed gas at ambient temperature to the dedicated tanks (TK-H2 and TK-O2). This cooling process is designed for better managing the pressure inside the compressed tank, avoiding overheating and overpressures.

The H_2 is then withdrawn from the tank and mixed with the CO_2 before being supplied to the methanation reactor (M-U). The CO_2 is captured from the biogas upgrading process of an anaerobic digestion plant. The anaerobic digester is fed with organic fraction of municipal solid wastes (OFMSW) and produces biogas, mainly supplied to the biogas upgrading unit, and digestate. The biogas upgrading unit is a three-stage compression membrane where membranes are made with hollow fiber. Thanks to the difference in permeability of the methane and the carbon dioxide at a given pressure, the gaseous compound is almost completely separated after three stages of filtering. In fact, the purity of the methane after the process is roughly 96%. Then, the carbon dioxide stream separated from the biomethane flow, is compressed (C-CO2) and supplied to the pressurized tank (TK-CO2). Note that the compressed hydrogen tank (TK-H2) and the compressed carbon dioxide tank (TK-CO2) operate also as buffer tanks, leading toa steady-state operation of the methanation unit. The methanation reactor operates with a rated inlet temperature of 250°C and a design inlet pressure of 15 bar. The H_2 tank and CO_2 tank are managed handling the tanks pressure. In fact, the inlet pressure of the mixture of gases in the methanation unit must be 15 bar and no further compression is required. Therefore, the tank is activated by the control unit only when the pressure level in the tank is such that the outlet pressure is greater than 15 bar. In fact, suitable dead bands are used, allowing the pressure to vary from 475 to 15 bar. Moreover, the controller managing the methanation unit is also designed for avoiding to fully consume reactants in the first reactor. In fact, considering the fact that the Sabatier reaction is highly exothermic , it is mandatory to supply a flow of reactants in the first reactor with ratio H_2/CO_2 lower than the stoichiometric one. Since the control strategy is developed to allow the methanation reactor to operate always in design conditions, the minimum pressure level of the tanks is the controlled variable to manage both requirements.

The control strategy on the heat recovery of the methanation reactor is applied with a cascade strategy involving the diverters D2, D7 and D3. In fact, the fraction of CO_2 supplied to the second reactor, which is managed by the diverter D2, is a known parameter and is roughly 65% of the total CO_2 flow rate [74]. Both the inlet temperature and the design outlet temperature of the gas are known. Therefore, the diverter D7 splits the products to provide the necessary flow rate of products to HE3. As a consequence, the fraction of products supplied to HE1 can be calculated. Moreover, the design outlet temperature of the fraction of reactants supplied to HE1 from D3 diverter is a known parameter, i.e. the inlet temperature of the reactor. Therefore, the bypass fraction of reactants is calculated for both sides. The remaining fraction is preheated in HE2 by means of the steam of the refrigeration loop. The reactor tubes are completely immersed in a shell filled with saturated water at 33 bar and 240°C, and a quality ranging from 0 to roughly

0.40 when the heat released by the reaction is absorbed. In fact, when absorbing heat from the methanation reaction, the water operates in pool boiling regime [138] with a recirculation fraction smaller than 40% [80]. The bi-phase stream directly flows into a steam drum (SD) where the saturated steam is separated from the liquid phase. The steam is used for preheating the reactants gaseous flows in HE2, whereas the liquid is recirculated into the shell, with a refill flow rate equal to the steam flow rate. The heat exchange in HE2 occurs between the steam and the fraction of the reactants gaseous flow bypassed by the diverter D3. The diverter D3 splits the reactants flow rate by operating in feedback according to the operation of the D2 and D7 diverters.

The diverter D3 manages the inlet mixture of hydrogen and carbon dioxide. Such diverter splits the reactants (CO_2 and H_2) flow rate to warm a fraction of this flow up to the set point of 240 °C by means of a fraction of the outlet products (CH_4 and H_2O) flow rate. This heat exchange occurs in the HE1 heat exchanger, where only a fraction of the products CH_4 and H_2O is supplied since the remaining fraction is used for the preheating of the CO_2 fraction supplied directly to the second stage of reactor. This heat transfer stage occurs in the HE3 heat exchanger. If further heat is necessary after preheating in the HE2, a biomass auxiliary boiler (A-B) is activated for final integration. Through the recirculation loop, made up by several mixers (M5-M6) and diverters (D4-D5-D6), the water is then refilled into the cooling shell of the reactors. Before being supplied to the gas grid, the steam included in the syngas flow rate is removed by means of the dry cooler DryC-C since the CH_4 content on volume basis necessary for injection into the gas grid is 95% [139].

5.4.2 System Model

The layout discussed in the previous section is developed in TRNSYS environment to perform the dynamic simulation. The main components of the plant, namely, anaerobic digester, SOEC, and methanation reactor are modelled in MatLab and then integrated in TRNSYS. These models are integrated by means of performance maps obtained from the simulation of the model under different operating conditions. Therefore, expected results are predicted considering different variables in a field of possible conditions and operating points within the field of operations are obtained by interpolation.

Minor components such as mixer, diverters, compressors, tanks, heat exchangers, and others are instead included in TRNSYS library. Details regarding the anaerobic digestion and solid oxide electrolysis modelling and validation are widely discussed in the previous sections. For the sake of brevity, only the methanation reactor model will be discussed in this section, followed by the thermoeconomic model.

Methanation reactor model

The methanation reactor modelled in this work is a three stage multi-tubular fixed-bed refrigerated reactor, whose main equations were provided by ref. [74]. According to this work, the model of the reactor is divided into three sub-models of three reactors operating in series, for which the equations developed in this section are the same. The cooling of the reactor is necessary to steer the temperature gradient along the tubular reactor and keep the temperature within the rated range, due to constructive limitation. Moreover, to avoid excessive heat release, the inlet reactants flow rate is split in order to divide the reaction in the first two reactors and then have a final conversion of CO_2 in the third and last reactor. The catalyst considered in this model is Ni/Al_2O_3. The model is a mono dimensional (1-D) plug flow reactor where the tubes are supposed to operate in parallel in a homogeneous cooling fluid. The mass and energy balances into the reactor are performed as follows:

$$\varepsilon \frac{\partial C_i}{\partial t} = k_D \cdot \frac{\partial^2 C_i}{\partial z^2} - u \cdot \frac{\partial C_i}{\partial z} + \nu_i \cdot (1-\varepsilon) \cdot \rho_S \cdot r \tag{65}$$

$$C_m \frac{\partial T}{\partial t} = k_L \cdot \frac{\partial^2 T}{\partial z^2} - \rho_G \cdot c_G \cdot u \cdot \frac{\partial T}{\partial z} + (1-\varepsilon) \cdot \rho_S \cdot (-\Delta h_r) r - \frac{UA}{V}(T - T_C) \tag{66}$$

Details of the terms are explained in the nomenclature section. For both the equations the term on the left side represents the accumulation term, whereas the terms on the right side are, respectively, the diffusive term, the convective term, and the term related to the chemical reaction. The last term on the right of the energy balance equation is the term related to the heat loss through the coolant. The term C_m represents the average thermal capacity between the catalyst bed and the gaseous flow rate per each section, thus it is calculated as:

$$C_m = \varepsilon \cdot c_G + (1-\varepsilon) \cdot \rho_S \cdot c_S \tag{67}$$

Where ε is the void fraction occupied by the gas, thus it is the part of the section which is not occupied by the catalyst. The thermal conductance through the tube wall U is calculated as a function of the convective heat transfer coefficient in the inner and outer sides of the tube. The pressure drop along the reactor is calculated according to Ergun's equation:

$$\frac{dp}{dz} = -150 \cdot \frac{(1-\varepsilon)^2 \cdot \mu_G}{D_p^2 \cdot \varepsilon^3} \cdot u - 1.75 \cdot \frac{(1-\varepsilon) \cdot \rho_G}{D_p \cdot \varepsilon^3} \cdot u^2 \tag{68}$$

The pressure drop is a function of the particle diameter, velocity, and viscosity, and it also depends on the void fraction ε. The overall velocity of the process strictly depends on the effective reaction rate, considering the resistance to mass transport due to the porous medium:

$$r = r_{intr} \cdot \eta \tag{69}$$

Where r_{intr} is the ideal reaction rate and η is the effectiveness factor which depends on the Thiele modulus θ according to:

$$\eta = \frac{3}{\theta^2} \cdot \left(\frac{\theta}{tanh(\theta)} - 1 \right) \tag{70}$$

The Thiele modulus θ, in turn, depends on the particle diameter. The Thiele modulus represents the ratio between two characteristic times: the time of the chemical reaction and the diffusion time. Therefore, depends on several factors as temperature, pressure, reaction rate, particle diameter:

$$\theta = \frac{D_p}{2} \cdot \sqrt{\left(\frac{r_{int\,r} \cdot R \cdot T}{p_{CO_2} \cdot D_e} \right)} \tag{71}$$

Where D_e is the effective diameter and is function of the bulk diameter, the void fraction, and the tortuosity. Further details regarding the model are shown in ref. [74].

The above presented partial differential equations (PDEs) are solved by means of a spatial discretization, following a finite difference approach. It was also necessary to develop a model to consider the variation of the thermo-fluid-dynamic properties and the conversion factors of the reactants. Initial conditions for the model were given by ref. [74].

The viscosity gaseous flow rate of reactants was calculated according to Chpman-Enskog equation coupled with the model of intermolecular potential given by Lennard-Jones [140]. Thermal conductivity was calculated according by Chung's method [140] and Wassijewa's equation, calculating the value of the specific heat at different temperatures [140], whereas Fuller-Froment method was used for calculating thermal diffusivity [140].

As already mentioned, the model was developed and solved in MatLab, getting a performance map imported in TRNSYS environment.

Thermoeconomic model

The thermoeconomic model is useful to deeply assess the performance of the system proposed (PS) with respect to a reference system (RS). In fact, it is possible to evaluate the primary energy consumption, the CO_2 emissions, and the capital and operative costs of both the systems and compare them. The primary energy consumption (*PES*) of the systems is calculated according to:

$$PE_{,RS} = \frac{E_{el,\,fromGRID}}{\eta_{el,GRID}} - V_{CH_4,UPG} \cdot LHV_{CH_4} \tag{72}$$

$$PE_{,PS} = \frac{E_{el,\,fromGRID} - E_{el,\,toGRID}}{\eta_{el,\,GRID}} - \left(V_{CH_4,UPG} + V_{CH_4,MET}\right) \cdot LHV_{CH_4} \tag{73}$$

The term $E_{el,fromGRID}$ is the electricity withdrawn from the gird, $E_{el,toGRID}$ is the electricity sent to the gird, $\eta_{el,grid}$ is the efficiency of the national electric grid, $V_{CH4,upg}$ is the biomethane produced by means of anaerobic digestion and upgraded, $V_{CH4,met}$ is the syngas produced by means of methanation, and LHV_{CH4} is the lower heating value of the natural gas. The CO_2 emissions are calculated on the basis of the CO_2 emission factor related to the electricity and the natural gas withdrawn from the grid.

To evaluate the economic feasibility of the PS, the capital costs are evaluated as:

$$C_{TOT} = C_{PV} + C_{SOEC} + C_{MET} + C_{TK_{H_2}} + C_{HE} + C_{AH} + C_{comp} + C_{DryC} + C_{HRSG} + M \tag{74}$$

Therefore, the cost of all the components is considered, namely: the PV field, the SOEC, the methanation reactor, the H_2 tank, the heat exchangers, the auxiliary heater, the intercooled compressors, the dry coolers, and the HRSG. Furthermore, the maintenance costs are considered.

Table 27 summarises the values of the unit costs and emissions factors considered, together with the unit costs of the technologies investigated.

The term ΔC, which is necessary to calculate the *SPB* of the technology proposed, is the difference between yearly operating costs for the RS (C_{RS}) and the PS (C_{PS}):

$$C_{RS} = E_{el,\,fromGRID} \cdot C_{u,EE} - V_{CH_4,upg} \cdot C_{CIC} \tag{75}$$

$$C_{PS} = E_{el,\,fromGRID} \cdot C_{u,EE} - E_{el,\,toGRID} \cdot p_{EE} - \left(V_{CH_4,upg} + V_{CH_4,met}\right) \cdot C_{CIC} - m_{O_2} \cdot C_{u,O_2} \tag{76}$$

The term C_{CIC} refers to the price of the biomethane produced by renewables also including to the incentives proposed by the Italian Government. The selling price of the oxygen is also considered in the economic analysis for the PS. Furthermore, some efficiency factors are calculated to investigate the performance of the system:

$$\eta_{SOEC} = \frac{M_{H2,inTK\text{-}H2} LHV_{H2}}{E_{el,toSOEC} + E_{th,AH} / \eta_{AH}} \quad (77)$$

$$\eta_{met} = \frac{M_{CH_4,met} LHV_{CH_4}}{M_{H_2,met} LHV_{H_2}} \quad (78)$$

$$\eta_{glob} = \frac{M_{CH_4,met} LHV_{CH_4}}{E_{el,toSOEC}} \quad (79)$$

$$\Phi = \frac{Eel_{fromGRID} \eta_{el,GRID}}{M_{CH_4,MET} LHV_{CH_4}} \quad (80)$$

Where the parameter Φ is an indicator of the primary energy consumption per kWh of synthetic natural gas produced. Furthermore, the cost of the methane produced in €/kg and €/kWh is calculated and compared to other works available in open literature.

Table 27. main parameters used for the thermoeconomic analysis.

Parameter	Description	Value	Unit
$C_{u,ee}$	Electricity purchasing cost	0.18	€/kWh
$p_{u,ee}$	Electricity energy exporting cost	0.06	€/kWh
$C_{u,NG}$	Natural-Gas purchasing price	0.18	€/Sm³
$C_{u,O2}$	Oxygen purchasing price	2 [141]	€/kg
LHV_{H2}	Hydrogen lower heating value	120.00	MJ/kg
LHV_{CH4}	Natural gas lower heating value	9.59	kWh/Sm³
$Cu_{,PV}$	PV unit cost	700 [142]	€/kW
$Cu_{,SOEC}$	SOEC unit cost	1500 [143]	€/kW
$Cu_{,TK\text{-}H2}$	Hydrogen tank cost	500 [144]	€/kg
C_{comp}	Compressor capital cost	$C_C = 5840 \cdot (P_{el,C,rated})^{0.82}$ [145]	€/comp
C_{HE}	Heat exchanger capital cost	$C_{HE} = 130 \cdot 1.4 \cdot \left[(A_{HE} / 0.093)^{0.78} \right]$ [127]	€/HE
C_{HRSG}	Heat recovery steam generator	0.368 [146, 147]	M€/HRSG
C_{dryC}	Dry cooler specific cost	200 [148]	€/kW
C_{AH}	Auxiliary heater specific cost	125 [149]	€/kW
$\eta_{el,grid}$	Conventional electric grid efficiency	0.46	-
η_B	Boiler efficiency	0.86	-
η_{SG}	Steam generator efficiency	0.98	-
η_{AH}	Steam heater efficiency	1	-
η_{inv}	Inverter efficiency	0.96	-

5.4.3 Case Study

The case study consists of a biomethane production plant, operating in the area of Campania, in the South of Italy. This plant includes an anaerobic digester of 2´580 m^3 continuously stirred tank reactors (CSTR), which elaborates a biomass flow rate of 2´016 kg/h of OFMSW. The flow rate of biogas produced is equal to roughly 83 Nm^3/h, once steady state conditions are reached. To prevent the biogas upgrading unit operation far from rated condition, a buffer is integrated downstream the anaerobic digesters. This upgrading unit is a three stage compression membrane operating at a rated pressure of 15 bar [132]. The biomethane flow rate produced is equal to roughly 56 Nm^3/h. Part of the biogas is used to feed the auxiliary boiler to keep the digester at the desired temperature level during the operation. The CO_2 available after the biogas cleaning and upgrading processes is roughly the 35% of the initial biogas flow rate.

The reference system (RS) is the above presented biomethane production plant. This plant includes one anaerobic digester operating with OFMSW, coupled to a 200 kW biogas upgrading unit which separates the methane from the carbon dioxide.

The proposed system (PS) aims at exploiting the CO_2 captured from the upgrading process of the biogas. Thus, this plant also includes a 20 MW PV field integrated with a SOEC of 10 MW of rated power. The H_2 produced by means of electrolysis from renewable power is mixed with the CO_2 captured from the biogas upgrading process. This gaseous compound of reactants is delivered to a three stage methanation reactor of roughly 8 MW. The CH_4 is then cooled down to reduce the steam content in the mixture and reach the volumetric percentage of CH_4 needed to allow injection into the Italian gas grid, i.e. 95%. Therefore, this plant produces methane from the OFMSW and from the methanation process. In addition to these main technologies, also some auxiliary systems for storage and heat recovery are considered in the PS. Technical data about the technology integrated in the PS are shown in Table 28. Further data about the reactor are shown in ref. [74].

Table 28. Technical data of the technologies considered.

Component	Parameter	Value	Unit
PV Field	Module efficiency	0.18	-
	Rated power	20.8	MW
	PV field area	128´720	m^2
SOEC	Cell operating pressure	1	-
	Number of cells in series	8	-
	Number of stacks in parallel	9´300	-
	Rated power	10.6	MW
Tank TK-H2	Tank Volume	50	m^3
	Max tank pressure	500	bar
Compressor H_2	Compressor isentropic efficiency	80	%

	Number of stages	4	-
	Compression ratio	3.8	-
	Rated pressure	500	bar
Compressor O_2	Compressor isentropic efficiency	80	%
	Number of stages	4	-
	Compression ratio	3.5	-
	Rated pressure	50	bar
Methanation reactor	Rated heat transfer rate	1.3	MW
	Rated power	7.93	MW
	Rated CO_2 conversion	0.989	-
	Rated hydrogen flow rate	290.3	kg/h
	Refrigerant water pressure	33	bar
	Refrigerant water temperature	240	°C
	Reactor operating pressure	15	bar
	Reactor inlet temperature	250	°C

5.4.4 Results

The results of the proposed model are shown and discussed in this section according to the following lineup: first the results of the validation of the methanation reactor model are presented, then the results from the dynamic simulation and thermoeconomic analysis are discussed. In conclusion, the optimization analysis is carried out to find the optimal design parameters for the technologies included in the system proposed.

Figure 76, Figure 77, and Figure 78 show the results of the validation of the three reactors. For all the three stages of the fixed-bed cooled reactor the value of the temperature in all the points along its length was calculated. The results from the simulation of the temperature gradient along the reactor were extremely accurate and close to the values obtained in ref. [74]. The maximum percentage error found in reactor 1 is less than 1.6% when the value of the temperature arises above 440 °C, at 1.2 m length. The same occurs for the second reactor, where the peak temperature is reached earlier in the tube and the percentage error at 445 °C is less than 1.2%. The temperature slope is due to the reactions occurring along the reactor pipe and the values are steered below the critical point (above 550°C) to prevent damage of the catalyst [74]. The results are consistent also for the last reactor, where the gradient inversion occurs at roughly half of the total length and the maximum percentage error is around 1.6 %. As it can be noticed, the higher the gradient, the greater the percentage error, which is still extremely low, because of the great variation in temperature within a small displacement. This result is mainly due to the discretization used for modelling the methanation process. In fact, where the temperature gradient is sharper, a smaller discretization step would allow the model to better mimic the variation in temperature gradient. However, the error assessed is still limited. Then, with the selected step is possible to achieve a good agreement between the needs of a precise model

and a not so heavy model from the computational point of view. The percentage error here shown was obtained with a discretization step of 0.15 meters, thus for an even smaller discretization step a smaller percentage error is expected. However, a smaller step would only slightly improve the accuracy of the model, but it would dramatically increase the computational time of the model.

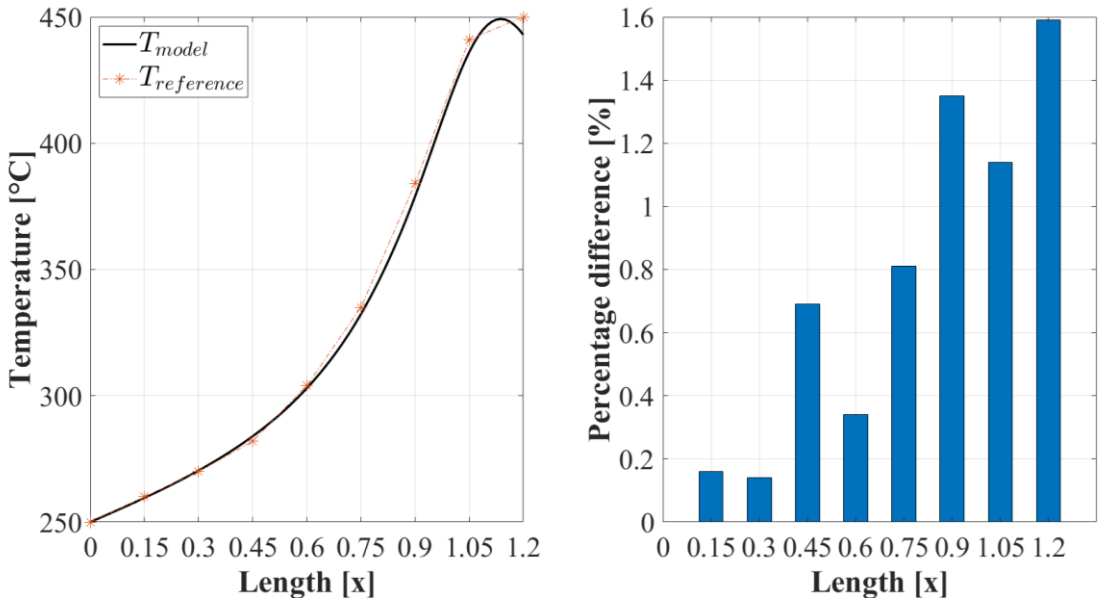

Figure 76. Validation of the first reactor.

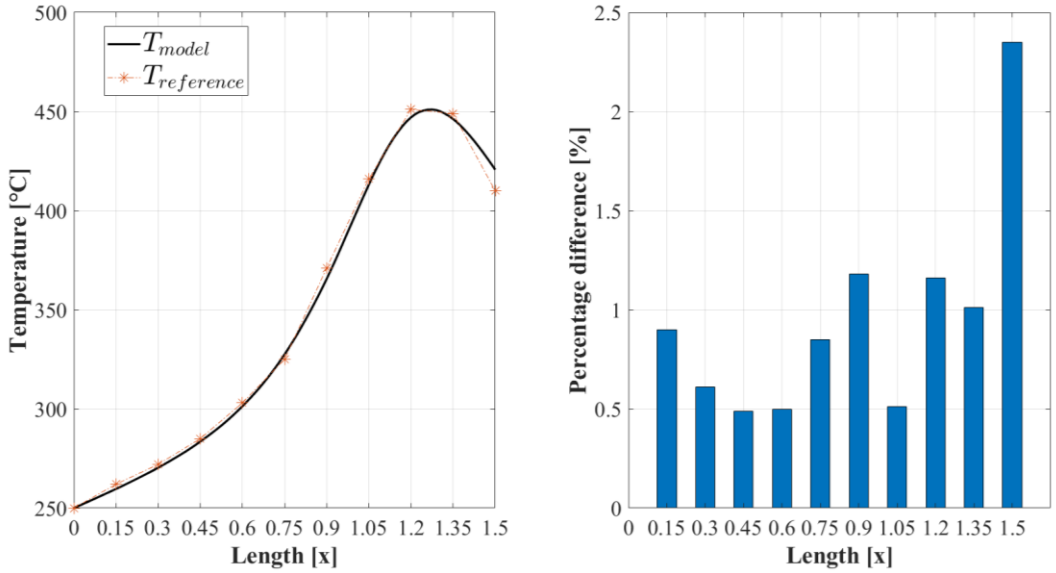

Figure 77. Validation of the second reactor.

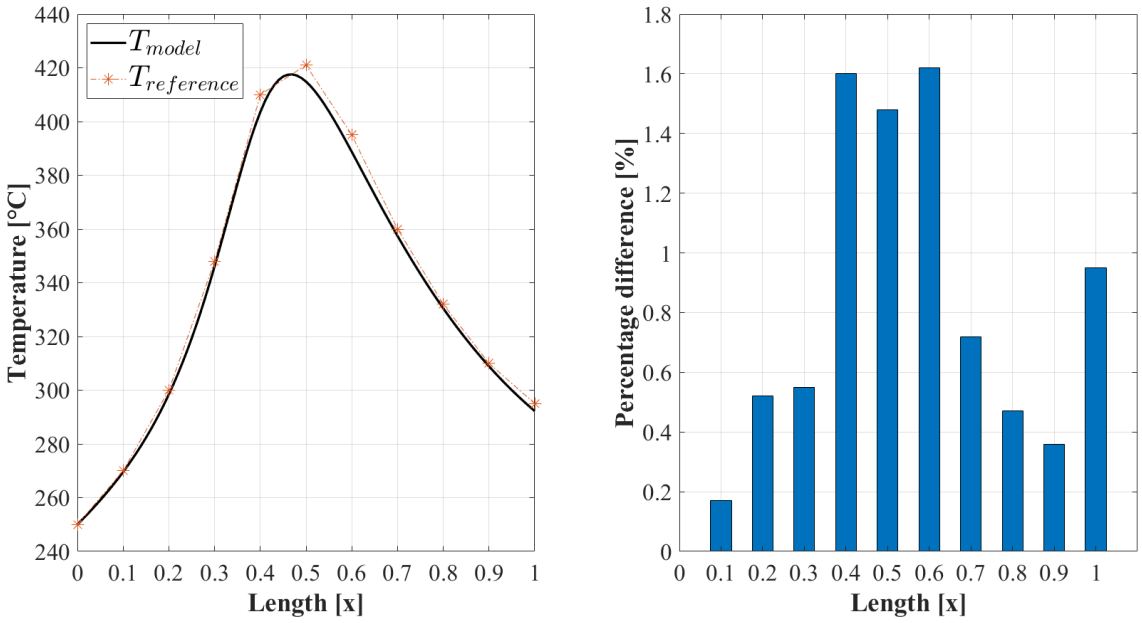

Figure 78. Validation of the third reactor.

Figure 79, Figure 80, and Figure 81 show the trend of the molar fraction of the chemical species along the three reactors. According to the assumption explained in the Layout section not all the flow rate of reactants is supplied directly to the first reactor. In fact, the percentage of H_2 and CO_2 at the inlet of the first reactor on molar basis are roughly 0.90 and 0.10, respectively. Since the stoichiometric ratio of the molar species is 4:1, large part of the CO_2 flow is straightly supplied to the second reactor, according to an optimal value selected in the reference work [74]. This strategy is purposely designed to avoid the complete reaction of the gases which would lead to excessive heat release and, therefore, a sharp increasing of the temperature. This should be avoided to prevent the burning of the catalytic bed in the inner pipes of methanation reactor.

In the first stage of reaction, the fraction of H_2 at the inlet is roughly 0.90 and so almost 0.10 is the fraction of CO_2, on molar basis, according to what said. Here it is possible to observe how the concentration of H_2 slightly decreases until the length of 0.75 is reached, then the conversion rate sharply accelerates. This is consistent to what observed in Figure 76 where at the same point on the x-axis a sharp increasing of the temperature is observed. In fact, from that point on the reaction is much more effective and the heat released increases accordingly. As a consequence, the conversion rate is greater. The reason is that the evolution of the reaction comes with a H_2/CO_2 ratio which is closer and closer to the stoichiometric one, therefore the reaction is always more efficient. The final molar concentration of H_2 at the outlet of the first reactor is 0.6, see Figure 79, meaning that the conversion is not yet completed. As a consequence, a small formation of H_2O and CH_4 can be observed.

In the second reaction stage, another efficient reaction is performed, with a sharp decreasing of the reactants concentrations and a great production of CH_4 and H_2O. In fact, it can be noticed how the concentration of the CO_2 at the outlet of the first reactor is almost zero, Figure 79, whereas the concentration of the CO_2 at the inlet of the second reactor is roughly 0.15, Figure 80. Here it can be observed the same trend of the reaction rates discussed for the first reactor, with a sharp decreasing of the H_2 concentration corresponding to the sharp increasing of the reactor temperature, Figure 77.

Since there is still a relevant concentration of at the outlet of the second reactor, roughly 20% on molar basis, a third stage of reaction is performed till the complete exhaustion of the reactants. Moreover, given the high concentration of H_2O at the outlet of the second stage of reactor, nearly 0.40, this is removed and mixed to the H_2O at the outlet of the third stage to perform the preheating of the inlet reactants. In the third stage, the final step of the reaction is performed, obtaining a gas flow of products with high concentration of CH_4. The methanation reaction is therefore successfully completed and the excessive release of heat during the whole process is avoided, guaranteeing correct operating conditions of the unit. It is worth noting that the increase of the conversion rate and the consequent increase of the temperature of the reactor is quite sharp, despite the controlled reaction. This is a further result to highlight because it shows how crucial is to control the reaction and manage the molar ratios of reactants to avoid sudden sharp increases of the temperatures which would severely damage the reactor pipes.

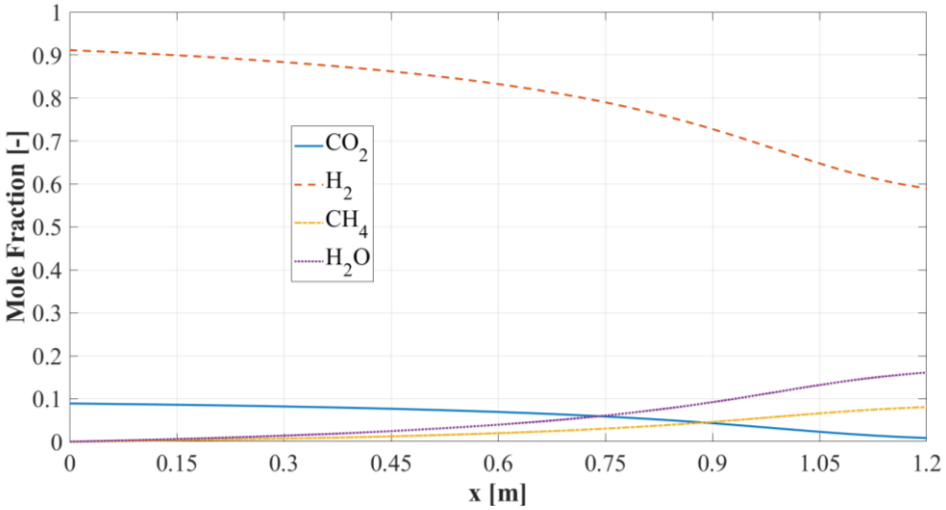

Figure 79. Molar concentration of the chemical species in the first stage of methanation reaction.

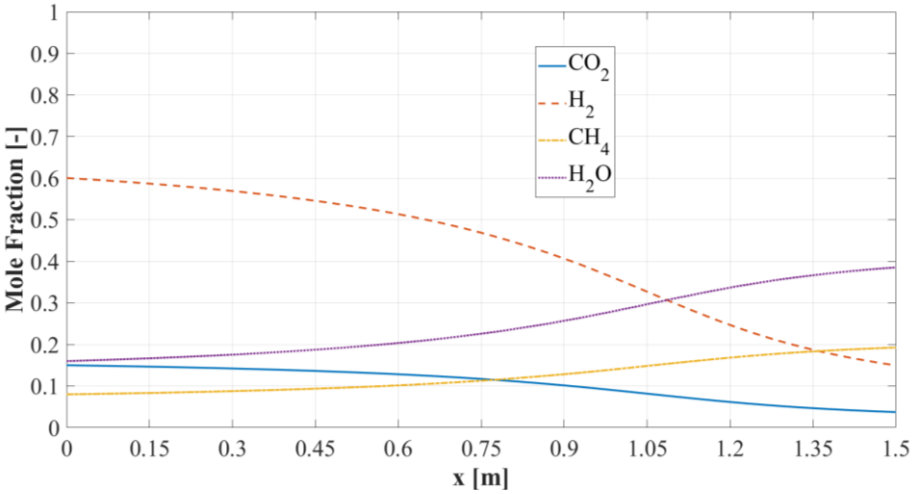

Figure 80. Molar concentration of the chemical species in the second stage of methanation reaction.

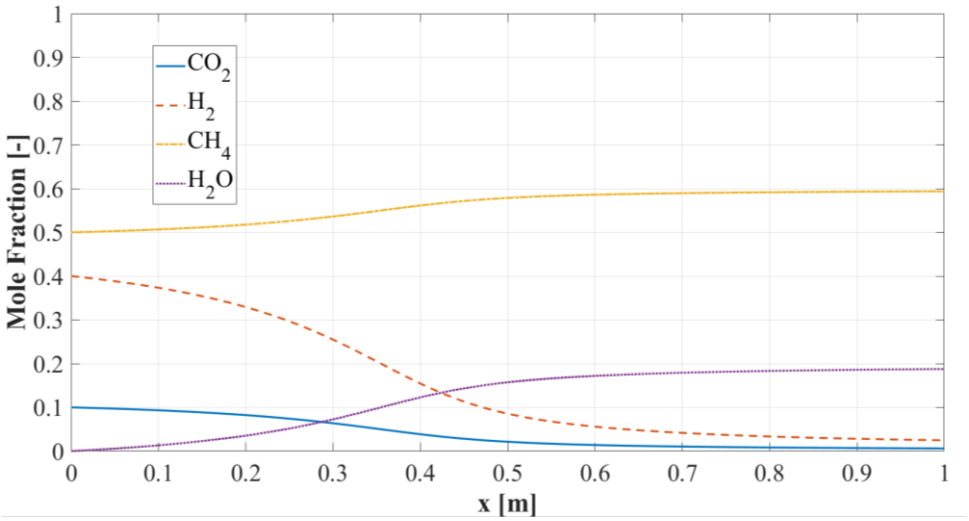

Figure 81. Molar concentration of the chemical species in the third stage of methanation reaction.

Figure 82 shows the dynamic trend of the power flows of the proposed system for a typical winter day. The dynamic results show that the difference between the power produced by the PV, $P_{el,PV}$, and the power supplied to the electrolyzer, $P_{el,toSOEC}$ is generally small but tends to increase when the SOEC power increases. The reason lies behind the fact that the power generated by the SOEC is greater and so are the gaseous flow rates at the outlet of the cell, see Figure 83. Therefore, the power needed for the H_2 and O_2 compression is greater as well as the power needed for the preheating of the cell. At the same time there is a greater heat recovery on the water needed for the electrolysis reaction and the efficiency of the SOEC increases as well.

Figure 83 shows the operation of the H_2 tank during the same operating hours. The H_2 tank pressure level increases up to the upper limit of 95% until 12 AM, after that time the H_2 is supplied to the methanation unit even if the SOEC production is slightly decreasing. From 12 PM to 3 PM, the H_2 is supplied to the methanation unit but the pressure level in the tank is still quite stable because of the SOEC production. After 3 PM the tank has still

enough H_2 to feed the methanation unit but the production is over and there a sharp decreasing in the pressure level of the tank, by 90%. The minimum gas pressure at the outlet is at least equal to the operating pressure of the methanation reactor, i.e. 15 bar. This strategy allows the methanation unit to operate at rated conditions from 12 PM to 10 PM, i.e. ten hours in a row, even in one of the coldest days of the year. It can be already noticed that the operating hours of the SOEC and the methanation unit are different, with a small overlapping of five hours.

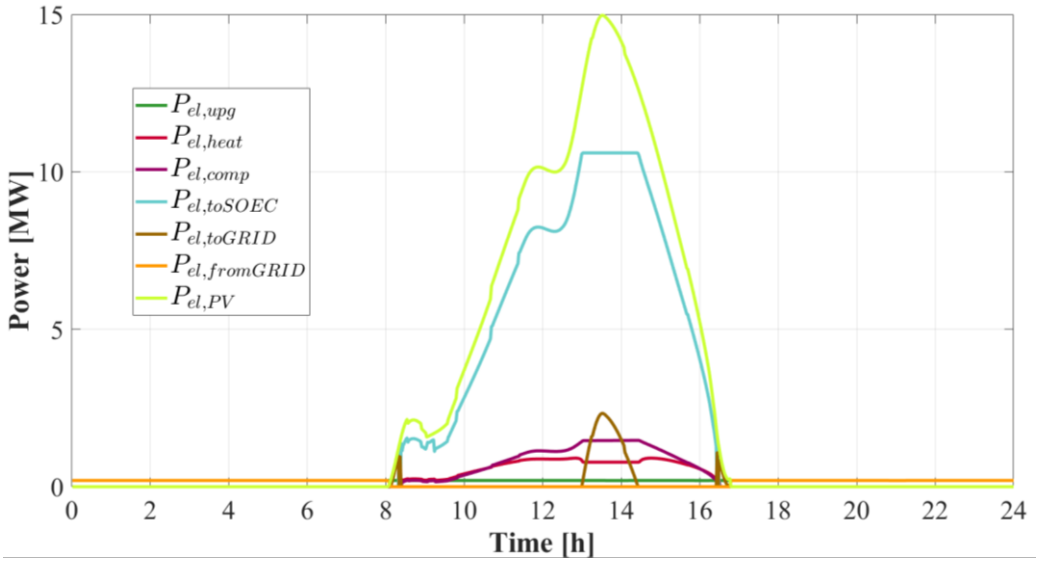

Figure 82. Dynamic trend of the power flows.

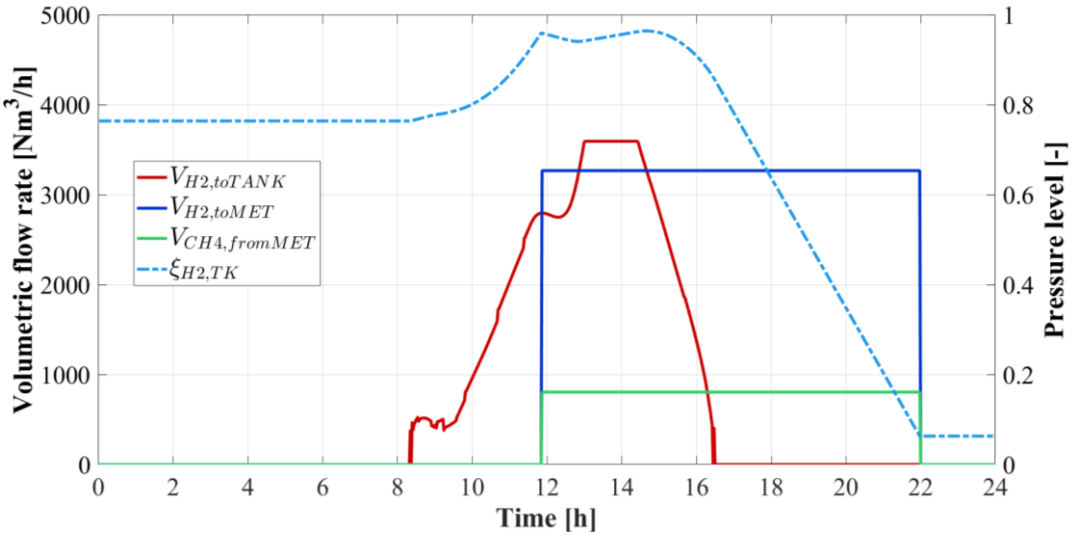

Figure 83. Methanation unit production.

Figure 84 shows the dynamic values of the operating temperatures of the SOEC and the HRSGs. The value of the operating temperature of the SOEC, T_{SOEC}, ranges between 600°C and 800°C, whereas the inlet temperature, $T_{in,SOEC}$, is set up to be equal to 800 °C. Therefore, the water inlet enthalpy is a set point value for the superheated steam at the given pressure and temperature conditions, roughly 4158 kJ/kg. The heat recovery is split in

equal parts in the steam generators operating with oxygen and the hydrogen-steam mixture, according to the heat transfer rate of the two flows. According to this strategy, both the HRSGs get to the same temperature, $T_{gas,HRSG}$, and enthalpy level, h_{gas}, of the steam, h_{steam}, which is up to roughly 320°C and 3120 kJ/kg. At the same time, both the gaseous flows reach the same temperature level, which is roughly 40 °C.

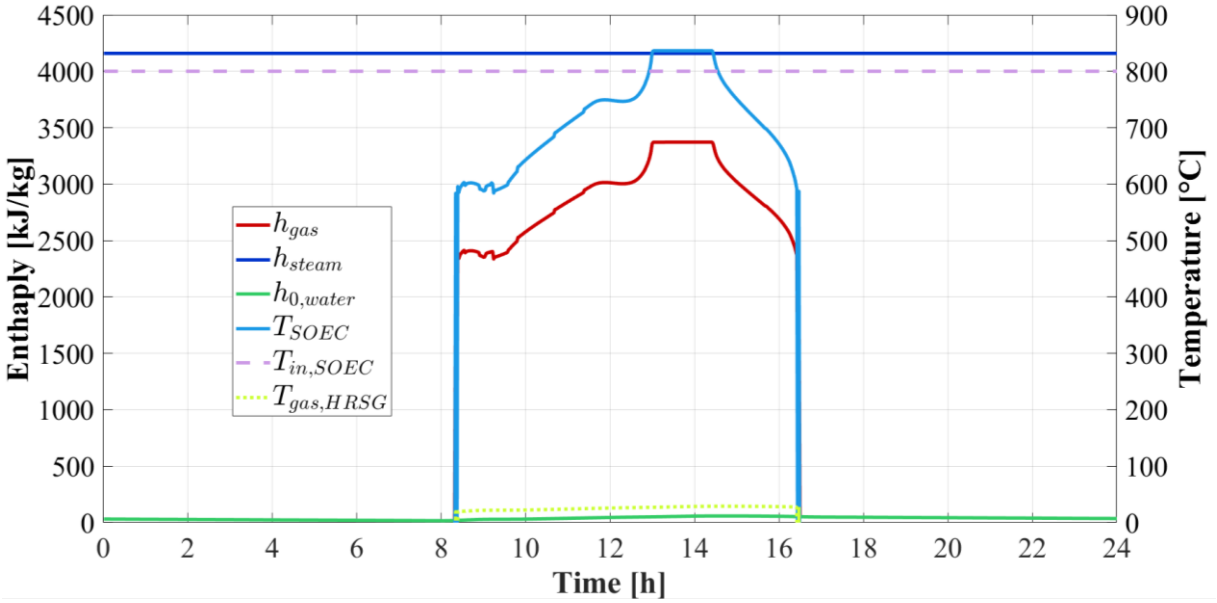

Figure 84. Dynamic trend of the HRSGs.

Figure 85 shows the dynamic trends of the gaseous flow rates of reactants and products, respectively $m_{reactants}$ and $m_{products}$, to and from the reactor. Clearly the temperature levels of the technologies are extremely different. The outlet flow rate of products, at the temperature of 292 °C, is used for preheating the inlet flow rate of reactants, at 250 °C. To get to this temperature level, the reactants flow rate entering the counterflow heat exchanger is partially bypassed. The bypass flow rate, m_{bypass}, is roughly 75% of the inlet flow rate, meaning that large part of the heat must come from another source. To this scope, the steam obtained from the refrigerant cooling water is used, allowing the remaining inlet flow rate to get up to the temperature of 240 °C. The difference of 10°C is met by the heat transfer rate produced by an auxiliary heater, $Q_{th,boiler}$, fed with the biogas produced by the anaerobic digester. This heat is equal to roughly 12 kW.

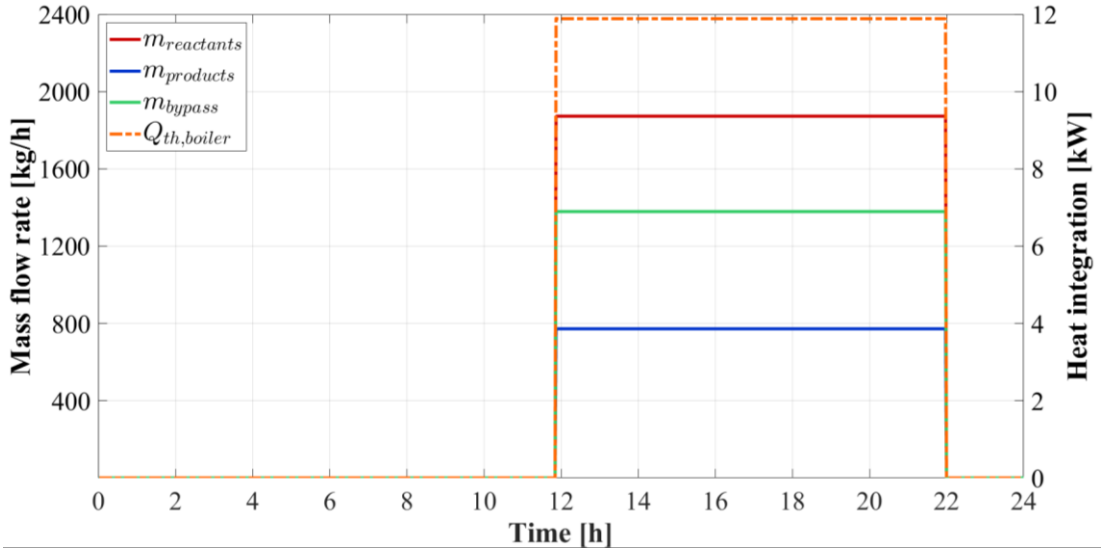

Figure 85. Heat recovery in the methanation unit.

In Figure 86, the main energy ratios per each month are shown. The ratio $E_{syn}/E_{CH4,tot}$ represents the fraction of syngas produced with respect to the total amount of natural gas produced by renewables and supplied to the grid, i.e. the sum of biomethane and syngas. This ratio is useful to understand how the H_2 production from renewable source affects the total natural gas production in the proposed power plant. The syngas accounts for roughly 70% during the winter period and almost 85% in the summer period of the total renewable methane production of the plant. This result is due to the higher solar availability during the summer months, which allows the electrolyzer to produce more hydrogen. The ratios E_{comp}/E_{LOAD} and E_{heat}/E_{LOAD} show the weight of the electric energy necessary for the compression of the gases and the heating of the electrolyzer on the total electric load, respectively.

Conversely, the electric energy needed for the preheating of the cell is nearly constant, meaning that the thermal recovery has quite almost the same effectiveness. However, the weight of the compressors on the total electric load hugely increases in the summer period, from 0.34 to 0.47. As already explained, this is due to the massive production of H_2 during the summer period due to the higher solar energy availability. The greater the solar production, the greater the hydrogen and oxygen generation from the electrolyzer is. The factor η_{glob} is the ratio between the syngas related energy and the total input in the system, as shown in the Model section. The value is averagely constant, roughly 75%, because of the implemented control strategies that allow system operation at nearly rated condition.

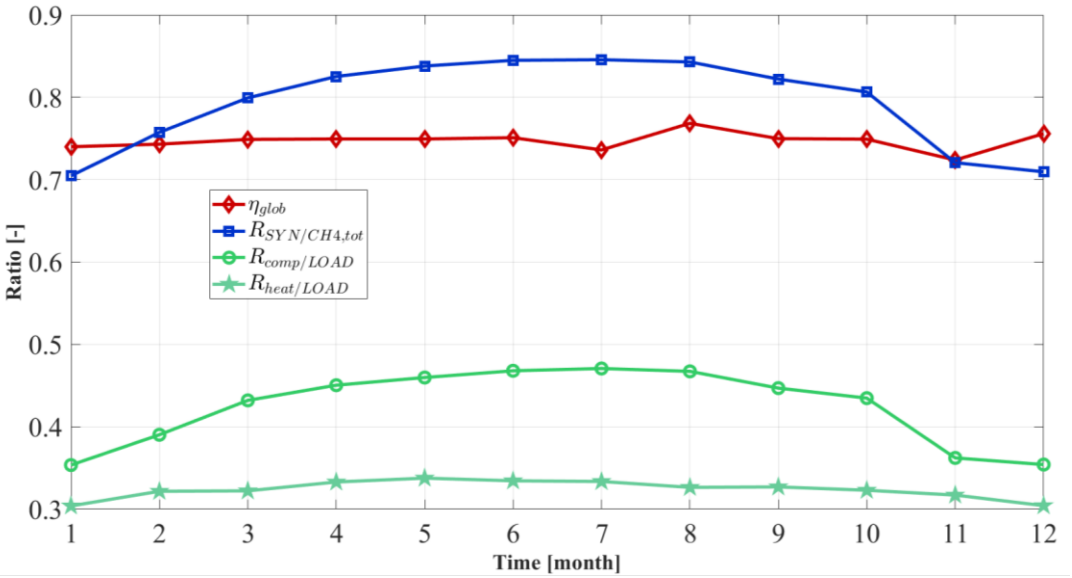

Figure 86. Monthly results in terms of energy ratios.

Results of the thermoeconomic analysis are shown in Table 29 and Table 30.

Table 29. Results of the thermoeconomic analysis.

Parameter	Description	Value		Unit
		RS	PS	
V_{bioCH4}	Volumetric flow rate of methane produced by renewables	492´003	2´523´525	Nm^3/year
$E_{el,fromGRID}$	Electric energy withdrawn from the grid	1.76	0.92	GWh/year
$E_{el,toGRID}$	Electric energy sent to the grid	-	3.81	GWh/year
PE	Primary energy consumed by the system	-1.07	-31.40	GWh/year
M_{CO2}	Total amount of CO_2 emissions due to the system	-139.76	-6´470.11	t_{CO2eq}/year
C	Operating costs of the system	-0.04	-1.91	M€/year
C_{O2}	Operating costs of the system considering O_2 selling	-0.04	-13.77	M€/year

The system proposed in this work is an innovative renewable-based plant which allows the production of a huge amount of natural gas. Both the primary energy PE_{RS} and the CO_2 emissions saved in the RS are remarkable and equal, respectively, to 1.07 GWh/year and 139.76 t_{CO2eq}/year. Note that both the values in the table are negative since they represent a value of energy and emissions saved by means of a huge production of biomethane injected into the gas grid. The value of the PE_{PS} and CO_2 saved in the PS are negative as well and equal to 31.40 GWh/year and 6´470.11 t_{CO2eq}/year respectively. The natural gas production by means of renewable sources in the PS is roughly three times the one in the RS, Table 8.

Table 30. Thermoeconomic indices.

Parameter	Description	Value	Unit
$E_{el,fromGRID}/E_{el,LOAD}$	Ratio of electricity withdrawn from grid	0.52	-

$E_{el,SOEC}/E_{el,PV}$	Fraction of PV electricity sent to the SOEC	0.71	-
$E_{SNG}/E_{el,PV}$	Syngas related energy respect to PV electricity	0.59	-
$E_{SNG}/E_{CH4,tot}$	Syngas related energy respect to total natural gas	0.81	-
$E_{comp}/E_{el,LOAD}$	Compressors electricity respect to total load	0.42	-
$E_{heat}/E_{el,LOAD}$	SOEC preheating respect to total load	0.32	-
η_{SOEC}	Average efficiency of the SOEC	0.92	-
η_{MET}	Average efficiency of the methanation reactor	0.82	-
η_{glob}	Average global efficiency of the system	0.75	-
Φ	Specific primary energy consumption	0.11	-
ΔPE	Annual primary energy difference	30.33	GWh/year
ΔM_{CO2}	Total amount of CO_2 savings	6´330	t_{CO2eq}/year
ΔC	Annual economic savings	1.87	M€/year
ΔC_{O2}	Annual economic savings with O_2 selling	13.72	M€/year
PES	Primary Energy Saving	28.25	-
C_{PV}	PV capital cost	14.53	M€
C_{SOEC}	Electrolyzer capital cost	17.95	M€
C_{MET}	Methanation reactor capital cost	2.57	M€
C_{TOT}	Total cost	36.15	M€
C_{CH4}	Unit cost of syngas produced	1.29	€/kg
C_{CH4}	Unit cost of syngas produced	0.09	€/kWh
M_{CH4}	Total syngas produced	1´452.54	t_{CH4}/year
SPB	Simple Pay Back period	19.33	year
SPB_{O2}	Simple Pay Back period with O_2 selling	2.63	year
NPV	Net Present Value	-9.97	M€
NPV_{O2}	Net Present Value with O_2 selling	155.98	M€
PI	Profitability Index	-0.28	-
PI_{O2}	Profitability Index with O_2 selling	4.31	-

The thermoeconomic analysis here proposed shows several interesting performance indicators, both in terms of energy and economic feasibility of the solution proposed. One of the most interesting indexes is the ratio $E_{SNG}/E_{el,PV}$ which assesses the roundtrip efficiency of the energy conversion system. This ratio, equal to 0.59, highlights how the conversion of 1 kWh of electricity into natural gas comes with an energy loss of roughly 40% per each kWh produced. Despite this, the renewable system produced is an important solution for the current energy framework because natural gas is an absolute necessity, as described in the Introduction section. Therefore, the proposed system is a promising solution for producing renewable methane. Moreover, the value of the index Φ of 0.11 reveals that the aim of abating the primary energy consumption is successful because per each kWh of natural gas produced, only 0.11 kWh of primary energy from fossil fuels is needed.

Therefore, the system also allows a huge saving of primary energy consumption, see the outstanding potential value of *PES* of roughly 29. This result is due to the huge amount of natural gas produced which is injected into the gas grid and dramatically reduce the consumption of natural gas produced by fossil fuels. On the other hand, the proposed solution suffers for the high capital cost, typical of some technologies as the electrolyzer. However, the economic feasibility of the system can be reached by means of the selling of the O_2 produced by the electrolyzer, which could lead to a *SPB* of 2.63 years. The O_2 is indeed widely used in industrial application and it can be sold to make the whole solution feasible. The *NPV* of the solution proposed is dramatically improved by the selling of O_2, in fact it is negative in case the O_2 is not sold and equal to roughly 156 M€ with O_2 selling. The same result is obtained when the profitability indexes are compared. The price of the natural gas produced is also competitive with the current market in Italy [150], where the solution is proposed.

In the previous analysis, a specific control strategy was discussed for the optimal operating conditions of the electrolyzer and the methanation unit. From an energy point of view, such system showed outstanding results demonstrating that the solution proposed optimally exploits the renewable energy surplus. Furthermore, the system so proposed can be furtherly optimized by the both the energy and economic point of view. To this scope, an optimization procedure to find out the values of the most important design parameters was carried out, by means of the TRNEdit tool of TRNSYS and computer Design of Experiment (DoE). Thanks to this technique, the set of synthesis/design parameters for optimizing the energy, environmental, and economic performances was detected. Thus, it is easy to obtain the best economic and environmental P2G plant solution changing the design parameters in a selected range. Statistical techniques are adopted to manage the high number of iterations and reduce the calculation time.

The DoE analysis is widely adopted both for commercial and academic purposes to maximize (or minimize) a selected objective function. More specifically, this methodology allows one to: (i) analyze the effects of the main design parameters on the considered objective function; (ii) create an analytic model of the selected objective function in relation to the system design variables; (iii) plot the optimum response surface, i.e., the graphical depiction of the assessed analytic function and (iv) perform an optimization procedure aiming at determining the optimal values of the design variables.

In this paper, the optimization procedure was achieved by means of computer simulations carried out by TRNEdit rather than using the conventional experimental campaign. This technique allows one to design a pre-optimized system, achieving significant energy and

economic savings with respect to the conventional approach based on standard energy and economic feasibility analyses.

In the DoE approach, a full factorial design was used in order to improve results accuracy, only paying the disadvantage of longer computational times. Therefore, the number of system design variables and the corresponding levels were selected to achieve reasonable computation times. For the optimization procedure considered in this paper, the following four design variables were selected: (i) the nominal capacity of the photovoltaic field; (ii) the nominal capacity of the SOEC; (iii) the total capacity of the H_2 tank; (iv) the nominal capacity of the methanation unit. It is worth noting that the variation of the capacity of the SOEC and the also determines a variation of the selection of a number of components (compressors, heat exchanger, etc.) which must be selected on the basis of those two capacities. For all the considered variables, the number of levels was set equal to 3 except for the PV field whose number of levels was equal to 4. The values and the corresponding levels are reported in Table 31.

Table 31. Optimization variables and corresponding levels.

Variable	Unit	Level 1	Level 2	Level 3	Level 4
PV size multiplier	-	0.05	0.4	0.8	1
SOEC size multiplier	-	0.2	0.6	1	-
H_2 tank size multiplier	-	1	1.4	1.8	-
MET size multiplier	-	0.2	0.6	1	-

For such operating conditions, 188 different simulations were conducted in TRNEdit. Each simulation was referred to a whole year with a time-step of 0.03 h. The resulting computational time was close to 1 h per each simulation. Therefore, the overall optimization can be completed in about 8 days of continuous calculations. In particular, the *SPB* and the *PES* objective functions were selected, so for each possible combination of the considered design variables, such functions were calculated. Through these different simulations, it is possible to observe the main effects of the selected variables on the system performance, optimizing on the basis of the energy and economic performance the system proposed.

By means of the main effect plots (factorial plots) the mean value of the selected objective functions for each level of the considered design variable was obtained, together with the influence of each design parameter variation on the objective functions. Figure 87 and Figure 88 show the main effect plots for *SPB* and *PES* objective functions.

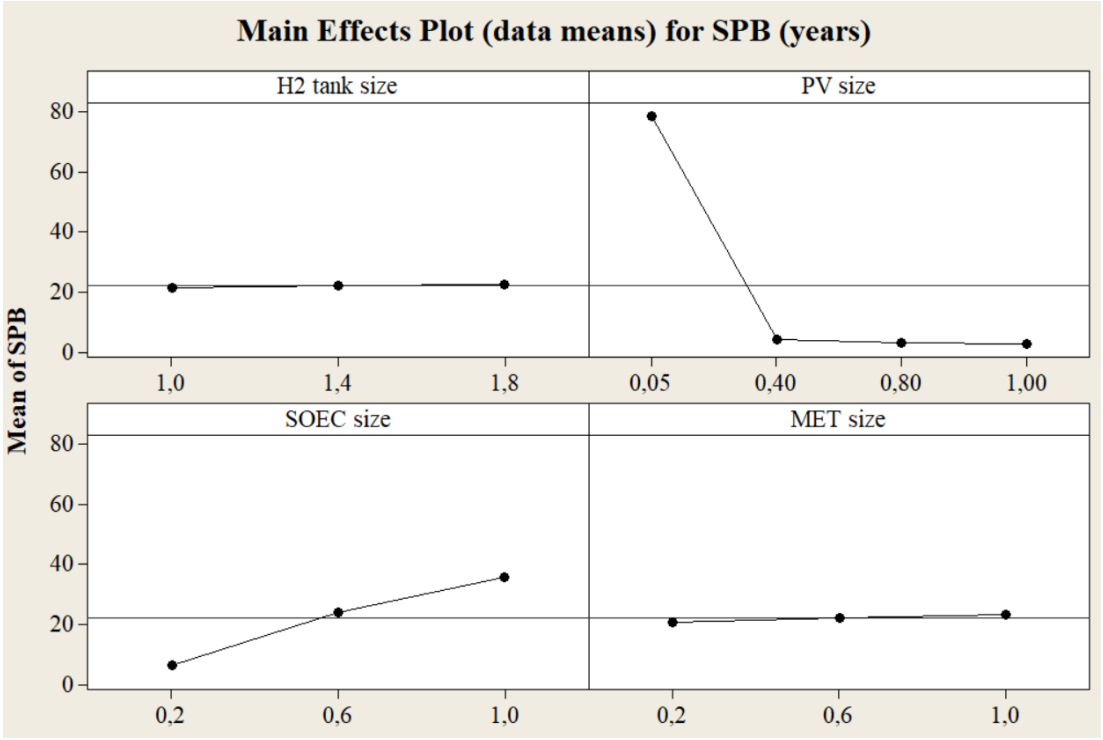

Figure 87. Main effects plot: *SPB*.

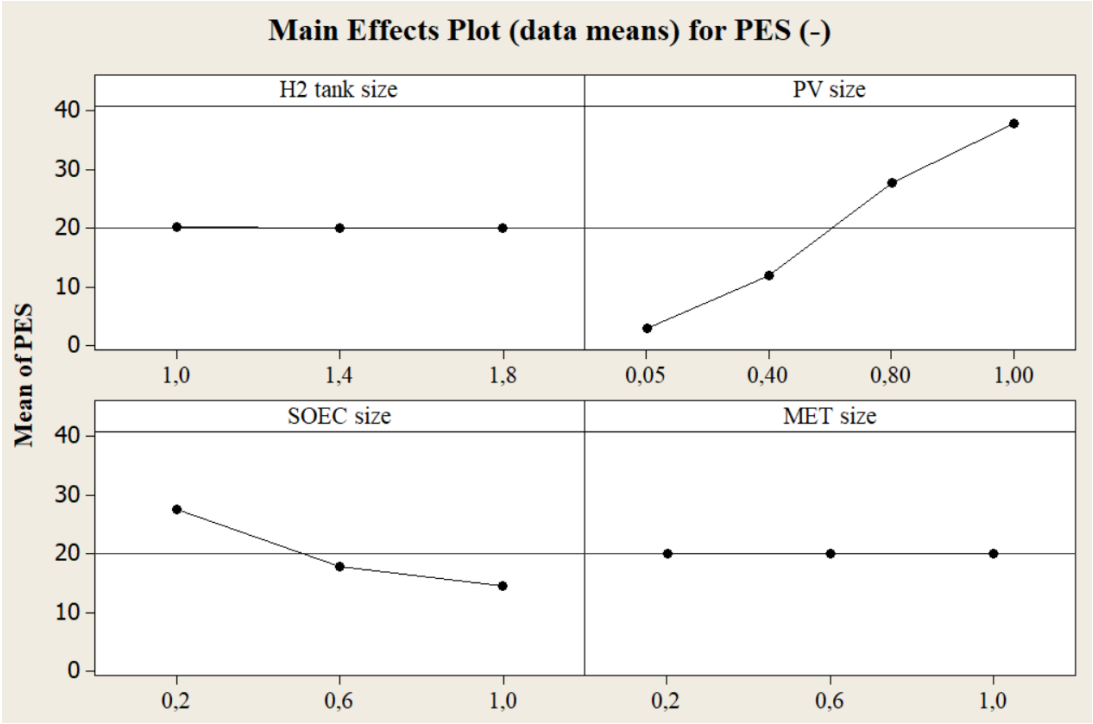

Figure 88. Main effects plot: *PES*.

Figure 87 shows a minimum for the *SPB* (equal to 2.5 years) obtained by selecting the same size of the PV field used in the results discussed but a much smaller SOEC capacity of 6 MW. The analysis also suggests using a 500 bar H_2 tank and a 6 MW methanation unit. However, it is clear that the most influencing variables for the *SPB* variation are the PV size and the SOEC size. In fact, despite the high capital cost of the PV field, the *SPB* values

with the size ratio equal to 1 are lower than the one with the size equal to 0.4. When the capacity ratio is even smaller, the renewable energy surplus available is much lower, decreasing the operating hours of the SOEC and the methanation unit.

Conversely, Figure 88 shows that the *PES* is directly proportional to the PV capacity. In fact, the maximum *PES* value is equal to roughly 40, obtained selecting PV capacity ratio equal to 1. At the same time, decreasing the size of the SOEC leads to an increase of the *PES*, this is due to a larger amount of electricity that is not used for the production of natural gas but it is supplied to the grid. Unfortunately, this solution is not accepted since it is in contrast with the initial aim of reducing the release of renewable excess to the electric grid. In fact, in the current energy framework, the excess of electricity sent to the grid must be minimized to avoid two main issues related to it: i) the overload of the grids at local level during the most irradiated hours, which may lead to overvoltages of the grid [151]; ii) the dissipation of the renewable energy produced which cannot be collected and exploited with the current infrastructures [152]. In fact, with the current electricity infrastructure the energy surplus would be mostly dissipated, and a real exploiting of the electricity surplus may occur in a future scenario which is not still practicable. The purpose of the P2G strategy is precisely to exploit the energy surplus to produce useful energy vector in the form of natural gas. Therefore, the solutions which are featured by a high amount of renewable power excess, although mathematically possible, are excluded from the solutions of the optimization problem. The methanation unit capacity and the H_2 tank capacity do not significantly affect the *PES* values. Tanks volumes do not significantly affect the costs. However, these analyses should consider that the value of the *PES* is always extraordinarily high, therefore, in this case the objective function must be focused on the economic parameters rather than the system environmental impact. Given the scarce influence of storage on the economic results, it is recommended to select sizes of storage with great capacity to stabilize the system more easily.

Figure 89 and Figure 90 show the interaction plots (factorial plots) where two factors per time were compared, unlike the previous plots in which only one factor was analyzed per time to find out the optimal values for *SPB* and *PES*. The results obtained from these plots confirm what hitherto achieved by the previous analyses. In fact, the optimal value of the *SPB* is obtained with PV and H_2 tank capacity ratio equal to 1, SOEC capacity ratio equal to 0.6, and methanation reactor capacity ratio equal to 0.2. The optimal *PES* value, instead, is obtained with PV capacity ratio equal to 0.8, H_2 tank capacity ratio equal to 1, SOEC capacity ratio equal to 0.6 and methanation reactor capacity ratio equal to 0.2. The values selected for the *PES* are not the highest shown in the graphs but are the ones which give the highest value according to a reduced excess of renewable power, according to the P2G strategy.

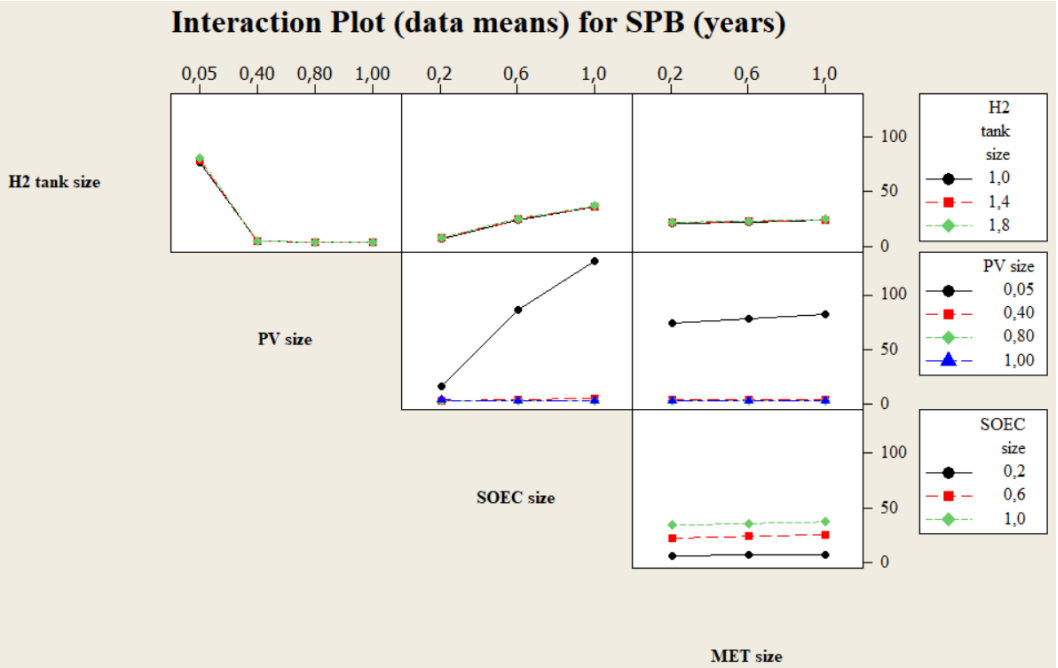

Figure 89. Interaction plot: *SPB*.

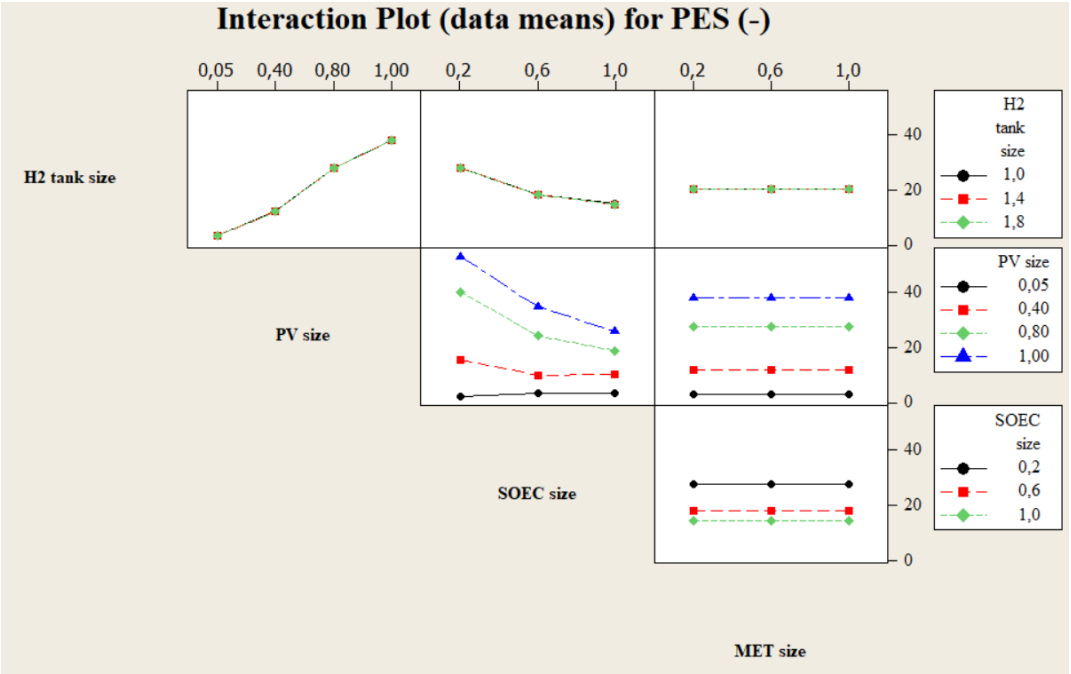

Figure 90. Interaction plot: *PES*.

Figure 91 and Figure 92 display the contour plots of the optimal response surface for *SPB* and *PES*, holding constant the extra factors.

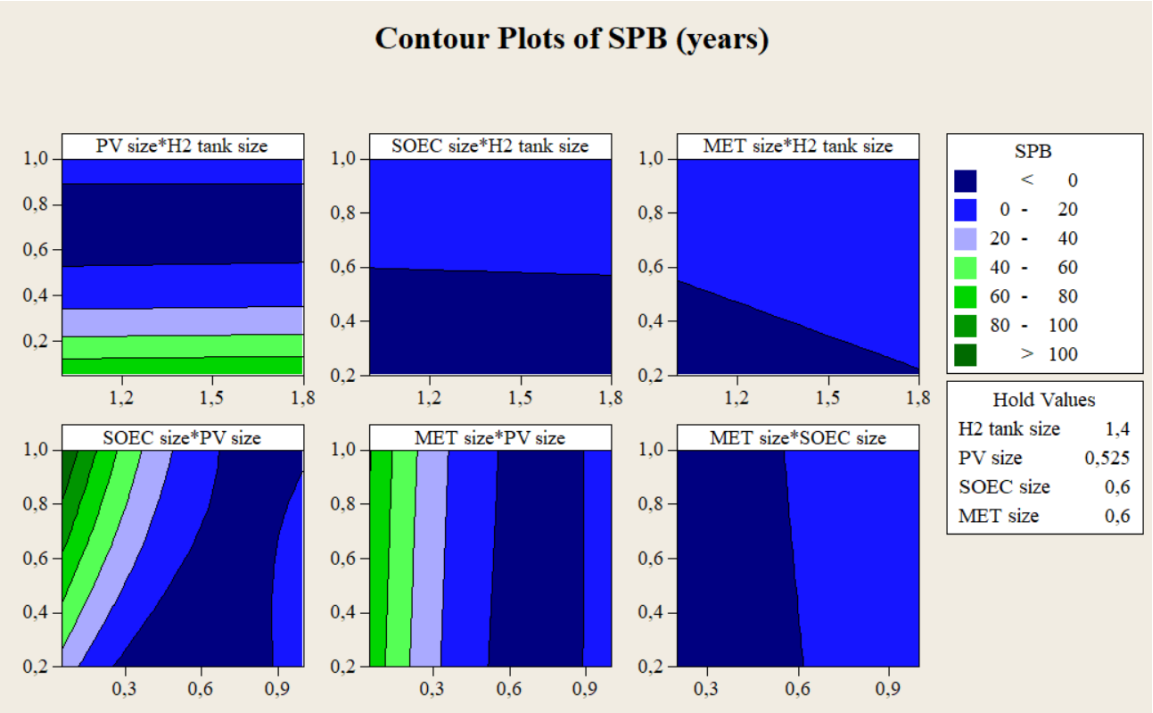

Figure 91. Contour plot: *SPB*.

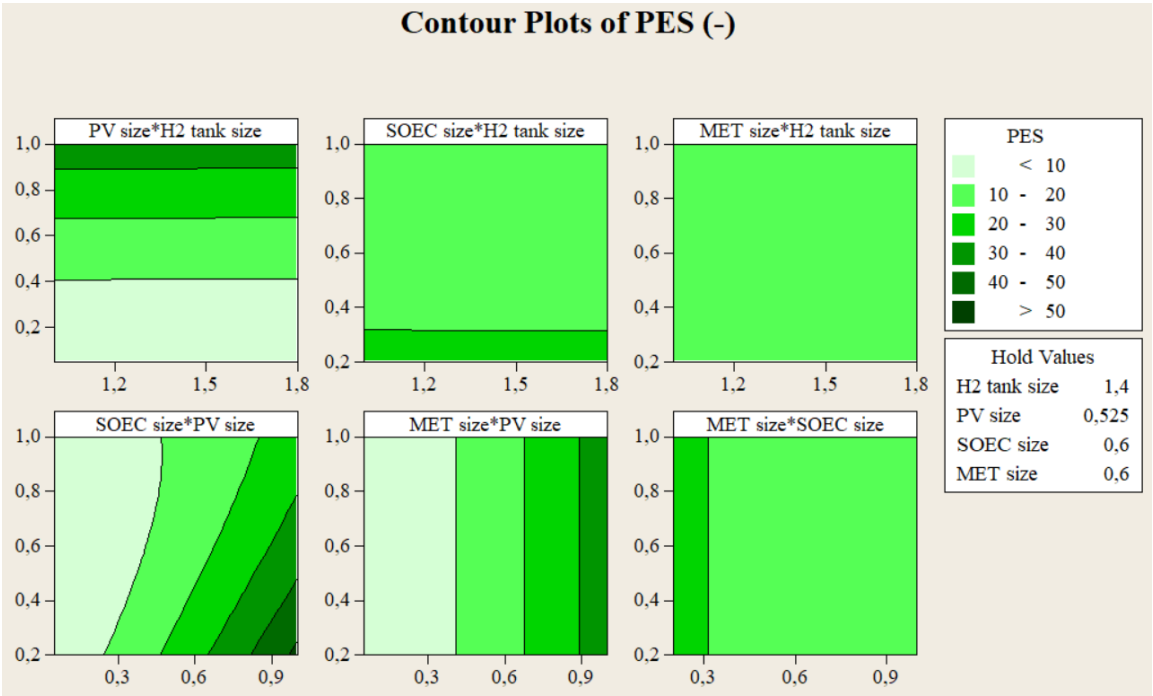

Figure 92. Contour plot: *PES*.

Each contour figure includes six subplots, obtained by the matching of all the possible combinations among the four considered design values. In each subplot the product between two independent variables considered is shown. Therefore, for each plot two design variables were considered at the same time, whereas fixed values were given for all the remaining variables. Such values are reported on the right side of each figure. From the

SPB plots, one can note that the system performance is particularly sensitive to the PV and SOEC capacity selection. In fact, the subplot showing the highest variation in *SPB* is the bottom left one, showing the combination of those two variables. The *SPB* is instead barely affected by the variation of the other variables. In fact, the remaining subplots show almost vertical and horizontal lines. In particular, the top right subplot shows that H_2 tank volumes negligibly affect system economic performance unless it gets too much small compared to the size of the methanation unit. By analysing the *PES* plots, it is possible to note that system performance is sensitive mainly to the PV size and specifically in combination with the SOEC size. In fact, the significant variations only occur when the PV capacity ratio is involved and the influence of this parameter barely depends on the variation of the other ones. The upper right subplot, which is featured by only one colour, shows that methanation unit capacity and H_2 tank volumes negligibly affect the economic performance of the system. In conclusion, the response surface analysis shows the same general trends obtained by the main effects plots. However, the analysis of the response surface is useful to detect the optimal configuration for all the combinations of the design parameters. The results in terms of optimal configuration for both the *SPB* and the *PES* are shown in Table 32.

Table 32. Optimal configuration for the objective functions of optimization analysis.

Variable	Unit	Optimal *SPB* value	Optimal *PES* value
PV size multiplier	-	1	0.8
SOEC size multiplier	-	0.6	0.6
H_2 tank size multiplier	-	1	1
MET size multiplier	-	0.2	0.2

5.5 Exergy and thermoeconomic analysis of a novel power-to-X polygeneration system integrating gasification, electrolysis, and anaerobic digestion

The scientific literature review discussed in this section deepened the framework of the most recent works on polygeneration systems dealing with biomass and solar energy sources. The analysis allowed to emphasize at the same time the innovations and the limits of the existing works. Many works dealing with solar energy based polygeneration systems consider PTC fields but neglect the possibility of adopting PV systems integrated with some other technologies. Furthermore, biomasses are mainly considered as a useful resource to feed boilers or to be used for feeding gasifiers when it comes to rural areas. In very few cases anaerobic digestion is integrated into more complex layouts but rarely used to observe how it helps to increase performance in connection with system dynamics.

Conversely, more innovative plants do not come with deep exergy or thermo-economic analysis of the solution proposed. For the sake of clarity and brevity, the main works presented in the literature review are summed up in Table 33. This research aims to bridge the gap in the existing literature within the framework of solar-driven polygeneration systems integrated with biomasses. In particular, this novel layout is based on a gasification unit fed by organic biomass and utilizing steam and oxygen as gasifying agents. The oxygen is provided as a by-product of an electrolyzer driven by renewable electricity surplus coming from a photovoltaic system. The hydrogen produced is stored and blended with the syngas produced by the gasification unit to drive a cogenerator entirely driven by renewable energy. Moreover, the fuel is also integrated with biogas produced by an anaerobic digestion unit to stabilize the gaseous mixture and exploit biomass wasted by the end user. To sum up, the main novelties of the work are the following:

- Innovative layout of a renewable based polygeneration system integrating power to X technology with biomass used for driving the operation of a gasification unit and an anaerobic digester.
- Accurate energy, exergy, and environmental analysis of the layout proposed to detect the main strengths and exergy deficiencies in the system, also assessing the final environmental impact and efficiency.
- Thermo-economic analysis to assess the economic feasibility of the solution proposed according to the environmental results obtained.
- Dynamic simulation of the system with hourly load from the real case study of the botanical garden José Celestino Mutis in Bogotá, Colombia.

Table 33. Summary of the main works investigated in the literature review.

Technologies	Inputs	Outputs	Analysis	Dynamics	Conclusions	Reference
PTC, PV, PEMEC, SOFC, ACH	Solar energy, grid electricity	Power, heating, cooling, hot water	Dynamic behaviour of components, response time	yes	Response times less than 1 s for PV, 3–22 s for PEMEC, and about 25 s for SOFC, whereas for PTC and ACH elapse from 10 to 30 min.	(Zheng,2023) [153]
Heliostat field, CO_2 cycle, desalination unit, electrodialysis unit, CCHP	Solar energy, seawater	Power, cooling, heating, desalinated water, NaClO, H_2	Energy, exergy, exergo-environmental, environmental	no	11.89 GWh/y electricity, 5.3 GWh/y cooling, 6.5 GWh/y heating, 9.8 t/y *NaClO*, $2.2_{\times 10^8}$ m^3/y H_2, $2.8_{\times 10^5}$ m^3/y desalinated water, η = 22.39 %, ψ = 40.24 %, *SPB* = 5 years.	(Esmaeilion, 2022) [154]
Flat plate STC, PV, Three fluids heat exchanger	Solar energy	Power, heating, cooling, hot water	Energy, exergy, economic	no	Optimal zone: PV production 1.75 MWh, *LCOE* = 0.1 €/kWh, η_{STC} = 64.6 %, ψ = 1.3 %, *SPB* = 5.2 years.	(Rout, 2021) [155]
KC, GT, double-pressure steam cycle, ORC, MED, RO, PEMEC	Biomass, seawater, solar energy	Power, heat, freshwater, H_2	Energy, exergy, economic, and environmental	no	η = 39 %, ψ = 32 %, power generation costs and environmental impacts for MSW biomass are 0.014 $/kWh and 0.002 Pts/kWh	(Rabeti, 2023) [156]
EFGT, ACH, ORC,	Biomass	Power, heating, cooling, hot water	Thermoeconomic	yes	ΔCO_2 = 582 t/y, *SPB* = 7.15 years, *NPV* = 1.4 M€, *PI* = 0.73.	(Di Fraia, 2023) [157]
Gasifier, PSA, GT, Allam cycle	Water, biomass	Power, heating, ammonia	Energy, exergy	no	η_{el} = 50.59 %, energy consumption of ammonia synthesis 30.25 GJ/t-NH_3, ψ = 51.5 %	(Xu, 2021) [158]
GHP, AD	Ground, biomass, electricity	Cooling, heating, biogas, fertilizer	Energy, exergy, thermoeconomic	yes	*PES* from 21.6% to 32.2%, ΔC from 35.6% to 34.4%, ψ = 32.2%.	(Luo, 2023) [159]
PTC, boiler, VAR	Solar energy, biomass	Power, heating, cooling, hot water	Energy, exergy, economic	no	η = 49.85 %, ψ = 20.94 %, VAR power 7.28 MW, desalination output 4.40 MW, total 14.61 MW, *SPB* = 1.5 years, *LCOE* = 0.08 €/kWh.	(Sahoo, 2018) [160]
PTC, boiler, ORC, vapor compression cycle	Solar energy, biomass	Power, heating, cooling	Energy, exergy, thermoeconomic	yes	η = 51.26 %, ψ = 21.77 %, ΔCO_2 = 125 t/y, *SPB* = 5.13 years, *NPV* = 165.6 k€.	(Bellos, 2018) [161]
PV, WT, AD, CHP	Solar energy, biomass	Power, heating, cooling	Technoeconomic	yes	*LCOE* from 0.044 to 0.070 USD/kWh, penetration of solar energy can reach up to 32%, ΔCO_2 from 109 to 127 t/y.	(Villarroel-Schneider, 2023) [162]

5.5.1 System Layout

The layout of the process plant proposed is shown in Figure 1.

In the polygeneration system presented, a PV generator reduces the amount of energy withdrawn from the electric grid. The electricity produced by the PV is, in part, used to meet the energy demand of the components of the plant that require power to operate. The surplus of the electricity produced by the PV is sent to an alkaline electrolysis cell (AEC), operating at 7 bar and 333 K (60 °C). The electrolyzer produces almost pure hydrogen (H_2) and oxygen (O_2) which are used for different purposes. The hydrogen is cooled down and compressed to be stored and used in the final mixture of the fuel to increase the lower heating value (LHV) of the syngas. The oxygen is sent to the gasification unit to operate as a gasifying agent and increase the efficiency of the system. When O_2 is not available, steam is used as gasifying agent to perform the gasification of the biomass. Both O_2 and steam entering the gasifier are preheated by means of the outgoing flow of syngas, up to a temperature of 700 K (427 °C). The syngas produced is used in the final mixture of fuel after a process of cleaning.

The syngas has a different composition depending on the gasifying agent used. In case steam is the gasifying agent, the content of H_2 in the syngas after cleaning is almost 50% in volume, with great percentages of both H_2O and CO_2, which negatively contribute to the chemical energy of the gaseous compound. When O_2 is the gasifying agent, the percentage of H_2 in volume increases above 60%, with much lower values for H_2O and CO_2. More details regarding the chemical composition of the syngas and the flow rates considered are given in the Case Study section. Air could also be used as gasifying agent but the performance of the gasifier would dramatically decrease, so this option is not considered in this layout, although it would be possible. The gasification unit is a downstream allothermal gasifier fed with lignocellulosic biomass and operating at a temperature of 850 °C. During the starting phase of the gasifier, the thermal energy is provided by a biomass-fed auxiliary heater, whereas in normal operating conditions the heat provided by the same syngas is sufficient. The polygeneration system is also integrated with an anaerobic digester operating with organic fraction of municipal solid wastes (OFMSW) at a temperature of 38°C, thus at mesophilic conditions. The biogas produced by the anaerobic digester is composed of roughly 65% CH_4 and 35% CO_2, with some other minor impurities. The biogas, the syngas, and the hydrogen produced with this system are then mixed together to feed an internal combustion engine (ICE) operating as a CCHP. This cogenerator is used to meet the energy demand of a hospital close to the botanical garden, which has demand for power, heating, cooling, and freshwater.

There are multiple control strategies applied to this process plant to ensure optimal operating conditions and highest flexibility of the system. The first control strategy is applied to the electricity surplus sent to the AEC from the PV when the production overcomes the demand of the botanical garden. In fact, this energy surplus is only sent to the AEC when it lies within a range of minimum and maximum power of the electrolyzer. This solution is applied both for guaranteeing an higher average operating efficiency of the device and a longer lifespan of the technology, avoiding detrimental operating conditions [163]. When the electric energy surplus is lower than the minimum allowed for the electrolyzer, or higher than the maximum value allowed, the electricity is directly sent to the electric grid and sold at the price of electricity selling price. A control strategy is also applied to the H_2, O_2, and biogas tanks for better managing of the syngas composition in the engine [164]. The strategy works this way: each gas is sent to the respective tank and stored until the tank gets up to the set point state of charge (SoC), which is equal to 0.40 for O_2 ($\Phi_{TK,O2} = 0.40$), 0.15 for H_2 ($\Phi_{TK,H2} = 0.15$), and 0.20 for the biogas ($\Phi_{TK,bio} = 0.20$), with a dead band to avoid excessive oscillations during charging and discharging phase.

For the sake of clarity, the flowchart of the control strategy considered for the tanks is shown in Figure 94. According to the flowchart, the gasifier operating with steam as gasifying agent is the backup technology, which operates when O_2 is not available. When the other tanks are not able to provide any other gas because their SoC is below the set point, the gasifier provides the syngas to the ICE. In case the biogas tank is at least 20% full - $\Phi_{TK,bio} = 0.20$ - the biogas is the first gas sent to the engine for driving its operation. The main reason lies behind the fact that the biogas flow rate produced by means of the AD is constant during normal operating conditions, and this guarantees a more stable LHV of the fuel. Stabilizing the fuel properties is advantageous for increasing the engine efficiency more easily [165]. To increase the LHV of the fuel, the H_2 is blended with the biogas when the biogas power is not sufficient to meet the energy demand. The H_2 is exploited when the SoC of the H_2 tank is at least equal to the set point of $\Phi_{TK,H2} \geq 0.15$ and there is necessity of fuel power. The minimum SoC required for the H_2 tank is lower since the aim is to exploit at most the operation of the AEC by always guaranteeing a certain amount of H_2 in the blending. The flow rates for all the gases are selected according to the primary energy required and the LHV of each of them.

When H_2 is not available or the fuel power is not sufficient to meet the demand of the ICE, the syngas is integrated in the gaseous compound. In this case, according to the same strategy, O_2 is used as gasifying agent if it is available, i.e. $\Phi_{TK,O2} \geq 0.40$, otherwise the gasification unit operates with steam as gasifying agent. There are two main reasons for adopting this strategy. The first one is to exploit at most the O_2 produced by the electrolyzer by increasing the energy and exergy efficiency of the gasifier when surplus of

renewable electricity are available [166]. This is a great contribution to increase the flexibility of the whole polygeneration system. The second reason is that in the case study proposed, there is no interest in storing O_2 for different usage, as for selling to industries or usage in pharmaceutical application. Nevertheless, if one wants to consider these options, it is sufficient to change the storage strategy to perform a different analysis including the new feature. Moreover, as it will be discussed in the Model section, using O_2 as gasifying agent also allows to decrease the biomass consumption, which could be a relevant strategy to cover periods of lack of resource. Therefore, O_2 is used as gasifying agent as long as it is available, according to the control strategy on the pressure level in the tank. When O_2 is not available, steam is used as gasifying agent, by assuming that there is always enough water for the operation of the gasifier. In this case, for calculating the flow rates of O_2 and steam needed to produce the syngas necessary to meet the fuel demand of the engine, a bottom-up calculation is provided. In fact, the syngas flow rate is first calculated depending on the LHV of the mixture, and in turn the biomass required is measured. Once the required amount of biomass necessary for producing the syngas is obtained, the gasifying agent flow rate is calculated by means of optimal agent/biomass ratio [167]. The final LHV of the fuel is calculated as the weighted average of the LHV of each component of the mixture (ξ) [168].

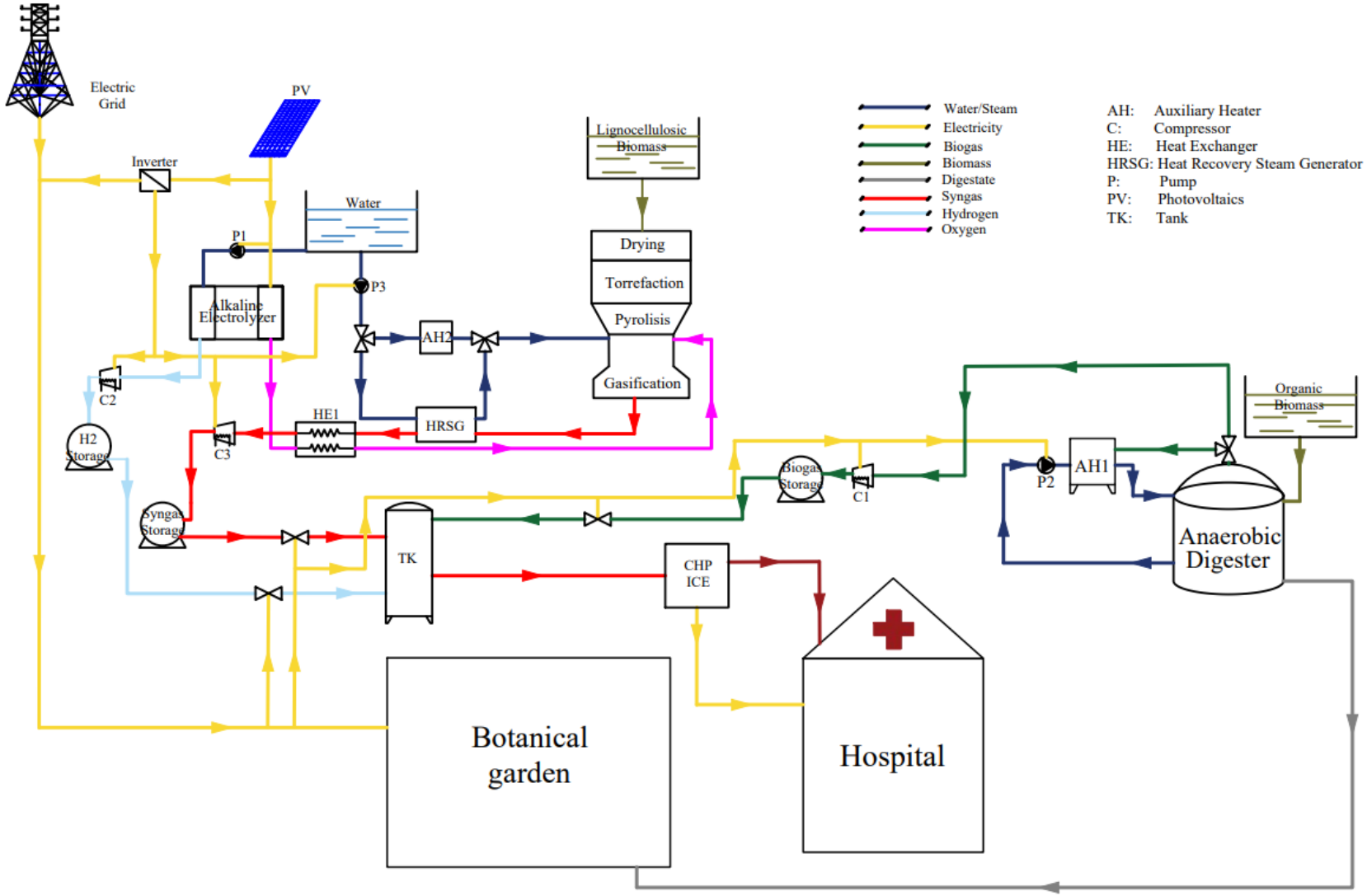

Figure 93. Layout of the novel polygeneration system proposed.

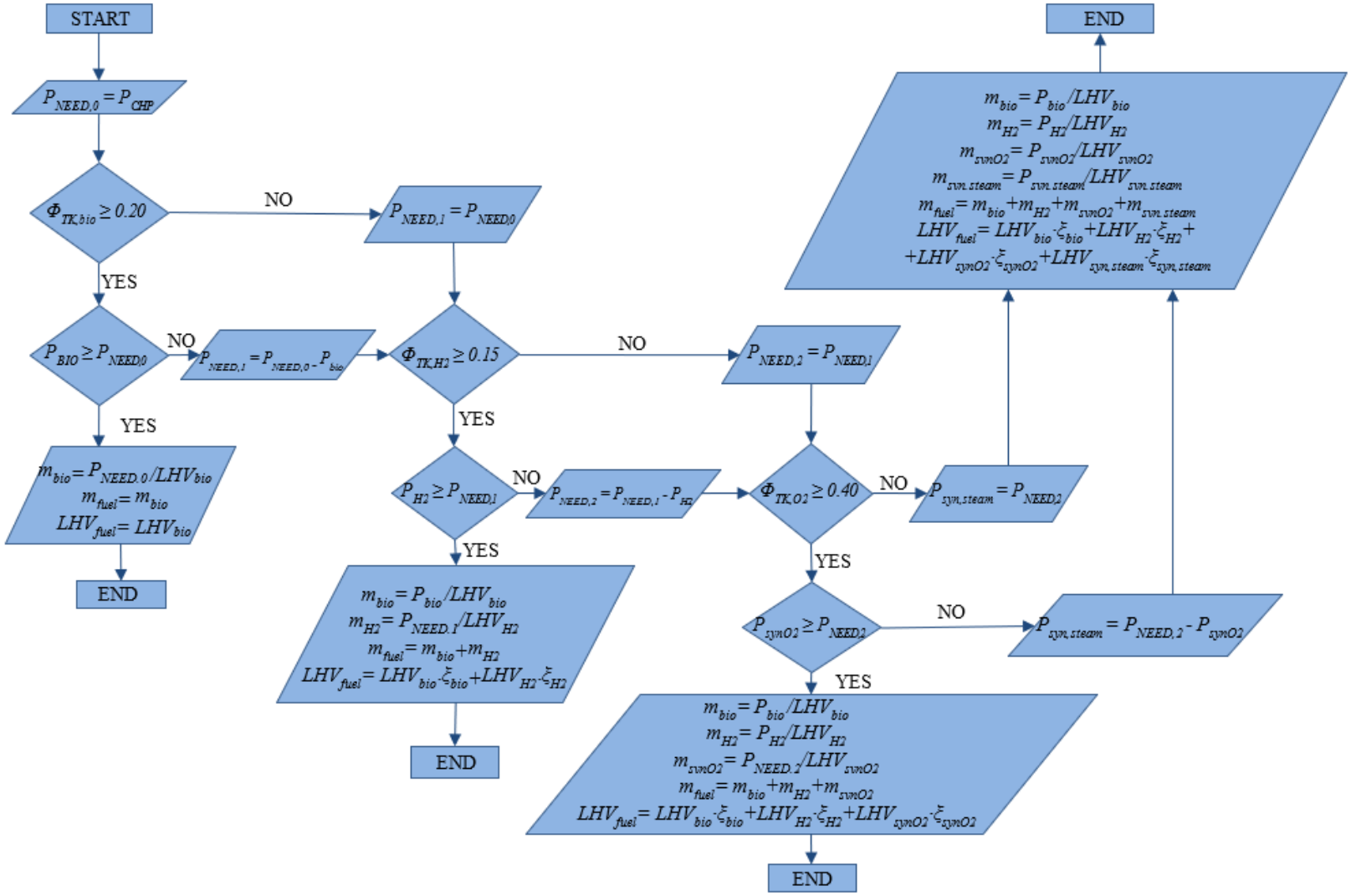

Figure 94. Flowchart of the control strategy applied to the H_2, O_2, and biogas tanks.

5.5.2 System Model

The model of the polygeneration system proposed in this work is a multi-interactive model developed by means of several tools which are then integrated to perform the simulation of the plant as a whole. In fact, each main component is developed with a different software, for example the electrolyzer model is developed in MatLab or the gasification model is developed in EES. After validation with experimental data measured or gathered from the scientific literature, the models are integrated into TRNSYS environment to perform the dynamic simulation of the whole plant [169]. TRNSYS is a widely adopted simulation environment for analysing transient operating conditions of RES based energy systems [96]. In fact, by means of TRNSYS is possible to evaluate the dynamic weather conditions and the dynamic load profiles of the end users and observe how the demand matches with the energy production [170]. Furthermore, detailed exergy and thermodynamic models are integrated to perform accurate analyses of the system proposed . For the sake of brevity, in this section only the main models are presented and thoroughly discussed.

The gasifier modelled in this work is a downstream allothermal gasification unit developed on the Engineering Equation Solver (EES) software. The model is integrated with some measured data collected from bench test for a real gasification unit, thus only a partial approach to the chemical equilibrium is achieved. The model is then validated with experimental data collected to evaluate the variation of the final syngas composition depending on different gasifying agents adopted. For the sake of brevity, details of the model and validation are omitted in this work, but an accurate explanation can be found in ref. [167].

The model of the alkaline electrolyzer is a coupled thermodynamic and electrochemical model which allows to calculate the polarization curve of the electrolyzer under different operating conditions. This model is first developed in [171] and describes an alkaline electrolyzer with Nickel (Ni) foam electrodes using an aqueous solution of Potassium Hydroxide (KOH) as electrolyte at 30 wt% [172] and a Zirfon membrane for separating the electrodes. The model is developed in MatLab and provides the voltage, losses, and efficiency of the electrolyzer, for a given spectrum of values of the input current density "*j*". In this case the model is a lumped parameters thermos-electric model useful for providing accurate simulations when integrated into a more complex dynamic simulation model. A more detailed model is not considered because it would need more complex numerical computations [173] which are not compatible with dynamic simulations. Further

details about the model can be found in [171] and in the Exergy model and Results sections.

The anaerobic digestion model was already widely discussed in the previous chapters; therefore it is not further analyzed in this section.

In this section the exergy balances on the main components of the plant are shown and discussed, explaining the assumptions made per each component to simplify the calculation, without affecting the accuracy of the results. The exergy analysis of a process plant is an useful tool to understand and predict where the main exergy destructions occur, which allows to detect the specific components and processes which mostly abate the efficiency of the plant.

When it comes to chemical process plants, the exergy analysis must include both physical and chemical exergy balances per chemical reaction processes. Thus, the definition of the "dead state", which means the thermodynamic state in which the system is in equilibrium with the environment, necessarily involve the knowledge of the concentration of the chemical species in a gaseous flow and their chemical potential[174]. In this work it is assumed that at the equilibrium state the pressure p_0 is the atmospheric pressure and the temperature T_0 = 298 K. Eq.(81) and eq.(82) show, respectively, the specific physical and chemical exergy of a thermodynamic state:

$$ex_{ph} = \left(h - h_0\right) - T_0 \cdot \left(s - s_0\right) \tag{81}$$

$$ex_{ch} = \sum_i \left[x_i R_0 T_0 ln\left(x_i\right) + x_i \varepsilon_{0,i} \right] \tag{82}$$

Where h and s are the specific enthalpy and entropy of the specific state, the subscript 0 refers to the dead state, x_i is the molar fraction of the i-th chemical species and $\varepsilon_{0,I}$ is the related chemical exergy content.

The value of chemical exergy content $\varepsilon_{0,i}$ per each chemical species is given from literature and is shown in Table 34.

Table 34. Chemical exergy, formation enthalpy and molecular weight of the chemical elements.

chemical	ε_0 (kJ/kmol)	h_f (kJ/kmol)	MW (kg/kmol)
H_2O (g)	11´710	-241´818	18.015
H_2O (l)	900	-285´830	18.015
CO	275´430	-110´525	28.01
H_2	238´490	0	2.016
O_2	3´970	0	31.999
N_2	720	0	28.014

CO_2	20´140	-393´509	44.01
CH_4	836´510	-74´520	16.043

The exergy analysis is performed for each of the main components of the system shown in Figure 93, namely: gasifier, alkaline electrolyzer, anaerobic digester, photovoltaic field, and heat exchangers. Then, once the exergy destruction rates and exergy efficiencies per each component are detected, the overall exergy efficiency of purpose of the polygeneration system is analyzed.

Exergy balance on the gasifier

In order to perform the exergy analysis of the gasifier, some simplifying assumptions are made, according to works available in literature [175]. The main assumptions of the model are:

- The input biomass is at ambient temperature, supposed equal to T_0
- Exergy terms related to ash and tar are neglected in the exergy balance
- Physical exergy is negligible for the input biomass and the output char
- Ideal gas behavior considered for all the gases, including the steam, because of the high temperature level of the process
- Pressure drops in the gasifier are neglected
- Kinetic and potential energy terms neglected in the analysis

As said, the gasifier may operate with three different gasifying agents, namely air, steam, and O_2. In the system proposed only steam and O_2 are considered because of the high exergy destruction rate and low heating value of the final syngas when air is considered. Thus, the exergy balance of the gasifier is the following:

$$\dot{E}x_{biomass} + \dot{E}x_{agent} = \dot{E}x_{syngas} + \dot{E}x_d \tag{83}$$

Where the terms on the left side are, respectively, the exergy of the biomass flow rate and the exergy of gasifying agent, whereas the terms on the right side represent, respectively, the exergy of syngas flow rate and the exergy destroyed. The exergy of the biomass is calculated as [176]:

$$\dot{E}x_{biomass} = \dot{m}_{biomass} \cdot \beta \cdot LHV_{biomass} + MC \cdot (ex_w + \beta \cdot h_w) \tag{84}$$

Where β is a correlation factor calculated according to [176], which is a function of the C, H and O concentration in the biomass:

$$\beta = \frac{1.044 + 0.016 \cdot \left[\frac{H}{C}\right] - 0.3493 \cdot \left[\frac{O}{C}\right] \cdot \left(1 + 0.531 \cdot \left[\frac{H}{C}\right]\right)}{1 - 0.4124 \cdot \left[\frac{O}{C}\right]} \tag{85}$$

The second term on the right side of eq.(84), is due to the presence of a moisture content in the input biomass, but it is negligible compared to the first term [176]. The exergy input of the gasifying agent and the output syngas are calculated as sum of the chemical and physical exergy flows of gaseous mixtures:

$$\dot{E}x_{gas} = \dot{m}_{gas} \cdot (ex_{ch} + ex_{ph}) \tag{86}$$

Where the physical exergy ex_{ph} was calculated according to the assumption of ideal gas behavior and the chemical exergy ex_{ch} according to values in Table 34. The extended form of the eq.(86) thus become:

$$\dot{E}x_{i,j} = \left(\dot{m}_{i,j} c_{p,i} \left(T - T_0\right) - \dot{m}_{i,j} T_0 ln\left(\frac{T}{T_0}\right)\right) + \left(\dot{n}_{i,j} R_0 T_0 ln\left(x_{i,j}\right) + \dot{n}_{i,j} \varepsilon_{0,i}\right) \tag{87}$$

Where $Ex_{i,j}$ is the output exergy of the i-th chemical species with the molar and mass fractions evaluated when the j-th gasifying agent is driving the operation of the gasifier. The exergy destruction rate Ex_d is calculated as the difference between the exergy input and output. The specific heat $c_{p,i}$ per each gas is calculated according to the well-known semi-empirical 4-th order correlation as a function of the temperature, where all the constants are given by thermodynamics books [177].

The exergy efficiency of the gasifier is calculated as:

$$\psi_{GAS} = \frac{\dot{E}x_{syn}}{\dot{E}x_{biomass} + \dot{E}x_{agent}} \tag{88}$$

For the alkaline electrolyzer some simplifying assumptions are made as for the gasifier. In this case, the water at the inlet of the electrolyzer is supposed to be at ambient pressure and temperature. The electrolyzer operates at a higher pressure level than the ambient pressure, so the gradient is not negligible at the outlet. The gases at the outlet are ideal gases. The exergy balance is the following:

$$\dot{E}x_{el} + \dot{E}x_{H_2O} = \dot{E}x_{H_2} + \dot{E}x_{O_2} + \dot{E}x_d \tag{89}$$

Where Ex_{H2O} is the exergy related to the inlet water flow, $E_{x,el}$ is the electric exergy, which is equal to the electric energy, and it is equal to the P_{el} is calculated in section

3.2. The physical and chemical exergy related to the inlet water flow rate and the outlet H_2 and O_2 flow rates are calculated as for the gasifier, according to eq.(87) and Table 34.

The exergy efficiency of the alkaline electrolyzer is calculated as:

$$\psi_{AEC} = \frac{\dot{E}x_{H_2}}{\dot{P}_{el} + \dot{Q}_{heat,H_2O} \cdot \tau} \tag{90}$$

The exergy balance on the anaerobic digester is the following:

$$\dot{E}x_{OFMSW} + \dot{E}x_{w,in} = \dot{E}x_{biogas} + \dot{E}x_{dig} + \dot{E}x_{w,out} + \dot{E}x_{loss} + \dot{E}x_{d} \tag{91}$$

Where Ex_{OFMSW} is the input exergy of the biomass used for the AD process, which is indeed the OFMSW, $Ex_{w,in}$ and $Ex_{w,out}$ are the exergy flows of the inlet and outlet water of the inner heat exchanger which is used to steer the temperature of the reactor [132], respectively, Ex_{biogas} is the exergy related to the biogas outlet flow rate, Ex_{dig} is the exergy of the outlet digestate flow rate, which is used a as a fertilizer in the botanical garden, and Ex_{loss} is the term referred to the thermal losses through the walls and the dome of the digester, calculated through the Carnot coefficient. In this case, the control volume selected for the exergy balance includes the inlet and outlet of the heat exchanger. Of course, one could perform the same balance by only considering the control volume of the digester and there would be only one term at the left side of the eq.(91) representing the heat provided by the heat exchanger. In this case, both inlet and outlet water flows are evaluated, and their physical exergy was calculated according to eq.(81). The same approach is used for the exergy flow rate of biogas which is calculated according to eq.(87) and Table 34.

The exergy related to the biomass and the digestate are calculated according to eq.(84) since the chemical exergy is assumed to be predominant for the term [176]. The parameter beta was calculated according to literature, where tables for diverse biomasses are available with the average composition in terms of C, H, and O content for each type. Furthermore, due to lack of data, the LHV value of the input OFMSW was supposed to be the same of the biomass entering the gasifier, which is close to values found in literature for municipal solid wastes [178]. At the same time, the LHV of the output digestate is assumed to be half of the LHV of the inlet biomass, according to the scientific literature [179].

The exergy efficiency of the anaerobic digester is calculated as:

$$\psi_{AD} = \frac{\dot{E}x_{biogas}}{\dot{E}x_{OFMSW}} \tag{92}$$

The exergy efficiency of the heat exchangers strictly depends on the aim of the heat transfer device. In fact, in case the goal of the heat transfer is to heat the cold fluid, as in this case, the exergy efficiency is calculated as

$$\psi_{HX} = \frac{\dot{E}x_{cold,out} - \dot{E}x_{cold,in}}{\dot{E}x_{hot,in} - \dot{E}x_{hot,out}} \tag{93}$$

Where the term $Ex_{cold,out}$ is the rate of physical exergy output of the cold fluid, $Ex_{cold,in}$ is the rate of physical exergy input of the cold fluid, $Ex_{hot,out}$ is the rate of physical exergy output of the hot fluid, and $Ex_{hot,in}$ is the rate of physical exergy input of the hot fluid. In both cases, the exergy considered is the physical part, assumed to be far greater than the chemical part. The inlet and outlet temperature of the gasifying agent are known as well as the inlet temperature of the syngas. Thus, by means of the theory of the heat exchangers, it is easy to calculate the outlet temperature of the syngas and then the exergy efficiency of the heat exchanger. The exergy destruction rate is calculated as:

$$\dot{E}x_{d,HX} = T_0 \cdot \dot{Q}_{HX} \cdot \left(\frac{1}{\overline{T}_c} - \frac{1}{\overline{T}_h} \right) \tag{94}$$

Where Q_{HX} is the heat transfer rate from the hot fluid to the cold fluid. In all the models proposed, the air was treated as an ideal gas mixture of N_2 and O_2, neglecting the presence of the other minor components that usually are part of the mixture. The percentages considered for the N_2 and O_2 were, respectively, 79% and 21% on volumetric base.

Once the exergy destruction rates and exergy efficiencies per each component are calculated, the overall exergy efficiency of purpose of the polygeneration system is analyzed. Furthermore, the exergy defects of the components are defined per each operating condition, with both steam and oxygen. Both the terms are calculated according to the control volume which includes the gas production units; therefore, neither the PV nor the CHP are considered. The exergy efficiency of the system is calculated as following:

$$\psi_{pol} = \frac{\dot{E}x_{fuel}}{\dot{P}_{el,PV} + \dot{E}x_{biomass}} \tag{95}$$

Where Ex_{fuel} and $Ex_{biomass}$ are the input exergy rates of the final fuel produced and the total input biomass, calculated according to the methodology discussed. The exergy defect instead relates the exergy destruction of the *i*-th component to the total exergy input, in this case the input biomass and PV power:

$$\delta_i = \frac{\dot{E}x_{d,i}}{\dot{P}_{el,PV} + \dot{E}x_{biomass}} \tag{96}$$

Thermoeconomic model

This paragraph includes the main equations adopted for the calculus of the primary energy savings obtained with the polygeneration system proposed. To perform the thermo-economic analysis, the evaluation of the primary energy consumption of both the reference system (RS) and the proposed system (PS) is pivotal.

In this case study, the RS is the one in which all the electricity demand of the botanical garden is met by the grid and the gas demand of the CHP which operates in the hospital is met by the natural gas grid. The PS is instead the one in which the polygeneration system meets the fuel demand of the CHP with the gasification and anaerobic digestion of the biomasses. Furthermore, in the PS the electricity demand of the botanical garden is met by PV and the surplus energy is used in a power to X process to increase the efficiency of the plant. The primary energy saving (*PES*) is then evaluated as follows:

$$PES = \frac{PE_{RS} - PE_{PS}}{PE_{RS}} = \frac{\left[\frac{E_{el,fromGRID}}{\eta_{el,GRID}} + V_{NG} \cdot LHV_{NG}\right]_{RS} - \left[\frac{E_{el,fromGRID}}{\eta_{el,GRID}}\right]_{PS}}{\left[\frac{E_{el,fromGRID}}{\eta_{el,GRID}} + V_{NG} \cdot LHV_{NG}\right]_{RS}} \tag{97}$$

Where $\eta_{el,GRID}$ is the average efficiency of the electricity grid in Colombia, and the term $E_{el,fromGRID}$ in the RS is referred to the electric load of the botanical garden whereas in the PS is referred to the residual electricity demand which is not met by the PV. The avoided CO_2 emissions are the difference between the CO_2 emissions in the RS and the PS, related to the primary energy consumption:

$$\Delta CO_2 = CO_{2,RS} - CO_{2,PS} = \left[E_{el,fromGRID} \cdot f_{CO_2,EE} + V_{NG} \cdot LHV_{NG} \cdot f_{CO_2,NG} \right]_{RS} - \left[E_{el,fromGRID} \cdot f_{CO_2,EE} \right]_{PS} \quad (98)$$

Where f_{EE} and f_{NG} are, respectively, the CO_2 equivalent emission factors for the electric grid and the natural gas in Colombia. The economic feasibility of the system is evaluated according to the commonly adopted calculus of the Simple Payback (*SPB*) of the solution proposed:

$$SPB = \frac{C_{TOT}}{\Delta C} = \frac{C_{GAS} + C_{AD} + C_{AEC} + C_{PV} + C_{comp} + C_{HE} + C_{TK}}{C_{RS} - C_{PS}} \quad (99)$$

Where C_{TOT} is the total capital cost of the technologies introduced in the system proposed, i.e. the cost of the gasifier, the anaerobic digester, the alkaline electrolyzer, the photovoltaic system, the compressors, the heat exchangers, and the storage tanks. The term ΔC is the economic saving obtained calculating the operating costs difference between the RS and PS:

$$\Delta C = C_{RS} - C_{PS} = \left[E_{el,fromGRID} \cdot j_{EE} + V_{NG} \cdot j_{NG} \right]_{RS} - \left[\left(E_{el,fromGRID} \cdot j_{EE} \right) + m_{POL} \right]_{PS} \quad (100)$$

Where j_{EE} and j_{NG} are the unit costs of electricity withdrawn from the grid and natural gas, respectively, and m_{POL} are the maintenance costs of the polygeneration system, assumed equal to 5% of capital costs. All the unit capital costs, operating costs, emission factors and other parameters adopted in this work to perform the thermo-economic analysis, related to Colombia [180], are listed in Table 35.

Table 35. Main parameters used for the Colombia case study in the thermo-economic analysis.

Parameter	Description	Value	Unit	Ref
$\eta_{el,GRID}$	Electric efficiency of the national grid	0.40	-	[180]
f_{EE}	Unit emission of CO_2 per kWh of electricity consumed	0.153	$kgCO_2$ /kWh	[180]
f_{NG}	Unit emission of CO_2 per kWh of natural gas consumed	0.202	$kgCO_2$ /kWh	[180]
j_{EE}	Purchasing unit cost of electric energy	0.25	$/kWh	[180]
j_{NG}	Unit cost of natural gas	0.65	$/Sm^3	[180]
$Cu_{,GAS}$	Unit cost of the gasifier	1'500	$/kW	[181]
$Cu_{,AD}$	Unit cost of the anaerobic digester	1'515	$/m^3	[182]
$Cu_{,PV}$	Unit cost of the photovoltaic field	1'000	$/kW	[129]
$Cu_{,AEC}$	Unit cost of the alkaline electrolyzer	1'500	$/kW	[144]
$Cu_{,comp}$	Unit cost of the compressors	$5.84(P_{el,comp})^{0.82}$	$/kW	[145]
$Cu_{,HE}$	Unit cost of the heat exchangers	$0.182(A_{HE}/0.093)^{0.78}$	$/m^2	[183]
$Cu_{,H2TK}$	Unit cost of the H_2 storage tank	500	$/kg	[183]

5.5.3 Case Study

The polygeneration system proposed in this paper is an innovative solution to address the energy demand of two non-residential end users located in the city of Bogotá, in Colombia. The system exploits the most available renewable energy sources in the area, i.e. sun and biomass, to meet electricity, heating, cooling, hot water, and fuels needing of the users. More specifically, the users considered are the botanical garden José Celestino Mutis (JBB) and the close by hospital San Juan de Dios.

Figure 95 shows the main areas of the botanical garden. The JBB covers an area of 20 hectares and withdraws electricity from the national grid through four meters dedicated to specific areas [184]. The Administrative Account supplies energy to the offices of urban agriculture, the warehouse, the herbal department, the herbarium, and the old house in Zone 1 Rojas. Zone 2 Scientific, powers the offices of the scientific sub-directorate, the maloca, and the tunnel. Zone 3 Administrative, provides energy to the main gate, the offices of the General Secretariat, the management, the ticket booth, the auditoriums, the library, the offices of the Educational Sub-Directorate, the systems offices, the Technical-Operational Sub-Directorate, the cafeteria, the waterfall, the lake, and the Environmental Classroom. Lastly, Zone 4 Tropicario, supplies energy to the four environments of the tropicario and the biodiversarium, in addition to the workshop. The consumption of electric energy in this entity is attributed to the operation of office equipment, appliances, office and trail lighting, pumping, air conditioning systems, water heating, and laboratory equipment of the Scientific Sub-Directorate.

Figure 95. Four electric submetering zones in the Botanical Garden of Bogota **[184]**.

The entity opens its doors for visits and tours from 8:00 AM to 5:00 PM from Tuesday to Friday, extending its opening hours to Saturdays, Sundays, and holidays from 9:00 AM to 5:00 PM. Both operational and administrative personnel work from Monday

to Saturday, with working hours spanning from 7:00 AM to 4:00 PM and 8:00 AM to 5:00 PM, respectively. In addition to their regular schedule, the Botanical Garden offers unique experiences, such as evening openings on the last Friday of each month, which extend from 5:00 PM to 10:00 PM. Office occupancy dynamics vary since they are not consistently filled to 100% capacity due to many contractors performing their tasks in the field and within the JBB premises. In addition, despite having natural lighting in the offices, on occasion, artificial lighting is required during the day due to cloud cover and the density of trees.

The construction of the energy demand curve was based on the consumption recorded in the monthly energy bills for each of the four energy accounts. Using this data and starting from the following assumptions:

- Saturdays see a 70% reduction in energy consumption compared to week daily consumption, considering that operational tasks conclude at noon, but cultural activities and some administrative tasks continue during the day.
- Sundays see a 50% decrease in daily consumption as there are no operational or administrative tasks, although cultural activities and visitor services continue.
- On the last Friday of each month, consumption increases to 110% of daily consumption because operations extend until 10:00 PM.
- The workday begins at 7:00 AM. and ends at 5:00 PM.
- Trail lighting is turned on at 6:00 PM. and turned off at 6:00 AM.
- Before opening the Tropicario, the baseload was 10.04 kW, corresponding to trail lighting and the herbarium pump. After entering the Tropicario, the baseload is 20.54 kW, covering trail lighting, the herbarium pump, the aeration pump, and the water heating system for the Pacific and Amazonia environments.
- The lunch break, which takes place between 12:00 PM and 2:00 PM, is associated with a 25% reduction in consumption.

With these assumptions, energy consumption was distributed in a detailed manner, daily and hourly. Figure 96 shows a typical weekly load profile based on the assumptions discussed for the JBB.

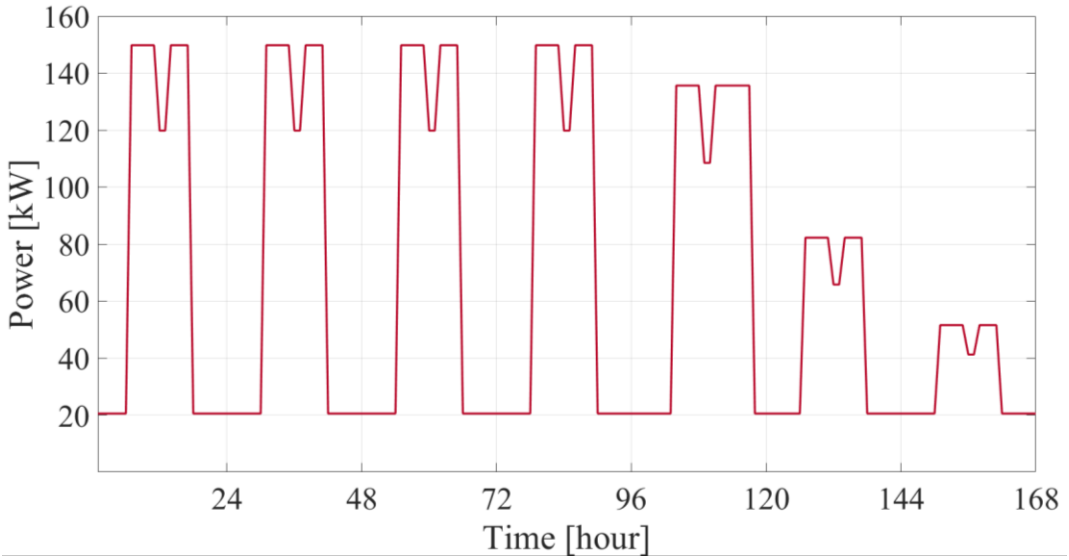

Figure 96. Typical load profile of the JBB derived from monthly data for one week of operation (from 20th of June to 27th of June, Monday to Sunday).

The dynamic load profiles for power, heating, and cooling demands of the hospital are shown and discussed in ref. [185]; here they are omitted for the sake of brevity. In general, the power demand of the hospital is quite stable over the year because of the intensive usage of electrical devices and hospital machineries. In the reference system (RS) of this work, the hospital is equipped with an internal combustion engine operating as a CCHP, which operates with natural gas withdrawn from the gas grid. At the same time, the botanical garden withdraws electricity from the electric grid. In the proposed system (PS), a polygeneration system based on biomasses and solar energy meets a large part of the total load of these end users. Table 36 lists the main design features for all the main components considered in the PS. More specifically, a 1.7 MW gasification unit produces syngas with high LHV by means of the lignocellulosic biomass harvested from the botanical garden. This unit is coupled to an 800 m^3 continuously stirred tank reactor (CSTR) anaerobic digester fed by organic fraction of municipal solid wastes (OFMSW) which produces biogas. Both gaseous flows are mixed and used as a fuel for the engine addressing the energy demands of the hospital. Moreover, the fuel is integrated with H_2 produced by a 1 MW alkaline electrolyzer which is fed by the surplus electricity of a 2.1 MW PV field. The PV electricity is primarily used to meet the energy demand of the JBB, the surplus is exploited according to the power-to-X strategy to generate H_2 and O_2 by means of electrolysis. The O_2 produced is used as gasifying agent in the gasification unit. H_2 is used to increase the LHV of the fuel feeding the cogenerator. Table 37 lists the thermochemical characteristics of the syngas produced by the gasification unit when different agents are considered.

Table 36. Design parameters for all major components.

Component	Parameter	Description	Value	Unit
Biomass feedstock (dry weight basis)	C	Carbon content	48	%
	O	Oxygen content	44	%
	H	Hydrogen content	6	%
	N	Nitrogen content	0.1	%
	LHV	Lower heating value	16.14	MJ/kg
	MC	Wood moisture content	11	%
Gasifier	-	Type	Downdraft allothermal	[-]
	P_{GAS}	Rated capacity of the gasifier	1'730	kW
	T_{gas}	Reactor temperature	1'123	K
	$m_{biomass,S}$	Biomass rated feeding rate with steam	386	kg/h
	$m_{biomass,O}$	Biomass rated feeding rate with O_2	144	kg/h
	dp_{GAS}	Pressure drops	0.15	bar
	p_{GAS}	Operating pressure	1.5	bar
	T_{agent}	Agent temperature	700	K
	m_{TAR}	Tar production	1-3	g/Nm^3
Anaerobic digester	*HRT*	Hydraulic Retention Time	30	day
	T_{dig}	Digester temperature	38	°C
	OLR	Organic loading rate of biomass	708	kg/h
	V_{dig}	Digester volume	800	m^3
	$c_{p,OFMSW}$	OFMSW specific heat	2.72	kJ/kgK
	$c_{p,digestate}$	Digestate specific heat	4.18	kJ/kgK
	$c_{p,biogas}$	Biogas specific heat	1.23	kJ/kgK
Photovoltaic panel	V_{oc}	Open-circuit voltage	37.7	V
	I_{sc}	Short-circuit current	9.01	A
	V_{mpp}	Voltage at maximum power point	30.5	V
	I_{mpp}	Current at maximum power point	8.51	A
	Ns	Number of modules in series	4	-
	Np	Number of modules in parallel	2'000	-
	A	Area of a single PV module	1.609	m^2
	$N_{cell,MOD}$	Number of cells in series in a module	60	-
	η_{PV}	Module efficiency	0.18	-
	A_{TOT}	PV field total area	11'600	m^2
	P_{PV}	Rated power of the photovoltaic field	2'076	kW
Alkaline electrolyzer	N_{cell}	Number of cells in series	49	-
	N_{stack}	Number of stacks in parallel	100	-
	$P_{el,AEC}$	Rated power of the electrolyzer	2'100	kW
	T_{cell}	Operating temperature	333	K
	p_{cell}	Operating pressure	8	bar
CHP	-	Model name	JMS-612-GS-N.L	-
	-	Manufacturer	GE Jenbacher	-

			GmbH & Co OHG	
	$P_{el,CHP}$	Rated power of the CHP	2002	kW
	$P_{th,fuel}$	Rated fuel input	4424	kW
	$\eta_{el,CHP}$	Rated electric efficiency	0.452	-
Storage	CAP_{H2}	H_2 storage capacity	82	kg
	CAP_{O2}	O_2 storage capacity	3'870	kg
	CAP_{bio}	Biogas storage capacity	1'040	kg

Table 37. Thermochemical characteristics of the syngas produced by the gasifier under different operating conditions, data measured experimentally.

Gasifying agent	**Air**	**Steam**	**Oxygen**
H_2 (vol.%)	22.56	48.2	60.25
CO (vol.%)	24.43	22	28.75
CO_2 (vol.%)	8.053	15.9	2.04
CH_4 (vol.%)	1.085	7.6	1.2
N_2 (vol.%)	37.41	3	2
LHV_{syngas} [MJ/kg]	31.76	62.03	79.31
Agent/Biomass ratio	0.42	0.85	0.26
Oxygen (%)	21	[-]	100
Dry biomass [kg/h]	569	386	144

These data were used to perform the calculations in the exergy analysis of the gasification unit, according to the equations discussed in Section 3.4.

5.5.4 Results

In this section, the hourly, monthly, and yearly results obtained from the dynamic simulation of the system proposed are presented and discussed. Moreover, a parametric thermo-economic optimization is performed to detect the optimal design of the polygeneration system.

Figure 97 shows the power flows matching for a typical day (February 1st), which is neither a winter nor a summer day due to the proximity to the equator which makes it difficult to distinguish between different climatic seasons. In this specific day the power produced by the PV field, $P_{el,PV}$, has an unusual pattern probably due to the presence of clouds in the mid of the day. This behaviour is typical of Latin American countries and it may affect the results, as it will be observed also in the monthly analysis.

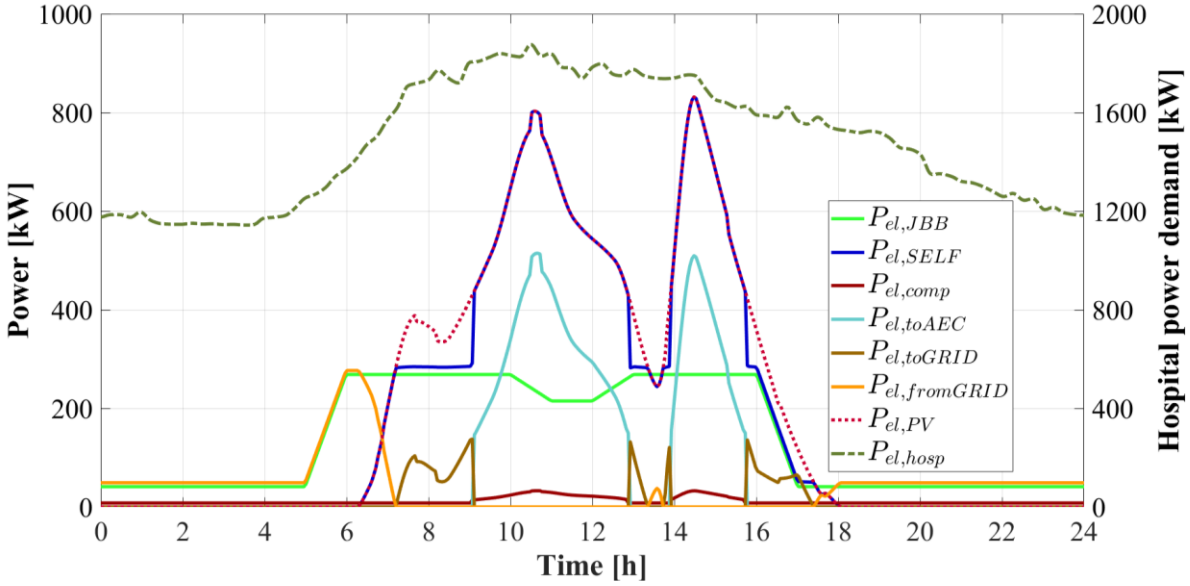

Figure 97. Dynamic power flows of the technologies integrated in the polygeneration system.

During the first hours of the day, roughly until 5 AM, the electric load is constant and equal to the sum of the baseload of the JBB, $P_{el,JBB}$, and the energy required for the compression of the biogas, which is operating to feed the CHP due to the nonzero power demand of the hospital, $P_{el,hosp}$. At 5 AM the activities in the JBB start and, due to the lack of power from the PV, $P_{el,fromGRID}$ increases. This occurs until 6 AM, when the PV power starts matching the energy demand of the system, and the whole load is almost completely met until almost 6 PM, i.e. roughly 12 hours in a row.

One can note that in some specific moments of the day, from 7 AM to 9 AM, from 12:30 PM to 2 PM, and from 3:45 PM to 6 PM, the surplus of PV electricity is not sent to the electrolyzer but it is instead sent directly to the electric grid, $P_{el,toGRID}$. The reason is that the value of the power excess is, in these cases, lower than the lower bound allowed for operation of the electrolyzer. Conversely, when this value of power lies in the range of operating conditions allowed for the electrolyzer, explained in the Layout section, this power, $E_{el,SOEC}$, is used to feed this unit and produce H_2 and O_2. This occurs for almost 6 hours during this day, i.e. from 9 AM to 1 PM and from 2 PM to 3:45 PM. It worths notice that during these hours, the electricity need for the compression of the gases, $P_{el,comp}$, increases due to higher amount of gas produced.

In Figure 97Figure *60*, the value of $P_{el,hosp}$ is shown on the right y-axis since it is much higher than the rest of the load. This power demand is entirely met by the CHP with the mixture of fuel produced. Figure 98 shows the dynamic mass flow rates of the various gases, while Figure 99 shows the pressure level of the three tanks of biogas, H_2 and O_2.

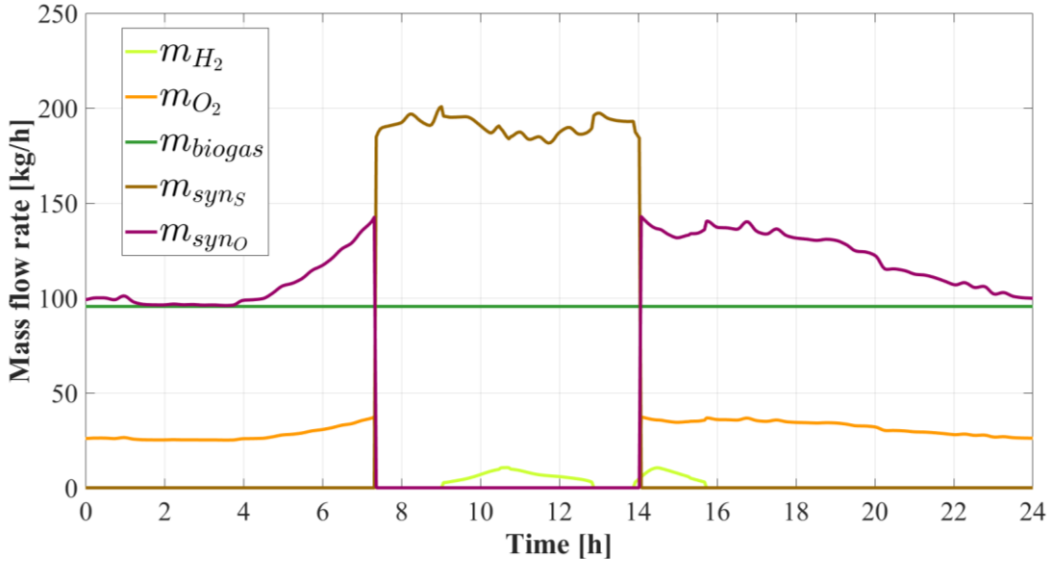

Figure 98. Dynamic mass flow rates of biogas, syngas, hydrogen, and oxygen.

The trend of the gaseous flows is consistent with the power flows and the control strategies already discussed. Until 7:30 AM, the mass flow rate of O_2 sent to the gasification unit, m_{O2}, is ever increasing, according to $P_{el,hosp}$. In fact, the syngas flow rate follows the same trend and it produced by the gasification unit operating with O_2 as the gasifying agent, see m_{synO}. This occurs both because the fuel demand of the CHP is lower than the maximum capacity available when O_2 is the gasifying agent, and there is availability of O_2 in the tank, see Φ_{O2} in Figure 99. In fact, the value of Φ_{O2} is constantly decreasing because the O_2 flow is being exploited and there is no power available from the PV to feed the electrolyzer.

This power demand is entirely met by the CHP with the mixture of fuel produced. From 7:30 AM on, the power demand required to the gasifier, in terms of fuel, is higher than the maximum capacity of the gasification unit when O_2 is used as gasifying agent. For this reason, steam is used as gasifying agent and the syngas production is much higher, see m_{synS} in Figure 98. In fact, m_{O2} is null and the pressure level Φ_{O2} increases until roughly 3 PM. It can also be noticed from Figure 99 that both the pressure level Φ_{H2} and Φ_{biogas} are constant because both the gaseous flows are used as baseload for the engine according to the strategy depicted in the Layout section.

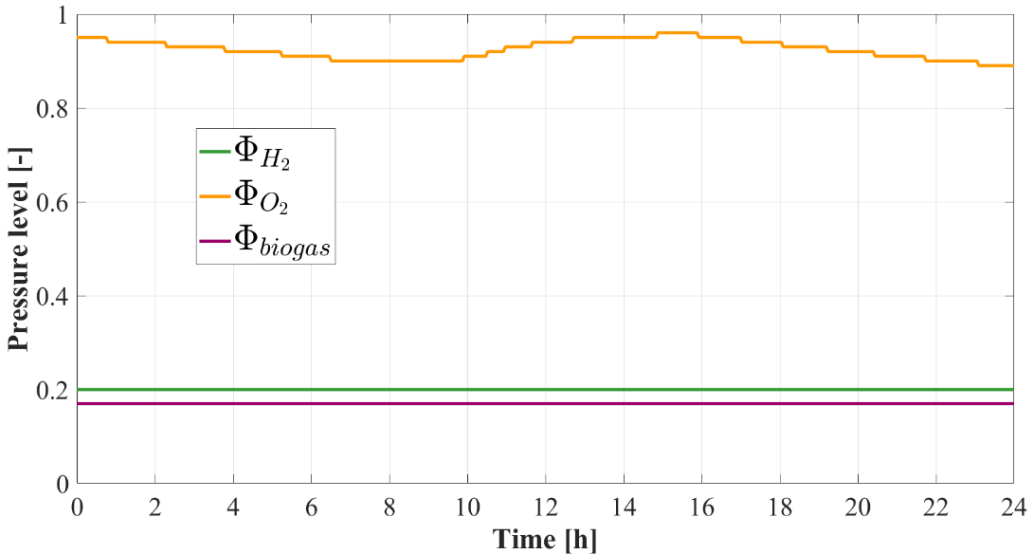

Figure 99. Dynamic pressure levels of the tanks.

Figure 100 displays the energy share of each unit, in terms of fuel power, with respect to the total fuel power demand of the engine which serves as CHP to the hospital. The baseload is provided first by means of the biogas flow, which is useful to stabilize engine conditions by means of a constant flow rate and immediately integrated with H_2 when this is available.

On average, the biogas and H_2 flow rate cover roughly 20 % of the fuel needing during the day, whereas 80 % of the energy demand is met by means of the gasification unit, operating with O_2 or steam depending on the availability of the several gases. In the first hours of the day the sharing of biogas (R_{biogas}) and syngas produced with O_2 (R_{synO}) is nearly constant because of the roughly constant hospital load.

R_{biogas} starts decreasing when the demand increases, from roughly 5:30 AM, because the biogas flow rate is constant and only the gasification unit can produce fuel. When H_2 is also available, R_{H2} is nonzero, the value of R_{biogas} stabilizes and the complementary energy demand is met by means of the gasification unit operating with steam R_{synS}, according to the control strategy.

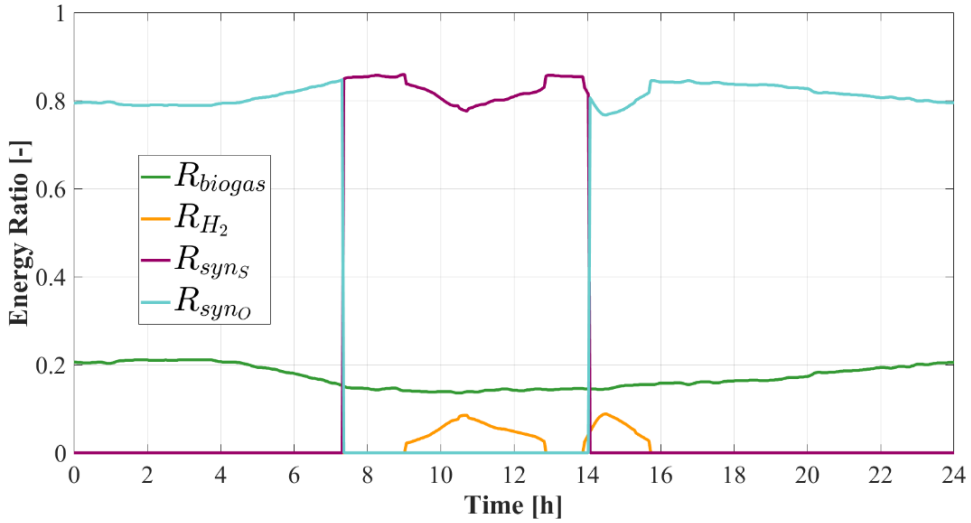

Figure 100. Dynamic values of the energy sharing ratio.

Figure 101 displays the dynamic profile of the LHV of the final fuel mixture feeding the engine. It can be observed that the value oscillates from 55 MJ/kg when the biogas is mixed with syngas produced by steam, to roughly 75 MJ/kg when the biogas, the H_2 and the syngas produced by means of O_2 are blended together. Even with a small amount of H_2, m_{H2} in Figure 98, the LHV of the fuel mixture can increase up to 62 MJ/kg when syngas produced by steam is blended in the compound.

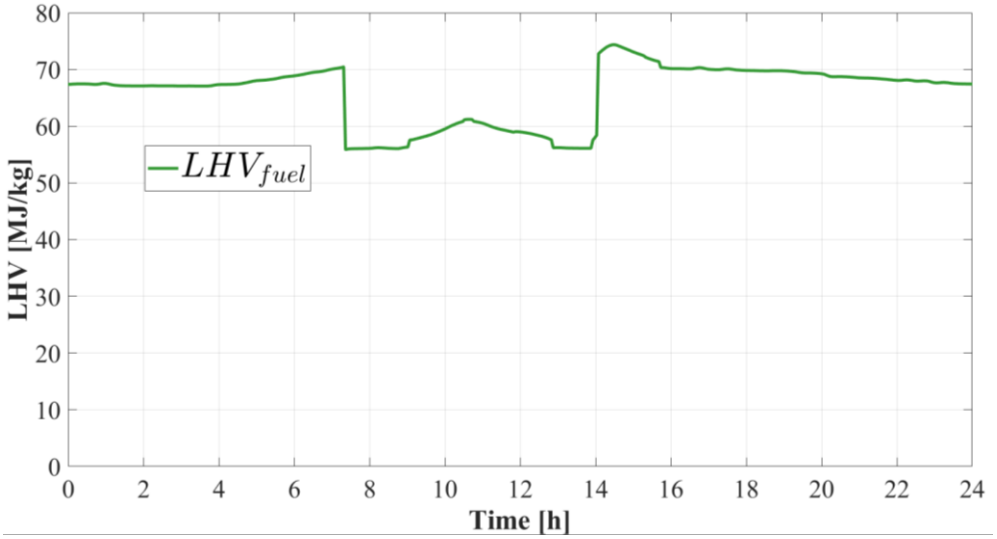

Figure 101. Dynamic flows of the lower heating value of the fuel produced.

Figure 102 shows the dynamic exergy flows of the units which produce gases blended in the fuel mixture. It is immediate to notice that the highest exergy flow is given by the input biomass which feeds the anaerobic digester (Ex_{OFMSW}). This high exergy flow of 3500 kW is due to the chemical exergy of a large amount of OFMSW biomass, 708 kg/h, which is constantly delivered to the digester. It is also worth noting that in this system the exergy rate related to the digestate, $Ex_{digestate}$, is equal to

roughly 1500 kW and is greater than the exergy related to the biogas produced, Ex_{biogas} equal to roughly 1100 kW. This difference is due to the much higher mass flow rate of digestate as output which makes extremely profitable the recovery of the digestate as fertilizer or even as input biomass for the gasifier. The input exergy rate of the gasification unit $Ex_{in,GAS}$ shows a step trend when the gasifying agent changes. In fact, when at 7:30 in the day selected the operation of the gasifier switches from the O_2 to the steam, $Ex_{in,GAS}$ abruptly increases from roughly 700 kW to 1400 kW, twice the initial value. This increase does not come with the same increase in the exergy output $Ex_{out,GAS}$, which is instead even lower. This is partly due to the contemporary presence of the H_2 exergy rate, Ex_{H2}, and partly due to the higher exergy destruction rate of the gasifier when the steam is the gasifying agent, as confirmed by Figure 103.

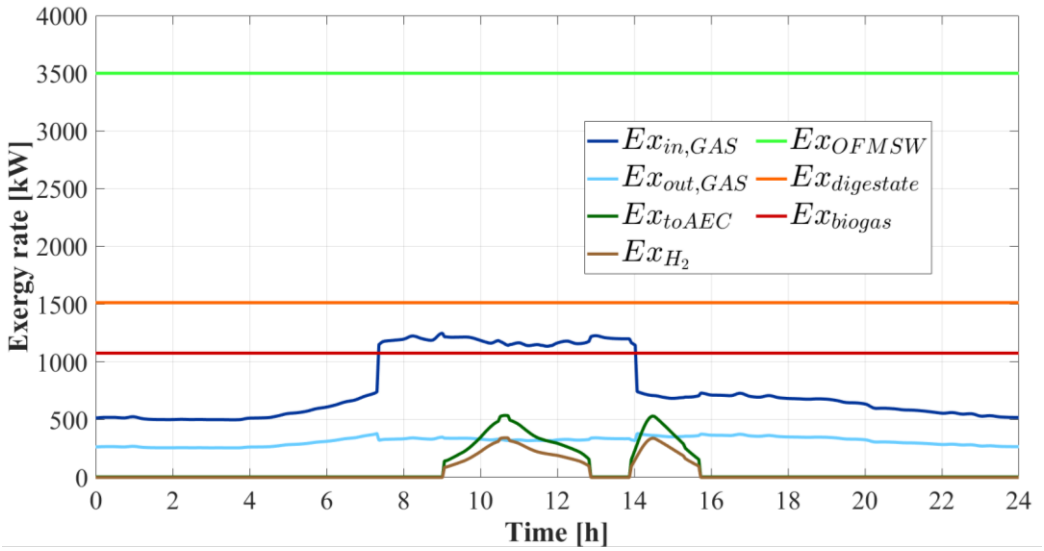

Figure 102. Dynamic exergy flows of the gas production units.

Figure 103 shows the exergy destruction rates of the alkaline electrolyzer, the gasification unit and the anaerobic digester. The step function of the exergy destruction in the gasification unit, $Ex_{d,GAS}$, is due to the fact that the gasification process is much more effective with O_2 than with steam. This result is in accordance with scientific literature. The exergy destruction rate of the anaerobic digester $Ex_{d,AD}$ is again much higher than the others, roughly equal to 900 kW, because of the relevant thermal losses and heat demand of the digester.

Figure 104 shows the exergy destruction rates of the heat exchangers used to bring the temperature of the gasifying agent up to the set point temperature to enter the gasifier. The hot fluid in this case is the output syngas, whereas the cold fluid is the steam or the O_2. In the case of steam, the exergy destruction rate $Ex_{d,HRSG}$ is around 45 kW whereas in the case of O_2, $Ex_{d,O2}$ is almost negligible. The reason lies behind the

much higher heat transfer rate when steam is used, according to eq.(41) in the Exergy model section.

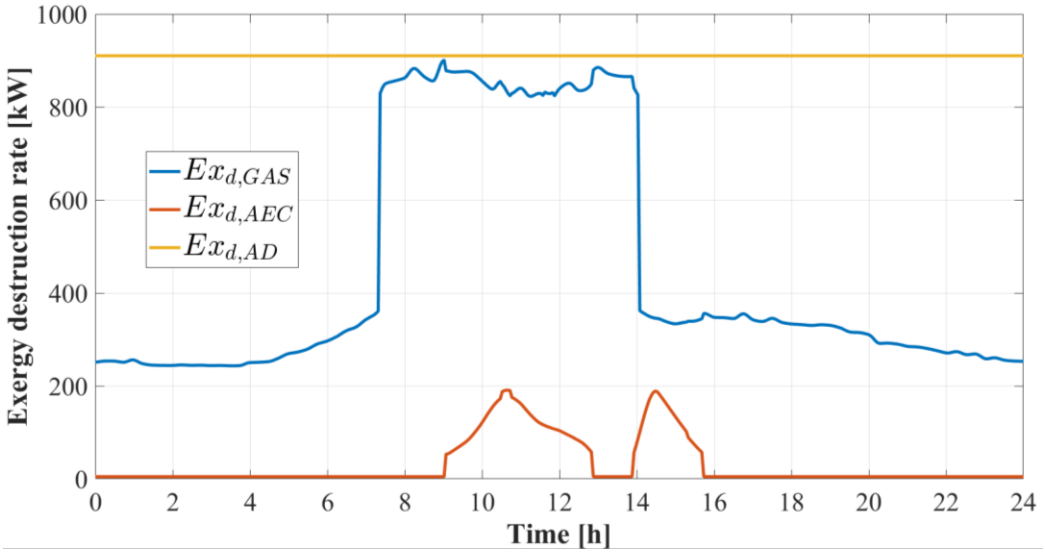

Figure 103. Exergy destruction rates of the gas production units.

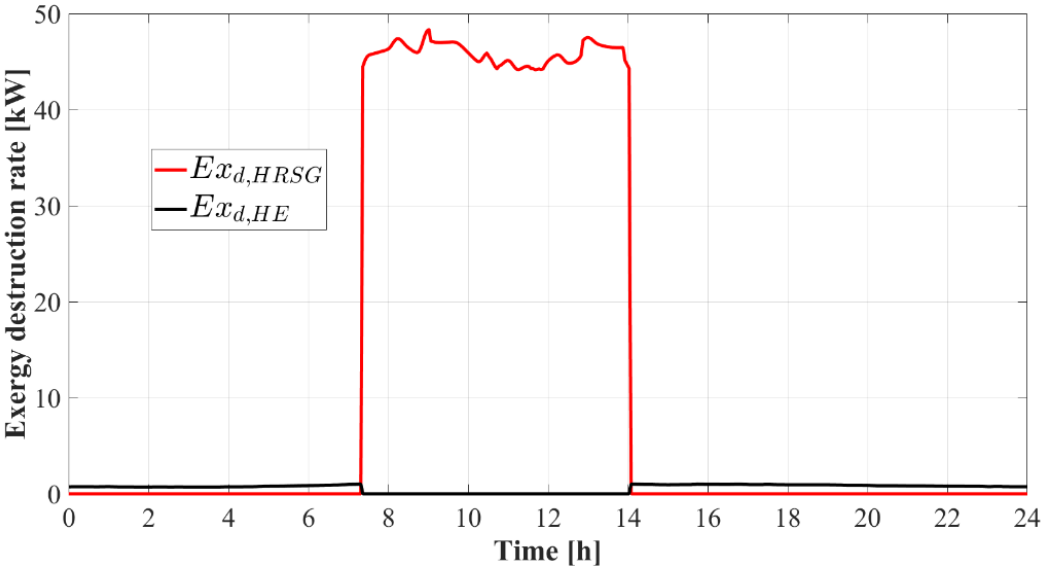

Figure 104. Exergy destruction rates of the heat recovery units.

Figure 105 shows the exergy effectiveness of the heat exchange in both cases. The exergy effectiveness is very similar both when O_2 and steam are used as gasifying agent. In particular, the exergy effectiveness of the HRSG, ψ_{HRSG}, is constant because of the strategy adopted which is made to get to set point of the outlet temperature. The outlet temperature of the O_2 flow rate is instead variable, since it is easier to guarantee that the lower temperature limit is reached and there is no risk of steam condensing, making the term ψ_{HE} to be ever oscillating.

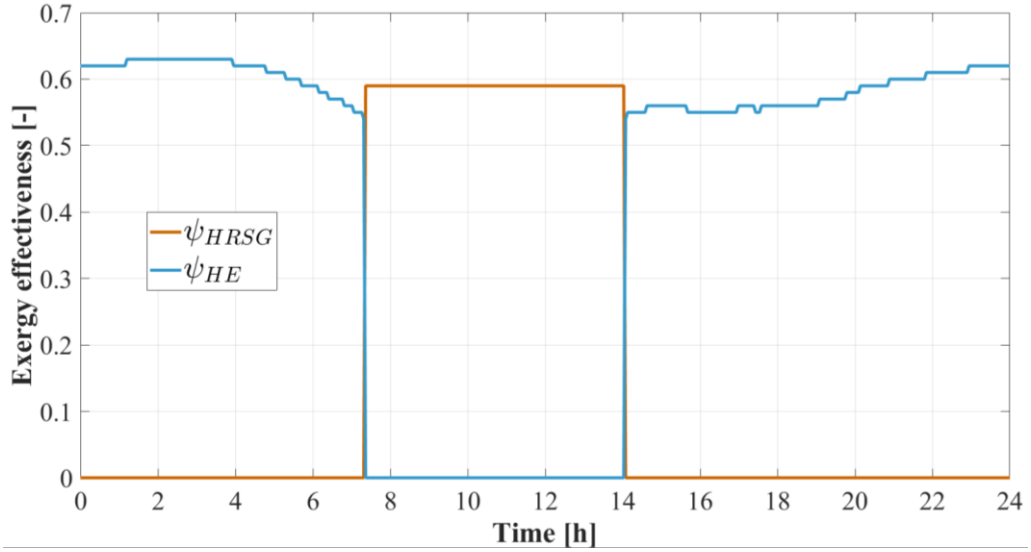

Figure 105. Dynamic exergy effectiveness of the heat recovery units.

Figure 106 and Figure 107 display, respectively, the exergy efficiency of the other components and the whole polygeneration system.

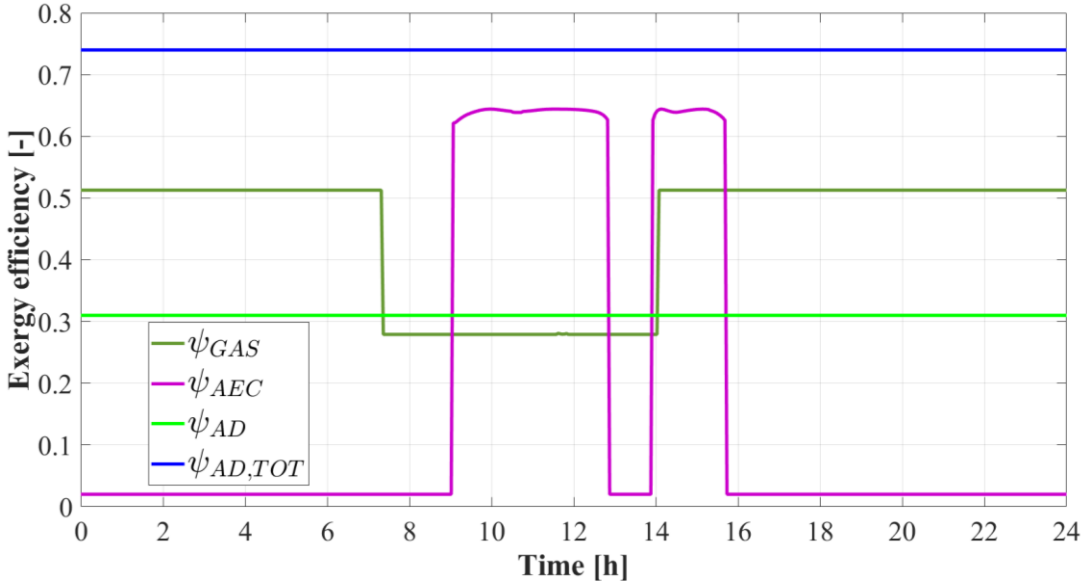

Figure 106. Exergy efficiency of the gas production units.

According to the already observed results, the exergy efficiency of the gasifier ψ_{GAS} is much higher when the O_2 is used instead of steam, with values of roughly 0.52 and 0.27, respectively. The exergy efficiency of the alkaline electrolyzer ψ_{AEC} is quite high compared to the values available from literature [171], being around 0.65. This can be explained by the operating conditions of the unit which are optimized by means of the control strategy integrated. The exergy efficiency of the anaerobic digester was calculated both in case of wasting and recovery of the digestate, ψ_{AD} and $\psi_{AD,TOT}$ respectively. In the former case, the exergy efficiency is roughly equal to 0.30 whereas in the latter case, the exergy efficiency is almost equal to 0.75. The exergy efficiency of

the polygeneration system, ψ_{POL}, is highly depending on how the technologies combine together during the operation of the system. In fact, in the worst operating condition, when the gasifier operates with steam and no H_2 is provided by the electrolyzer, the exergy efficiency of the system is equal to 0.30. In the optimal operating condition, when the gasifier operates with O_2 as gasifying agent and the H_2 is added to the fuel mixture, the exergy efficiency is almost 0.38.

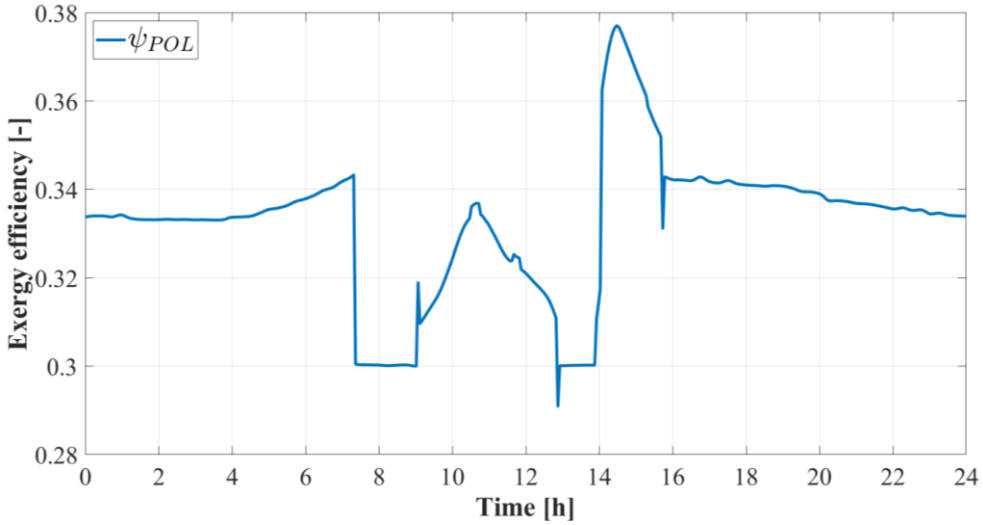

Figure 107. Exergy efficiency of the polygeneration system.

Figure 108 shows the exergy defects of every unit producing gas. This analysis is extremely useful to detect which component is the most responsible for exergy losses and decrease the overall efficiency of the process. As can be observed, the defect of the anaerobic digester δ_{AD} is the highest one because of the huge size of the digester, 800 $m^{3,}$ which comes with great thermal dissipation. As expected, the exergy defect of the heat exchanger δ_{HE} is extremely low and it is not negligible only when steam must be heated. Also the exergy defect of the alkaline electrolyzer δ_{AEC} is extremely low, highlighting how useful the power to X strategy is in such a system. As confirmed by the results of the exergy destruction rates and exergy efficiency, the operation of the gasification unit with O_2 instead of steam is much more efficient. In fact, during the operation with steam the exergy defect of the gasifier δ_{GAS} rises from 0.07 to roughly 0.17, with only a slow decreasing when the gasifier operation is partialized by the presence of H_2 in the blending.

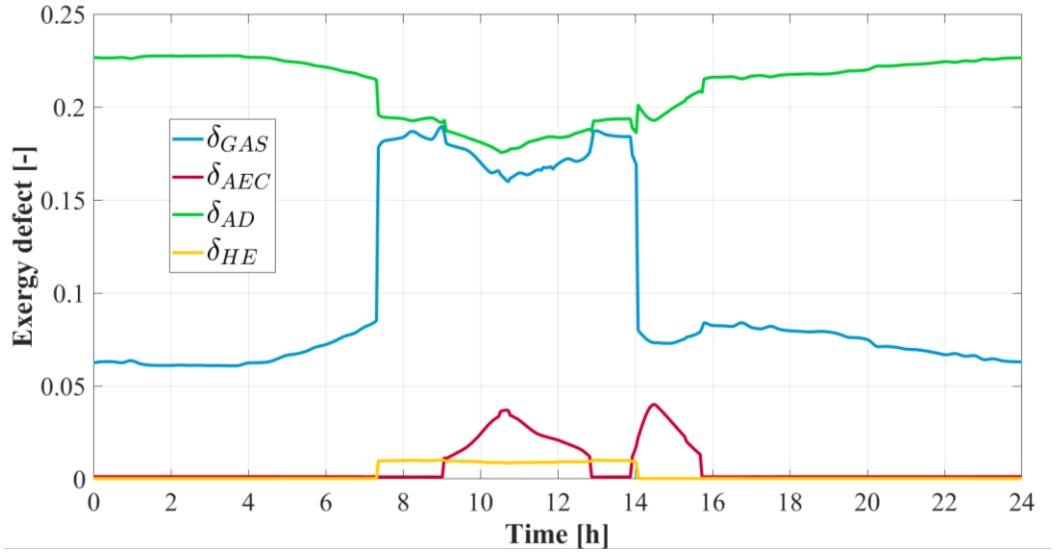

Figure 108. Dynamic flows of the exergy defects.

Figure 109 shows the values of the electric energy flows involved per each month of operation of the system. As said in the dynamic results section, in Colombia the weather seasons are not varying much and so the electric energy production from the PV system is quite stable during the year. In fact, the value of the electricity produced by the PV system, $E_{el,PV}$ in Figure 109, shows an almost constant production being averagely 260 MWh. The highest value is shown for March with more than 300 MWh produced and the lower in April, with roughly 200 MWh produced.

It can be observed also how the self-consumed energy, $E_{el,SELF}$, is always extremely close to the total production, especially in the period from April to September. The reason is that during the first three months of the year, the PV production is high, the energy demand, $E_{el,LOAD}$, shows a decreasing trend and, as a consequence, the electricity sent to the electrolyzer, $E_{el,toAEC}$, is ever increasing. Observing that the electricity sharing with the grid is nearly constant, it means that there is a large storage of energy in these months, which is exploited afterwards.

This result is confirmed by Figure 110, where is displayed the value of the ratio between the energy self-consumed and the energy produced by the PV per each month ($E_{el,SELF}/E_{el,PV}$). According to what hitherto discussed, this value is very close to 1 from April to September, decreasing again in October because of the huge increasing of $E_{el,LOAD}$ in September. From Figure 110 one can notice also how the control strategy applied to guarantee optimal operation of the alkaline electrolyzer allows one to have an average efficiency η_{AEC} constant and equal to 0.70, and an average global efficiency of the system η_{glob} of roughly 0.34. the only drawback is the quite high absolute value of the electricity sent to and withdrawn from the grid, meaning that probably the integration of an electric battery or a fuel cell would even

increase the performance of the system. In this case also a net-metering scheme for electricity sharing with the grid would be extremely interesting to analyze.

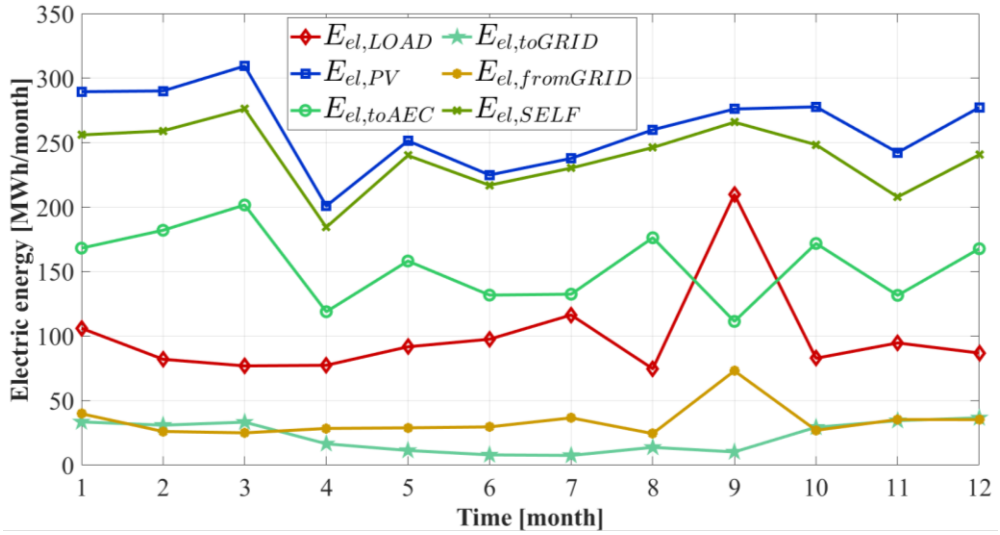

Figure 109. Monthly values of the electric energy flows involved in the system.

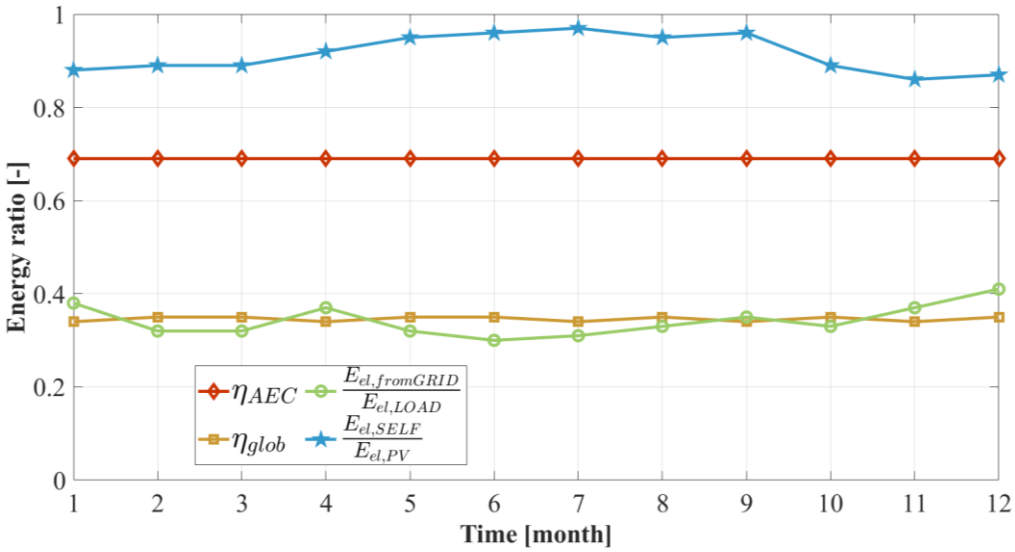

Figure 110. Monthly energy ratios of the system.

Figure 111 and Figure 112 show, respectively, the exergy efficiency and the exergy defect of the units per each month of operation. The flexibility of the system is again confirmed by the fact that the exergy efficiency of each component is nearly constant every month. This result is surely influenced by the geographical area selected but the utilization of biomasses is surely pivotal for balancing the fluctuations of energy production. Most importantly, it can be noticed from Figure 111 that the exergy efficiency of the gasifier when operates with O_2 $\psi_{GAS,O}$ is constantly around 0.50 whereas when operating with steam $\psi_{GAS,S}$ decreases to roughly 0.25. The system with highest exergy efficiency is the electrolyzer, showing an average value ψ_{AD} of roughly 0.6. The value of the exergy efficiency of the polygeneration system ψ_{POL} is

almost equal to the global energy efficiency because of the control volume selected for the analysis, i.e. roughly 0.35 every month. The exergy defect of the AD is the highest every month, being more than 20 % of the total exergy input, whereas the monthly exergy defect of the gasification unit operating with O_2 is higher than the exergy defect observed when steam is used. This result is only due to the fact that the gasification unit operates with O_2 most of the time, and the few times steam is adopted for the peaks of the hospital load, it has a much greater exergy destruction rate.

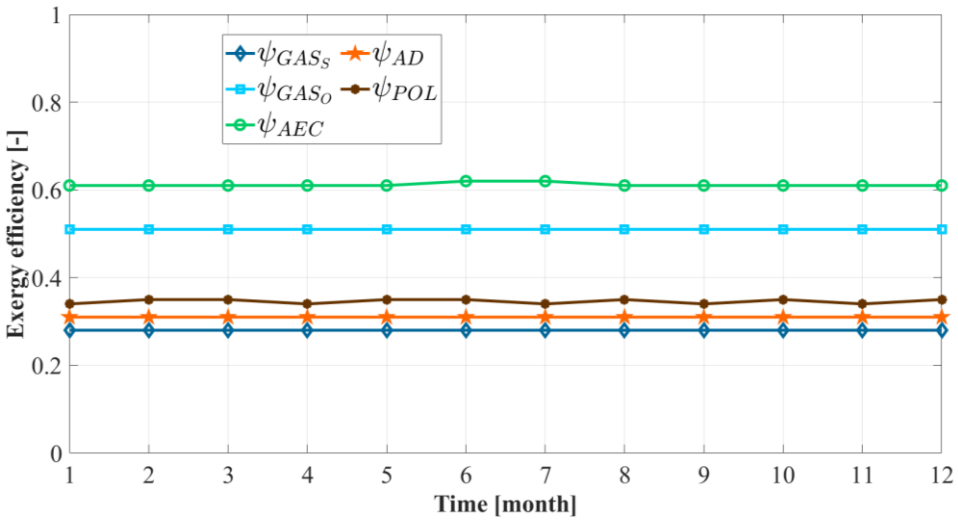

Figure 111. Monthly exergy ratios of the system.

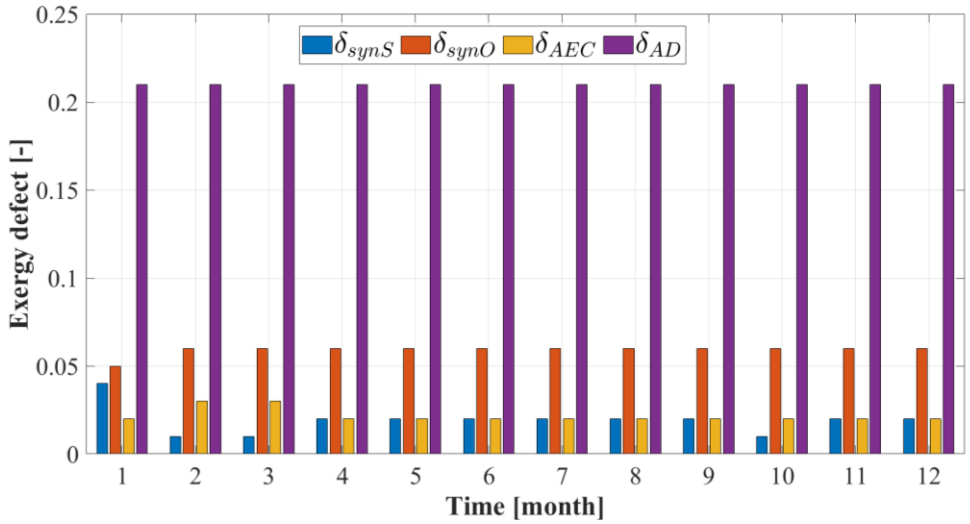

Figure 112. Monthly exergy defects of the gas production units.

In this section results from the yearly analysis are presented. Yearly results are consistent with the dynamic and monthly analyses, showing that a remarkable fraction of PV electricity is sent to the electrolyzer, making it profitable to adopt the power-to-X strategy in this configuration. The massive production of H_2 is in fact

used to produce useful fuel for the engine meeting the demands of the hospital and abate the primary energy consumption.

Table 38. Results from the yearly analysis.

Parameter	Value	Unit
$E_{el,LOAD}$	1'197.15	MWh/year
$E_{el,PV}$	3'137.55	MWh/year
$E_{el,heat}$	14.58	MWh/year
$E_{el,comp}$	154.67	MWh/year
$E_{el,toAEC}$	1'852.40	MWh/year
$E_{el,toGRID}$	265.62	MWh/year
$E_{el,fromGRID}$	409.64	MWh/year
$E_{el,SELF}$	2'871.92	MWh/year
$E_{el,HOSP}$	12'457.06	MWh/year
$E_{p,CHP}$	28'462.86	MWh/year
M_{H2}	38.56	tons/year
M_{biogas}	835.57	tons/year
M_{syngas}	1'045.01	tons/year

This result is confirmed by the thermoeconomic analysis, whose results are shown in Table 39. The ratio between the energy self-consumption and the PV production equal to 0.92 demonstrate how the system is able to exploit at most the renewable energy sources. This is furtherly confirmed by the fact that almost 60 % of the PV energy is provided to the electrolyzer, meaning that the power to X strategy is pivotal to increase the flexibility of the system. Moreover, the use of biomasses allows one to minimize the withdrawal of energy from the grid, which is only 3 % of the total energy demand of the users. The electricity sent to the grid, $E_{el,toGRID}$, is also remarkable, being equal to 265 MWh per year. Considering an acceptable selling price of electricity around 60 $/MWh, it means that this electricity sold to the grid leads to roughly 16 k$/year saved as operating costs. In the table is also shown the total amount of primary energy saved from the consumption of natural gas due to the CHP, $E_{p,CHP}$, which is almost 30 GWh/year. This means that the integration of renewable fuels to meet the energy demand of the CHP, addressing the demand of the hospital, leads to a groundbreaking environmental impact of this solution.

The Primary Energy Saving of the proposed system with respect to the reference system is, in fact, equal to 99 percent. Therefore, the system proposed has a great environmental impact which is also confirmed by a huge amount of 5'906.21 tons saved per year of CO_2 equivalent emissions; 90% of these are due to the CHP natural gas demand. Despite the relevant costs of the technologies proposed, the Simple Payback of the solution proposed is equal to 3.66, which is extremely low and the Net

Present Value is equal to 14.40 M$, which is almost twice the capital cost. It is worth noting that in this case the technology which represents the largest economic expense is the photovoltaic field. According to this result, some relevant subsidies for the purchasing of this technology would be needed to strongly improve the economic performance of the solution proposed.

Table 39. Results from the thermoeconomic analysis.

Parameter	Description	Value	Unit
$E_{el,SELF}/E_{el,PV}$	Energy self-consumed to total PV production	0.92	-
$E_{el,toAEC}/E_{el,PV}$	Energy sent to the AEC to total PV production	0.59	-
$E_{el,toGRID}/E_{el,PV}$	Energy sent to the grid to total PV production	0.08	-
$E_{el,fromGRID}/E_{el,LOAD}$	Energy from the grid to total PV production	0.03	-
PES	Primary energy saving	0.99	-
ΔMCO_2	CO_2 emission saving	5'906.21	tons/year
C_{TOT}	Capital cost	7.79	M$
C_{PV}	PV cost	2.08	M$
C_{GAS}	Gasifier cost	1.43	M$
C_{AEC}	Electrolyzer cost	1.81	M$
C_{AD}	Anaerobic digester cost	2.01	M$
ΔC	Operating costs saving	2.13	M$/year
SPB	Simple payback period	3.66	years
NPV	Net present value	14.40	M$
PI	Profit index	1.85	-

Chapter 6
Conclusions

In this comprehensive exploration of Power-to-X technologies, this research has delved into the complexities and technical feasibilities of dynamic models, crucial in matching the intermittency of renewable energy sources with user load demands and the operational constraints of the associated technologies. The heart of this investigation lies in the sophisticated dynamic matching process, a critical component for the successful implementation and optimization of Power-to-X systems.

The findings reveal that despite the inherent complexities, such as fluctuating energy inputs and the need for stable energy outputs, these technologies hold significant potential for sustainable energy conversion. The dynamic models developed in this study have not only highlighted the feasibility of these systems but also outlined the essential role of advanced control mechanisms and modular system designs in managing the variable nature of renewable energy sources.

The technical feasibility of the proposed Power-to-X systems, as demonstrated by the models developed, is promising, albeit with certain challenges. These systems have shown capabilities in effectively converting renewable energy into various usable forms, maintaining operational integrity, and accommodating the flexibility required for energy transition. The modularity and scalability of system designs emerged as key factors, enabling adaptability to changing energy needs and reducing initial investment barriers.

One of the most significant challenges encountered in this thesis is aligning intermittent renewable energy sources with the continuous energy demands of the users. This research has addressed this through innovative energy storage solutions and conversion strategies, ensuring consistent energy supply and system efficiency. The introduction of large-scale battery systems and the use of hydrogen as an energy carrier have been particularly noteworthy in mitigating the effects of energy intermittency.

This compilation of research offers in-depth insights into the development and analysis of sustainable energy solutions, with a strong emphasis on numerical outcomes that underscore the efficiency, environmental impact, and economic viability of various innovative systems:

In the realm of Power-to-Heat systems, 4th and 5th generation district heating and cooling systems driven by renewables were investigated. A 5th generation district heating and cooling network, leveraging seawater and renewable energy, achieves near-zero primary energy consumption and CO_2 emissions, with a calculated simple payback period of 14.7 years. Renewable energy production accounts for 57 % of the district electricity demand, but only 37 % is used on-site, suggesting room for improvement in energy self-consumption strategies.

Comparative studies between 4th and 5th generation district heating and cooling systems for residential applications show a 97 % and 81 % reduction in primary energy consumption, respectively. Despite the substantial energy and environmental benefits, both systems face economic challenges, with payback periods of 16 and 21 years, attributed to high initial costs. The most intriguing result obtained from the comparison is that in case of residential districts, the 4th generation is preferable to the 5th generation.

A hybrid system integrating photovoltaics, solid-oxide cells, and hydrogen storage demonstrates an overall system efficiency of nearly 47 %, with primary energy savings of 73% and a profitable payback period under 10 years. This approach presents a compelling case for the economic and environmental benefits of renewable energy integration. In fact, with this simulation work it has been possible to demonstrate the competitiveness of Power-to-Power solutions in the next future, provided that fundings are guaranteed to pave the way to this technology.

The novel strategy proposed for waste management and reducing public transport pollution through a biomethane plant supported by photovoltaics and solar thermal energy shows a 45 % self-consumption rate of produced electric energy and a substantial increase in renewable energy use, with promising economic outcomes including a simple payback period of 11 years, improving to 6.8 years with public incentives.

The comparison between biogas upgrading technologies, focusing on water scrubbing and membrane separation coupled with photovoltaics and energy storage, showcases water scrubbing as the superior technology, achieving grid independence and a primary energy reduction of -5.22 GWh/y, alongside a yearly cost saving of -488 k€/y.

A thermodynamic and economic analysis of a fully-renewable Power-to-Gas production plant reveals a remarkable efficiency ($\eta glob = 0.75$), significant primary energy reduction (~30 GWh/year), and substantial CO_2 savings (6,330 t_{CO2eq}/year). The

economic analysis suggests a viable project with a payback time of less than 3 years, provided oxygen is sold as a by-product.

Lastly, a Power-to-X polygeneration system combining solar power and biomass in Bogotá achieves an exergy efficiency of 0.35 and nearly total primary energy savings compared to a reference system, with a 3.66-year payback period and a net present value of 14.40 M$, indicating exceptional economic and environmental performance. The system also shows incredible flexibility of operation when solar source is combined with biomasses.

The implications of this research extend far beyond the current scope of Power-to-X technologies. The dynamic models developed offer a foundational framework for future investigations into other Power-to-X systems under dynamic operations. There is immense potential for these technologies to revolutionize the way we store, convert, and utilize renewable energy, paving the way for a more sustainable and resilient energy future.

In conclusion, this research underscores the critical importance of dynamic modelling in the development and implementation of Power-to-X technologies. While challenges remain, particularly in economic viability and system integration, the advancements and insights gained through this study are instrumental in driving the field forward. The journey towards fully realizing the potential of Power-to-X technologies is ongoing, and this work contributes a significant step towards achieving a sustainable, efficient, and technically feasible energy future.

Nomenclature

ASR Area Specific Resistance (Ω cm^2)

E Energy (kWh)

C Cost (€)

INV Capital cost (€)

j Unit cost (€ kW^{-1})

k First order rate (kg_{COD} d^{-1})

l Membrane thickness (cm)

LHV Lower heating value (kWh $Nm^{3\,-1}$)

MH Metal hydride mass (kg)

NPV Net Present Value (€)

OFMSW Organic fraction of municipal solid waste (-)

P Power (kW)

PE Primary energy (kWh)

PES Primary Energy Saving (-)

PI Profit Index (-)

PM Molar mass (g mol^{-1})

pr Pressure (bar)

Q Volume (m^3)

$\dot{Q}$ Heat transfer rate (kW)

R Gas constant (kJ kg^{-1} K^{-1})

r Reaction rate (d^{-1})

S Concentration of the soluble components (kg_{COD} $(m^3)^{-1}$)

SPB Simple payback period (years)

T Temperature (°C)

t Time (d)

V Voltage (V)

Greek symbols

α Separation factor (-)

β Overvoltage fraction (-)

γ Biochemical coefficient (-)

ε Fluid volume variation rate (s^{-1})

η Efficiency (-)

τ Time space of the reactor (s^{-1})

φ Kinetic equation (-)

Subscripts and superscripts

A Reactant (-)

amb Ambient (-)

CH_4 Referred to methane (-)

CO_2 Referred to carbon dioxide (-)

el Electric (-)

liq Liquid (-)

NG Natural gas (-)

grid National electric grid (-)

H_2 Referred to hydrogen (-)

i About the component "i" (-)

in Inlet (-)

j About the process "j" (-)

sub Subsidy (-)

th Thermal (-)

Bibliography

1. Kuzniecow Bacchin, T., F. Hooimeijer, and B. Kothuis, *Prospects.* Journal of Delta Urbanism, 2023(4).
2. Analysis, U.S.B.o.E., *Gross Domestic Product (Third Estimate), Corporate Profits (Revised Estimate), and GDP by Industry, Third Quarter 2023.* 2023.
3. Romero, H.L.a.J., *Climate Change 2023: Synthesis Report*, in *Contribution of Working Groups I, II and III to the Sixth Assessment Report of the Intergovernmental Panel on Climate Change*. 2023, IPCC, Geneva, Switzerland. p. pp. 35-115.
4. IEA, *World Energy Outlook 2023, IEA, Paris*, in *CC BY NC SA 4.0 (Annex A)*. 2023.
5. Zhang, Q., et al., *Unveiling the impact of geopolitical conflict on oil prices: A case study of the Russia-Ukraine War and its channels.* Energy Economics, 2023. **126**: p. 106956.
6. Kaandorp, C., et al., *Reducing committed emissions of heating towards 2050: Analysis of scenarios for the insulation of buildings and the decarbonisation of electricity generation.* Applied Energy, 2022. **325**: p. 119759.
7. Chiaramonti, D., et al., *The challenge of forecasting the role of biofuel in EU transport decarbonisation at 2050: A meta-analysis review of published scenarios.* Renewable and Sustainable Energy Reviews, 2021. **139**: p. 110715.
8. Deng, H., W. Zhang, and D. Liu, *Does carbon emission trading system induce enterprises' green innovation?* Journal of Asian Economics, 2023. **86**: p. 101597.
9. Mirza, N., et al., *Fiscal or monetary? Efficacy of regulatory regimes and energy trilemma of the inflation reduction act (IRA).* International Review of Financial Analysis, 2023. **90**: p. 102821.
10. McPherson, M., et al., *Modeling the transition to a zero emission energy system: A cross-sectoral review of building, transportation, and electricity system models in Canada.* Energy Reports, 2023. **9**: p. 4380-4400.
11. IEA. *Japan will have to tread a unique pathway to net zero, but it can get there through innovation and investment*. 2021; Available from: https://www.iea.org/commentaries/japan-will-have-to-tread-a-unique-pathway-to-net-zero-but-it-can-get-there-through-innovation-and-investment.
12. Moreno, J., et al., *Role of low carbon emission H2 in the energy transition of Colombia: Environmental assessment of H2 production pathways for a certification scheme.* Energy Conversion and Management: X, 2022. **16**: p. 100312.
13. (IRENA), I.R.E.A., *Renewable Capacity Statistics 2022.* 2022.
14. Sassenou, L.N., L. Olivieri, and F. Olivieri, *Challenges for positive energy districts deployment: A systematic review.* Renewable and Sustainable Energy Reviews, 2024. **191**: p. 114152.
15. Deka, C., et al., *Can gain motivation induce Indians to adopt electric vehicles? Application of an extended theory of Planned Behavior to map EV adoption intention.* Energy Policy, 2023. **182**: p. 113724.

16. Detsios, N., et al. *Recent Advances on Alternative Aviation Fuels/Pathways: A Critical Review*. Energies, 2023. **16**, DOI: 10.3390/en16041904.
17. Sica, D., et al., *Biogas-based systems: An opportunity towards a post-fossil and circular economy perspective in Italy.* Energy Policy, 2023. **182**: p. 113719.
18. Prussi, M., et al., *Biomethane as alternative fuel for the EU road sector: analysis of existing and planned infrastructure.* Energy Strategy Reviews, 2021. **33**: p. 100612.
19. Kazak, T., *European Green Deal.* Yearbook of the Law Department, 2020. **9**(10): p. 304-315.
20. Lehtveer, M., S. Brynolf, and M. Grahn, *What Future for Electrofuels in Transport? Analysis of Cost Competitiveness in Global Climate Mitigation.* Environmental Science & Technology, 2019. **53**(3): p. 1690-1697.
21. Tech, P. *More lines, more digitalisation, more climate resilience: Grids must be priority for Europe's net zero plans*. 2023; Available from: https://www.pv-tech.org/more-lines-more-digitalisation-more-climate-resilience-grids-must-be-priority-for-europes-net-zero-plans/.
22. Samadi, E., A. Badri, and R. Ebrahimpour, *Decentralized multi-agent based energy management of microgrid using reinforcement learning.* International Journal of Electrical Power & Energy Systems, 2020. **122**: p. 106211.
23. Dusonchet, L., et al., *Technological and legislative status point of stationary energy storages in the EU.* Renewable and Sustainable Energy Reviews, 2019. **101**: p. 158-167.
24. Jäger-Waldau, A., et al., *How photovoltaics can contribute to GHG emission reductions of 55% in the EU by 2030.* Renewable and Sustainable Energy Reviews, 2020. **126**: p. 109836.
25. Henni, S., et al., *Infrastructural coupling of the electricity and gas distribution grid to reduce renewable energy curtailment.* Applied Energy, 2021. **288**: p. 116597.
26. Schmidt, O., et al., *The future cost of electrical energy storage based on experience rates.* Nature Energy, 2017. **2**(8): p. 17110.
27. IRENA, *Hydrogen: A renewable energy perspective*. 2023.
28. Nazari-Heris, M., et al., *Economic-environmental effect of power to gas technology in coupled electricity and gas systems with price-responsive shiftable loads.* Journal of Cleaner Production, 2020. **244**: p. 118769.
29. Hernandez, D.D. and E. Gençer, *Techno-economic analysis of balancing California's power system on a seasonal basis: Hydrogen vs. lithium-ion batteries.* Applied Energy, 2021. **300**: p. 117314.
30. Jannik Burre, D.B., Luisa Brée, Kosan Roh, Alexander Mitsos, *Power-to-X: Between Electricity Storage, e-Production, and Demand Side Management.* Chemie Ingenieur Technik, 2019. **92**: p. 74-84.
31. Michael Sterner, p.o.O.R.U. 2021.
32. ENERGI, D. 2020.

33. Lim, J.Y., et al., *Nationwide sustainable renewable energy and Power-to-X deployment planning in South Korea assisted with forecasting model.* Applied Energy, 2021. **283**: p. 116302.
34. Incer-Valverde, J., et al., *Hydrogen-driven Power-to-X: State of the art and multicriteria evaluation of a study case.* Energy Conversion and Management, 2022. **266**: p. 115814.
35. Koj, J.C., C. Wulf, and P. Zapp, *Environmental impacts of power-to-X systems - A review of technological and methodological choices in Life Cycle Assessments.* Renewable and Sustainable Energy Reviews, 2019. **112**: p. 865-879.
36. Galimova, T., et al., *Global trading of renewable electricity-based fuels and chemicals to enhance the energy transition across all sectors towards sustainability.* Renewable and Sustainable Energy Reviews, 2023. **183**: p. 113420.
37. Bogdanov, D., et al., *Low-cost renewable electricity as the key driver of the global energy transition towards sustainability.* Energy, 2021. **227**: p. 120467.
38. Götz, M., et al., *Renewable Power-to-Gas: A technological and economic review.* Renewable Energy, 2016. **85**: p. 1371-1390.
39. Calise, F., et al., *Dynamic simulation and thermoeconomic analysis of a power to gas system.* Renewable and Sustainable Energy Reviews, 2023. **187**: p. 113759.
40. Crespi, E., et al., *Energy storage with Power-to-Power systems relying on photovoltaic and hydrogen: modelling the operation with secondary reserve provision.* Journal of Energy Storage, 2022. **55**: p. 105613.
41. Gravelsins, A., et al., *Power Sector Flexibility through Power-to-Heat and Power-to-Gas Application – System Dynamics Approach.* Environmental and Climate Technologies, 2019. **23**(3): p. 319-332.
42. Scholz, D. and F. Müsgens. *Increasing flexibility of combined heat and power plants with Power-to-Heat*. in *2015 12th International Conference on the European Energy Market (EEM)*. 2015.
43. Gjorgievski, V.Z., et al., *The potential of power-to-heat demand response to improve the flexibility of the energy system: An empirical review.* Renewable and Sustainable Energy Reviews, 2021. **138**: p. 110489.
44. Vannoni, A., et al., *Techno-Economic Analysis of Power-to-Heat Systems.* 2021. **238**: p. 03003.
45. Ambrosetti, M., *A perspective on power-to-heat in catalytic processes for decarbonization.* Chemical Engineering and Processing - Process Intensification, 2022. **182**: p. 109187.
46. Bloess, A., W.-P. Schill, and A. Zerrahn, *Power-to-heat for renewable energy integration: A review of technologies, modeling approaches, and flexibility potentials.* Applied Energy, 2018. **212**: p. 1611-1626.
47. Belik, S., V. Dreissigacker, and S. Zunft, *Power-to-heat integration in regenerator storage: Enhancing thermal storage capacity and performance.* Journal of Energy Storage, 2022. **50**: p. 104570.

48. Bordignon, S., et al., *A solar-assisted low-temperature district heating and cooling network coupled with a ground-source heat pump.* Energy Conversion and Management, 2022. **267**: p. 115838.
49. Akkurt, G.G., et al., *Dynamic thermal and hygrometric simulation of historical buildings: Critical factors and possible solutions.* Renewable and Sustainable Energy Reviews, 2020. **118**: p. 109509.
50. Mi, P., et al., *Study on energy efficiency and economic performance of district heating system of energy saving reconstruction with photovoltaic thermal heat pump.* Energy Conversion and Management, 2021. **247**: p. 114677.
51. Fiorentini, M., P. Heer, and L. Baldini, *Design optimization of a district heating and cooling system with a borehole seasonal thermal energy storage.* Energy, 2023. **262**: p. 125464.
52. Luo, Y., Y. Shi, and N. Cai, *Chapter 5 - Stabilization of intermittent renewable energy using power-to-X*, in *Hybrid Systems and Multi-energy Networks for the Future Energy Internet*, Y. Luo, Y. Shi, and N. Cai, Editors. 2021, Academic Press. p. 113-140.
53. Pratschner, S., et al., *Off-grid vs. grid-based: Techno-economic assessment of a power-to-liquid plant combining solid-oxide electrolysis and Fischer-Tropsch synthesis.* Chemical Engineering Journal, 2024. **481**: p. 148413.
54. Zhao, J., et al., *How the power-to-liquid technology can contribute to reaching carbon neutrality of the China's transportation sector?* Energy, 2022. **261**: p. 125058.
55. Sánchez-Luján, J., Á. Molina-García, and J.J. López-Cascales, *Optimal integration modeling of Co – Electrolysis in a power-to-liquid industrial process.* International Journal of Hydrogen Energy, 2024. **52**: p. 1202-1219.
56. Markowitsch, C., M. Lehner, and M. Maly, *Evaluation of process structures and reactor technologies of an integrated power-to-liquid plant at a cement factory.* Journal of CO2 Utilization, 2023. **70**: p. 102449.
57. Skov, I.R. and N. Schneider, *Incentive structures for power-to-X and e-fuel pathways for transport in EU and member states.* Energy Policy, 2022. **168**: p. 113121.
58. Rojas-Michaga, M.F., et al., *Sustainable aviation fuel (SAF) production through power-to-liquid (PtL): A combined techno-economic and life cycle assessment.* Energy Conversion and Management, 2023. **292**: p. 117427.
59. Chen, X., et al., *Photovoltaic-driven liquid air energy storage system for combined cooling, heating and power towards zero-energy buildings.* Energy Conversion and Management, 2024. **300**: p. 117959.
60. Bahnamiri, F.K., et al., *Techno-economic assessment of a novel power-to-liquid system for synthesis of formic acid and ammonia, based on CO2 electroreduction and alkaline water electrolysis cells.* Renewable Energy, 2022. **187**: p. 1224-1240.
61. Hu, X., et al., *Advanced Fault Diagnosis for Lithium-Ion Battery Systems: A Review of Fault Mechanisms, Fault Features, and Diagnosis Procedures.* IEEE Industrial Electronics Magazine, 2020. **14**(3): p. 65-91.

62. Mazumder, S.K., et al., *A Review of Current Research Trends in Power-Electronic Innovations in Cyber–Physical Systems.* IEEE Journal of Emerging and Selected Topics in Power Electronics, 2021. **9**(5): p. 5146-5163.
63. Genovese, M., et al., *Power-to-hydrogen and hydrogen-to-X energy systems for the industry of the future in Europe.* International Journal of Hydrogen Energy, 2023. **48**(44): p. 16545-16568.
64. Escamilla, A., D. Sánchez, and L. García-Rodríguez, *Assessment of power-to-power renewable energy storage based on the smart integration of hydrogen and micro gas turbine technologies.* International Journal of Hydrogen Energy, 2022. **47**(40): p. 17505-17525.
65. Zhao, P., et al., *Assessment the hydrogen-electric coupled energy storage system based on hydrogen-fueled CAES and power-to-gas-to-power device considering multiple time-scale effect and actual operation constraints.* International Journal of Hydrogen Energy, 2023. **48**(25): p. 9198-9218.
66. Ren, J., et al., *Methanation of CO/CO2 for power to methane process: Fundamentals, status, and perspectives.* Journal of Energy Chemistry, 2023. **80**: p. 182-206.
67. Izzeldin, M., et al., *The impact of the Russian-Ukrainian war on global financial markets.* International Review of Financial Analysis, 2023. **87**: p. 102598.
68. Sodiq, A., et al., *A review on progress made in direct air capture of CO2.* Environmental Technology & Innovation, 2023. **29**: p. 102991.
69. Arshad, N. and A. Alhajaj, *Process synthesis for amine-based CO2 capture from combined cycle gas turbine power plant.* Energy, 2023. **274**: p. 127391.
70. Gruber, M., et al., *Insights into the catalytic CO2 methanation of a boiling water cooled fixed-bed reactor: Simulation-based analysis.* Chemical Engineering Journal, 2021. **406**: p. 126788.
71. Jensen, M.B., L.D.M. Ottosen, and M.V.W. Kofoed, *H2 gas-liquid mass transfer: A key element in biological Power-to-Gas methanation.* Renewable and Sustainable Energy Reviews, 2021. **147**: p. 111209.
72. Klimenko, V., & Suprun, T., *Methanation technologies for producing synthetic renewable methane.* Thermophysics and Thermal Power Engineering, 2022. **44**(3): p. 63-72.
73. Sekoai, P.T., et al., *Thermophilic Biogas Upgrading via ex Situ Addition of H2 and CO2 Using Codigested Feedstocks of Cow Manure and the Organic Fraction of Solid Municipal Waste.* ACS Omega, 2020. **5**(28): p. 17367-17376.
74. Giglio, E., R. Pirone, and S. Bensaid, *Dynamic modelling of methanation reactors during start-up and regulation in intermittent power-to-gas applications.* Renewable Energy, 2021. **170**: p. 1040-1051.
75. Anuar Sharuddin, S.D., et al., *A review on pyrolysis of plastic wastes.* Energy Conversion and Management, 2016. **115**: p. 308-326.
76. Du, Y., et al., *Core-shell equivalent reactor network model to bridging CFD and process simulations of a fluidized bed reactor.* Chemical Engineering Science, 2024. **287**: p. 119772.

77. Salmi, T., et al., *Kinetics and reactor modelling of a complex three-phase system: Carbonation of epoxides on grafted catalysts.* Chemical Engineering Science, 2024. **285**: p. 119578.
78. Quarton, C.J. and S. Samsatli, *Power-to-gas for injection into the gas grid: What can we learn from real-life projects, economic assessments and systems modelling?* Renewable and Sustainable Energy Reviews, 2018. **98**: p. 302-316.
79. Bolt, A., I. Dincer, and M. Agelin-Chaab, *Design and assessment of a new helical fixed bed type CO2 methanation reactor.* Fuel, 2023. **337**: p. 127176.
80. Aubin, P., L. Wang, and J. Van herle, *Evaporating water-cooled methanation reactor for solid-oxide stack-based power-to-methane systems: Design, experiment and modeling.* Chemical Engineering Journal, 2023. **456**: p. 140256.
81. Patcharavorachot, Y., et al., *Comparative energy, economic, and environmental analyses of power-to-gas systems integrating SOECs in steam-electrolysis and co-electrolysis and methanation.* Thermal Science and Engineering Progress, 2023. **42**: p. 101873.
82. Zhong, L., et al., *Optimal design and off-design performance improvement for power-to-methane system integrating solid oxide electrolysis cell with methanation reactor.* Fuel, 2024. **356**: p. 129314.
83. Prabhakaran, P., et al., *Modelling and validation of energy systems with dynamically operated Power to Gas plants for gas-based sector coupling in de-central energy hubs.* Energy Conversion and Management, 2023. **276**: p. 116534.
84. Mazza, A., et al., *Impact of Power-to-Gas on distribution systems with large renewable energy penetration.* Energy Conversion and Management: X, 2020. **7**: p. 100053.
85. Abugabbara, M., et al., *Bibliographic analysis of the recent advancements in modeling and co-simulating the fifth-generation district heating and cooling systems.* Energy and Buildings, 2020. **224**: p. 110260.
86. Bünning, F., et al., *Bidirectional low temperature district energy systems with agent-based control: Performance comparison and operation optimization.* Applied Energy, 2018. **209**: p. 502-515.
87. Reiners, T., et al., *Heat pump efficiency in fifth generation ultra-low temperature district heating networks using a wastewater heat source.* Energy, 2021. **236**: p. 121318.
88. Puttige, A.R., et al., *Modeling and optimization of hybrid ground source heat pump with district heating and cooling.* Energy and Buildings, 2022. **264**: p. 112065.
89. Calise, F., et al., *A solar-driven 5th generation district heating and cooling network with ground-source heat pumps: a thermo-economic analysis.* Sustainable Cities and Society, 2022. **76**: p. 103438.
90. Lund, H., et al., *Perspectives on fourth and fifth generation district heating.* Energy, 2021. **227**: p. 120520.
91. Buffa, S., et al., *5th generation district heating and cooling systems: A review of existing cases in Europe.* Renewable and Sustainable Energy Reviews, 2019. **104**: p. 504-522.

92. Calise, F., et al., *Optimal design of a 5th generation district heating and cooling network based on seawater heat pumps.* Energy Conversion and Management, 2022. **267**: p. 115912.
93. Meha, D., et al., *A novel spatial–temporal space heating and hot water demand method for expansion analysis of district heating systems.* Energy Conversion and Management, 2021. **234**: p. 113986.
94. Calise, F., et al., *A novel hybrid polygeneration system supplying energy and desalinated water by renewable sources in Pantelleria Island.* Energy, 2017. **137**: p. 1086-1106.
95. Calise, F., et al., *Water-energy nexus: A thermoeconomic analysis of polygeneration systems for small Mediterranean islands.* Energy Conversion and Management, 2020. **220**: p. 113043.
96. Buonomano, A., F. Calise, and G. Ferruzzi, *Thermoeconomic analysis of storage systems for solar heating and cooling systems: A comparison between variable-volume and fixed-volume tanks.* Energy, 2013. **59**: p. 600-616.
97. Republic, P.o.t.I., *D.P.R. 26 agosto 1993, n. 412, Regolamento recante norme per la progettazione, l'installazione, l'esercizio e la manutenzione degli impianti termici degli edifici, in attuazione dell'art. 4, comma 4, della L. 9 gennaio 1991, n. 10 (in Italian).* 1993.
98. Calise, F., et al., *A comparative thermoeconomic analysis of fourth generation and fifth generation district heating and cooling networks.* Energy, 2023. **284**: p. 128561.
99. Østergaard, D.S., et al., *Low-temperature operation of heating systems to enable 4th generation district heating: A review.* Energy, 2022. **248**: p. 123529.
100. Wirtz, M., et al., *Quantifying Demand Balancing in Bidirectional Low Temperature Networks.* Energy and Buildings, 2020. **224**: p. 110245.
101. Gesteira, L.G., et al. *Thermoeconomic Optimization of a Polygeneration System Based on a Solar-Assisted Desiccant Cooling*. Sustainability, 2023. **15**, DOI: 10.3390/su15021516.
102. Calise, F., et al., *A novel smart energy network paradigm integrating combined heat and power, photovoltaic and electric vehicles.* Energy Conversion and Management, 2022. **260**: p. 115599.
103. Estadistica, I.N.d.
104. Casquero-Modrego, N. and M. Goñi-Modrego, *Energy retrofit of an existing affordable building envelope in Spain, case study.* Sustainable Cities and Society, 2019. **44**: p. 395-405.
105. Calise, F., et al., *Dynamic modelling and thermoeconomic analysis for the energy refurbishment of the Italian building sector: Case study for the "Superbonus 110 %" funding strategy.* Applied Thermal Engineering, 2022. **213**: p. 118689.
106. Maximov, S.A., S. Mehmood, and D. Friedrich, *Multi-objective optimisation of a solar district heating network with seasonal storage for conditions in cities of southern Chile.* Sustainable Cities and Society, 2021. **73**: p. 103087.
107. Caleffi, M., ed. Impianti a pompe di calore geotermiche. 2010.

108. Zhu, J., X. Cui, and W. Ni, *Model predictive control based control strategy for battery energy storage system integrated power plant meeting deep load peak shaving demand.* Journal of Energy Storage, 2022. **46**: p. 103811.
109. Kim, J., Y. Suharto, and T.U. Daim, *Evaluation of Electrical Energy Storage (EES) technologies for renewable energy: A case from the US Pacific Northwest.* Journal of Energy Storage, 2017. **11**: p. 25-54.
110. Zubi, G., et al., *The lithium-ion battery: State of the art and future perspectives.* Renewable and Sustainable Energy Reviews, 2018. **89**: p. 292-308.
111. Ahmadian, A., et al., *Plug-in electric vehicle batteries degradation modeling for smart grid studies: Review, assessment and conceptual framework.* Renewable and Sustainable Energy Reviews, 2018. **81**: p. 2609-2624.
112. Tolomeo, R., et al., *Application of Life Cycle Assessment to Lithium Ion Batteries in the Automotive Sector.* Sustainability, 2020. **12**(11).
113. Shen, M., et al., *Progress and prospects of reversible solid oxide fuel cell materials.* iScience, 2021. **24**(12): p. 103464.
114. Venkataraman, V., et al., *Reversible solid oxide systems for energy and chemical applications – Review & perspectives.* Journal of Energy Storage, 2019. **24**: p. 100782.
115. Beigzadeh, M., et al., *Energy and exergy analyses of solid oxide fuel cell-gas turbine hybrid systems fed by different renewable biofuels: A comparative study.* Journal of Cleaner Production, 2021. **280**: p. 124383.
116. Calise, F., et al. *Dynamic Simulation and Thermoeconomic Analysis of a Hybrid Renewable System Based on PV and Fuel Cell Coupled with Hydrogen Storage*. Energies, 2021. **14**, DOI: 10.3390/en14227657.
117. Wang, C., et al., *Dynamic modeling and parameter analysis study on reversible solid oxide cells during mode switching transient processes.* Applied Energy, 2020. **263**: p. 114601.
118. Hajimolana, S.A., et al., *Mathematical modeling of solid oxide fuel cells: A review.* Renewable and Sustainable Energy Reviews, 2011. **15**(4): p. 1893-1917.
119. Calise, F., et al., *Energy efficiency in small districts: Dynamic simulation and technoeconomic analysis.* Energy Conversion and Management, 2020. **220**: p. 113022.
120. Calise, F., et al., *Renewable smart energy network: A thermoeconomic comparison between conventional lithium-ion batteries and reversible solid oxide fuel cells.* Renewable Energy, 2023. **214**: p. 74-95.
121. Safaei, A., A. Hossein Nezhad, and A. Rashidi, *High temperature nanofluids based on therminol 66 for improving the heat exchangers power in gas refineries.* Applied Thermal Engineering, 2020. **170**: p. 114991.
122. Nissan. *https://www.nissan.it/veicoli/veicoli-nuovi/leaf.html - 06/2019*. 2019 06/2019]; Available from: https://www.nissan.it/veicoli/veicoli-nuovi/leaf.html.
123. Buonomano, A., et al., *Dynamic analysis of the integration of electric vehicles in efficient buildings fed by renewables.* Applied Energy, 2019. **245**: p. 31-50.

124. Renault. *https://www.renault.it/veicoli/auto-elettriche-e-veicoli-elettrici/nuova-zoe.html - 06/2019*. Available from: https://www.renault.it/veicoli/auto-elettriche-e-veicoli-elettrici/nuova-zoe.html.
125. Calise, F., et al., *A novel paradigm for a sustainable mobility based on electric vehicles, photovoltaic panels and electric energy storage systems: Case studies for Naples and Salerno (Italy).* Renewable and Sustainable Energy Reviews, 2019. **111**: p. 97-114.
126. Calise, F., et al., *A novel approach for the calculation of the energy savings of heat metering for different kinds of buildings.* Energy and Buildings, 2021. **252**: p. 111408.
127. Calise, F., et al., *Smart grid energy district based on the integration of electric vehicles and combined heat and power generation.* Energy Conversion and Management, 2021. **234**: p. 113932.
128. https://global.aermec.com/it/.
129. Calise, F., et al., *Integration of photovoltaic panels and solar collectors into a plant producing biomethane for the transport sector: Dynamic simulation and case study.* Heliyon, 2023. **9**(4): p. e14681.
130. Calise, F., *Modeling of the anaerobic digestion of organic wastes: integration of heat transfer and biochemical aspects.* Energies, 2020(13).
131. Tica, S., *Study of the fuel efficiency and ecological aspects of CNG buses in urban public transport in Belgrade.* Journal of applied engineering science, 2019(17): p. 65-73.
132. Calise, F., et al., *Dynamic analysis and investigation of the thermal transient effects in a CSTR reactor producing biogas.* Energy, 2023. **263**: p. 126010.
133. Calise, F., et al., *Concentrating photovoltaic/thermal collectors coupled with an anaerobic digestion process: Dynamic simulation and energy and economic analysis.* Journal of Cleaner Production, 2021. **311**: p. 127363.
134. Wylock, C.E. and W.M. Budzianowski, *Performance evaluation of biogas upgrading by pressurized water scrubbing via modelling and simulation.* Chemical Engineering Science, 2017. **170**: p. 639-652.
135. Nock, W.J., et al., *Modeling the Water Scrubbing Process and Energy Requirements for CO2 Capture to Upgrade Biogas to Biomethane.* Industrial & Engineering Chemistry Research, 2014. **53**(32): p. 12783-12792.
136. Bozorg, M., et al., *Optimal process design of biogas upgrading membrane systems: Polymeric vs high performance inorganic membrane materials.* Chemical Engineering Science, 2020. **225**: p. 115769.
137. Fini, S., *K-MAX Series technical data*, in *V60PU97FNM760*, M. service, Editor. 2020: online.
138. Shi, J., et al., *Numerical study of a hybrid thermal lattice Boltzmann method for pool boiling heat transfer on a modeled hydrophilic metal foam surface.* Applied Thermal Engineering, 2023. **229**: p. 120535.
139. SNAM. *snam websites*. 2018; Available from: https://www.snam.it/it/transizione_energetica/biometano/benefici_e_utilizzo/.

140. R. Byron Bird, W.E.S., Edwin N. Lightfoot, *Transport Phenomena*. 19883.
141. Maggio, G., G. Squadrito, and A. Nicita, *Hydrogen and medical oxygen by renewable energy based electrolysis: A green and economically viable route.* Applied Energy, 2022. **306**: p. 117993.
142. Pastore, L.M., et al., *Power-to-gas as an option for improving energy self-consumption in renewable energy communities.* International Journal of Hydrogen Energy, 2022. **47**(69): p. 29604-29621.
143. Böhm, H., et al., *Projecting cost development for future large-scale power-to-gas implementations by scaling effects.* Applied Energy, 2020. **264**: p. 114780.
144. Carr, S., et al., *Hydrogen storage and demand to increase wind power onto electricity distribution networks.* International Journal of Hydrogen Energy, 2014. **39**(19): p. 10195-10207.
145. Luyben, W.L., *Capital cost of compressors for conceptual design.* Chemical Engineering and Processing - Process Intensification, 2018. **126**: p. 206-209.
146. Musharavati, F. and S. Khanmohammadi, *Performance improvement of a heat recovery system combined with fuel cell and thermoelectric generator: 4E analysis.* International Journal of Hydrogen Energy, 2021.
147. Nadir, M., A. Ghenaiet, and C. Carcasci, *Thermo-economic optimization of heat recovery steam generator for a range of gas turbine exhaust temperatures.* Applied Thermal Engineering, 2016. **106**: p. 811-826.
148. Zhai, H. and E.S. Rubin, *Performance and cost of wet and dry cooling systems for pulverized coal power plants with and without carbon capture and storage.* Energy Policy, 2010. **38**(10): p. 5653-5660.
149. https://eshop.czechminibreweries.com/.
150. Assometano. *Natural gas cost*. 2023; Available from: https://www.assogasmetano.it/distributori/prezzo-medio-nazionale/.
151. Vaziri Rad, M.A., et al., *Excess electricity problem in off-grid hybrid renewable energy systems: A comprehensive review from challenges to prevalent solutions.* Renewable Energy, 2023. **212**: p. 538-560.
152. Erdiwansyah, et al., *A critical review of the integration of renewable energy sources with various technologies.* Protection and Control of Modern Power Systems, 2021. **6**(1): p. 3.
153. Zheng, N., et al., *Dynamic modeling and response characteristics of a solar-driven polygeneration system coupled with hydrogen and thermal energy storage.* Energy Conversion and Management, 2023. **293**: p. 117496.
154. Esmaeilion, F., M. Soltani, and J. Nathwani, *Assessment of a novel solar-powered polygeneration system highlighting efficiency, exergy, economic and environmental factors.* Desalination, 2022. **540**: p. 116004.
155. Rout, A., et al., *Energy, exergy, and economic analysis of an off-grid solar polygeneration system.* Energy Conversion and Management, 2021. **238**: p. 114177.
156. Mousavi Rabeti, S.A., M.H. Khoshgoftar Manesh, and M. Amidpour, *Techno-economic and environmental assessment of a novel polygeneration system based on*

integration of biomass air-steam gasification and solar parabolic trough collector. Sustainable Energy Technologies and Assessments, 2023. **56**: p. 103030.
157. Fraia, S.D., M. Shah, and L. Vanoli, *A biomass-based polygeneration system for a historical building: A techno-economic and environmental analysis.* Energy Conversion and Management, 2023. **291**: p. 117336.
158. Xu, C., et al., *Thermodynamic analysis of a novel biomass polygeneration system for ammonia synthesis and power generation using Allam power cycle.* Energy Conversion and Management, 2021. **247**: p. 114746.
159. Luo, L., et al., *Energy, exergy and economic analysis of an integrated ground source heat pump and anaerobic digestion system for Co-generation of heating, cooling and biogas.* Energy, 2023. **282**: p. 128220.
160. Sahoo, U., et al., *Energy, exergy, economic analysis and optimization of polygeneration hybrid solar-biomass system.* Applied Thermal Engineering, 2018. **145**: p. 685-692.
161. Bellos, E., et al., *Investigation of a solar-biomass polygeneration system.* Energy Conversion and Management, 2018. **173**: p. 283-295.
162. Villarroel-Schneider, J., et al., *Open-source model applied for techno-economic optimization of a hybrid solar PV biogas-based polygeneration plant: The case of a dairy farmers' association in central Bolivia.* Energy Conversion and Management, 2023. **291**: p. 117223.
163. Barco-Burgos, J., et al., *Thermal characterization of an alkaline electrolysis cell for hydrogen production at atmospheric pressure.* Fuel, 2020. **276**: p. 117910.
164. Cimmino, L.B., J. B.; Eicker, U., *Optimal Control Strategy for Mixed Fuel Use in a Renewable Polygeneration System.* Proceedings of the 12th International Conference on Smart Cities and Green ICT Systems - SMARTGREENS, 2023. **70**(78).
165. Jatana, G.S., et al., *Strategies for high efficiency and stability in biogas-fuelled small engines.* Experimental Thermal and Fluid Science, 2014. **54**: p. 189-195.
166. Kalinci, Y. and I. Dincer, *Analysis and performance assessment of NH3 and H2 fed SOFC with proton-conducting electrolyte.* International Journal of Hydrogen Energy, 2018. **43**(11): p. 5795-5807.
167. Barco-Burgos, J., et al., *Hydrogen-rich syngas production from palm kernel shells (PKS) biomass on a downdraft allothermal gasifier using steam as a gasifying agent.* Energy Conversion and Management, 2021. **245**: p. 114592.
168. Ermolaev, D.V., et al., *Modeling of air gasification of dark fermentation digestate in a downdraft gasifier.* International Journal of Hydrogen Energy, 2023. **48**(63): p. 24255-24263.
169. Buonomano, A., et al., *Transient analysis, exergy and thermo-economic modelling of façade integrated photovoltaic/thermal solar collectors.* Renewable Energy, 2019. **137**: p. 109-126.
170. Buonomano, A., F. Calise, and A. Palombo, *Buildings dynamic simulation: Water loop heat pump systems analysis for European climates.* Applied Energy, 2012. **91**(1): p. 222-234.

171. Firtina-Ertis, I., *Thermodynamic and electrochemical assessment of an alkaline electrolyzer (AE) at different operating parameters.* Journal of Environmental Chemical Engineering, 2022. **10**(2): p. 107225.
172. Hammoudi, M., et al., *New multi-physics approach for modelling and design of alkaline electrolyzers.* International Journal of Hydrogen Energy, 2012. **37**(19): p. 13895-13913.
173. Di Giulio, E., et al., *Effective Thermal Conductivity Model for Tetragonal Pin Array Stack.* Journal of Fluid Flow, Heat and Mass Transfer, 2022. **9**: p. 38-42.
174. Dincer, I. and M.A. Rosen, *Chapter 3 - Chemical Exergy*, in *Exergy (Second Edition)*, I. Dincer and M.A. Rosen, Editors. 2013, Elsevier. p. 31-49.
175. Palange, R., C. De Blasio, and M. Krishnan, *Energy and exergy analysis of gasification of solid fuels by optimization of chemical kinetics.* Energy, 2023. **285**: p. 129487.
176. Jiao, L., et al., *Microwave torrefaction integrated with gasification: Energy and exergy analyses based on Aspen Plus modeling.* Applied Energy, 2022. **319**: p. 119255.
177. Frenkel, D. and B. Smit, *Chapter 2 - Thermodynamics and statistical mechanics*, in *Understanding Molecular Simulation (Third Edition)*, D. Frenkel and B. Smit, Editors. 2023, Academic Press. p. 11-51.
178. Zhu, X., et al., *Flue gas torrefaction of municipal solid waste: Fuel properties, combustion characterizations, and nitrogen /sulfur emissions.* Bioresource Technology, 2022. **351**: p. 126967.
179. Castro, L., et al., *Low cost digester monitoring under realistic conditions: Rural use of biogas and digestate quality.* Bioresource Technology, 2017. **239**: p. 311-317.
180. UPME, U.d.P.M.E., *Balance Energético Colombiano* 2020, MECANISMO PARA LA MITIGACIÓN VOLUNTARIA DE EMISIONES DE GASES EFECTO INVERNADERO PARA COLOMBIA: observatoriodeenergia.gov.co.
181. Bocci, E., et al., *State of Art of Small Scale Biomass Gasification Power Systems: A Review of the Different Typologies.* Energy Procedia, 2014. **45**: p. 247-256.
182. Demichelis, F., et al., *Life cycle assessment and life cycle costing of advanced anaerobic digestion of organic fraction municipal solid waste.* Chemosphere, 2022. **289**: p. 133058.
183. Calise, F., et al., *Dynamic simulation modelling of reversible solid oxide fuel cells for energy storage purpose.* Energy, 2022. **260**: p. 124893.
184. Bogotá, J.B.d., *Informe de Gestion Jardín Botánico de Bogotá a 30 de Junio de 2023*. 2023.
185. Cappiello, F.L. and T.G. Erhart, *Modular cogeneration for hospitals: A novel control strategy and optimal design.* Energy Conversion and Management, 2021. **237**: p. 114131.